Nanomedicines in Cancer Therapy: From Long-Circulating Drug Carriers to Novel Therapeutic Concepts

Inauguraldissertation

zur

Erlangung der Würde eines Doktors der Philosophie
vorgelegt der
Philosophisch-Naturwissenschaftlichen Fakultät
der Universität Basel

von

Philip Grossen

aus der Schweiz
Basel, 2017

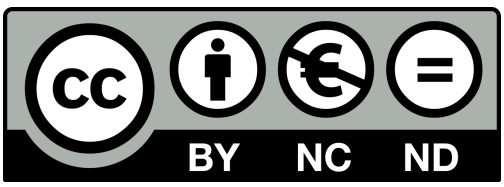

Genehmigt von der Philosophisch-Naturwissenschaftlichen Fakultät

auf Antrag von

Prof. Dr. Jörg Huwyler

Prof. Dr. Gert Fricker

Basel, den 20. Juni 2017

Prof. Dr. Martin Spiess (Dekan)

"I may not have gone where I intended to go, but I think I have ended up where I needed to be."

Douglas Adams, *The Long Dark Tea-Time of the Soul*

TABLE OF CONTENT

ZUSAMMENFASSUNG FÜR LAIEN

Krebserkrankungen sind nach wie vor ein Hauptgrund für vorzeitige Sterblichkeit. Während Fortschritte im Verständnis von Krebs auf molekularer und genetischer Ebene zur Identifizierung neuer potentieller therapeutischer Ansätze geführt haben, gibt es weiterhin viel Potential bei der Entwicklung von effizienten und spezifischen Krebstherapien. Viele Wirkstoffe in der frühen Entwicklung sind durch schlechte physiko-chemische Eigenschaften charakterisiert (bspw. eine schlechte Löslichkeit in Wasser). Als Konsequenz haben diese Wirkstoffe oft eine problematische Pharmacokinetik und zeigen eine hohe Anreicherung in Nicht-Tumor Gewebe, welche zu Dosis-limitierenden Nebenwirkungen führen kann. Neue Ansätze zur Formulierung solcher Wirkstoffe sind daher von grossem Nutzen. Nanomedizin stellt eine vielversprechende Strategie dar, um die physiko-chemischen Eigenschaften von Wirkstoffen zu optimieren, und um Wirkstoffe gezielt an ihren Wirkort (die Krebszelle) zu navigieren. Dies kann über passive Akkumulierung oder über aktives Binden der Nanopartikel an Rezeptoren auf der Zielzelle passieren. Das Ziel dieses Projektes war die Entwicklung von Nanopartikeln für die Formulierung von Zytostatika, sowie die Entwicklung eines neuen Ansatzes zur Therapie von Leberkrebs. Diese Arbeit kann deshalb folgendermassen in zwei Hauptteile zusammengefasst werden:

Erstens wurden biokompatible und bioabbaubare Polymere verwendet um Nanopartikel herzustellen welche als Plattform zum Transport von zytostatischen Medikamenten dienen können. Die Partikel wurden *in vitro* in humanen Zellen sowie im Tiermodell getestet. Die Nanopartikel wurden mit Doxorubicin, einem zugelassenen Krebstherapeutikum, beladen und die Stabilität sowie die Effizienz der Beladung getestet. Anschliessend wurde die zelluläre Aufnahme der Nanopartikel in humanen Krebszellen analysiert und der therapeutische Effekt getestet. In einem nächsten Schritt wurde die Pharmacokinetik der Nanopartikel in Ratten getestet und die Plasma-Konzentrations-Zeit Profile mit dem Gold-Standard für lang-zirkulierende Nanopartikel (PEGylierte Liposomen) verglichen. Eine lange Plasma Halbwertszeit ist eine wichtige Voraussetzung für effiziente Akkumulation im Tumor Gewebe. Es wurde zudem ein Protokoll zur Herstellung von sogenannten Gold-Nanohybrid Partikeln entwickelt. Diese Nanopartikel eignen sich besonders für die Darstellung der zellulären Aufnahme von Nanopartikeln und können somit für die Aufschlüsselung von Aufnahmemechanismen oder bei der Diagnose eingesetzt werden. In einem letzten Schritt wurden die Nanopartikel mit einem Antikörper funktionalisiert welcher Rezeptoren auf Zielzellen erkennt und bindet. Dies ermöglicht eine effiziente und spezifische zelluläre Aufnahme der Nanopartikel. Die Interaktion dieser funktionalisierten Nanopartikel mit den Zielzellen wurde *in vitro* mit verschiedenen Methoden analysiert.

Zweitens wurde das Effektorprotein des onkotoxischen Virus „H-1 Parvovirus“ als neuartige Therapie bei Leberkrebs getestet. Dieses Virus wurde in präklinischen Studien bereits gegen verschiedene Krebsarten eingesetzt und wird in einer klinischen Studie in Patienten mit Hirntumoren getestet. Trotz dieser vielversprechenden Resultate kann die virale Krebstherapie mit einigen

Problemen verbunden sein. Ziel dieser Studie war es deshalb, das therapeutische Potential des Effektorproteins (NS1) in Leberkrebszellen nach nicht-viralem Gen-Transfer zu untersuchen. In einem ersten Schritt wurde die Effizienz der Genexpression in einem Set von Leberkrebszellen untersucht und der therapeutische Effekt von NS1 charakterisiert. Um zu zeigen dass die Therapie spezifisch für Krebszellen ist und kein Effekt auf gesunde Zellen hat, wurden ebenfalls frisch isolierte humane Leberzellen getestet. In weiteren mechanistischen *in vitro* Experimenten wurde der NS1-induzierte Zelltod detailliert untersucht. Zusätzlich wurde ein Biomarker für die Sensitivität von Krebszellen auf NS1 getestet und evaluiert. Als letztes wurde die Verträglichkeit dieses neuen therapeutischen Ansatzes nach einmaliger oder multipler Dosierung in Mäusen getestet.

SUMMARY

Cancer is still a leading cause of death worldwide. Despite the progress in the molecular understanding of cancer diseases, there's an urgent need in novel therapeutics and drug delivery strategies. Many novel anti-cancer compounds in early development are characterized by unfavorable physico-chemical properties and lack in drug-like properties. As a result, many of these compounds suffer from insufficient pharmacokinetic properties and show a high accumulation in off-target tissue that can induce dose-limiting side effects. Nanomedicines depict a promising strategy to optimize the pharmacokinetics of such compounds and to deliver them to their site of action: The cancer cell. The goal of this thesis was to develop nanoparticulate drug delivery platforms for passive and active drug targeting. In addition, a novel nanoparticle-based gene therapeutic for the treatment of liver cancer was evaluated. This thesis can be summarized in two main parts as follows:

In a first part, a biocompatible and biodegradable polymer was used to prepare micelles for the delivery of small molecular anticancer drugs. These micelles were tested subsequently on *in vitro* and *in vivo* models. A highly reproducible protocol for the formulation of doxorubicin-loaded micelles was developed and micelles were characterized extensively for their physico-chemical properties. Cellular uptake of micelles was analyzed and their therapeutic potential was assessed *in vitro* on human cancer cells. To passively accumulate in solid tumors, nanoparticles need to be long-circulating and must remain in the blood circulation for hours. Therefore, the pharmacokinetic profile and biodistribution of doxorubicin-loaded micelles in rats was analyzed and compared to the gold standard of long-circulating nanoparticles: PEGylated liposomes. In a next step, a protocol for the preparation of so-called gold-nanohybrids was developed. Such nanohybrids are valuable tools to analyze nanoparticle-cell interactions and the intracellular fate of nanoparticles in detail. Further, such nanoparticles can be used as diagnostic tools. In a last step, micelles were functionalized with an antibody for targeted drug delivery. Cellular internalization of these micelles was analyzed using an array of methods.

In a second part, a novel therapeutic strategy using the main effector protein of the rat parvovirus (H-1) for the treatment of hepatocellular carcinoma (HCC) was developed. H-1 parvovirus showed promising results in the preclinical setting and was consequently tested in a clinical trial in patients suffering form glioma. Despite this development, viral therapies may be linked with several issues. Therefore, the potential of the viral effector protein NS1 for the treatment of liver cancer was analyzed after non-viral gene delivery. In a first step, the gene-delivery efficiency and the therapeutic effect were analyzed in a panel of human liver cancer-derived cell lines. Various *in vitro* assays were used to study the NS1-induced cell death in detail. To show that this therapeutic approach is specific for cancer cells, the treatment was furthermore tested on healthy human liver cells. To identify cells that are susceptible for this therapeutic approach, a biomarker for the sensitivity to non-viral NS1 therapy was evaluated. Finally, safety of this therapy was analyzed in mice after single and multiple dosing.

INTRODUCTION

1 NANOMEDICINES

The use of nanoparticulate drug carriers for the delivery of small molecules and biologics (e.g. proteins or nucleic acids) gained increasing interest within the last decades. Whereas the principle of the "magic bullet" was already introduced by Paul Ehrlich in the beginning of the last century [1], recent progress in the development of engineered nanomaterials (ENMs) allows to translate this theoretical paradigm into drug therapies. Several nanoparticulate drug delivery platforms were approved by health care authorities recently and are successfully used in clinical practice [2,3].

1.1 HISTORY OF NANOMEDICINES

The development of nanomedicines was revolutionized by the use of liposomes [4]. First used to study membrane behavior [5], their potential in the encapsulation and delivery of drugs was discovered in the early 1960s [6–8]. At the beginning, major drawbacks of their use were burst drug release after dilution and substantial uptake by mononuclear macrophages. To overcome these issues, the principle of PEGylation was implemented and resulted in so-called "stealth liposomes" [9]. These liposomes show less protein opsonization, reduced uptake by the mononuclear phagocyte system (MPS), and as a consequence a prolonged plasma circulation half-life. With the approval of Doxil® in the 1990s, the first nanoparticulate (i.e. liposomal) formulation was successfully introduced in to clinical practice [10]. This approval paved the way for more advanced systems, e.g. for the delivery of complex biologics such as proteins and nucleic acids using nanoparticles (NPs), as outlined in the next sections.

1.2 TYPES OF NANOPARTICLES

According to the European Commission, ENMs are defined as '*intentionally manufactured material, containing particles, in an unbound state or as an aggregate or as an agglomerate and where, for 50% or more of the particles in the number size distribution, one or more external dimensions is in the size range 1 nm to 100 nm*' [11,12]. ENMs share distinct characteristics such as a minute size, a high surface to volume ratio, and unique physico-chemical properties. With respect to pharmaceutical applications, NPs can be classified e.g. according to their chemical composition and their morphology. Besides lipid-based NPs mentioned above, nanomedicine platforms based on viruses, inorganic materials, and polymers were developed and reached market approval in the last decade [2]. The following section is providing an overview about the different nanomedicine platforms used in drug delivery (Fig. 1).

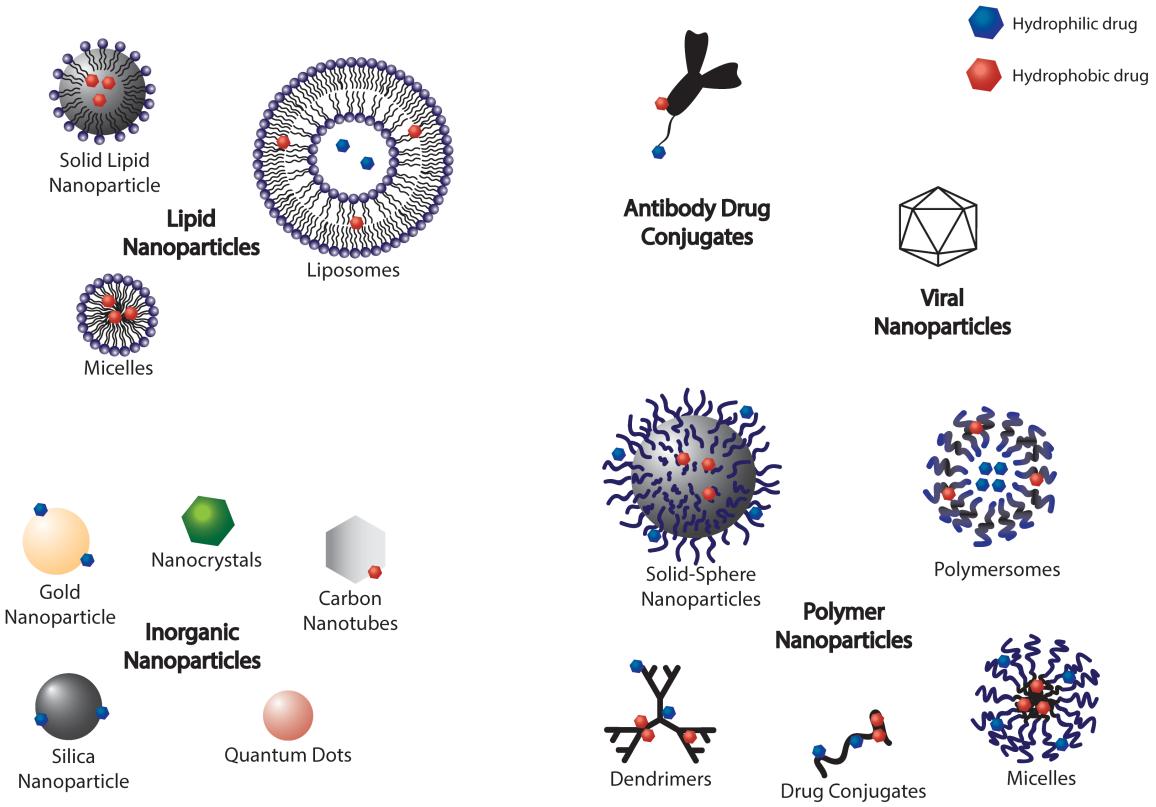

Figure 1 Schematic overview about types of nanomedicines.

Materials such as colloidal gold, iron oxide, silica, and graphene are used for the production of **inorganic nanoparticles** [13]. Characterized by unique physico-chemical properties (e.g. photo-thermal features, high electron density, and optical properties), inorganic NPs are of big interest as therapeutics, drug carriers, imaging tools, and as theranostics, combining diagnosis and treatment of a disease [14]. Quantum dots and nanocrystals, for example, with their size-tunable absorption and emission properties, are dominant classes of *in vitro* and *in vivo* optical imaging probes [13]. Several diagnostic inorganic NPs were approved by health care authorities and some therapeutic inorganic constructs such as AuroLase™ are in clinical development. AuroLase™, i.e. PEGylated silica-gold nanoshells, are used for the treatment of head and neck cancer via laser-induced thermal ablation [15].

Viral nanoparticles are used as gene delivery vectors. Viruses evolved to transfer their nucleic acids payload in a highly efficient way to specific cell types [16]. When genetically modified, recombinant viral vectors can be used to deliver therapeutic nucleic acids such as DNA or RNA into target cells. Retroviruses, adenoviruses, adeno-associated viruses (AAV), and herpes viruses are frequently used gene delivery vectors [17]. In addition, some viruses are characterized by an (inherent) ability to specifically kill transformed cells. Oncolytic viruses such as the herpes simplex virus and the H-1 parvovirus are therefore tested as cancer therapeutics [18]. With T-Vec™ (talimogene laherparepvec), the first oncolytic virus for the treatment of melanoma was approved by health care authorities in 2015 [19,20].

Lipid-based nanoparticles were pioneers in the field of nanomedicines [4]. Drug delivery systems based on lipids can be classified according to their morphology into liposomes, micelles, lipoplexes, and solid-lipid NPs [21,22]. Besides natural occurring lipids such as phosphatidylcholine (PC) or phosphatidylinositol, both structural lipids of eukaryotic cell membranes and big libraries containing artificial synthetic lipids are used for the formulation of lipid-based NPs [23,24]. With such artificial lipids, advanced drug delivery strategies (e.g. triggered drug release and gene delivery platforms) were implemented. Until today, more than 10 lipid-based drug carriers for various indications such as cancer (e.g. Doxil®), pain (e.g. DepoDur™), and infectious diseases (e.g. AmBisome™) reached market approval [25].

Natural polymers such as polysaccharides (e.g. chitosan or cyclodextrins) and proteins (e.g. gelatin or albumin) are used to develop drug delivery systems [26–29]. They are characterized by a high biocompatibility and biodegradability, are low in their production costs, and show a high structural flexibility [29]. For example, a formulation of albumin-bound paclitaxel (Abraxane™) was approved by health care authorities and is used in the treatment of several solid tumors [30,31]. Antibodies are another class of promising nano-sized therapeutics. They can have an inherent therapeutic effect that can be further potentiated by conjugating small molecular drugs to the antibody (antibody drug conjugates, ADC) [32].

Because of their versatile chemistry and low batch-to-batch variability as compared to natural polymers, **synthetic polymers** are widely used in pharmaceutical applications. Synthetic polymers are used in the production of solid-sphere NPs, polymeric micelles, dendrimers, polymersomes, polyplexes, and polymer-drug conjugates [33]. Due to their biocompatibility, biodegradable aliphatic polyesters and their copolymers are of special interest. They were successfully used to develop medicinal devices, e.g. for tissue engineering and in the production of implants [34–37] and were further developed for the implementation of nanoparticulate drug delivery platforms. Typical examples are poly(lactic acid) [PLA], poly(glycolic acid) [PGA], poly(lactide-co-glycolide) [PLGA], or poly(ε-caprolactone) [PCL] and their copolymers [38,39]. In 2007, PEG-PLA-based polymeric micelles (Genexol-PM™) were approved by health care authorities as delivery vehicle for paclitaxel [40]. A recent and promising synthetic polymer, which is of special importance for this PhD thesis project is PEG-PCL. A detailed overview about PEG-PCL, including its synthesis, preparation of PEG-PCL NPs, and their application is provided in **Chapter I** of this thesis.

1.3 Clinical Application

Although the principles of nanomedicine are applicable to a broad range of indications, cancer therapy is the most advanced application of NPs. More than 4 out of 5 clinical trials testing NPs are registered in the field of cancer therapy [3]. Two main reasons may account for this. First, although there was major progress in the development of efficient cancer therapies (e.g. biologics), there is still

a high mortality for patients diagnosed with certain tumors [41]. Second, since many chemotherapeutic drugs are cytotoxic and lack in specificity, severe, dose limiting off-target effects are observed frequently. These side effects dramatically decrease the quality of life for patients and may even force therapy stops prior to successful management of the disease [42]. Thus cancer is a life-threatening disease and the therapy of cancer is still an unmet medical need. Since many drug candidates in development pipelines that show promising results in preclinical trials lack in drug-like properties (e.g. metabolic stability, solubility, unfavorable pharmacokinetics), their application is challenging and clinical translation is inefficient [43,44]. Therefore, advanced drug delivery systems and novel therapeutic strategies are of urgent need. The following section of this PhD thesis is focusing on the application of nanomedicines in cancer therapy.

2 Cancer Therapy

2.1 Basics

Cancer remains a major cause of death worldwide [41]. According to the World Health Organization (WHO), cancer is defined as the uncontrolled growth and spread of cells. Since cancer can develop in various cell types throughout the body and may metastasize to other organs during progression of the disease, cancer is characterized by a high heterogeneity [45,46]. However, a set of general hallmarks of cancer such as unlimited replication and proliferation, evading of apoptosis, and sustained angiogenesis was defined [47,48]. These cancer-cell related features were targeted by various therapeutic strategies [49]. Current options to treat cancer can be classified into surgical resection, radiation, and chemotherapy including immunotherapy. Whereas surgery and radiation depict first-line choice for some solid cancers, by far not all types of cancer can be treated this way. Especially when cancer becomes a systemic rather than a localized disease, chemotherapy becomes an important treatment option [50].

2.2 Delivery of Small Molecular Drugs

The development of chemotherapeutics was launched in the 1940s with the clinical use of alkylating agents developed during World War I [51]. Conventional chemotherapeutics are often unspecifically targeting rapidly growing and dividing cells and can therefore cause severe off-target effects [42]. These non-specific therapies are often characterized by a small therapeutic window and are thus limited in their clinical use despite potential benefits. With increasing understanding of cancer biology as well as major progress in combinatory chemistry and high-throughput screening techniques, big libraries of more specific chemotherapeutics (i.e. molecularly targeted therapies) were identified [52,53]. However, these compounds often have unfavorable physico-chemical characteristics and are lacking drug-like properties as defined by Lipinski and coworkers [43,54,55]. This often results in problems regarding drug formulation and negatively influences pharmacokinetics (PK). After systemic administration of these low molecular weight compounds, a rapid clearance from the systemic circulation, a large volume of distribution, a high tissue accumulation, and efficient metabolism and inactivation (e.g. by the liver) can be observed [56]. Such unfavorable PK may result in a low tumor

accumulation and increased off-target effects. Consequently, toxicity concerns and non-favorable PK properties are major reasons for the high attrition rate during clinical development of new chemotherapeutics: The likelihood of oncology drugs to be approved by health care authorities after reaching Phase-I clinical trials is less than 10% [55,57,58]. Nanomedicines depict a promising strategy to overcome these drawbacks and to dramatically increase the therapeutic index of potent chemotherapeutics. Nanoparticles can **(I)** increase the solubility of hardly soluble drugs, **(II)** prolong the plasma circulation time of drugs, **(III)** passively or **(IV)** actively target diseased cells, tissues, or organs, **(V)** increase efficiency of combination therapies and reduce drug resistances, **(VI)** release their drug payload upon internal or externally applied triggers, and **(VII)** be combined with diagnostic tools (i.e. theranostics). The following section is giving an overview. More detailed information with a major emphasis on PEG-PCL-based drug delivery systems is proved in **Chapter I** of this thesis.

(I) Unfavorable physico-chemical properties of promising therapeutic compounds are often resulting in drug formulation problems and are limiting their clinical use. NPs can improve the **solubility** of highly potent compounds and are thus sound candidates for the formulation of such drugs. Paclitaxel, for example, has a very low solubility in water (<0.3 µg/mL). Conventional marketed products contain emulsifiers like Cremophor® EL that can provoke undesirable side effects [59]. Therefore, PEG-PLA biodegradable polymeric micelles were developed for the delivery of paclitaxel [60]. This formulation (Genexol-PM®) was successfully tested in clinics and received market approval in 2007 [40]. In another approach, paclitaxel was conjugated to the protein albumin, a naturally occurring polymer. Again, albumin-based NPs showed promising clinical results and were approved by health care authorities in 2005 under the brand name Abraxane® [30,31].

(II) After encapsulation, nanoparticulate drug delivery systems can change **pharmacokinetics and biodistribution** of their drug payload. A long plasma half-life ($t_{1/2}$) and a high area under the plasma concentration curve (AUC) are prerequisites for efficient delivery of drugs since the dose reaching the target tissue increases with the number of passages through the organ and the organ permeability-surface area (see passive targeting) [39,61]. In addition, by preventing accumulation in e.g. metabolizing organs such as spleen and liver or fat tissue, off-target effects can be reduced. Anthracyclines, for example, are characterized by a high plasma clearance (CL), a low AUC, and a short plasma half-life after i.v. administration. However, encapsulation in PEG-liposomes results in a prominent increase in AUC and a significant prolongation of $t_{1/2}$ as shown in various preclinical and clinical studies [62]. This formulation was approved by health care authorities and was the first nanoparticulate drug delivery system to reach the market.

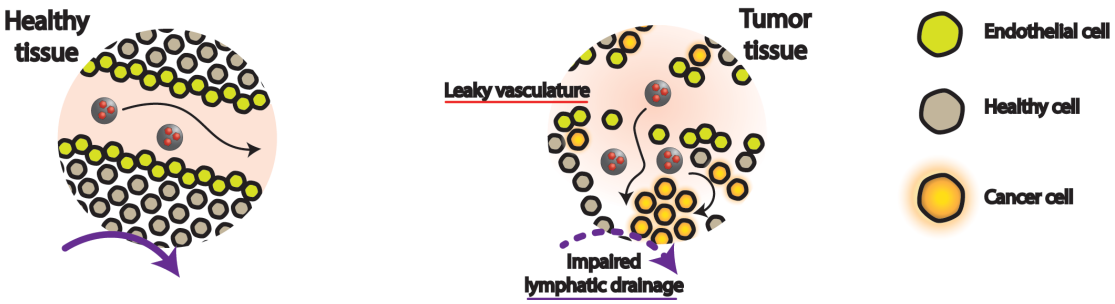

Figure 2 Passive targeting of solid tumors.

(III) The rapid cell proliferation of cancer cells increases the local demand for oxygen and nutrients supply that requires growth of new blood vessels. These fast growing blood vessels are often characterized by endothelial fenestration [63]. Long-circulating NPs can extravasate from such leaky blood vessels and can passively accumulate in solid tumors. In addition, many solid tumor lack in sufficient lymphatic drainage resulting in reduced clearance of macromolecules and NPs from the interstitial space [64]. In sum, this phenomenon is called enhanced permeability and retention (EPR) effect [65,66]. The extent of **passive drug targeting** (Fig. 2) strongly depends on tumor biology (e.g. blood flow, intratumoral pressure, and pore size of vascular fenestration) as well as key characteristics of the NPs such as size, shape, and surface charge [63,67]. The choice of the tumor model strongly influences the outcome of preclinical testing and establishment of relevant animal models depicts a major issue in the development of NPs for tumor therapy [68,69]. For example, a long-circulating liposomal formulation of the anticancer drug lurtotecan (NK 211) was evaluated in an ovary cell carcinoma xenograft model. Delivery of lurtotecan using liposomes resulted in a 9 to 67-fold increase in tumor exposure and superior therapeutic efficacy as compared to administration as free drug [70]. As a consequence, liposomal lurtotecan was tested in several clinical trials [71,72].

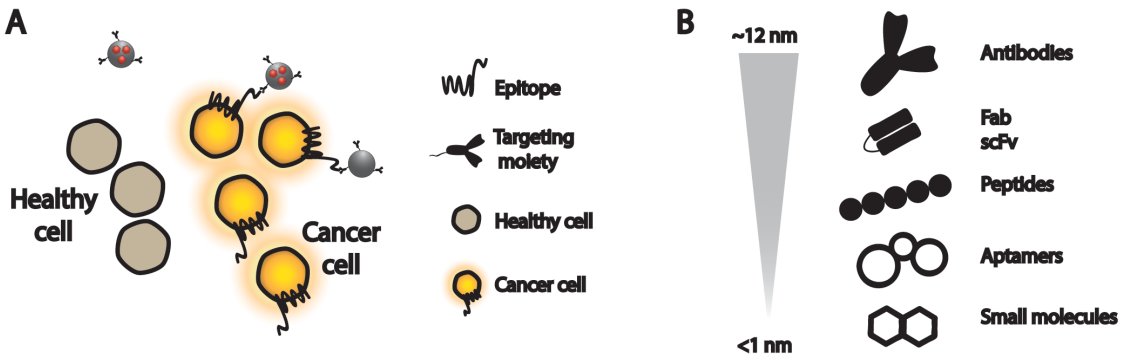

Figure 3 Active targeting of cancer cells. Schematic drawing of (A) targeted nanoparticles and (B) targeting ligands.

(IV) To specifically target cells and to improve cellular uptake, **active drug targeting** strategies were implemented. Active targeting takes advantage of specific surface-accessible receptors or epitopes overexpressed on target cells (Fig. 3A) [67]. Small molecular ligands (e.g. vitamins or carbohydrates)

as well as biologics (e.g. antibodies and aptamers) are therefore conjugated to the nanocarrier surface (Fig. 3B) [73]. Ligands should have sufficient binding affinity to their target, should be non-immunogenic, and not exceed certain size ranges [74]. Moreover, the amount of ligand per NP dramatically influences the drug targeting efficiency. On one hand, multivalent binding with high ligand densities can enhance the binding and uptake to target cells (i.e. avidity) [75]. On the other hand, loss of camouflage (i.e. stealth properties) and subsequent increase of NP uptake by mononuclear macrophages may decrease the circulation half-life and by this the targeting efficiency [76]. Cetuximab, a chimeric monoclonal antibody against the epidermal growth factor receptor (EGFR), was conjugated to FDA approved doxorubicin-loaded PEG-liposomes (Caelyx®) to treat patients with advanced solid tumors. The targeted delivery system successfully completed a Phase-I clinical trial recently and exceeded the therapeutic potential of free drug or drug encapsulated into non-targeted PEG-liposomes due to dramatically increased intracellular drug concentrations in tumor cells [77,78].

(V) For certain diseases, single drug therapies may not be sufficient and therefore **combination therapies** are often superior. Synergistic effects, that overwhelm simple additive effects of two drugs, can only occur at certain defined drug-to-drug ratios [79]. These ratios are often determined *in vitro* but translation of these results to the *in vivo* situation is difficult because of differences in drug metabolism and PK (DMPK) of the compounds. The synchronized delivery of a certain drug-to-drug ratio using NPs may help to translate these preclinical results into clinically relevant therapies [80,81]. A liposomal formulation combining the chemotherapeutics cytarabine and daunorubicin in a molar ratio of 5:1 (CPX-351) showed promising results in a Phase-III clinical trial treating patients suffering from acute myeloid leukemia [82–84]. Delivery of chemosensitizing agents (e.g. inhibitors of efflux transporters) and chemotherapeutics in the same delivery vehicle may in addition be a powerful tool to tackle multi-drug resistance [80].

(VI) Nanosized drug delivery systems can be tuned to efficiently release their drug cargo at the site of action. **Stimuli responsive** (“smart”) nanomedicines sensitive to internal (e.g. enzymes) or external (e.g. radiation) triggers were designed [85]. Matrix metalloprotease 2/-9 (MMP-2 and MMP-9) cleavable linkers, for example, are widely used. MMP-2 and MMP-9 are overexpressed in the extracellular matrix of several tumors. MMP-2 and MMP-9-cleavable linkers can thus be used to activate NPs in the tumor microenvironment [86]. For example, a PEG-PCL copolymer linked by an enzyme-cleavable linker was synthesized. Upon exposure to MMP-2 and MMP-9, PEG is cleaved and “stealth” properties are lost. This results in a high tumor uptake and superior therapeutic effects as compared to conventional PEG-PCL micelles [86]

(VI) Nanomedicines have the great potential to combine diagnostic tools and therapeutic compounds in a single agent. These multifunctional systems are called **theranostics** [87]. Imaging probes suitable for non-invasive imaging techniques such as optical imaging (e.g. near-infrared (NIR) imaging), computer tomography (CT), magnetic resonance (MR) imaging, or positron-emission

spectroscopy (PET) are therefore used [87]. Some of these probes can be activated as therapeutics by external stimuli e.g. in photodynamic or photothermal therapy, others are combined with conventional chemotherapeutics or biologics such as nucleic acids [88–91]. For example, PEG-PCL-tethered gold NPs (GNPs) were tested as theranostics *in vivo*. Dense packaging of GNPs resulted in a strong NIR absorption due to plasmon coupling. When injected in melanoma-bearing mice, tumor imaging and prolongation of the mean survival time was achieved [89].

2.3 Delivery of Macromolecules

2.3.1 Delivery of Proteins And Peptides

Peptide and protein therapeutics are of increasing interest. Whereas in the early 1990s only a few biotechnology products were available, more than 200 products were approved by health care authorities in 2012 [92]. However, the administration of proteins *in vivo* is linked with major issues. Proteins often show inadequate stability, can be excreted via glomerular filtration, and can induce immunogenic reactions. As a result, therapeutic proteins are often characterized by unfavorable PK properties, i.e. a short plasma circulation half-life [93].

In order to overcome this issue, modification of therapeutic proteins via PEGylation is a frequently used and well-established concept. The hydrophilic polymer PEG is approved by health care authorities and is non-toxic. Conjugation of PEG to proteins increases their size and PEGylated proteins can be considered as nanomedicines. For example, type I interferon (IFN) that regulates the expression of genes linked with cancer growth, proliferation, differentiation, and migration [94]. PEGylation of IFN increases the hydrodynamic diameter of the protein from 2.73 nm to 9.46 nm, decreases the systemic clearance of IFN, and reduces IFN side effects while remaining the therapeutic activity of IFN [94,95]. A class of therapeutic proteins with increasing interest is monoclonal antibody fragments (Fab'). However, they show a relatively short plasma half-life and their application is therefore limited [96]. A Fab' directed against the vascular endothelial growth factor receptor 2 (VEGFR-2) was modified with a 40 kDa PEG fragment (CDP791) and was tested in a clinical trial in patients with solid tumors. Whereas the free Fab' was rapidly cleared from the systemic blood circulation, the PEG-protein conjugate showed a prolonged plasma half-life after injection [97]. A PEG-conjugate of the enzyme asparaginase (Oncaspar™) received market approval in 2006 for the treatment of leukemia [98]. In contrast to the free enzyme that frequently induces hypersensitivity reactions due to anti-asparaginase antibody production requiring adaptation or even stop of therapy, the PEG-protein conjugate decreases the risk for these side effects and shows a prolonged therapeutic effect [99,100]. In summary, PEG-protein conjugates show reduced immunogenicity and toxicity, a prolonged blood circulation time, and an optimized biodistribution [9,101–106].

To further improve chemical stability of therapeutic proteins (e.g. to prevent proteolysis in plasma and after cellular internalization), they were encapsulated in nanoparticulate drug delivery systems. PLGA-lipid hybrid NPs were developed for the simultaneous delivery of the immunostimulant interleukin-2

(IL-2) and a small molecule inhibitor of the transforming growth factor β (TGF-β). This formulation showed promising results against melanoma [107]. Another interesting approach is the use of phosphatase and tensin homolog deleted on chromosome 10 (PTEN), a tumor suppressor that is inactivated in many human tumors. Restoring the function of PTEN may therefore depict a promising therapeutic option for these cancers. However, PTEN is an intracellular protein and artificial PTEN thus needs to be internalized. Encapsulation of recombinant PTEN in lipidoids resulted in efficient intracellular delivery of this therapeutic protein and induced apoptosis in prostate cancer cells [108]. In addition, nanomedicines are promising candidates for the oral delivery of peptides and proteins. Liposomal formulations containing tetraether lipids that naturally occur in archaea bacteria were successfully used to deliver peptides such as ocreotide or myrcludex B after oral dosage [109,110]. Keeping in mind that peptide and protein therapeutics are a rapidly growing class of therapeutics, such non-invasive drug delivery strategies are of high importance [111].

2.3.2 Delivery of Nucleic Acids

Gene therapy is a promising strategy for the treatment of cancer diseases. However, the delivery of nucleic acids such as micro RNA (miRNA), small interfering RNA (siRNA), messenger RNA (mRNA), and plasmid DNA (pDNA) remains challenging [112]. Unprotected nucleic acids are prone to degradation and hardly cross biological membranes due to their hydrophilicity and negative charge [113]. Thus, advanced delivery systems are currently under investigation in preclinical and clinical studies. These nanosized carriers can mainly be divided into two classes: **(I)** viral and **(II)** non-viral gene delivery systems.

(I) Viruses are natural occurring vectors for nucleic acids and are therefore used to deliver therapeutic genes [16]. Various genetically engineered **viral vectors** can be used, each with its strengths and weaknesses. Frequently used viruses for gene delivery are retroviruses, adenoviruses, AAVs, and herpes viruses, amongst others [17]. The choice of the viral vectors depends on the type of genetic material, packaging capacity, and tropism of the virus. In addition, some viruses are able to insert therapeutic genes into the host cellular chromatin, whereas others persist in the nucleus as extrachromosomal nucleic acids [114]. Pexa-Vec (JX-594), a replication competent poxvirus expressing granulocyte-monocyte colony-stimulating factor (GM-CSF), for example, was used in the treatment of renal cell caner, colorectal cancer, and advanced hepatocellular carcinoma [115–118]. Via oncolysis and immunotherapy, this virus showed promising results in clinical trials in solid tumors. However, several hurdles limit the clinical use of viral gene delivery vectors. First, immunological defense mechanisms decrease the therapeutic benefit of viral agents. Second, recombinant viral vectors may not show the same tropism as their natural occurring counterparts and can therefore infect a broad range of host cells [114]. Whereas this may depict a benefit in some cases, lack of specificity may provoke severe side effects to other organs and may be fatal [119]. Third, integrating vectors (e.g. retroviruses) may randomly integrate their genome in the host cell chromatin and may in long-term induce cancer [114]. Forth, although viral vectors for gene delivery are rendered non-

replicative, there remains the possibility of reversion to a pathogenic wild-type (i.e. replication competent) virus [120].

(II) To address the potential drawbacks of viruses, **non-viral gene delivery systems** for therapeutic applications are of increasing interest. In comparison to viral vectors, non-viral gene delivery systems have several advantages. Non-viral delivery systems reduce risks for insertional mutagenesis, are less immunogenic, can carry larger genetic payloads, and are more flexible [113,120–122]. Most systems for the delivery of genes are based on cationic lipids (e.g. Lipofectamine™) or polymers such as poly(ethyleneimine) [PEI]. In addition, positively charged peptides such as poly-lysine were tested for their potential as gene carriers [113,121,122]. However, due to their positive charge, these carriers accumulate in the lung after i.v. administration and are rapidly cleared from the systemic circulation [123,124]. Therefore, long-circulating delivery systems such as liposomes or polymeric micelles with a gene delivery capacity are developed. For example, a PEG-PCL-PEI tri-block copolymer construct was used for the simultaneous delivery of siRNA and quantum dots [125]. An increase of the plasma half-life was observed upon systemic administration as compared to non-modified PEI. When modified with folic acid, *in vivo* targeted delivery of siRNA to tumors was achieved [126]. Despite their benefits as compared to viral vectors, several problems need to be solved to enable clinical translation of non-viral gene delivery systems [121]. Overall, these systems are characterized by a poor transfection efficiency *in vivo* [122]. Recent efforts were focusing on enhancing endosomal escape, unpacking, and nuclear transport [120]. In addition, special tools are needed to confer long-term gene expression by gene editing techniques such as CRISPR/Cas9 or to decrease the epigenetic shutdown of extra-chromosomal DNA [121].

2.4 Future Trends and Perspectives: Oncolytic Viruses

Whereas the development of specific drugs interfering with single pathways may be effective for some tumors, the high frequency of acquired resistances and inefficient therapies resulted in a change in paradigm in cancer therapy. In tumors, abnormal cell growth hardly depends on single dysregulations [127]. In addition, acquired drug resistances caused by mutations during drug therapy can occur and render tumor cells non-permissive for these drugs [128,129]. Thus, targeting various signaling pathways (e.g. kinases) either by compounds such as multi-kinase inhibitors or by the combination of multiple highly specific drugs may help to increase therapeutic success and to bypass acquired resistances [130,131]. Whereas this concept still needs to be implemented in the drug discovery process and therapeutic dosage schemes, some natural occurring infectious agents such as bacteria and viruses have already developed strategies to avoid cellular defense mechanisms by interacting with multiple cellular targets. If targeted towards transformed cells, these pathogens can be potent weapons for the treatment of cancer [132,133]. Viral infections are closely related to cancer. On one hand, 20% of all human cancers can be associated with infectious diseases. Viruses, such as the Rous-Sarcoma Virus, can induce uncontrolled cell proliferation and it's infection can therefore result in neoplastic tissue and subsequently tumor formation [134]. On the

other hand, some naturally acquired viral infections were linked with tumor regression in patients with hematological malignancies. As a consequence, oncolytic viruses were tested for their therapeutic potential in preclinical and clinical trials [19,135–137]. These studies revealed the encouraging potential of viral cancer therapy and T-VEC®, a viral cancer therapeutic gained market approval recently.

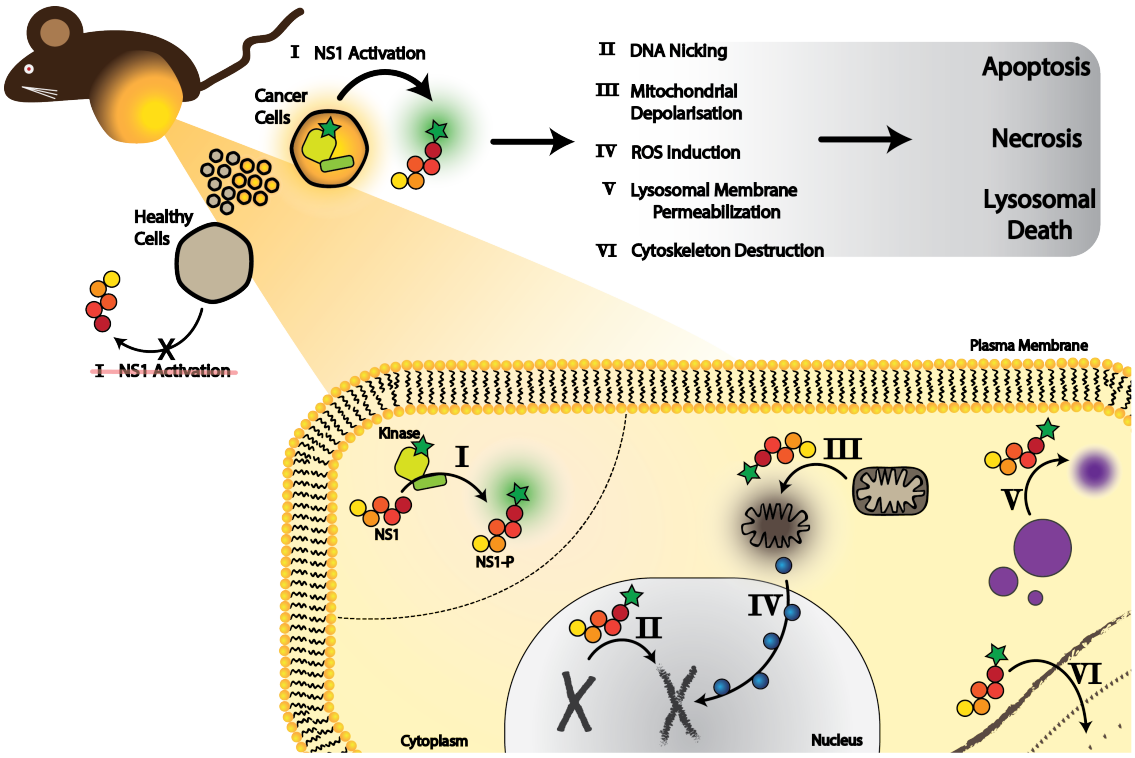

Figure 4 Effects of the H-1PV large non-structural protein NS1 on cancer cells. Adapted from [138].

A virus that successfully reached clinical trials for the treatment of recurrent glioblastoma multiforma (GBM) is the **rat parvovirus H-1** (H-1PV). Rodent parvoviruses (PV), such as the minute virus of mice (MVM) and the H1-PV, belong to the smallest mammalian viruses known. The diameter of the icosahedral capsid is around 25 nm and the genetic information is stored on a small 5.1 kb linear single strand DNA (ssDNA) [139]. Due to this limited coding capacity (2 structural proteins, at least 6 non-structural proteins) [138], expressed proteins need to exert several functions in a timely highly coordinated manner throughout the viral life cycle. Only a handful of non-structural proteins are sufficient to hijack the host cell and take control of its functions [140]. The large non-structural protein (NS1) plays essential roles in viral propagation and the induction of H-1PV-mediated cell death [141]. NS1 is highly regulated by phosphorylation throughout the viral life cycle. At least 10 different phosphorylated species of NS1 were identified [141,142]. Interestingly, cytotoxic effects induced by NS1 can be switched on and off by site-directed mutagenesis at potential phosphorylation sites without interfering with viral replication [143]. Regulation of NS1 via phosphorylation (e.g. by protein kinase C isoforms, PKC) is dependent on phosphoinositide-dependent kinase-1 (PDK1) signaling and was shown to be a major reason for H-1PV oncotropism [143–148]. A mutant, constitutive active isoform of PDK1 was identified in human glioma samples permissive for H-1PV-induced toxicity and

was proposed as a marker for sensitivity to H-1PV therapy [149]. After infection, H-1PV can induce apoptosis, necrosis, and so-called lysosomal death resulting in killing of permissive cells (Fig. 4) [138,150,151]. NS1 was identified to be a major driver of these oncotoxic effects. Despite the promising preclinical and clinical results in the treatment of GBM, several issues need to be ruled out regarding viral therapies as mentioned above. Lack in patient safety (e.g. carcinogenesis), inherent immunogenicity, environmental toxicity, and difficulties in viral production are major obstacles in the development and approval of viral therapies [122,133,137]. Delivery of therapeutic genes (e.g. coding for NS1) by non-viral vectors can therefore improve the therapeutic performance and rule out potential safety drawbacks [152].

AIM OF THE THESIS

The use of advanced drug delivery systems may improve the performance of established chemotherapeutics and may open the door for novel therapeutic approaches such as gene therapy. Therefore, the aim of this PhD thesis was to develop a biocompatible nanoparticulate drug delivery platform and a novel therapeutic approach for liver cancer using a virus-derived anticancer gene. Major project milestones were defined as followed:

Evaluation of nanoparticulate drug delivery platforms based on PEG-PCL

- What are the characteristics of PEG-PCL nanoparticles?
- How can PEG-PCL nanoparticles be used for drug delivery?

Preparation of long-circulating PEG-PCL micelles

- How can PEG-PCL micelles be produced?
- Do PEG-PCL micelles show stealth properties comparable to established PEG-liposomes?

Modification of nanoparticles for cellular imaging and diagnosis

- How can nanoparticles be tracked after cellular uptake?
- How can the preparation protocol be modified to improve labeling efficiency and reproducibility?

Active targeting of PEG-PCL micelles

- How can PEG-PCL micelles be modified to target specific cell types?
- Do modified PEG-PCL micelles show specific and enhanced cellular uptake as compared to non-modified PEG-PCL micelles?

Non-viral gene delivery of a virus-derived anticancer gene

- Can the parvovirus-derived anticancer gene be delivered via non-viral gene delivery methods?
- Can this therapeutic approach be used to specifically treat liver cancer?

RESULTS

Chapter I:

PEG-PCL-Based Nanomedicines: A Biodegradable Drug Delivery System and its Application

Chapter II:

Biodegradable PEG-PCL Micelles as Long-Circulating Drug Carriers

Chapter III:

Formation of lipid and polymer based gold nanohybrids using a nanoreactor approach

Chapter IV:

Functionalized Solid-Sphere PEG-b-PCL Nanoparticles to Target Brain Capillary Endothelial Cells In Vitro

Chapter V:

Non-viral gene delivery of a parvovirus-derived anticancer gene for the therapy of hepatocellular carcinoma

CHAPTER I

PEG-PCL-based nanomedicines: A biodegradable drug delivery system and its application

Grossen P, Witzigmann D, Sieber S, Huwyler J

Manuscript: Published in J. Controlled Release. 260 (2017) 46–60.
DOI: 10.1016/j.jconrel.2017.05.028

Highlights: Nanoparticulate drug delivery platforms are promising strategies to improve the therapeutic performance of drugs by changing their PK and pharmacodynamic properties. This review article highlights the great potential of nanoparticulate drug delivery systems based on the biodegradable and non-toxic synthetic polymer PEG-PCL. Established synthesis routes are described and state-of-the-art preparation methods are highlighted. An overview about the diverse range of encapsulated drugs ranging from lipophilic small molecules to hydrophilic high molecular weight biologics is given. Furthermore, recent advances in the application of PEG-PCL drug delivery systems for passive and active drug targeting, trigged drug release, theranostics, and gene delivery are outlined.

Journal of Controlled Release 260 (2017) 46–60

Contents lists available at ScienceDirect

Journal of Controlled Release

journal homepage: www.elsevier.com/locate/jconrel

Review article

PEG-PCL-based nanomedicines: A biodegradable drug delivery system and its application

Philip Grossen, Dominik Witzigmann, Sandro Sieber, Jörg Huwyler*

Division of Pharmaceutical Technology, Department of Pharmaceutical Sciences, University of Basel, Basel, Switzerland

ARTICLE INFO

Keywords:
Nanomedicine
Nanoparticle
Polymer
Peg-PCL
Drug delivery
Drug targeting

ABSTRACT

The lack of efficient therapeutic options for many severe disorders including cancer spurs demand for improved drug delivery technologies. Nanoscale drug delivery systems based on poly(ethylene glycol)-poly(ε-caprolactone) copolymers (PEG-PCL) represent a strategy to implement therapies with enhanced drug accumulation at the site of action and decreased off-target effects. In this review, we discuss state-of-the-art nanomedicines based on PEG-PCL that have been investigated in a preclinical setting. We summarize the various synthesis routes and different preparation methods used for the production of PEG-PCL nanoparticles. Additionally, we review physico-chemical properties including biodegradability, biocompatibility, and drug loading. Finally, we highlight recent therapeutic applications investigated in vitro and in vivo using advanced systems such as triggered release, multi-component therapies, theranostics, or gene delivery systems.

1. Introduction

Nanomedicine is an emerging discipline in pharmaceutical science. Engineered nanomaterials (ENM), defined by one or more external dimension in the size range of 1 nm to 100 nm, are used to implement various drug delivery platforms [1,2]. Many promising candidates are in clinical and preclinical research and some nanoparticle (NP) formulations, e.g. Genexol-PM™, recently gained market approval by health care authorities such as the FDA [3–5]. Different materials are used for the production of such nanoparticulate drug delivery systems (nanoDDS) including inorganic NPs, viral NPs, lipid based NPs, and polymer based NPs [3]. Among these, synthetic copolymers gained much attention due to their versatile and tunable chemistry. Synthetic copolymers can be used to produce solid sphere nanoparticles, micelles, vesicular polymersomes, polyplexes, polymer-drug conjugates, and dendrimers [6]. A schematic overview about polymer-based nanostructures is given in Fig. 1A. Notably, copolymers of the hydrophilic PEG and hydrophobic PCL are characterized by a high biocompatibility and biodegradability (Fig. 1B). PEG has a long history of use in therapeutic strategies. PEGylation of therapeutic proteins or liposomes is used to reduce immunogenicity and toxicity, prolong blood circulation time, change biodistribution, and optimize protein activities [4,7–12]. PCL, a semi-crystalline and biodegradable polymer, was successfully used in medical devices and tissue engineering [13–16]. In this review, we will focus on the synthesis, production, characterization, and application of PEG-PCL-based nanomedicines. Therapeutic effects induced in vivo via targeted and non-targeted drug delivery, application routes, triggered drug release, theranostic NPs, and progress in PEG-PCL-based gene delivery strategies will be discussed. For the sake of simplicity, PEG-*b*-PCL will be used for di-block copolymers of PEG and PCL, whereas PEG-PCL will be used for copolymers of PEG and PCL (and others) with various architectures.

2. Synthesis

During the last decades a vast number of different PEG-PCL-based copolymers have been developed and various synthetic routes have been investigated. The most established method to synthesize PEG-*b*-PCL di-block copolymers is the ring-opening polymerization of ε-caprolactone (CL) with methoxy poly(ethylene glycol) (mPEG) as an initiator using catalysts such as stannous octate ($Sn(Oct)_2$), calcium, or aluminum complexes [17–23]. Alternative synthesis routes using biocatalysts (e.g. enzymes) or using "click" chemistry were described [24,25]. For the synthesis of PEG-*b*-PCL di-block copolymers, various block lengths of PEG and PCL were combined. The molecular weight of the PCL block is mainly controlled by the molar ratio of CL to the initiator mPEG [26]. The mass or volume fraction (f) of each block and the molecular weight of the copolymer mainly dictate the resulting structure of the NP [27–31]. Amphiphilic block copolymers with a hydrophilic weight fraction similar to phospholipids ($f \approx 25$–45%) tend to form vesicular structures, a hydrophilic weight fraction of $f > 50\%$ usually results in micellar structures [27,30,32]. The composition of the

* Corresponding author at: Department of Pharmaceutical Sciences, University of Basel, Klingelbergstrasse 50, CH-4056 Basel, Switzerland.
E-mail address: joerg.huwyler@unibas.ch (J. Huwyler).

http://dx.doi.org/10.1016/j.jconrel.2017.05.028
Received 11 April 2017; Received in revised form 19 May 2017; Accepted 20 May 2017
Available online 20 May 2017

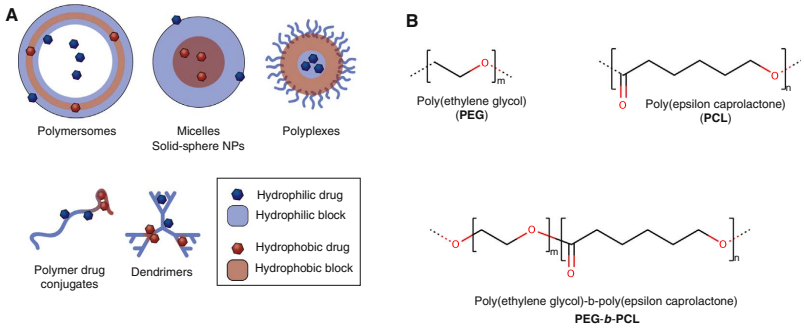

Fig. 1. Types of polymer-based nanoparticles. (A) Schematic representation of polymer-based nanomedicines. (B) Chemical structure of PEG, PCL, and PEG-*b*-PCL.

block copolymers can be optimized using methods such as full factorial design [33]. In addition to di-block copolymers, tri-block copolymers, i.e. PCL-*b*-PEG-*b*-PCL (PCEC) and PEG-*b*-PCL-*b*-PEG (PECE), as well as branched, brushed, and star-shaped PEG-PCL copolymers were generated. Synthesis strategies using different PEG variants as initiator, "click" chemistry, or coupling reagents such as hexamethylendiisocyanate (HMDI) or N-hydroxysuccinimide (NHS) and N,N′-dicyclohexylcarbodiimide (DCC) resulted in a big arsenal of PEG-PCL copolymers for the potential use in drug delivery [23,34–41]. These polymers show different assembly behavior, drug loading properties, and cellular uptake behavior and can thus be chosen according to the therapeutic strategy [40,42]. PEG-PCL graft copolymers (PEG-*g*-PCL) were synthesized via a thiol-yne approach [43]. Polymer amphilicity was highly tunable and easy to control. Thus, PEG-PCL copolymers with a broad range of molecular weights, various architectures, and tunable amphiphilicity can be synthesized. Using systematic approaches such as design of experiments (DoE), tailor-made polymers for specific drugs can be produced and NPs with a homogeneous size distribution can be prepared.

3. Nanoparticle preparation methods

PEG-PCL NPs for biomedical applications can be produced using various types of methods. Mostly, these are based either on spontaneous self-assembly or emulsification. A suitable protocol depending e.g. on stability of the drug or the targeting ligand in organic solvents or at high temperatures can be chosen.

In solvent-displacement, also called nanoprecipitation, the polymer is dissolved in a water-miscible organic solvent and subsequently, an aqueous phase (i.e. non-solvent) is added dropwise. Due to reduced polymer solubility and interfacial hydrodynamic phenomena (i.e. Marangoni effect), spontaneous NP formation is induced. The organic solvent is subsequently removed by evaporation [44,45]. Various organic solvents such as acetone, dimethylformamide (DMF), or tetrahydrofuran (THF) were used in the production of PEG-PCL NPs [17,18,42,46–50]. The type of organic solvent, the ratio of organic to aqueous phase, and the order of phase addition can be changed to control NP size, morphology, and to optimize drug loading [51]. Recently, PEG-*b*-PCL micelles with mean diameters of 82.9 nm, 87.8 nm, and 109.0 nm were prepared by using either acetonitrile, acetone, or THF as organic phase [51]. A modification of the solvent-displacement method is the so-called dialysis method. In this method, the polymer is dissolved in a water-miscible organic solvent, mixed with an aqueous phase, and then dialyzed against aqueous media [22,52,53]. Film rehydration is widely used in the production of liposomes and was also used for the production of polymer NPs [54–57]. In film rehydration, the polymer is dissolved in an organic solvent (e.g. chloroform, methanol, or acetone) that is subsequently removed by evaporation to obtain a thin polymer film. After rehydration of the polymer film, small micelles are formed that can further rearrange to form spherical micelle-like NPs or vesicles (i.e. polymersomes) [58]. An adaptation of film rehydration, melting/sonication, was developed [59]. Heating of the sample above the polymer melting temperature (T_m) and subsequent sonication after rehydration of the polymer thin film led to the formation of mono-disperse PEG-*b*-PCL micelles [59–62]. Several approaches for the preparation of NPs using emulsification or double emulsification for the encapsulation of hydrophilic drugs were described. In the so-called emulsion solvent evaporation technique, the polymer is dissolved in a volatile and water-immiscible organic solvent such as dichloromethane (DCM) or chloroform. This solution is emulsified in an aqueous phase containing stabilizers (e.g. polyvinyl alcohol (PVA), trehalose, or sodium cholate) in combination with ultrasonication or other methods. The organic solvent is then removed by heat and NP formation is induced [44,45,63–67]. Especially, novel methods such as microfluidics have gained much attention for the preparation of PEG-PCL NPs. Microfluidic mixing of PEG-*b*-PCL-*b*-poly(**ethylene** imine) (PEI) for siRNA complexation resulted in smaller and more homogeneous micelles, enhanced siRNA stability, and higher transfection efficiency as compared to micelles produced by bulk mixing (i.e. solvent-displacement) [68]. Interestingly, this technique can be used for scale-up production as well as *in process*-sterilization of NPs which is a prerequisite for the preparation of clinical trial samples [69–71]. Importantly, the great variety of preparation methods for the production of PEG-PCL NPs offers the possibility to choose the ideal strategy, e.g. depending on the drug stability in organic solvents or at different temperatures. Recently developed preparation methods for different drugs and PEG-PCL copolymers are summarized in Table 1.

4. Degradation and colloidal stability

4.1. Stability and degradation

In order to improve the therapeutic value (i.e., biocompatibility and excretion of nanoparticles), the degradability of polymer nanoparticles is a major issue. During the last years, the biodegradation of PCL and PEG-PCL-based medical devices was studied extensively [16,72–75]. It has been shown that controllable factors such as polymer composition and molecular weight as well as other factors like temperature and pH strongly influence the degradation rate, reflected by a decreasing molecular weight of the polymer [76–79]. Mainly, polymers can degrade and erode via surface or bulk process [80,81]. The latter is defined by polymer loss from the entire volume and seems to be the mechanism highly contributing to the degradation of PCL-based films and medical devices [82]. In an initial phase, a random hydrolytic chain scission can be observed followed by polymer weight loss and diffusion

Table 1
PEG-PCL-based drug carriers. Selected PEG-PCL-based nanoparticles (NP) are shown. NP formulations are sorted according to increasing lipophilicity of their drug payload.

[a]Drug	[b]XLogP3[b]	[c]Mw [g/mol]	[d]Polymer	[e]Preparation method	[f]NP size [nm]	[g]DLE [%]	[h]DLC [% w/w]	[i]Ref.
Ovalbumin	− 9.9	1773.4	PEG-*b*-PCL	EM	220	15.7	1.2	[199]
Goserelin	− 1.5	1269.4	PEG-*b*-PCL	EM	174	44.2	–	[110]
NAPVSIPQ	− 5.6	824.4	PEG-*b*-PCL	EM	76.2	54.3	0.7	[214]
Etoposide	0.6	588.6	PEG-*b*-PCL	CS	36.5–90.2	61.4–96.8	2.7–5.3	[248]
Oxymatrine	1	264.4	PEG-*b*-PCL	TF	96.7	34.0	6.7	[54]
Camptothecin	1	348.4	PEG-*b*-PCL	EM	116	71.7	6.0	[220]
Ocreotide	1	1019.2	PEG/PCL	EM				[249]
Doxorubicin	1.3	543.5	PEG-*b*-PCL	CS	110–202	81–95.5	–	[164]
			PEG-*b*-PCL	OT	30.1	93.6	4.5	[106]
			PEG-*b*-PCL	CS	104.9	–	4.3	[17]
			PCEC	MS	130.8	86.7	8.7	[62]
			PEG-*b*-PCL	CS	37.7	70	7	[222]
Sulforaphane	1.4	177.3	PEG-*b*-PCL	EM	118	86.0	20.0	[111]
Luteolin	1.4	286.2	PEG-*b*-PCL	TF	38.6	98.3	3.9	[107]
SN38	1.4	392.4	PEG-*b*-PCL	TF	128.3	83.8	20.7	[108]
Docetaxel	1.6	807.9	PEG-*b*-PCL	MS	53–87	41–90	4.9–8.7	[61]
			PCEC					
			PEG-*b*-PCL	CS	85.7	80.7	20.3	[48]
			PEG-*b*-PCL	DL	51.4	64.2	8.2	[22]
TGX-221 and BL05-HA	1.9	364.5	PEG-*b*-PCL	CS	54.5	74.5	9.5	[145]
Dexamethasone	1.9	392.5	PEG-*b*-PCL	TF	45.2	94.2	2.2	[116]
Chetomin	1.9	710.9	PECE	TF	26.5	98.4	4.92	[57]
Triamcinolone	2.5	434.5	PEG-*b*-PCL	CS	130	97.0	10.0	[250]
Paclitaxel	2.5	853.9	PEG-*b*-PCL	EM	< 100	–	–	[142]
			PEG-*b*-PCL	EM	72.5	90.4	8.2	[66]
			PEG-*b*-PCL	CS	19.6	85.5	4.6	[143]
			PEG-*b*-PCL	EM	107	49.8	1.3	[64]
			PEG-*b*-PCL	EM	102.81	47.7	0.9	[63]
Noscapin	2.7	413.4	PEG-*b*-PCL	CS	65.61	3.2	34.6	[50]
Curcumin	3.2	368.4	PEG-*b*-PCL	CS	65.3–196	5.7–40.9	0.1–4.7 [mol/mol]	[47]
			PEG-*b*-PCL	TF	27.4	99.0	14.9	[109]
			PCEC	EM	38.9	95.5	11.9	[166]
Capsaicin	3.6	305.4	PEG-*b*-PCL	EM	82.5	81.5	14.0	[67]
Dasatinib	3.6	488.0	PEG-*b*-PCL	CS	54.3	95.4	1.9	[192]
Tetradine (Disulfiram)	3.9	296.5	PEG-*b*-PCL	EM	190.3–444.3	29.9–91.4	0.9–2.5	[65]
			PCEC					
Indometacin	4.3	357.8	PEG-*b*-PCL	DL	191	77.5	–	[52]
Honokiol	5	266.3	PEG-*b*-PCL	OT	29.19–165	56.9–95.8	4.6–27.4	[21]
Rapamycin	6	914.2	PEG-*b*-PCL	CS	76	50.0	11.0	[144]
Cyclosporin A	7.5	1202.6	PEG-*b*-PCL	CS	98.6	63.8	1.9	[18]
Paclitaxel	2.5	853.9	PEG-*b*-PCL	CS	80	9.4	3.2	[189]
Cyclopamine	3.5	411.6					3.1	
Gossypol	6.9	518.6					3.1	
VAAP	–	–	PEG-*b*-PCL	DL	106	–	4.2	[251]
RU 58668	–	658.8	PEG-*b*-PCL	CS	100	–	–	[104]
Cisplatin	–	300.1	PEG-*b*-PCL	CS	78.8	86.7	–	[46]
PC-4	–	717.0	PEG-*b*-PCL	CS	88	–	5	[208,209]
NC-1900	–	–	PEG-*b*-PCL	DL	107	20.6	–	[20]

[a] Name of the drug. VAAP: cis,cis,trans-diaminedichlorobisvalproato-platinum(IV).
[b] Calculated octanol-water partition coefficients (XlogP3) [139], from [pubchem.ncbi.nlm.nih.gov].
[c] Molecular weight (Mw) of the drug in [g/mol], from [pubchem.ncbi.nlm.nih.gov].
[d] Type of copolymer used.
[e] Preparation method: solvent-displacement (SD), thin-film rehydration (TF), dialysis (DL), oil-in-water (OW) or WOW emulsification (EM), melting/sonication (MS), and others (OT).
[f] Diameter of the drug loaded NP in [nm].
[g] Drug-loading efficiency (DLE) expressed as [%] of the initial drug concentration recovered after preparation and purification.
[h] Drug-loading content (DLC) expressed as [% w/w] drug to polymer.
[i] References.

of small CL oligomers out of the polymer bulk. This process is autocatalytic, i.e. free carboxylic groups catalyze the cleavage of remaining ester groups [82]. Consequently, water-soluble and insoluble CL oligomers as well as PEG segments were identified as first degradation products of PEG-PCL [83]. Additionally, enzymes such as lipases increase PEG-PCL degradation in vitro. These enzymes are present intra- and extracellularly and catalyze the hydrolysis of triglycerides. However, their contribution for the in vivo degradation is still unclear [80,82,84]. Regarding PEG-PCL NPs, several other factors such as route of administration and NP characteristics (e.g. size, shape, and zeta potential) strongly influence the degradation and elimination from the body. A study on the in vivo degradation of di-block copolymer micelles showed, that in vitro degradation kinetics should be used with precaution to predict the in vivo situation. The in vivo degradation was much faster than the weight decrease measured in vitro [84,85]. Polymer bioresorption, degradation, and subsequent elimination or metabolism of the degradation products will determine the residual time in the body after administration [73]. Colloidal stability and biodistribution of the NP will therefore dramatically influence the mean residual time (MRT) of the polymer [85,86]. PEG-PCL micelles are stable in phosphate buffered saline (PBS) for months [67]. However, in biological media such as cell culture medium or blood, protein

opsonization can affect the micelle stability [87–89]. It is thus recommended, that the colloidal stability should be tested in an environment similar to in vivo conditions [89,90]. For example, stability of PEG-PCL micelles was tested in serum containing medium. In contrast to the high stability in PBS, micelles showed changes in size and size distribution in a time and serum-concentration dependent manner [91–93]. Large NP aggregates can be taken up by the mononuclear phagocyte system (MPS) [94,95]. In contrast, individual PEG-PCL block copolymers (unimers) that may occur after NP disassembly can be cleared via different mechanisms. When PEG-*b*-PCL was injected into experimental animals as unimers (i.e. below the critical aggregation concentration; CAC), a high uptake by liver, spleen, and kidney already after one hour of injection was observed as indicated by high tissue to plasma concentration ratios of 1.90, 1.30, and 1.70, respectively [96]. As a consequence, PEG-*b*-PCL unimers were rapidly removed from the plasma compartment (half-life: 10.2 h), whereas PEG-*b*-PCL micelles remained three times longer in the blood circulation [96]. Importantly, resulting metabolites did not accumulate and were cleared from the body via feces and urine efficiently [97]. A schematic overview about PEG-PCL NP behavior after injection is given in Fig. 2.

4.2. Shelf half-life

To prolong the shelf half-life of PEG-PCL-based formulations and to prevent premature nanoparticle degradation, NPs can be freeze-dried. This technique is widely used in pharmaceutical industry to increase storage stability of drugs, especially biologics. In order to preserve the physico-chemical characteristics of the NP formulation after reconstitution, cryoprotectants and stabilizers can be added to the formulation to optimize freeze drying [98]. Layre and colleagues analyzed the effect of different additives on the lyophilization of PEG-*b*-PCL micelles. Best results with only little aggregation of micelles after reconstitution were obtained by adding the surfactant Poloxamer 188 and trehalose to the micelle formulation before freeze-drying [99]. Importantly, reconstituted samples were still able to exert their biologic activities [100].

5. Biocompatibility and safety

The repeated use of nanomedicine products bears the risk of unwanted side-effects. Thus, an important step in the development of a nanomedicine product is the assessment of any safety risk. Especially, the biocompatibility and cytotoxicity of the nanocarrier on an acute and chronic level (i.e. short and long-term effects) have to be evaluated. PEG, PCL, and PEG-PCL products were approved by health care authorities such as the FDA [97,101,102]. Long-term experience with medical products consisting of these materials revealed a high biocompatibility and no concerns about toxic side effects [15,16,72]. In nanotoxicology, however, additional factors such as particle size, geometry and morphology, surface-to-volume ratio, and protein adsorption capacity of NPs have to be considered. Thus, each new NP formulation should be tested individually for toxic effects [103]. A precise physico-chemical characterization of NP properties is a prerequisite for any nanotoxicity profiling. Many PEG-PCL NPs in vitro toxicity studies (i.e. MTT cell viability assays or cell growth assays) using various established cell lines were performed. PEG-PCL-based NPs within a size range of around 20 nm to 200 nm and slightly negative zeta potentials were tested. No or only minor toxic effects on cell viability were detected up to concentrations of 1.5 mg/mL [22,42,49,61,104–111]. Shi and coworkers incubated human umbilical vein endothelial cells (HUVEC) with 0.2 mg/mL up to 1.2 mg/mL of PEG-*b*-PCL micelles for 48 h and observed no decrease in cell viability when analyzed using the MTT assay [105]. A slight elevation of reactive oxygen species (ROS) levels in macrophages was observed in vitro, whereas no induction of nitric oxide (NO) was detected [112,113]. In addition, PEG-PCL micelles did not induced hemolysis when incubated with freshly isolated human blood or rabbit erythrocytes [61,106,113]. Although in vitro studies revealed no cytotoxic effects of PEG-PCL NPs, data from experimental animals are needed to confirm such findings [114]. Several studies on the in vivo toxicity of PEG-PCL micelles were conducted in mice and rats. In vivo studies using high single doses of PEG-PCL micelles up to 2.4 g/kg injected i.v. did not reveal any signs of acute toxicity. No histological changes in heart, liver, spleen, lung, and kidney were observed. Behavior and food consumption of the animals were comparable to untreated animals [21,113]. PCEC was injected s.c. at a dose of 5 g/kg. Again, no toxic effects or behavioral changes were observed in BALB/c mice [115]. It should be noted that BALB/c mice are frequently used for immunological studies due to their potential to develop (Th2-biased) immune responses. No changes in plasma levels of serum aspartate transaminase (AST) and alanine transaminase (ALT) were measured in animals treated i.v. with a single dose of 36 mg/kg dexamethasone-loaded PEG-*b*-PCL micelles (the used concentration of the model compound dexamethasone was 0.8 mg/kg). A slight activation of the complement system was observed as measured by elevated C3a levels in treated rats [116]. PEG-*b*-PCL micelles induced no changes in levels of inflammatory factors in mice plasma when injected i.v. at a dose of 8 mg/kg. IL-6, IL-10, IL-12p70, IFN-γ, TNF, and MCP-1 levels were comparable to control animals treated with saline [112]. PCEC micelles did not induce any mutagenic effects in vitro and in vivo [117]. PEG-*b*-PCL micelles were also tested for sub-chronic toxicity in vivo. Daily i.v. administration of 100 mg/kg for one week in rats and mice did not induce any changes in weight gain. No acute inflammation or toxic effects on liver, kidney, or the brain parenchyma were observed [117,118]. AST, ALT, total bilirubin, ureanitrogen (BUN), and creatinin levels were comparable to those of control animals treated with saline [118]. PEG-PCL NPs are well tolerated and have not induced any acute toxicity in experimental animals in vivo after single or multiple dosing. No changes in histology or markers of inflammation were detected. Thus, it is expected that PEG-PCL based nanomedicines should be safe and well tolerated in human. As of today, long-term toxicity studies were performed in experimental animals only.

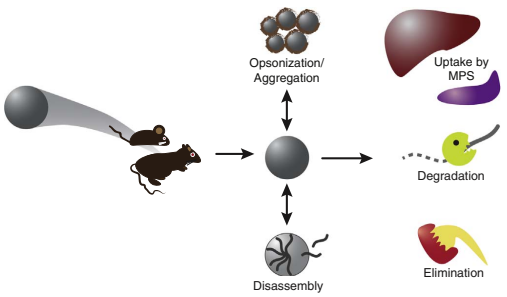

Fig. 2. Degradation and biodistribution of PEG-PCL-based nanoparticles. Schematic representation of nanoparticle (NP) stability, degradation, and biodistribution. Stability and degradation are summarized in Section 4, NP pharmacokinetics and biodistribution are reviewed in Section 7. MPS: mononuclear phagocyte system.

6. Drug loading and release

6.1. General principles

In order to induce a desired pharmacological effect, drugs of interest can be combined with PEG-PCL-based formulations. Therefore, non-covalent drug encapsulation (based on hydrogen bonding, hydrophobic interactions, or ionic interactions) or covalent drug conjugation can be used [119]. Several factors such as the solubility of the drug, the affinity of the drug to the polymer, the NP core volume, and the ability of the drug to self-aggregate can influence the drug loading content (DLC), i.e. the mass ratio of drug to polymer [120]. Paclitaxel loading

content in PEG-*b*-PCL micelles for example increased with increasing length of the hydrophobic PCL block [121]. In contrast, no significant increase was observed when a similar experiment was performed with the less hydrophobic compound doxorubicin [17]. Besides experimental approaches, physico-chemical models were used to predict drug loading and stability based on polymer-drug compatibility parameters [122]. The Flory-Huggins interaction parameter (X_{FH}), for example, was successfully used to characterize drug polymer compatibilities [123–125]. Methods to calculate interaction parameters of PEG-PCL copolymers and various drugs based on molecular dynamics were developed [126,127]. A rational coarse grain model for the partitioning of paclitaxel in PEG-*b*-PCL micelles and worm-like nanocarriers was generated. The authors showed that not only the composition of the polymer, but also the NP shape heavily influences drug loading [32]. Worm-like structures are characterized by increased polymer packaging constraints: PEG moieties show a higher packaging density on surfaces with a reduced curvature. Under this condition, PEG chains extend resulting in an increased thickness of the outer PEG layer [32]. Consequently, worm-like structures showed a two fold increase in drug loading as compared to spherical NPs [32]. Such methods can facilitate formulation screening and can be used for the rational design of novel drug-specific polymers and nanocarriers [122,128–131]. It should be noted that combination of a given drug with a nanocarriers can strongly influence the PK profile of the drug and its pharmacological effect [132].

Encapsulated drugs can be released from NPs via diffusion through the polymer matrix or water filled pores or after erosion of the polymer micelle [133]. In addition to passive release, triggered release of drugs may be favorable as discussed in Section 8.3 of this review. For the analysis of drug release from PEG-PCL-based nanomedicines in vitro, different methods can be applied: The gold standard is dialysis against an appropriate recipient medium. Alternative methods make use of continuous flow systems or microdialysis [134,135]. Due to missing sink conditions, extrapolation of these in vitro results to the in vivo situation is difficult. Other approaches, such as determination of the unbound fraction (*fu*) of the drug when drug loaded PEG-PCL micelles are incubated with red blood cells are therefore good alternatives to simulate in vivo stability and release behavior [136]. Methods to measure the intracellular drug release after NP uptake [137] can additionally be of particular interest when “smart” drug formulations with triggered release kinetics upon intracellular stimuli exposure (e.g. pH) are designed. Scarpa and colleagues established a method to quantify the real-time intracellular release of a fluorescent dye from PEG-*b*-PCL NPs after in vitro cell uptake [138].

6.2. Examples

PEG-PCL block copolymers and their derivatives offer a large variety of physico-chemical features including variable hydrophilic and lipophilic properties and self-assembly into nano-sized structures. A vast number of active compounds can be encapsulated into PEG-PCL-based nanoDDS. Drugs with molecular weights ranging from 177 g/mol up to 1269 g/mol and a wide range of XLogP3 [139] values (− 9.9 to 7.5) were successfully incorporated into PEG-PCL NPs. XLogP3 is a method for Log*P* computation (i.e. prediction of octanol-water partition coefficients) and can thus be used to characterize the lipophilicity of compounds [139]. A detailed overview about drug-loaded PEG-PCL-based nanoDDS is given in Table 1. The following section highlights some examples from the preclinical setting.

Sulforaphane, a potent natural compound against various cancers lacks of chemical stability (i.e. sensitivity to heat and oxygen) and suffers from poor water solubility. Sulphoraphane was encapsulated in PEG-*b*-PCL micelles with a homogeneous size distribution around 120 nm and a high encapsulation efficiency (EE) [111]. This formulation showed therapeutic activity in MCF-7 breast cancer cells in vitro. Paclitaxel, an inhibitor of the microtubule rearrangement, is widely used in cancer therapy. Due to its low water solubility, the excipient Cremophor EL is used in the approved formulation (Taxol™). However, this excipient has certain limitations and is characterized by severe toxic side effects [140,141]. To overcome this issue, PEG-*b*-PCL micelles were successfully used in various experimental settings for the encapsulation of paclitaxel [63,64,66,118,142,143]. Xin and coworkers produced PEG-*b*-PCL NPs with a high EE of > 90% and a DLC of 8.2% that were tested in vitro and in vivo in experimental animals and showed promising results [66,118,142]. Another PEG-*b*-PCL-based formulation of paclitaxel showed a remarkable stability with < 50% of the initial drug content released within 24 h [64].

Co-encapsulation strategies, chemical optimization of the drug, and active drug loading strategies were successfully used to improve EE and DLC of PEG-PCL NPs. Rapamycin, used for immunosuppression and cancer treatment, was encapsulated in PEG-*b*-PCL micelles. Interestingly, optimization of the encapsulation protocol by co-incorporation of the excipient α-tocopherol increased the EE and the release half-life of rapamycin [144]. A high EE of 11% and a slow drug release (50% released after 31 h) were achieved. The authors speculated that similar chemical motifs in α-tocopherol and rapamycin as well as their high lipophilicity were major reasons for this phenomenon. In another study, a PEG-*b*-PCL micelle formulation of TGX-221, a PI3K inhibitor, was developed. A fast release half-life of < 1 h was observed. In sharp contrast, synthesis of a TGX-221 prodrug, i.e. BL05-HA, resulted in significantly improved micelle stability and an increase of the release half-life to 6.5 days. Still, the micelle formulation showed selective inhibition of prostate cancer cells in vitro [145]. Active drug loading strategies using e.g. transmembrane pH gradients were developed for liposomal formulations [146–148] and adopted to PEG-PCL NPs. For example, active loading of doxorubicin into PEG-*b*-PCL polymersomes was performed using proton gradients. Despite the high membrane thickness of 16 nm, a high EE of 96% was achieved [149]. It can be concluded that various parameters can influence loading efficiency into PEG-PCL NPs and drug release. Optimized PEG-PCL copolymers can be designed and preparation protocols adapted to improve encapsulation of specific drugs. Application of PEG-PCL-based nanoDDS inducing therapeutic effects in both in vitro and in vivo settings will be highlighted in the following sections.

7. Pharmacokinetics and biodistribution

A prerequisite for successful active or passive drug targeting is a long plasma half-life. To obtain long circulating formulations, several factors such as size, shape, and surface characteristics need to be considered in the design of NPs [150,151]. NPs with a size below 5–6 nm can be excreted by renal filtration, while NPs with > 500 nm in diameter or with a positive surface charge are recognized and removed from the blood circulation by the reticulo-endothelial system (i.e. MPS) [152–156]. Especially, protein opsonization plays a critical role in cellular uptake of NPs [157]. PEGylation of NPs was shown to influence the total amount and composition of adsorbed proteins on the NP surface; thus, changing NP-cell interactions as well as NP PK properties [8,11,158–160]. Most PEG-PCL NPs used in in vitro or in vivo studies showed a size between 20 and 200 nm and a slightly negative zeta potential, both indicators for long circulating nanocarriers [161,162]. Several in vivo PK and biodistribution studies in experimental animals (i.e. rats and mice) were performed [20,50,64,96,106,136,142,163–165]. Different strategies for the labeling and detection of PEG-PCL NPs were applied, i.e. tracking the drug or the nanocarrier in vivo. In most experimental settings, drug loaded PEG-PCL NPs were produced. Drug concentrations were analyzed by high performance liquid chromatography (HPLC), mass spectrometry (LC-MS/MS), or liquid scintillation counting (LSC) and used to determine the PK parameters of the drug carrier [20,50,64,107,136,165].

As noted above, morphology and polymer characteristics of PEG-PCL NPs can vary considerably. Consequently, a certain variability of PK parameters can be observed as summarized below. PEG-*b*-PCL

micelles with an average hydrodynamic diameter of 89.3 ± 15.3 nm loaded with cyclosporine A were injected i.v. into male Sprague-Dawley rats at a dose of 5 mg/kg. A low volume of distribution (V_D) of 0.167 L/kg, a slow clearance (CL) of 0.0223 L/kg/h, and a high mean residual time (MRT) of 11.1 h were measured [163]. Similar results were observed for paclitaxel-loaded PEG-*b*-PCL micelles with a size of ≈ 100 nm [20]. PCEC NPs loaded with curcumin and a size of 38.9 nm were administered in Wistar rats at a dose of 15 mg/kg via single tail vein injection. The PK parameters of curcumin were dramatically changed. A V_D of 0.216 L/kg, a CL of 0.005 L/kg/h, and a long MRT of 30.07 h were observed [166]. Capsaicin-loaded PEG-*b*-PCL micelles were administered orally to Sprague-Dawley rats. Capsaicin is characterized by a high hepatic first pass metabolism and a short plasma half-life. Encapsulation in PEG-*b*-PCL micelles with an average diameter of 82.5 ± 0.5 nm resulted in a 6-fold increase in AUC and prolonged the MRT by a factor of 3 [67]. Whereas these studies aimed to detect changes in PK parameters of the encapsulated drug, covalent labeling of PEG-PCL by tritium or gamma emitters such as ^{99}mTC was used to analyze polymer concentration by scintillation counting [96,164]. Tritium labeled PEG-*b*-PCL micelles with a size of 56 ± 6 nm were injected i.v. into female BALB/c mice at a dose of 250 mg/kg. Comparable to the results obtained in rats (see above), a low V_D of 1.75 mL (corresponding to 0.6 L/kg), a low CL, and a high MRT of 43.3 h were observed [96]. Up to 12 h after i.v. injection, only small fractions of PEG-PCL micelles were detected in liver, spleen, and kidney [96,163,164]. Near-infrared (NIR) imaging is a promising non-invasive imaging technique to study NP distribution in vivo using NIR dyes such as DiR. NIR imaging was used to further analyze accumulation of NPs in various tissues and tumors [64,116,167–172]. Moreover, NIR dye loaded PEG-*b*-PCL NPs were proposed as tools to guide surgical resection in cancer patients suffering from tumors with pronounced EPR effects [169]. Due to their favorable pharmacokinetic profile, i.e. long-circulating properties, PEG-PCL NPs offer a promising option for nano-based drug formulations. In addition, this characteristic is an important prerequisite for further implementation of drug targeting strategies. Notably, a big toolbox of labeling and detection strategies of PEG-PCL NPs was developed that is applicable for various PEG-PCL constructs. Nevertheless, comparison of PEG-PCL NPs to the gold standard long-circulating drug delivery system, i.e. PEGylated liposomes, should be performed in the same experimental settings.

8. Applications in the preclinical setting

In order to improve the therapeutic index of a drug, different approaches in combination with PEG-PCL copolymers were developed. The following section will focus on non-targeted (i.e. passive) and targeted (i.e. active) delivery systems. In addition, advanced technologies such as stimuli-responsive systems, theranostics, and gene therapeutics will be highlighted. In each section, examples will be given with increasing complexity from small molecules to macromolecules or from single drug applications to drug combinations. Fig. 3 summarizes various applications of PEG-PCL-based NPs.

8.1. Non-targeted drug delivery

In contrast to some organs (e.g. the brain) that are highly protected by tightly sealed endothelial cell layers, other tissues are characterized by fenestrated (i.e. permeable) blood vessels (e.g. the liver). Interestingly, diseases such as cancer and inflammatory states are also linked with leaky vasculature [173,174]. In cancer for example, rapid cell proliferation increases the local demand for oxygen and nutrients that requires the generation of new blood supply. These fast growing blood vessels are often irregular and can have fenestrations of 100 nm up to 2 μm, depending on the localization and type of tumor [175–177]. As a consequence, macromolecules or long-circulating NPs can extravasate and can therefore passively accumulate in the tumor. Additionally, many solid tumors lack in sufficient lymphatic drainage and thus clearance of nanoparticles from the interstitial space is reduced [178]. This phenomenon is called enhanced permeability and retention (EPR) effect [179]. The efficiency of passive tumor targeting strongly depends on tumor biology (e.g. the type and location of the tumor, the extracellular matrix, and the presence of necrotic domains) and the physico-chemical properties of the NP such as size, shape, and zeta potential [175,180,181]. Because of significant inter- and intra-individual differences in tumor biology, screening of patients that could potentially benefit from long-circulating NPs using diagnostic tools needs to be considered [182,183]. Furthermore, detailed characterization of NPs is required, since even small differences in e.g. the particle diameter can dramatically influence the potential tumor accumulation [167]. A non-targeted micellar PEG-*b*-PCL formulation of paclitaxel was injected i.v. in mice carrying MDA-MB-468 breast cancer cells in their mammary fat pad and compared to the approved formulation Taxol™. Mice were treated twice per week at a dose of 15 mg/kg via i.v. injection and the tumor volume was measured. Whereas a relapse in tumor growth was observed in animals treated with Taxol™, a constant reduction of the tumor volume was achieved in animals treated with paclitaxel PEG-*b*-PCL micelles [143]. PEG-*b*-PCL micelles loaded with doxorubicin and a size around 100 nm preferentially accumulated in tumor tissue when administered i.v. in Ehrlich-ascites tumor (EAT)-bearing mice. Animals treated with the micelle formulation showed a reduced tumor size as compared to animals treated with free doxorubicin [164]. Doxorubicin-loaded PCEC with a size of 130.8 nm showed a 2.38-fold higher accumulation after 24 h in tumor tissue as compared to free doxorubicin after single i.v. injection in EMT-6 breast cancer-bearing mice [62]. Chemotin, a hydrophobic anti-cancer compound, was encapsulated in PECE micelles. PECE NPs were injected in transgenic zebrafish, xenograft-bearing zebrafish, and mice. Chemotin showed increased intratumoral accumulation when injected as micelle formulation and inhibited angiogenesis and tumor growth in vivo [57]. Goserelin is a synthetic analogue of luteinizing hormone-releasing hormone, used in the treatment of prostate cancer. Its half-life is rather short, so continuous application is needed to reach therapeutic relevant plasma concentrations in patients. Encapsulation into PEG-*b*-PCL micelles resulted in a depot effect with constant goserelin plasma levels and long-term suppression of serum testosterone over 28 days when administered s.c [110]. The use of combination therapies is a major strategy in the treatment of resistant cancers. The combination of

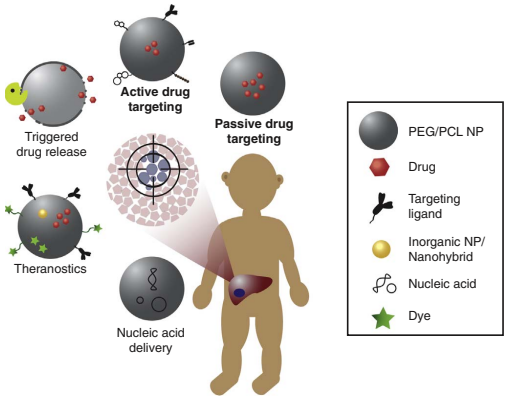

Fig. 3. Application of PEG-PCL-based nanoparticles. Schematic representation of PEG-PCL nanoparticle (NP) application: Passive and active drug delivery (Section 8.1 and 8.2), triggered drug release (Section 8.3), theranostics (Section 8.4), and the delivery of nucleic acids to target cells (Section 8.5).

Table 2
Ligands and ligand-conjugation strategies for the preparation of targeted PEG-PCL-based drug carriers. Selected strategies for the implementation of targeted PEG-PCL nanoparticles are highlighted. Ligands are sorted by decreasing average molecular weight.

[a]Class	[b]Name	[c]Target	[d]Disease	[e]Polymer	[f]Conjugation	[g]Ref.
Antibodies	83–14	Insulin receptor	CNS disorders	NH2-PEG-*b*-PCL	Bifunctional linker Maleimide-/NHS chemistry	[49]
	OX26	Transferin Receptor	CNS disorders	Mal-PEG-*b*-PCL	Maleimide chemistry	[20]
Nanobodies	VHH1	HER2 receptor	Breast cancer	Mal-PEG-*b*-PCL	Maleimide chemistry	[56]
Proteins	Low molecular weight protamine	–	Glioma	Mal-PEG-PCL	Maleimide chemistry	[64]
Polymers	Poly-dopamine	–	Malignant melanoma	PEG-b-PCL	Oxidative-self polymerization	[252]
Peptides	RGD RGDp cRGD LDVd LDVp	beta1-integrins	M cells for oral vaccination	PEG-*b*-PCL	Photografting	
	CGKRK	Heparan sulfate	Tumors/blood vessels	Mal-PEG-*b*-PCL	Maleimide chemistry	[63]
	Angiopep	LRP receptor	Glioma	Mal-PEG-*b*-PCL	Maleimide chemistry	[118,142]
	cRGD	Alpha 5-beta3 integrins	Glioma	COOH-PEG-PCL	NHS chemistry	[171]
	cRGD	Alpha 5-beta3 integrins	Glioma	COOH-PEG-PCL	NHS chemistry	[223]
	TGN (12mer peptide)	–	CNS disorders	Mal-PEG-*b*-PCL	Maleimide chemistry	[172]
	GE11	EGFR	Epidermioid carcinoma	Mal-PEG-*b*-PCL	Maleimide chemistry	[208,209]
Nucleic acids	PSMAa10	Prostate specific membrane antigen (PSMA)	Prostate cancer	N3-PEG-*b*-PCL	“Click” chemistry	[145]
	AS1411	Nucleolin	Glioma	COOH-PEG-*b*-PCL	NHS chemistry	[172]
Carbohydrates	Hyaluronic acid (HA)	HA receptors (CD44, RHAMM)	Ehrlich ascites carcinoma	NH2-PEG-*b*-PCL	Carbodiimide chemistry	[164]
	Galactose	Asialoglycoprotein receptor	Hepatocellular carcinoma (HCC)	NH2-PEG-*b*-PCL	NHS chemistry	[196]
	Mannan	Mannan receptor	Dendritic cells/vaccination	PCEC	Non-covalent adsoprtion	[194]
Small molecules	Manose	beta1-integrins	M cells for oral vaccination	PEG-*b*-PCL	Photografting	[199]
	Galactose	ASGPR	HCC	NH2-PEG-*b*-PCL	NHS chemistry	[196]
	Folate	Folate receptor	HCC	NH2-PEG-*b*-PCL	NHS chemistry	[239]
			Epidermiod carcinoma	NH2-PEG-*b*-PCL	NHS chemistry	[253]
			Retinal cells	NH2-PEG-*b*-PCL	Carbodiimide chemistry	[250]
			–	NH2-PEG-*b*-PCL	NHS chemistry	[60]
			Pancreas tumors	NH2-PEG-*b*-PCL	Carbodiimide chemistry	[254]
	Small molecular ligand PSMA	PSMA	Prostate cancer	COOH-PEG-*b*-PCL	NHS chemistry	[22]

[a] Classification of ligands in antibodies, nanobodies, proteins, peptides, sugars, nucleic acids, and small molecules.
[b] Name of the ligands.
[c] Molecular target.
[d] Disease or target organ.
[e] Type of copolymer used.
[f] Conjugation strategy applied.
[g] References.

potent inhibitors of efflux transporters and chemotherapeutics, for example, can increase the exposure of cancer cells to the cytotoxic drug and by this restore therapeutic effects [184]. At certain drug-to-drug ratios, synergistic effects (in contrast to simple additive effects) can occur [185]. Whereas these combinations of drugs are often tested on in vitro cell culture models, the translation of results into the patient situation is difficult due to inter- and intra-individual differences in drug metabolism and pharmacokinetics (DMPK). The encapsulation of a specific combinations of drugs into a NP formulation and the subsequent synchronized delivery of this drug payload to the cancer cell can overcome this hurdle [184,186–188]. Paclitaxel, cyclopamine, and gossypol were loaded in PEG-*b*-PCL micelles and used for the treatment of ovarian cancer xenografts. All tumor-bearing animals treated with the triple therapy NP survived (58 days), whereas 75% of all animals in the control group died during this period [189]. Local delivery of PEG-PCL NPs on e.g. the skin [60,190,191] or the eye [192] was used to increase the therapeutic effect at the site of action.

8.2. Targeted drug delivery

In contrast to non-targeted delivery systems, active targeting is directed towards specific, accessible receptors or epitopes preferentially (over)-expressed on target cells. The NP is designed to specifically interact with the cellular surface, increasing the NP binding to its target cell, retention at the site of action, and cellular uptake [174]. Various types of ligands such as antibodies or antibody fragments, aptamers, proteins, peptides, carbohydrates, and small molecules such as vitamins can be used for targeted drug delivery [193]. An overview of ligands used in combination with PEG-PCL NPs is shown in Table 2 and Fig. 4. Different strategies were applied to conjugate targeting ligands to PEG-

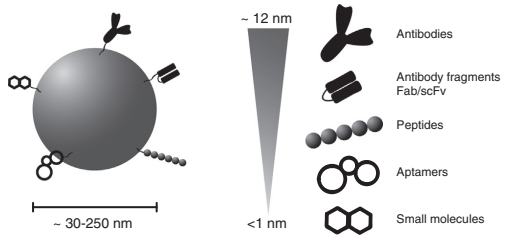

Fig. 4. Targeting ligands used in combination with PEG-PCL-based nanoparticles. Schematic representation of various ligands used for targeted delivery based on PEG-PCL nanoparticles. Targeting strategies are summarized in Section 8.2 and on Table 2.

PCL NPs. Gou and coworkers produced mannan-functionalized PCEC NPs by passively adsorbing this linear polysaccharide to the NP surface [194]. Such non-covalent conjugation techniques were largely replaced by covalent conjugation [195]. A widely used strategy is the conjugation of ligands to amino-terminated PEG-PCL (e.g. NH_2-PEG-*b*-PCL), carboxyl-terminated PEG-PCL, or maleimide-terminated PEG-PCL [49,54,56,60,64,196,197]. Pourcelle and coworkers developed a photoimobilization-based conjugation strategy using aryl azide "molecular clip". NHS-activated PEG-*b*-PCL was generated by light-induced conjugation of a bi-functional "molecular clip" (*O*-Succinimidyl-4-(*p*-azidophenyl)-*N*-butanoate) to PEG-*b*-PCL [198,199]. Azide-modified PEG-*b*-PCL was synthesized for the conjugation of alkyne-modified aptamers using "click" chemistry [145]. Typical conjugation strategies for PEG-PCL NPs are summarized in Fig. 5.

Doxorubicin was encapsulated into PEG-*b*-PCL micelles functionalized with hyaluronic acid (HA), a linear polysaccharide that can be used to target a variety of tumor. Ehrlich ascites tumor (EAT)-bearing mice were treated via tail vein injection over 7 days at a dose of 0.24 mg/kg/day. Tumor size was measured over 20 days. A 2.6-fold reduction in tumor volume after 20 days as compared to free doxorubicin was observed [164]. Paclitaxel-loaded PEG-*b*-PCL micelles decorated with aniopep-2, a specific ligand to low density lipoprotein receptor related protein 1 (LRP1) expressed on endothelial cells of the blood-brain barrier (BBB), were tested in an intracranial glioma mouse model [142,200,201]. PEG-*b*-PCL micelles were injected daily at dose of 10 mg/kg three times within 9 days and compared to Taxol™, the approved formulation of paclitaxel. Tumor volume in animals treated with targeted PEG-*b*-PCL micelles was reduced > 2-fold as compared to Taxol™. In addition, mean survival time (MST) was prolonged to 37 days, whereas mean survival time in animals treated with Taxol™ was 25 days only [118]. Dual targeted docetaxel loaded PEG-*b*-PCL micelles were modified with TGN, a peptide obtained by phage display to enhance BBB permeability, and with the aptamer AS1411, targeted against nucleolin, a protein highly expressed in glioma cells [91,172]. Targeted PEG-*b*-PCL micelles showed an increased therapeutic efficiency in vivo as compared to free drug and non-targeted NPs. The MST of orthotropic glioma bearing mice was prolonged to 32 days, whereas animals treated with free drug had a MST of 18 days [172]. The density of the ligand on the NP surface is a critical characteristic for successful targeting. Quantification of the ligand/NP ratio was performed using radio-, fluorescent-, and immunogold-labeling of the targeting moiety [49,160,198,202–204]. Scanning transmission electron microscopy can additionally give insight into the spatial organization of immunogold-labeled ligands on the NP surface [205]. Multivalent binding enabled by high ligand densities on the NP surface can enhance binding affinity to the target receptor [206]. For example, PEG-*b*-PCL micelles were prepared with different ratios of PEG-*b*-PCL and folate-modified PEG-*b*-PCL. Cellular uptake was enhanced with increasing amounts of folate per micelle [207]. Similarly, PEG-*b*-PCL micelles decorated with a peptide ligand of the endothelial growth factor receptor (EGFR) showed maximal cellular uptake in EGFR overexpressing cells in vitro for micelles with the highest peptide surface density [208,209]. However, loss of stealth properties by high ligand surface densities can reduce the NP targeting efficiency in vivo [202]. NC-1900, a vasopressin fragment analog with a great potential in the treatment of neurological disorders (i.e. spatial memory impairments) but with a poor permeation across the BBB, was encapsulated within PEG-*b*-PCL NPs [20,210]. OX26, an antibody against the transferrin receptor that was used in brain-targeting in various studies, was conjugated to these PEG-*b*-PCL NPs [20,203,211–213]. NPs with a high surface density of OX26 (i.e. 92 per NP) showed a significantly reduced AUC and no increase in brain delivery capacity. In contrast, the optimized formulation with 34 molecules of OX26 per NP was able to deliver its payload 2.6-fold more efficient to the brain as compared with non-modified NPs and improved scopolamine-induced learning and memory deficits when injected i.v. in Sprague-Dawley rats [20]. In another study, the neuroprotective peptide NAP was encapsulated in lactoferrin-modified PEG-*b*-PCL micelles. After intranasal administration in an in vivo Alzheimer model of mice, a neuroprotective effect was reached as shown by behavioral improvements and histological analysis [214]. PEG-*b*-PCL micelles were conjugated to a cell penetrating peptide (Tat). Modified micelles were able to deliver siRNA and fluorescently labeled dextran more efficient to the brain than non-modified PEG-*b*-PCL micelles or free dextran after intranasal administration [215,216].

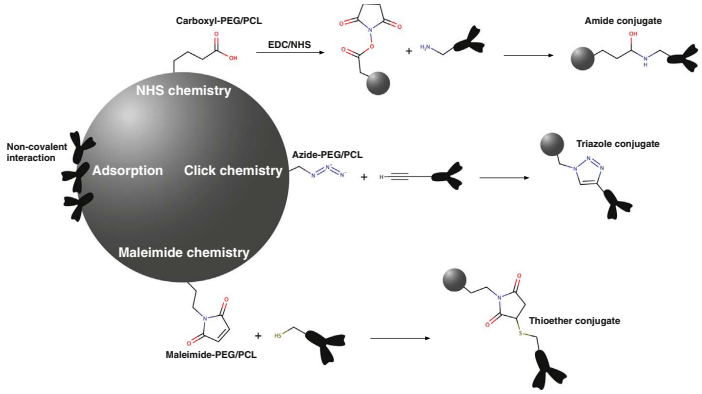

Fig. 5. Conjugation of targeting ligands to PEG-PCL-based nanoparticles. Schematic representation of selected ligand conjugation strategies (Section 8.2 and Table 2).

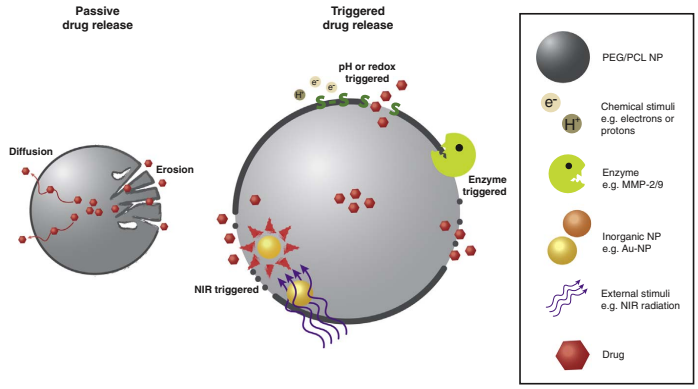

Fig. 6. Triggered drug release. Schematic representation of strategies for triggered drug release using PEG-PCL-based nanoparticles. Strategies are reviewed in Section 8.3 and Table 3.

PEG-*b*-PCL poly(lactic acid)-hydrid micelles were designed for oral vaccination. Modification of the NP surface with different peptidic and small molecular peptides resulted in enhanced cellular uptake and transport in vitro and increased immune response when administered orally in experimental animals [199]. The ease of chemical modification of PEG-PCL copolymers can thus be exploited to conjugate various ligands to the surface of PEG-PCL NPs and to implement drug targeting strategies. Detailed understanding of the NP-cell interaction as well as optimization of the ligand density is furthermore needed to improve the performance of these systems.

8.3. Stimuli-responsive nanoparticles and triggered drug release

Stimuli-responsive "smart" NPs, e.g. controlled drug release formulations, can improve therapeutic efficiency by increasing the drug release at the site of action. In such systems, drug release can be triggered by either externally applied or internal stimuli. Systems responsive to changes in e.g. pH, temperature, irradiation, magnetism, concentration gradients, or enzymatic activity were designed [217]. A schematic overview about PEG-PCL-based stimuli-responsive NPs is given in Fig. 6 and Table 3.

Overexpression of matrix metalloproteases (MMP), especially MMP-2 and MMP-9, are linked with progression of cancer [218]. Thus, prodrug strategies depending on MMP activity are promising candidates to increase therapeutic selectivity to tumors [219]. A PEG-PCL copolymer with a MMP-cleavable peptide linker (PEG-*b*-Pep-*b*-PCL) was synthesized and used to produce campothecin-loaded micelles. After passive accumulation in the tumor, loss of stealth properties as a consequence of MMP-mediated detachment of PEG should lead to increased cellular uptake by tumor cells. Indeed, this formulation showed superior effects as compared to PEG-*b*-PCL micelles or free drug as shown by a high tumor accumulation of the drug and a reduced tumor volume in treated xenograft-bearing mice [220]. In another study, a cell-penetrating peptide with a MMP-cleavable protection

Table 3
Design of stimuli-sensitive nanoparticles using PEG-PCL polymers. Strategies for triggered drug release and stimuli-responsive targeting are highlighted.

[a]Trigger	[b]Polymer	[c]Drug	[d]Stimuli	[e]Stimuli-responsive mechanism	[f]Ref.
Internal triggers					
Enzymatic cleavage	PEG-*Pep*-PCL	Campothecin	Matrix metalloprotease 2/9	Disruption of PEG-Pep-PCL in the presence of MMP 2/9 and subsequent enhanced drug release	[220]
	Pep-PEG-*b*-PCL	Paclitaxel	Matrix metalloprotease 2/9	Activation of the cell penetrating peptide low molecular weight protamine (LMWP) after MMP 2/9 exposure	[64]
pH	PEG-*b*-PCL(*COOH*)	Ibuprofen/ campothecin	pH ≥ 7	Vesicle disruption and drug release at pH ≥ 7 (i.e. small intestine), stable at pH < 6	[221]
Redox	PEG-*SS*-PCL	Doxorubicin	Reduction (10 mM DTT) Reduction (10 mM glutathione)	Disruption of PEG-*SS*-PCL at a reductive environment similar to cytosol and enhanced subsequent drug release	[222] [223]
Temperature	PEG-*b*-PCL/PCL-*b*-PNIPAM	–	Temperature (37 °C)	Collapse of PNIPAM chains due to hydrophilic to hydrophobic transformation at physiological temperatures and subsequent adsorption of Aβ mono- and small oligomers	[228]
pH/Redox/ Temperature (Multi trigger)	PEG-*b*-(PCL_2/$PNIPAM_2$) PEG-*b*-(PCL_2/PAA_2)	Doxorubicin	pH (5.3), reduction (10 mM DTT), and temperature (37 °C)	Disruption of mixed micelles composed of PEG-PCL-based star-shaped copolymers and subsequent drug release after changes in temperature, reductive environment, and/or pH.	[229]
External triggers					
Light	PEG-*b*-PCL/Gold-nanorod hydrid NPs	Doxorubicin	Near infrared (NIR)	Phase transition of PCL from crystalline to amorphous after NIR exposure and subsequent enhanced drug release	[171] [224] [225]

[a] Classification of triggers.
[b] Type of copolymer used.
[c] Name of encapsulated drugs.
[d] Stimuli and experimental conditions applied.
[e] Stimuli-responsive mechanism and effect after stimuli exposure.
[f] References.

group was conjugated to PEG-*b*-PCL micelles loaded with paclitaxel. Again, enzyme-triggered activation resulted in higher anti-tumor activity in vitro as well as in vivo [64].

PEG-*b*-PCL NPs with carboxylic functionalized PCL were synthesized for pH-responsive drug release, e.g. after oral administration. Vesicles were produced and loaded with various drugs. Whereas a slow and incomplete drug release was observed in acidic conditions, a burst release was obtained at pH > 7 [221]. Such systems could be used to implement targeting strategies for specific sections of the gastrointestinal tract (GIT) after oral application although a proof-of-concept in vivo is still missing.

Zhong and coworkers synthesized PEG-PCL copolymers containing a disulfide linkage (PEG-*SS*-PCL). Reductive sensitive micelles were produced and loaded with doxorubicin. At redox potentials similar to the physiological intracellular level, a complete release of doxorubicin was observed within 10 h, whereas only 20% of the drug was released in PBS [222]. Furthermore, PEG-*SS*-PCL micelles showed increased anti-tumor activity in experimental animals as compared to PEG-*b*-PCL micelles [223].

PEG-*b*-PCL-gold nanorods loaded with doxorubicin were prepared for NIR triggered thermochemotherapy. When hybrid nanorods were irradiated with a NIR laser source, an increase in temperature and a triggered release of doxorubicin was observed [171,224,225]. The core of PEG-*b*-PCL micelles is crystalline at temperatures below the melting point of PCL. As soon as the temperature is elevated above the melting point of the micelle core (e.g. by NIR irradiation), increased drug release can be observed [226,227].

Huang and colleagues produced mixed micelles consisting of PEG-*b*-PCL and poly(N-isopropylacrylamide)-*b*-PCL (PNIPAM-PCL). Due to its spontaneous hydrophilic to hydrophobic transformation at physiological temperatures, PNIPAM builds hydrophobic domains on the micelle surface that have high affinity for toxic Aβ oligomers. These micelles were capable to inhibit the Aβ fibrillation process and to enhance proteolytic degradation of Aβ in vitro. They could thus be used as artificial scavengers in the therapy of Alzheimer's disease [228]. Another group synthesized *star*-shaped PEG-PCL-poly(acrylic acid) (PEG-PCL-PAA) and PEG-PCL-PNIPAM copolymers. These particles were sensitive to temperature, pH, and chemical reduction. Release of doxorubicin was enhanced upon exposure to those stimuli [229].

Covalent chemical modification of PEG-PCL copolymers, synthesis of PEG-PCL tri-block copolymers, and production of PEG-PCL mixed-micelles was used to develop stimuli-responsive PEG-PCL NPs. Upon exposure to disease-related or externally applied triggers, these NPs showed increased drug release or cellular uptake in vitro and superior therapeutic effects induced in animal models.

8.4. Theranostics

Theranostics combine diagnosis, treatment, and monitoring of the therapeutic effect using a single nanocarrier system [230–234]. A variety of non-invasive diagnostic imaging tools such as NIR fluorescence imaging, magnetic resonance imaging (MRI), computed tomography (CT), or positron emission tomography (PET) is in use [235]. These methods require contrast agents or probes, e.g. quantum dots (QDs), inorganic dyes, supramagnetic iron oxide NPs (SPIONs), gold NPs (GNPs), or radioisotopes [230,235]. Some of these probes can be activated by external stimuli to exert an inherent therapeutic effect, e.g. in photodynamic or photothermal therapy [230]. Vesicles of PEG-*b*-PCL-tethered GNPs were used for photoacoustic imaging and enhanced photothermal therapy [236]. Dense packaging and specific orientation of GNPs in PEG-*b*-PCL nanohybrid vesicles induced strong NIR absorption by plasmon coupling and enabled tumor ablation and prolongation of the mean survival time in MDA-MB-435 tumor-bearing mice [236]. BBT−2FT, a small molecule with strong absorbance in the NIR window, was encapsulated in PEG-*b*-PCL micelles. A strong photoacoustic signal and a high photothermal conversion efficiency upon NIR laser irradiation resulted in a high anti-tumor efficiency in vitro and a high penetration depth of 4 cm in ex vivo tissue [237]. Alternatively, drugs (e.g. cytostatic compounds) can be administered simultaneously. SPIONs and doxorubicin were encapsulated in folate-targeted PEG-*b*-PCL micelles. These micelles showed efficient uptake in hepatoma cells and enhanced MRI T_2-weighed signal in vitro and in vivo [238,239]. In highly heterogeneous diseases such as cancer, patients could benefit from such personalized therapies. Inter- and intra-individual variability of tumors require adequate diagnosis and an adapted treatment, as for example the selection of patient populations that benefit from passive tumor accumulation (i.e. EPR effect) upon NP treatment. PEG-PCL-based theranostics were successfully used for the simultaneous detection and treatment of cancer diseases in vivo. Future challenges include the adaptation of this promising strategy to various diseases in combination with established biomarkers.

8.5. Delivery of nucleic acids

Nucleic acids are promising therapeutics for many diseases. Their metabolic instability requires drug delivery systems that protect them from rapid degradation in the circulation to enable efficient delivery to the target cells. Several strategies were used to implement gene delivery platforms using PEG-PCL NPs. Synthesis of tri-block copolymers by chemical modification of PEG-PCL or the preparation of mixed micelles using various copolymers showed promising results. Conjugation of positively charged cationic segments such as linear or branched poly (ethylene imine) (PEI) and poly(**aminoethyl** methacrylate) (PAMA) to PEG-*b*-PCL di-block copolymers results in PEG-*b*-PCL-*b*-PEI or PEG-*b*-PCL-*b*-PAMA tri-block copolymers. Alternatively, esterification of the mPEG-*b*-PCL hydroxyl group by acryloyl chloride and subsequent Michael-type addition of PEI was used [240,241]. Optimizations in the self-assembly process and the molecular composition of the tri-block copolymer resulted in efficient encapsulation of small interfering RNA (siRNA) and high gene delivery capacity [68,241,242]. PEG-*b*-PCL-*b*-PEI micelles loaded with siRNA, targeted against GAPDH, showed high transfection efficiency and were able to knock down target gene expression in vitro and in vivo when administered intratracheally [240]. Another PEG-PCL-PEI tri-block copolymer targeted to the folate receptor was used to simultaneously deliver doxorubicin and to knock down P-glycoprotein (P-gp) expression using siRNA. Micelles were able to restore sensitivity of MCF-7/ADR cells to doxorubicin in an attempt to treat multi-drug resistant (MDR) cancer [243]. Mixed micelles composed of PEG-*b*-PCL, poly(2-(dimethylamino)ethyl methacrylate)-*b*-PCL (PDMA-b-PCL), and pegylated anti-VEGF siRNA were produced. In addition, micelles were loaded with SN-38, a cytotoxic drug, and iron oxide nanoparticles for MRI contrast enhancement. This multi-component formulation was able to knock down VEGF expression, served as MRI contrast agent, and showed promising anti-tumor efficiency in vivo [244]. The high chemical stability of PEG-PCL copolymers can efficiently prevent the extracellular degradation of nucleic acid-based therapeutics: The future challenges lay in the extrapolation from test systems and animal models to possible clinical applications in human.

9. Conclusion

PEG-PCL NPs are promising candidates as drug delivery tools characterized by a high biocompatibility, biodegradability, and long-circulating properties. Chemical versatility and ease of modification led to the development of drug carriers for targeted and non-targeted delivery of various drugs ranging from small molecules to macromolecules such as proteins or nucleic acids. Although no candidate reached market approval from regulatory authorities so far, further improvement and research on PEG-PCL-based nanomedicines will increase the chance for a clinical application in humans. As lesson from history, the development of liposomal drug delivery systems have shown that

transferring novel technologies from bench to bedside needs to overcome several hurdles and can take decades [245]. The implication of scalable and reproducible production processes using e.g. microfluidics and extensive physico-chemical characterization should therefore be addressed. With this knowledge, disease-driven design and development of PEG-PCL nanoDDS can enhance the therapeutic efficacy and potential patient benefit. Long-term safety and efficacy studies in vivo need to be performed. Suitable preclinical models should be selected carefully and used for the development of patient pre-selection tools [246,247]. This will open up paths for first in human trials and clinical implication of promising PEG-PCL-based nanoDDS candidates. At present, a vast number of synthetic polymers are developed in preclinical research. PEG-*b*-PCL-based micelles are among the most advanced and best-characterized systems and therefore have a great potential to successfully enter translational research in the near future.

Acknowledgements

The authors would like to thank Dr. Gabriela Québatte for editorial assistance. Financial support was provided by the Swiss National Science Foundation (SNF grant No. 31003A_173057).

References

[1] J.M. Barroso, Commission Delegated Regulation (EU) No 1363/2013, (2013).
[2] E.A.J. Bleeker, W.H. de Jong, R.E. Geertsma, M. Groenewold, E.H.W. Heugens, M. Koers-Jacquemijns, et al., Considerations on the EU definition of a nanomaterial: science to support policy making, Regul. Toxicol. Pharmacol. 65 (2013) 119–125.
[3] A. Wicki, D. Witzigmann, V. Balasubramanian, J. Huwyler, Nanomedicine in cancer therapy: challenges, opportunities, and clinical applications, J. Control. Release 200 (2015) 138–157.
[4] D. Bobo, K.J. Robinson, J. Islam, K.J. Thurecht, S.R. Corrie, Nanoparticle-based medicines: a review of FDA-approved materials and clinical trials to date, Pharm. Res. 33 (2016) 2373–2387.
[5] I.H. Park, J.H. Sohn, S.B. Kim, K.S. Lee, J.S. Chung, S.H. Lee, et al., An open-label, randomized, parallel, phase III trial evaluating the efficacy and safety of polymeric micelle-formulated paclitaxel compared to conventional cremophor EL-based paclitaxel for recurrent or metastatic HER2-negative breast cancer, Cancer Res. Treat. (2016), http://e-crt.org/journal/view.php?doi=10.4143/crt.2016.289 (accessed December 21, 2016).
[6] M.D. Joshi, V. Patravale, R. Prabhu, Polymeric nanoparticles for targeted treatment in oncology: current insights, Int. J. Nanomedicine 10 (2015) 1001–1018.
[7] A. Abuchowski, T. Van Es, N.C. Palczuk, F.F. Davis, Alteration of immunological properties of bovine serum albumin by covalent attachment of polyethylene glycol, J. Biol. Chem. 252 (1977) 3578–3581.
[8] T.M. Allen, C. Hansen, F. Martin, C. Redemann, A. Yau-Young, Liposomes containing synthetic lipid derivatives of poly(ethylene glycol) show prolonged circulation half-lives in vivoLiposomes containing synthetic lipid derivatives of poly(ethylene glycol) show prolonged circulation half-lives in vivo, Biochim. Biophys. Acta BBA-Biomembr. (1991) 29–36.
[9] K.D. Bagshawe, S.K. Sharma, P.J. Burke, R.G. Melton, R.J. Knox, Developments with targeted enzymes in cancer therapy, Curr. Opin. Immunol. 11 (1999) 579–583.
[10] P. Bailon, W. Berthold, Polyethylene glycol-conjugated pharmaceutical proteins, Pharm. Sci. Technol. Today 1 (1998) 352–356.
[11] J.M. Harris, N.E. Martin, M. Modi, Pegylation, Clin. Pharmacokinet. 40 (2001) 539–551.
[12] H. Wada, I. Imamura, M. Sako, S. Katagiri, S. Tarui, H. Nishimura, et al., Antitumor enzyme: polyethylene glycol–modified asparaginase, Ann. N. Y. Acad. Sci. 613 (1990) 95–108.
[13] T.K. Dash, V.B. Konkimalla, Poly-ϵ-caprolactone based formulations for drug delivery and tissue engineering: a review, J. Control. Release 158 (2012) 15–33.
[14] L.W. McKeen, Plastics used in medical devices, Handb. Polym. Appl. Med. Med. Devices, Elsevier, 2014, pp. 21–53 http://linkinghub.elsevier.com/retrieve/pii/B9780323228053000037 (accessed September 19, 2016).
[15] C.X.F. Lam, D.W. Hutmacher, J.-T. Schantz, M.A. Woodruff, S.H. Teoh, Evaluation of polycaprolactone scaffold degradation for 6 months *in vitro* and *in vivo*, J. Biomed. Mater. Res. A 90A (2009) 906–919.
[16] S. Martinez-Diaz, N. Garcia-Giralt, M. Lebourg, J.-A. Gomez-Tejedor, G. Vila, E. Caceres, et al., In vivo evaluation of 3-dimensional polycaprolactone scaffolds for cartilage repair in rabbits, Am. J. Sports Med. 38 (2010) 509–519.
[17] X. Shuai, H. Ai, N. Nasongkla, S. Kim, J. Gao, Micellar carriers based on block copolymers of poly(ε-caprolactone) and poly(ethylene glycol) for doxorubicin delivery, J. Control. Release 98 (2004) 415–426.
[18] H.M. Aliabadi, A. Mahmud, A.D. Sharifabadi, A. Lavasanifar, Micelles of methoxy poly(ethylene oxide)-b-poly(ε-caprolactone) as vehicles for the solubilization and controlled delivery of cyclosporine A, J. Control. Release 104 (2005) 301–311.
[19] N. Fairley, B. Hoang, C. Allen, Morphological Control of poly(ethylene glycol)-*block*-poly(ε-caprolactone) copolymer aggregates in aqueous solution, Biomacromolecules 9 (2008) 2283–2291.
[20] Z. Pang, W. Lu, H. Gao, K. Hu, J. Chen, C. Zhang, et al., Preparation and brain delivery property of biodegradable polymersomes conjugated with OX26, J. Control. Release 128 (2008) 120–127.
[21] M. Gou, X. Zheng, K. Men, J. Zhang, B. Wang, L. Lv, et al., Self-assembled hydrophobic honokiol loaded MPEG-PCL diblock copolymer micelles, Pharm. Res. 26 (2009) 2164–2173.
[22] J. Jin, B. Sui, J. Gou, J. Liu, X. Tang, H. Xu, et al., PSMA ligand conjugated PCL-PEG polymeric micelles targeted to prostate cancer cells, PLoS One 9 (2014) e112200.
[23] L. Piao, Z. Dai, M. Deng, X. Chen, X. Jing, Synthesis and characterization of PCL/PEG/PCL triblock copolymers by using calcium catalyst, Polymer 44 (2003) 2025–2031.
[24] Y. Huang, L. Li, G. Li, An enzyme-catalysed access to amphiphilic triblock copolymer of PCL-b-PEG-b-PCL: synthesis, characterization and self-assembly properties, Des. Monomers Polym. 18 (2015) 799–806.
[25] K. Zhang, Y. Wang, W. Zhu, X. Li, Z. Shen, Synthesis, characterization, and micellization of PCL-g-PEG copolymers by combination of ROP and "click" chemistry via "graft onto" method, J. Polym. Sci. Part Polym. Chem. 50 (2012) 2045–2052.
[26] M. Yuan, Y. Wang, X. Li, C. Xiong, X. Deng, Polymerization of lactides and lactones. 10. Synthesis, characterization, and application of amino-terminated poly(ethylene glycol)-*co*-poly(ε-caprolactone) block copolymer, Macromolecules 33 (2000) 1613–1617.
[27] S. Jain, F.S. Bates, On the origins of morphological complexity in block copolymer surfactants, Science 191 (2003) 460–464.
[28] Z. Chen, P.A. FitzGerald, Y. Kobayashi, K. Ueno, M. Watanabe, G.G. Warr, et al., Micelle structure of novel diblock polyethers in water and two protic ionic liquids (EAN and PAN), Macromolecules 48 (2015) 1843–1851.
[29] J. Zhu, S. Zhang, K. Zhang, X. Wang, J.W. Mays, K.L. Wooley, et al., Disk-cylinder and disk-sphere nanoparticles via a block copolymer blend solution construction, Nat. Commun. 4 (2013), http://www.nature.com/doifinder/10.1038/ncomms3297 (accessed October 13, 2016).
[30] D.E. Discher, F. Ahmed, POLYMERSOMES, Annu. Rev. Biomed. Eng. 8 (2006) 323–341.
[31] D.E. Discher, A. Eisenberg, Polymer vesicles, Science 297 (2002) 967–973.
[32] S.M. Loverde, M.L. Klein, D.E. Discher, Nanoparticle shape improves delivery: rational coarse grain molecular dynamics (rCG-MD) of Taxol in worm-like PEG-PCL micelles, Adv. Mater. 24 (2012) 3823–3830.
[33] L. Barghi, D. Asgari, J. Barar, H. Valizadeh, Synthesis of PCEC copolymers with controlled molecular weight using full factorial methodology, Adv. Pharm. Bull. 5 (2015) 51.
[34] M.J. Huang, M.L. Gou, Z.Y. Qian, M. Dai, X.Y. Li, M. Cao, et al., One-step preparation of poly(ε-caprolactone)-poly(ethylene glycol)-poly(ε-caprolactone) nanoparticles for plasmid DNA delivery, J. Biomed. Mater. Res. A 86A (2008) 979–986.
[35] C. Gong, S. Shi, P. Dong, B. Kan, M. Gou, X. Wang, et al., Synthesis and characterization of PEG-PCL-PEG thermosensitive hydrogel, Int. J. Pharm. 365 (2009) 89–99.
[36] F. Bahadori, A. Dag, H. Durmaz, N. Cakir, H. Onyuksel, U. Tunca, et al., Synthesis and characterization of biodegradable amphiphilic star and Y-shaped block copolymers as potential carriers for vinorelbine, Polymer 6 (2014) 214–242.
[37] C. Lu, S. Guo, Y. Zhang, M. Yin, Synthesis and aggregation behavior of four types of different shaped PCL-PEG block copolymers, Polym. Int. 55 (2006) 694–700.
[38] F. Wang, T.K. Bronich, A.V. Kabanov, R.D. Rauh, J. Roovers, Synthesis and characterization of star poly(ε-caprolactone)-*b*-poly(ethylene glycol) and poly(L-lactide)-*b*-poly(ethylene glycol) copolymers: evaluation as drug delivery carriers, Bioconjug. Chem. 19 (2008) 1423–1429.
[39] Y. Zhang, Q. Zhao, H. Shao, S. Zhang, X. Han, Synthesis and characterization of star-shaped block copolymer sPCL-b-PEG-GA, Adv. Mater. Sci. Eng. 2014 (2014) 1–6.
[40] P. Tirino, C. Conte, M. Ordegno, R. Palumbo, F. Ungaro, F. Quaglia, et al., Y- and H-shaped amphiphilic PEG-PCL block copolymers synthesized combining ring-opening polymerization and click chemistry: characterization and self-assembly behavior, Macromol. Chem. Phys. 215 (2014) 1218–1229.
[41] J. Rieger, P. Dubois, R. Jérôme, C. Jérôme, Controlled synthesis and interface properties of new amphiphilic PCL-g-PEO copolymers, Langmuir 22 (2006) 7471–7479.
[42] Y. Hu, J. Xie, Y.W. Tong, C.-H. Wang, Effect of PEG conformation and particle size on the cellular uptake efficiency of nanoparticles with the HepG2 cells, J. Control. Release 118 (2007) 7–17.
[43] A. Al Samad, A. Bethry, E. Koziolová, M. Netopilík, T. Etrych, Y. Bakkour, et al., PCL–PEG graft copolymers with tunable amphiphilicity as efficient drug delivery systems, J. Mater. Chem. B 4 (2016) 6228–6239.
[44] P. Ahlin Grabnar, J. Kristl, The manufacturing techniques of drug-loaded polymeric nanoparticles from preformed polymers, J. Microencapsul. 28 (2011) 323–335.
[45] C.E. Mora-Huertas, H. Fessi, A. Elaissari, Polymer-based nanocapsules for drug delivery, Int. J. Pharm. 385 (2010) 113–142.
[46] P. Xu, E.A. Van Kirk, S. Li, W.J. Murdoch, J. Ren, M.D. Hussain, et al., Highly stable core-surface-crosslinked nanoparticles as cisplatin carriers for cancer chemotherapy, Colloids Surf. B: Biointerfaces 48 (2006) 50–57.
[47] Z. Ma, A. Haddadi, O. Molavi, A. Lavasanifar, R. Lai, J. Samuel, Micelles of poly

(ethylene oxide)-*b*-poly(ε-caprolactone) as vehicles for the solubilization, stabilization, and controlled delivery of curcumin, J. Biomed. Mater. Res. A 86A (2008) 300–310.
[48] B.-R. Liu, Gelatinase-stimuli strategy enhances the tumor delivery and therapeutic efficacy of docetaxel-loaded poly(ethylene glycol)-poly(& amp; epsilon; -caprolactone) nanoparticles, Int. J. Nanomedicine 281 (2012).
[49] P. Grossen, G. Québatte, D. Witzigmann, C. Prescianotto-Baschong, L.-H. Dieu, J. Huwyler, Functionalized solid-sphere PEG-b-PCL nanoparticles to target brain capillary endothelial cells in vitro, J. Nanomater. 2016 (2016) 1–13.
[50] K.S. Shalaby, M.E. Soliman, G. Bonacucina, M. Cespi, G.F. Palmieri, O.A. Sammour, et al., Nanoparticles based on linear and star-shaped poly(ethylene glycol)-poly(ε-caprolactone) copolymers for the delivery of antitubulin drug, Pharm. Res. 33 (2016) 2010–2024.
[51] H. Aliabadi, S. Elhasi, A. Mahmud, R. Gulamhusein, P. Mahdipoor, A. Lavasanifar, Encapsulation of hydrophobic drugs in polymeric micelles through co-solvent evaporation: the effect of solvent composition on micellar properties and drug loading, Int. J. Pharm. 329 (2007) 158–165.
[52] I.G. Shin, S.Y. Kim, Y.M. Lee, C.S. Cho, Y.K. Sung, Methoxy poly (ethylene glycol)/ε-caprolactone amphiphilic block copolymeric micelle containing indomethacin.: I. Preparation and characterization, J. Control. Release 51 (1998) 1–11.
[53] X.-J. Du, J.-L. Wang, W.-W. Liu, J.-X. Yang, C.-Y. Sun, R. Sun, et al., Regulating the surface poly(ethylene glycol) density of polymeric nanoparticles and evaluating its role in drug delivery in vivo, Biomaterials 69 (2015) 1–11.
[54] J. Yang, Y. Hou, G. Ji, Z. Song, Y. Liu, G. Dai, et al., Targeted delivery of the RGD-labeled biodegradable polymersomes loaded with the hydrophilic drug oxymatrine on cultured hepatic stellate cells and liver fibrosis in rats, Eur. J. Pharm. Sci. 52 (2014) 180–190.
[55] F. Ahmed, D.E. Discher, Self-porating polymersomes of PEG–PLA and PEG–PCL: hydrolysis-triggered controlled release vesicles, J. Control. Release 96 (2004) 37–53.
[56] T. Zou, F. Dembele, A. Beugnet, L. Sengmanivong, S. Trepout, S. Marco, et al., Nanobody-functionalized PEG-b-PCL polymersomes and their targeting study, J. Biotechnol. 214 (2015) 147–155.
[57] Q. Wu, G. Li, S. Deng, L. Ouyang, L. Li, L. Liu, et al., Enhanced antitumor activity and mechanism of biodegradable polymeric micelles-encapsulated chetomin in both transgenic zebrafish and mouse models, Nano 6 (2014) 11940–11952.
[58] R. Bleul, R. Thiermann, M. Maskos, Techniques to control polymersome size, Macromolecules 48 (2015) 7396–7409.
[59] F. Quaglia, L. Ostacolo, G. De Rosa, M.I. La Rotonda, M. Ammendola, G. Nese, et al., Nanoscopic core-shell drug carriers made of amphiphilic triblock and star-diblock copolymers, Int. J. Pharm. 324 (2006) 56–66.
[60] C. Conte, I. Fotticchia, P. Tirino, F. Moret, B. Pagano, R. Gref, et al., Cyclodextrin-assisted assembly of PEGylated polyester nanoparticles decorated with folate, Colloids Surf. B: Biointerfaces 141 (2016) 148–157.
[61] F. Ungaro, C. Conte, L. Ostacolo, G. Maglio, A. Barbieri, C. Arra, et al., Core-shell biodegradable nanoassemblies for the passive targeting of docetaxel: features, antiproliferative activity and in vivo toxicity, Nanomedicine Nanotechnol. Biol. Med. 8 (2012) 637–646.
[62] L. Zhang, Z. Chen, H. Wang, S. Wu, K. Zhao, H. Sun, et al., Preparation and evaluation of PCL–PEG–PCL polymeric nanoparticles for doxorubicin delivery against breast cancer, RSC Adv. 6 (2016) 54727–54737.
[63] Q. Hu, X. Gao, T. Kang, X. Feng, D. Jiang, Y. Tu, et al., CGKRK-modified nanoparticles for dual-targeting drug delivery to tumor cells and angiogenic blood vessels, Biomaterials 34 (2013) 9496–9508.
[64] G. Gu, H. Xia, Q. Hu, Z. Liu, M. Jiang, T. Kang, et al., PEG-co-PCL nanoparticles modified with MMP-2/9 activatable low molecular weight protamine for enhanced targeted glioblastoma therapy, Biomaterials 34 (2013) 196–208.
[65] R. Li, X. Li, L. Xie, D. Ding, Y. Hu, X. Qian, et al., Preparation and evaluation of PEG–PCL nanoparticles for local tetradrine delivery, Int. J. Pharm. 379 (2009) 158–166.
[66] H. Xin, L. Chen, J. Gu, X. Ren, Z. Wei, J. Luo, et al., Enhanced anti-glioblastoma efficacy by PTX-loaded PEGylated poly(ε-caprolactone) nanoparticles: in vitro and in vivo evaluation, Int. J. Pharm. 402 (2010) 238–247.
[67] W. Peng, X. Jiang, Y. Zhu, E. Omari-Siaw, W. Deng, J. Yu, et al., Oral delivery of capsaicin using MPEG-PCL nanoparticles, Acta Pharmacol. Sin. 36 (2015) 139–148.
[68] T. Endres, M. Zheng, M. Beck-Broichsitter, O. Samsonova, H. Debus, T. Kissel, Optimising the self-assembly of siRNA loaded PEG-PCL-lPEI nano-carriers employing different preparation techniques, J. Control. Release 160 (2012) 583–591.
[69] L. Gomez, V. Sebastian, S. Irusta, A. Ibarra, M. Arruebo, J. Santamaria, Scaled-up production of plasmonic nanoparticles using microfluidics: from metal precursors to functionalized and sterilized nanoparticles, Lab Chip 14 (2014) 325–332.
[70] G.T. Vladisavljević, N. Khalid, M.A. Neves, T. Kuroiwa, M. Nakajima, K. Uemura, et al., Industrial lab-on-a-chip: design, applications and scale-up for drug discovery and delivery, Adv. Drug Deliv. Rev. 65 (2013) 1626–1663.
[71] S. Badilescu, M. Packirisamy, Microfluidics-nano-integration for synthesis and sensing, Polymer 4 (2012) 1278–1310.
[72] S.I. Jeong, B.-S. Kim, Y.M. Lee, K.J. Ihn, S.H. Kim, Y.H. Kim, Morphology of elastic poly(L-lactide-*co*-ε-caprolactone) copolymers and in vitro and in vivo degradation behavior of their scaffolds, Biomacromolecules 5 (2004) 1303–1309.
[73] C.X.F. Lam, M.M. Savalani, S.-H. Teoh, D.W. Hutmacher, Dynamics of *in vitro* polymer degradation of polycaprolactone-based scaffolds: accelerated versus simulated physiological conditions, Biomed. Mater. 3 (2008) 34108.
[74] R.M. Felfel, L. Poocza, M. Gimeno-Fabra, T. Milde, G. Hildebrand, I. Ahmed, et al., *In vitro* degradation and mechanical properties of PLA-PCL copolymer unit cell scaffolds generated by two-photon polymerization, Biomed. Mater. 11 (2016) 15011.
[75] B.B. Christensen, C.B. Foldager, O.M. Hansen, A.A. Kristiansen, D.Q.S. Le, A.D. Nielsen, et al., A novel nano-structured porous polycaprolactone scaffold improves hyaline cartilage repair in a rabbit model compared to a collagen type I/III scaffold: in vitro and in vivo studies, Knee Surg. Sports Traumatol. Arthrosc. 20 (2012) 1192–1204.
[76] C. Engineer, J. Parikh, A. Raval, Review on hydrolytic degradation behavior of biodegradable polymers from controlled drug delivery system, Trends Biomater. Artif. Organs 25 (2011) 79–85.
[77] Z. Qian, S. Li, Y. He, H. Zhang, X. Liu, Hydrolytic degradation study of biodegradable polyesteramide copolymers based on ε-caprolactone and 11-aminoundecanoic acid, Biomaterials 25 (2004) 1975–1981.
[78] M. Chasin, R.S. Langer (Eds.), Biodegradable Polymers as Drug Delivery Systems, M. Dekker, New York, 1990.
[79] M.-H. Huang, S. Li, D.W. Hutmacher, J.-T. Schantz, C.A. Vacanti, C. Braud, et al., Degradation and cell culture studies on block copolymers prepared by ring opening polymerization of caprolactone in the presence of poly(ethylene glycol), J. Biomed. Mater. Res. 69A (2004) 417–427.
[80] A. Göpferich, Mechanisms of polymer degradation and erosion, Biomaterials 17 (1996) 103–114.
[81] J.A. Tamada, R. Langer, Erosion kinetics of hydrolytically degradable polymers, Proc. Natl. Acad. Sci. 90 (1993) 552–556.
[82] C.G. Pitt, Poly-E-caprolactone and its copolymers, in: R.S. Langer, M. Chasin (Eds.), Biodegrad. Polym. Drug Deliv. Syst, M. Dekker, New York, 1990, pp. 71–193.
[83] X.J. Loh, The effect of pH on the hydrolytic degradation of poly(ε-caprolactone)-block-poly(ethylene glycol) copolymers, J. Appl. Polym. Sci. 127 (2013) 2046–2056.
[84] J.-Z. Bei, J.-M. Li, Z.-F. Wang, J.-C. Le, S.-G. Wang, Polycaprolactone–poly (ethylene-glycol) block copolymer. IV: biodegradation behavior in vitro and in vivo, Polym. Adv. Technol. 8 (1997) 693–696.
[85] A.K. Mohammad, J.J. Reineke, Quantitative detection of PLGA nanoparticle degradation in tissues following intravenous administration, Mol. Pharm. 10 (2013) 2183–2189.
[86] M.G. Carstens, C.F. van Nostrum, R. Verrijk, L.G.J. de Leede, D.J.A. Crommelin, W.E. Hennink, A mechanistic study on the chemical and enzymatic degradation of PEG-oligo(ε-caprolactone) micelles, J. Pharm. Sci. 97 (2008) 506–518.
[87] M. Hadjidemetriou, Z. Al-Ahmady, M. Mazza, R.F. Collins, K. Dawson, K. Kostarelos, *In vivo* biomolecule corona around blood-circulating, clinically used and antibody-targeted lipid bilayer nanoscale vesicles, ACS Nano 9 (2015) 8142–8156.
[88] C.C. Fleischer, C.K. Payne, Nanoparticle–cell interactions: molecular structure of the protein corona and cellular outcomes, Acc. Chem. Res. 47 (2014) 2651–2659.
[89] M. Hadjidemetriou, Z. Al-Ahmady, K. Kostarelos, Time-evolution of in vivo protein corona onto blood-circulating PEGylated liposomal doxorubicin (DOXIL) nanoparticles, Nano 8 (2016) 6948–6957.
[90] T.L. Moore, L. Rodriguez-Lorenzo, V. Hirsch, S. Balog, D. Urban, C. Jud, et al., Nanoparticle colloidal stability in cell culture media and impact on cellular interactions, Chem. Soc. Rev. 44 (2015) 6287–6305.
[91] H. Gao, Z. Yang, S. Zhang, Z. Pang, X. Jiang, Internalization and subcellular fate of aptamer and peptide dual-functioned nanoparticles, J. Drug Target. 22 (2014) 450–459.
[92] R. Savić, T. Azzam, A. Eisenberg, D. Maysinger, Assessment of the integrity of poly (caprolactone)-*b*-poly(ethylene oxide) micelles under biological conditions: a fluorogenic-based approach, Langmuir 22 (2006) 3570–3578.
[93] R. Ferrari, C. Colombo, C. Casali, M. Lupi, P. Ubezio, F. Falcetta, et al., Synthesis of surfactant free PCL–PEG brushed nanoparticles with tunable degradation kinetics, Int. J. Pharm. 453 (2013) 551–559.
[94] J.A. Champion, A. Walker, S. Mitragotri, Role of particle size in phagocytosis of polymeric microspheres, Pharm. Res. 25 (2008) 1815–1821.
[95] S. Chono, T. Tanino, T. Seki, K. Morimoto, Uptake characteristics of liposomes by rat alveolar macrophages: influence of particle size and surface mannose modification, J. Pharm. Pharmacol. 59 (2007) 75–80.
[96] J. Liu, F. Zeng, C. Allen, In vivo fate of unimers and micelles of a poly(ethylene glycol)-block-poly(caprolactone) copolymer in mice following intravenous administration, Eur. J. Pharm. Biopharm. 65 (2007) 309–319.
[97] H. Sun, L. Mei, C. Song, X. Cui, P. Wang, The in vivo degradation, absorption and excretion of PCL-based implant, Biomaterials 27 (2006) 1735–1740.
[98] W. Abdelwahed, G. Degobert, S. Stainmesse, H. Fessi, Freeze-drying of nanoparticles: formulation, process and storage considerations☆, Adv. Drug Deliv. Rev. 58 (2006) 1688–1713.
[99] A.-M. Layre, P. Couvreur, J. Richard, D. Requier, N. Eddine Ghermani, R. Gref, Freeze-drying of composite Core-Shell nanoparticles, Drug Dev. Ind. Pharm. 32 (2006) 839–846.
[100] G.R. Ramos Yacasi, M.L. García Lopéz, M. Espina García, A. Parra Coca, A.C. Calpena Campmany, The influence of freeze drying and & upsih;-irradiation in pre-clinical studies of flurbiprofen polymeric nanoparticles for ocular delivery using D-(+)-trehalose and polyethylene glycol, Int. J. Nanomedicine 11 (2016) 4093–4106.
[101] J.-T. Schantz, S.H. Teoh, T.C. Lim, M. Endres, C.X.F. Lam, D.W. Hutmacher, Repair of calvarial defects with customized tissue-engineered bone grafts I. Evaluation of osteogenesis in a three-dimensional culture system, Tissue Eng. 9 (2003) 113–126.
[102] J.-H. Byun, H.A.R. Lee, T.H. Kim, J.H. Lee, S.H. Oh, Effect of porous polycaprolactone beads on bone regeneration: preliminary in vitro and in vivo studies, Biomater. Res. 18 (2014) 1.
[103] L. Shang, K. Nienhaus, G.U. Nienhaus, Engineered nanoparticles interacting with

cells: size matters, J. Nanobiotechnol. 12 (2014), http://www.biomedcentral.com/content/pdf/1477-3155-12-5.pdf (accessed March 9, 2015).
[104] T. Ameller, V. Marsaud, P. Legrand, R. Gref, J.-M. Renoir, Pure antiestrogen RU 58668—loaded nanospheres: morphology, cell activity and toxicity studies, Eur. J. Pharm. Sci. 21 (2004) 361–370.
[105] S. Shi, M. Fan, X. Wang, C. Zhao, Y. Wang, F. Luo, et al., Synthesis and characterization of mPEG-PCL-g-PEI and self-assembled nanoparticle uptake in vitro and in vivo, J. Phys. Chem. C 114 (2010) 21315–21321.
[106] X. Gao, M. Huang Gou, N. Huang, Wei Qian, et al., Preparation, characterization and application of star-shaped PCL/PEG micelles for the delivery of doxorubicin in the treatment of colon cancer, Int. J. Nanomedicine 971 (2013).
[107] M. Huang, X. Gao, Jinfeng Qiu, Xiawei Wei Wang, M. Gou, et al., Preparation and characterization of monomethoxy poly(ethylene glycol)-poly(& amp;epsilon;-caprolactone) micelles for the solubilization and in vivo delivery of luteolin, Int. J. Nanomedicine 3061 (2013).
[108] Q. Gu, J.Z. Xing, M. Huang, C. He, J. Chen, SN-38 loaded polymeric micelles to enhance cancer therapy, Nanotechnology 23 (2012) 205101.
[109] C. Gong, S. Deng, Q. Wu, M. Xiang, X. Wei, L. Li, et al., Improving antiangiogenesis and anti-tumor activity of curcumin by biodegradable polymeric micelles, Biomaterials 34 (2013) 1413–1432.
[110] P. Tomar, N. Jain, V.K. Dixit, Nanoparticulate delivery of LHRH analogue for the treatment of prostate cancer, Pharm. Dev. Technol. 18 (2013) 645–652.
[111] H. Danafar, A. Sharafi, H. Kheiri Manjili, S. Andalib, Sulforaphane delivery using mPEG–PCL co-polymer nanoparticles to breast cancer cells, Pharm. Dev. Technol. (2016) 1–10.
[112] B. Zhao, X.-Q. Wang, X.-Y. Wang, H. Zhang, W.-B. Dai, J. Wang, et al., Nanotoxicity comparison of four amphiphilic polymeric micelles with similar hydrophilic or hydrophobic structure, Part. Fibre Toxicol. 10 (2013) 47.
[113] N.-V. Cuong, J.-L. Jiang, Y.-L. Li, J.-R. Chen, S.-C. Jwo, M.-F. Hsieh, Doxorubicin-loaded PEG-PCL-PEG micelle using xenograft model of nude mice: effect of multiple administration of micelle on the suppression of human breast cancer, Cancer 3 (2010) 61–78.
[114] C. Hoskins, L. Wang, W.P. Cheng, A. Cuschieri, Dilemmas in the reliable estimation of the in-vitro cell viability in magnetic nanoparticle engineering: which tests and what protocols? Nanoscale Res. Lett. 7 (2012) 1–12.
[115] F. Fang, C.Y. Gong, P.W. Dong, S.Z. Fu, Y.C. Gu, G. Guo, et al., Acute toxicity evaluation of *in situ* gel-forming controlled drug delivery system based on biodegradable poly(ε-caprolactone)–poly(ethylene glycol)–poly(ε-caprolactone) copolymer, Biomed. Mater. 4 (2009) 25002.
[116] Q. Wang, J. Jiang, W. Chen, H. Jiang, Z. Zhang, X. Sun, Targeted delivery of low-dose dexamethasone using PCL–PEG micelles for effective treatment of rheumatoid arthritis, J. Control. Release 230 (2016) 64–72.
[117] Y. Huang, H. Gao, M. Gou, H. Ye, Y. Liu, Y. Gao, et al., Acute toxicity and genotoxicity studies on poly(ε-caprolactone)-poly(ethylene glycol)-poly(ε-caprolactone) nanomaterials, Mutat. Res. Toxicol. Environ. Mutagen. 696 (2010) 101–106.
[118] H. Xin, X. Sha, X. Jiang, W. Zhang, L. Chen, X. Fang, Anti-glioblastoma efficacy and safety of paclitaxel-loading angiopep-conjugated dual targeting PEG-PCL nanoparticles, Biomaterials 33 (2012) 8167–8176.
[119] X. Ke, V.W.L. Ng, R.J. Ono, J.M.W. Chan, S. Krishnamurthy, Y. Wang, et al., Role of non-covalent and covalent interactions in cargo loading capacity and stability of polymeric micelles, J. Control. Release 193 (2014) 9–26.
[120] S. Khoee, S. Hassanzadeh, B. Goliaie, Effects of hydrophobic drug–polyesteric core interactions on drug loading and release properties of poly(ethylene glycol)–polyester–poly(ethylene glycol) triblock core–shell nanoparticles, Nanotechnology 18 (2007) 175602.
[121] X. Shuai, T. Merdan, A.K. Schaper, F. Xi, T. Kissel, Core-cross-linked polymeric micelles as paclitaxel carriers, Bioconjug. Chem. 15 (2004) 441–448.
[122] L. Huynh, C. Neale, R. Pomès, C. Allen, Computational approaches to the rational design of nanoemulsions, polymeric micelles, and dendrimers for drug delivery, Nanomedicine Nanotechnol. Biol. Med. 8 (2012) 20–36.
[123] R. Nagarajan, M. Barry, E. Ruckenstein, Unusual selectivity in solubilization by block copolymer micelles, Langmuir 2 (1986) 210–215.
[124] V. Kumar, D.H. Adamson, R.K. Prud'homme, Fluorescent polymeric nanoparticles: aggregation and phase behavior of pyrene and amphotericin B molecules in nanoparticle cores, Small 6 (2010) 2907–2914.
[125] G. Riess, Micellization of block copolymers, Prog. Polym. Sci. 28 (2003) 1107–1170.
[126] S.K. Patel, A. Lavasanifar, P. Choi, Molecular dynamics study of the encapsulation capability of a PCL–PEO based block copolymer for hydrophobic drugs with different spatial distributions of hydrogen bond donors and acceptors, Biomaterials 31 (2010) 1780–1786.
[127] S. Patel, A. Lavasanifar, P. Choi, Application of molecular dynamics simulation to predict the compatability between water-insoluble drugs and self-associating poly (ethylene oxide)-*b*-poly(ε-caprolactone) block copolymers, Biomacromolecules 9 (2008) 3014–3023.
[128] F. Cheng, X. Guan, H. Cao, T. Su, J. Cao, Y. Chen, et al., Characteristic of core materials in polymeric micelles effect on their micellar properties studied by experimental and dpd simulation methods, Int. J. Pharm. 492 (2015) 152–160.
[129] Y. Tian, C. Shi, Y. Sun, C. Zhu, C.C. Sun, S. Mao, Designing micellar nanocarriers with improved drug loading and stability based on solubility parameter, Mol. Pharm. 12 (2015) 816–825.
[130] A.D. Costache, L. Sheihet, K. Zaveri, D.D. Knight, J. Kohn, Polymer – drug interactions in tyrosine-derived triblock copolymer nanospheres: a computational modeling approach, Mol. Pharm. 6 (2009) 1620–1627.
[131] C. Shi, D. Guo, K. Xiao, X. Wang, L. Wang, J. Luo, A drug-specific nanocarrier design for efficient anticancer therapy, Nat. Commun. 6 (2015) 7449.
[132] K.S. Chu, A.N. Schorzman, M.C. Finniss, C.J. Bowerman, L. Peng, J.C. Luft, et al., Nanoparticle drug loading as a design parameter to improve docetaxel pharmacokinetics and efficacy, Biomaterials 34 (2013) 8424–8429.
[133] S. Fredenberg, M. Wahlgren, M. Reslow, A. Axelsson, The mechanisms of drug release in poly(lactic-co-glycolic acid)-based drug delivery systems—a review, Int. J. Pharm. 415 (2011) 34–52.
[134] S. D'Souza, A review of *in vitro* drug release test methods for nano-sized dosage forms, Adv. Pharm. 2014 (2014) 1–12.
[135] L. Xie, S. Beyer, V. Vogel, M.G. Wacker, W. Mäntele, Assessing the drug release from nanoparticles: overcoming the shortcomings of dialysis by using novel optical techniques and a mathematical model, Int. J. Pharm. 488 (2015) 108–119.
[136] H.M. Aliabadi, D.R. Brocks, P. Mahdipoor, A. Lavasanifar, A novel use of an in vitro method to predict the in vivo stability of block copolymer based nanocontainers, J. Control. Release 122 (2007) 63–70.
[137] A. Cerletti, J. Drewe, G. Fricker, A. Eberle, J. Huwyler, Endocytosis and transcytosis of an immunoliposome-based brain drug delivery system, J. Drug Target. 8 (2000) 435–446.
[138] E. Scarpa, J.L. Bailey, A.A. Janeczek, P.S. Stumpf, A.H. Johnston, R.O.C. Oreffo, et al., Quantification of intracellular payload release from polymersome nanoparticles, Sci. Rep. 6 (2016) 29460.
[139] T. Cheng, Y. Zhao, X. Li, F. Lin, Y. Xu, X. Zhang, et al., Computation of octanol – water partition coefficients by guiding an additive model with knowledge, J. Chem. Inf. Model. 47 (2007) 2140–2148.
[140] E.K. Rowinsky, R.C. Donehower, Paclitaxel (taxol), N. Engl. J. Med. 332 (1995) 1004–1014.
[141] R.B. Weiss, R.C. Donehower, P.H. Wiernik, T. Ohnuma, R.J. Gralla, D.L. Trump, et al., Hypersensitivity reactions from taxol, J. Clin. Oncol. 8 (1990) 1263–1268.
[142] H. Xin, X. Jiang, J. Gu, X. Sha, L. Chen, K. Law, et al., Angiopep-conjugated poly (ethylene glycol)-co-poly(ε-caprolactone) nanoparticles as dual-targeting drug delivery system for brain glioma, Biomaterials 32 (2011) 4293–4305.
[143] E. Blanco, T. Sangai, A. Hsiao, S. Ferrati, L. Bai, X. Liu, et al., Multistage delivery of chemotherapeutic nanoparticles for breast cancer treatment, Cancer Lett. 334 (2013) 245–252.
[144] M.L. Forrest, C.-Y. Won, A.W. Malick, G.S. Kwon, In vitro release of the mTOR inhibitor rapamycin from poly(ethylene glycol)-b-poly(ε-caprolactone) micelles, J. Control. Release 110 (2006) 370–377.
[145] Y. Zhao, S. Duan, X. Zeng, C. Liu, N.M. Davies, B. Li, et al., Prodrug strategy for PSMA-targeted delivery of TGX-221 to prostate cancer cells, Mol. Pharm. 9 (2012) 1705–1716.
[146] A.T. Horowitz, Y. Barenholz, A.A. Gabizon, In vitro cytotoxicity of liposome-encapsulated doxorubicin: dependence on liposome composition and drug release, Biochim. Biophys. Acta BBA-Biomembr. 1109 (1992) 203–209.
[147] T.D. Madden, P.R. Harrigan, L.C. Tai, M.B. Bally, L.D. Mayer, T.E. Redelmeier, et al., The accumulation of drugs within large unilamellar vesicles exhibiting a proton gradient: a survey, Chem. Phys. Lipids 53 (1990) 37–46.
[148] S.A. Abraham, D.N. Waterhouse, L.D. Mayer, P.R. Cullis, T.D. Madden, M.B. Bally, The liposomal formulation of doxorubicin, Methods Enzymol. 391 (2005) 71–97.
[149] Z. Pang, H. Gao, Y. Yu, L. Guo, J. Chen, S. Pan, et al., Enhanced intracellular delivery and chemotherapy for glioma rats by transferrin-conjugated biodegradable polymersomes loaded with doxorubicin, Bioconjug. Chem. 22 (2011) 1171–1180.
[150] G. Gaucher, M.-H. Dufresne, V.P. Sant, N. Kang, D. Maysinger, J.-C. Leroux, Block copolymer micelles: preparation, characterization and application in drug delivery, J. Control. Release 109 (2005) 169–188.
[151] N. Bertrand, J.-C. Leroux, The journey of a drug-carrier in the body: an anatomo-physiological perspective, J. Control. Release 161 (2012) 152–163.
[152] M. Hamidi, A. Azadi, P. Rafiei, Pharmacokinetic consequences of pegylation, Drug Deliv. 13 (2006) 399–409.
[153] H. Kobayashi, B. Turkbey, R. Watanabe, P.L. Choyke, Cancer drug delivery: considerations in the rational design of nanosized bioconjugates, Bioconjug. Chem. 25 (2014) 2093–2100.
[154] H. Soo Choi, W. Liu, P. Misra, E. Tanaka, J.P. Zimmer, B. Itty Ipe, et al., Renal clearance of quantum dots, Nat. Biotechnol. 25 (2007) 1165–1170.
[155] M. Longmire, P.L. Choyke, H. Kobayashi, Clearance properties of nano-sized particles and molecules as imaging agents: considerations and caveats, Nanomedicine 3 (2008) 703–717.
[156] J. Huwyler, H. Kettiger, A. Schipanski, P. Wick, Engineered nanomaterial uptake and tissue distribution: from cell to organism, Int. J. Nanomedicine (2013) 3255–3269.
[157] S. Ritz, S. Schöttler, N. Kotman, G. Baier, A. Musyanovych, J. Kuharev, et al., Protein corona of nanoparticles: distinct proteins regulate the cellular uptake, Biomacromolecules 16 (2015) 1311–1321.
[158] R. Ferrari, M. Lupi, C. Colombo, M. Morbidelli, M. D'Incalci, D. Moscatelli, Investigation of size, surface charge, PEGylation degree and concentration on the cellular uptake of polymer nanoparticles, Colloids Surf. B: Biointerfaces 123 (2014) 639–647.
[159] S. Schöttler, G. Becker, S. Winzen, T. Steinbach, K. Mohr, K. Landfester, et al., Protein adsorption is required for stealth effect of poly(ethylene glycol)- and poly (phosphoester)-coated nanocarriers, Nat. Nanotechnol. 11 (2016) 372–377.
[160] K. Kristensen, A. Urquhart, E. Thormann, T. Andresen, Binding of human serum albumin to PEGylated liposomes: insights into binding numbers and dynamics by fluorescence correlation spectroscopy, Nanoscale (2016), http://pubs.rsc.org/en/Content/ArticleLanding/2016/NR/C6NR05455B (accessed October 19, 2016).
[161] S.-D. Li, L. Huang, Pharmacokinetics and biodistribution of nanoparticles, Mol. Pharm. 5 (2008) 496–504.

[162] F. Alexis, E. Pridgen, L.K. Molnar, O.C. Farokhzad, Factors affecting the clearance and biodistribution of polymeric nanoparticles, Mol. Pharm. 5 (2008) 505–515.
[163] H.M. Aliabadi, S. Elhasi, D.R. Brocks, A. Lavasanifar, Polymeric micellar delivery reduces kidney distribution and nephrotoxic effects of cyclosporine A after multiple dosing, J. Pharm. Sci. 97 (2008) 1916–1926.
[164] A.K. Yadav, P. Mishra, S. Jain, P. Mishra, A.K. Mishra, G.P. Agrawal, Preparation and characterization of HA–PEG–PCL intelligent core–corona nanoparticles for delivery of doxorubicin, J. Drug Target. 16 (2008) 464–478.
[165] W.-J. Lin, Y.-C. Chen, C.-C. Lin, C.-F. Chen, J.-W. Chen, Characterization of pegylated copolymeric micelles andin vivo pharmacokinetics and biodistribution studies, J. Biomed. Mater. Res. B Appl. Biomater. 77B (2006) 188–194.
[166] R. Feng, Z. Song, G. Zhai, Preparation and in vivo pharmacokinetics of curcumin-loaded PCL-PEG-PCL triblock copolymeric nanoparticles, Int. J. Nanomedicine 4089 (2012).
[167] A. Schädlich, H. Caysa, T. Mueller, F. Tenambergen, C. Rose, A. Göpferich, et al., Tumor accumulation of NIR fluorescent PEG–PLA nanoparticles: impact of particle size and human xenograft tumor model, ACS Nano 5 (2011) 8710–8720.
[168] A. Schädlich, C. Rose, J. Kuntsche, H. Caysa, T. Mueller, A. Göpferich, et al., How stealthy are PEG-PLA nanoparticles? An NIR in vivo study combined with detailed size measurements, Pharm. Res. 28 (2011) 1995–2007.
[169] H. Cho, G.L. Indig, J. Weichert, H.-C. Shin, G.S. Kwon, In vivo cancer imaging by poly(ethylene glycol)-b-poly(ε-caprolactone) micelles containing a near-infrared probe, Nanomedicine Nanotechnol. Biol. Med. 8 (2012) 228–236.
[170] J. Hong, Y. Li, Y. Li, Y. Xiao, H. Kuang, X. Wang, Annonaceous acetogenins nanosuspensions stabilized by PCL & ndash;PEG block polymer: significantly improved antitumor efficacy, Int. J. Nanomedicine 11 (2016) 3239–3253.
[171] Y. Zhong, C. Wang, R. Cheng, L. Cheng, F. Meng, Z. Liu, et al., cRGD-directed, NIR-responsive and robust AuNR/PEG–PCL hybrid nanoparticles for targeted chemotherapy of glioblastoma in vivo, J. Control. Release 195 (2014) 63–71.
[172] H. Gao, J. Qian, S. Cao, Z. Yang, Z. Pang, S. Pan, et al., Precise glioma targeting of and penetration by aptamer and peptide dual-functioned nanoparticles, Biomaterials 33 (2012) 5115–5123.
[173] F.A. Khaja, O.M.Y. Koo, H. Önyüksel, Nanomedicines for inflammatory diseases, Methods Enzymol, Elsevier, 2012, pp. 355–375 http://linkinghub.elsevier.com/retrieve/pii/B9780123918604000185 (accessed September 22, 2016).
[174] S.M. Moghimi, A.C. Hunter, J.C. Murray, Long-circulating and target-specific nanoparticles: theory to practice, Pharmacol. Rev. 53 (2001) 283–318.
[175] N. Bertrand, J. Wu, X. Xu, N. Kamaly, O.C. Farokhzad, Cancer nanotechnology: the impact of passive and active targeting in the era of modern cancer biology, Adv. Drug Deliv. Rev. 66 (2014) 2–25.
[176] S.K. Hobbs, W.L. Monsky, F. Yuan, W.G. Roberts, L. Griffith, V.P. Torchilin, et al., Regulation of transport pathways in tumor vessels: role of tumor type and microenvironment, Proc. Natl. Acad. Sci. 95 (1998) 4607–4612.
[177] V. Kumar Khanna, Targeted delivery of nanomedicines, ISRN Pharmacol. 2012 (2012) 1–9.
[178] J. Fang, H. Nakamura, H. Maeda, The EPR effect: unique features of tumor blood vessels for drug delivery, factors involved, and limitations and augmentation of the effect, Adv. Drug Deliv. Rev. 63 (2011) 136–151.
[179] Y. Matsumura, H. Maeda, A new concept for macromolecular therapeutics in cancer chemotherapy: mechanism of tumoritropic accumulation of proteins and the antitumor agent smancs, Cancer Res. 46 (1986) 6387–6392.
[180] Y. Sakurai, T. Hada, S. Yamamoto, A. Kato, W. Mizumura, H. Harashima, et al., Remodeling of the extracellular matrix by endothelial cell-targeting siRNA improves the EPR-based delivery of 100 nm particles, Mol. Ther. (2016), http://www.nature.com/doifinder/10.1038/mt.2016.178 (accessed September 28, 2016).
[181] M. Yu, J. Zheng, Clearance pathways and tumor targeting of imaging nanoparticles, ACS Nano 9 (2015) 6655–6674.
[182] A. Karageorgis, S. Dufort, L. Sancey, M. Henry, S. Hirsjärvi, C. Passirani, et al., An MRI-based classification scheme to predict passive access of 5 to 50-nm large nanoparticles to tumors, Sci. Rep. 6 (2016) 21417.
[183] E. Karathanasis, S. Suryanarayanan, S.R. Balusu, K. McNeeley, I. Sechopoulos, A. Karellas, et al., Imaging nanoprobe for prediction of outcome of nanoparticle chemotherapy by using mammography 1, Radiology 250 (2009) 398–406.
[184] C.-M.J. Hu, L. Zhang, Nanoparticle-based combination therapy toward overcoming drug resistance in cancer, Biochem. Pharmacol. 83 (2012) 1104–1111.
[185] E. Manchado, S. Weissmueller, J.P. Morris, C.-C. Chen, R. Wullenkord, A. Lujambio, et al., A combinatorial strategy for treating KRAS-mutant lung cancer, Nature 534 (2016) 647–651.
[186] J. Meng, F. Guo, H. Xu, W. Liang, C. Wang, X.-D. Yang, Combination therapy using co-encapsulated resveratrol and paclitaxel in liposomes for drug resistance reversal in breast cancer cells in vivo, Sci. Rep. 6 (2016) 22390.
[187] P. Tardi, S. Johnstone, N. Harasym, S. Xie, T. Harasym, N. Zisman, et al., In vivo maintenance of synergistic cytarabine:daunorubicin ratios greatly enhances therapeutic efficacy, Leuk. Res. 33 (2009) 129–139.
[188] C.-M.J. Hu, S. Aryal, L. Zhang, Nanoparticle-assisted combination therapies for effective cancer treatment, Ther. Deliv. 1 (2010) 323–334.
[189] H. Cho, T.C. Lai, G.S. Kwon, Poly(ethylene glycol)-block-poly(ε-caprolactone) micelles for combination drug delivery: evaluation of paclitaxel, cyclopamine and gossypol in intraperitoneal xenograft models of ovarian cancer, J. Control. Release 166 (2013) 1–9.
[190] C. Conte, G. Costabile, I. d'Angelo, M. Pannico, P. Musto, G. Grassia, et al., Skin transport of PEGylated poly(ε-caprolactone) nanoparticles assisted by (2-hydroxypropyl)-β-cyclodextrin, J. Colloid Interface Sci. 454 (2015) 112–120.
[191] F. Laredj-Bourezg, M.-A. Bolzinger, J. Pelletier, J.-P. Valour, M.-R. Rovère, B. Smatti, et al., Skin delivery by block copolymer nanoparticles (block copolymer micelles), Int. J. Pharm. 496 (2015) 1034–1046.
[192] Q. Li, K.L. Lai, P.S. Chan, S.C. Leung, H.Y. Li, Y. Fang, et al., Micellar delivery of dasatinib for the inhibition of pathologic cellular processes of the retinal pigment epithelium, Colloids Surf. B: Biointerfaces 140 (2016) 278–286.
[193] E. Nogueira, A.C. Gomes, A. Preto, A. Cavaco-Paulo, Design of liposomal formulations for cell targeting, Colloids Surf. B: Biointerfaces 136 (2015) 514–526.
[194] M. Gou, M. Dai, X. Li, L. Yang, M. Huang, Y. Wang, et al., Preparation of mannan modified anionic PCL–PEG–PCL nanoparticles at one-step for bFGF antigen delivery to improve humoral immunity, Colloids Surf. B: Biointerfaces 64 (2008) 135–139.
[195] N. Karra, S. Benita, The ligand nanoparticle conjugation approach for targeted cancer therapy, Curr. Drug Metab. 13 (2012) 22–41.
[196] R. Yang, F. Meng, S. Ma, F. Huang, H. Liu, Z. Zhong, Galactose-decorated cross-linked biodegradable poly(ethylene glycol)-*b*-poly(ε-caprolactone) block copolymer micelles for enhanced hepatoma-targeting delivery of paclitaxel, Biomacromolecules 12 (2011) 3047–3055.
[197] S. Ji, Z. Zhu, T.R. Hoye, C.W. Macosko, Maleimide functionalized poly(ε-caprolactone)-*block*-poly(ethylene glycol) (PCL-PEG-MAL): synthesis, nanoparticle formation, and thiol conjugation, Macromol. Chem. Phys. 210 (2009) 823–831.
[198] V. Pourcelle, H. Freichels, F. Stoffelbach, R. Auzély-Velty, C. Jérôme, J. Marchand-Brynaert, Light induced functionalization of PCL-PEG block copolymers for the covalent immobilization of biomolecules, Biomacromolecules 10 (2009) 966–974.
[199] V. Fievez, L. Plapied, A. des Rieux, V. Pourcelle, H. Freichels, V. Wascotte, et al., Targeting nanoparticles to M cells with non-peptidic ligands for oral vaccination, Eur. J. Pharm. Biopharm. 73 (2009) 16–24.
[200] M. Demeule, A. Regina, C. Che, J. Poirier, T. Nguyen, R. Gabathuler, et al., Identification and design of peptides as a new drug delivery system for the brain, J. Pharmacol. Exp. Ther. 324 (2007) 1064–1072.
[201] M. Demeule, J.-C. Currie, Y. Bertrand, C. Ché, T. Nguyen, A. Régina, et al., Involvement of the low-density lipoprotein receptor-related protein in the transcytosis of the brain delivery vector angiopep-2, J. Neurochem. 106 (2008) 1534–1544.
[202] J. Huwyler, D. Wu, W.M. Pardridge, Brain drug delivery of small molecules using immunoliposomes, Proc. Natl. Acad. Sci. 93 (1996) 14164–14169.
[203] J. Huwyler, J. Yang, W.M. Pardridge, Receptor mediated delivery of daunomycin using immunoliposomes: pharmacokinetics and tissue distribution in the rat, J. Pharmacol. Exp. Ther. 282 (1997) 1541–1546.
[204] L.-H. Dieu, D. Wu, C.G. Palivan, V. Balasubramanian, J. Huwyler, Polymersomes conjugated to 83-14 monoclonal antibodies: invitro targeting of brain capillary endothelial cells, Eur. J. Pharm. Biopharm. (2014), http://linkinghub.elsevier.com/retrieve/pii/S093964111400188X (accessed July 9, 2014).
[205] P.M. Kelly, C. Åberg, E. Polo, A. O'Connell, J. Cookman, J. Fallon, et al., Mapping protein binding sites on the biomolecular corona of nanoparticles, Nat. Nanotechnol. 10 (2015) 472–479.
[206] J.T. Duskey, K.G. Rice, Nanoparticle ligand presentation for targeting solid tumors, AAPS PharmSciTech 15 (2014) 1345–1354.
[207] W.-L.L. Suen, Y. Chau, Size-dependent internalisation of folate-decorated nanoparticles via the pathways of clathrin and caveolae-mediated endocytosis in ARPE-19 cells: size-dependent endocytosis of folate-decorated NPs, J. Pharm. Pharmacol. 66 (2014) 564–573.
[208] A.M. Master, M. Livingston, N.L. Oleinick, A. Sen Gupta, Optimization of a nanomedicine-based silicon phthalocyanine 4 photodynamic therapy (pc 4-PDT) strategy for targeted treatment of EGFR-overexpressing cancers, Mol. Pharm. 120719134106003 (2012).
[209] A.M. Master, Y. Qi, N.L. Oleinick, A.S. Gupta, EGFR-mediated intracellular delivery of Pc 4 nanoformulation for targeted photodynamic therapy of cancer: in vitro studies, Nanomedicine Nanotechnol. Biol. Med. 8 (2012) 655–664.
[210] T. Tanaka, K. Yamada, K. Senzaki, H. Narimatsu, K. Nishimura, T. Kameyama, et al., NC-1900, an active fragment analog of arginine vasopressin, improves learning and memory deficits induced by b-amyloid protein in rats, Eur. J. Pharmacol. 2–3 (1998) 135–142.
[211] T. Yoshikawa, W.M. Pardridge, Biotin delivery to brain with a covalent conjugate of avidin and a monoclonal antibody to the transferrin receptor, J. Pharmacol. Exp. Ther. 263 (1992) 897–903.
[212] U. Bickel, Y.S. Kang, T. Yoshikawa, W.M. Pardridge, In vivo demonstration of subcellular localization of anti-transferrin receptor monoclonal antibody-colloidal gold conjugate in brain capillary endothelium, J. Histochem. Cytochem. 42 (1994) 1493–1497.
[213] U. Bickel, T. Yoshikawa, E.M. Landaw, K.F. Faull, W.M. Pardridge, Pharmacologic effects in vivo in brain by vector-mediated peptide drug delivery, Proc. Natl. Acad. Sci. 90 (1993) 2618–2622.
[214] Z. Liu, M. Jiang, T. Kang, D. Miao, G. Gu, Q. Song, et al., Lactoferrin-modified PEG-co-PCL nanoparticles for enhanced brain delivery of NAP peptide following intranasal administration, Biomaterials 34 (2013) 3870–3881.
[215] T. Kanazawa, F. Akiyama, S. Kakizaki, Y. Takashima, Y. Seta, Delivery of siRNA to the brain using a combination of nose-to-brain delivery and cell-penetrating peptide-modified nano-micelles, Biomaterials 34 (2013) 9220–9226.
[216] T. Kanazawa, Brain delivery of small interfering ribonucleic acid and drugs through intranasal administration with nano-sized polymer micelles, Med. Devices Evid. Res. 57 (2015).
[217] C.P. McCoy, C. Brady, J.F. Cowley, S.M. McGlinchey, N. McGoldrick, D.J. Kinnear, et al., Triggered drug delivery from biomaterials, Expert Opin. Drug Deliv. 7 (2010) 605–616.
[218] C. Gialeli, A.D. Theocharis, N.K. Karamanos, Roles of matrix metalloproteinases in cancer progression and their pharmacological targeting: MMPs as potential targets in malignancy, FEBS J. 278 (2011) 16–27.

[219] J. Vandooren, G. Opdenakker, P.M. Loadman, D.R. Edwards, Proteases in cancer drug delivery, Adv. Drug Deliv. Rev. 97 (2016) 144–155.
[220] H. Yu, J. Chen, S. Liu, Q. Lu, J. He, Z. Zhou, et al., Enzyme sensitive, surface engineered nanoparticles for enhanced delivery of camptothecin, J. Control. Release 216 (2015) 111–120.
[221] B. Surnar, M. Jayakannan, Stimuli-responsive poly(caprolactone) vesicles for dual drug delivery under the gastrointestinal tract, Biomacromolecules 14 (2013) 4377–4387.
[222] H. Sun, B. Guo, R. Cheng, F. Meng, H. Liu, Z. Zhong, Biodegradable micelles with sheddable poly(ethylene glycol) shells for triggered intracellular release of doxorubicin, Biomaterials 30 (2009) 6358–6366.
[223] Y. Zhu, J. Zhang, F. Meng, C. Deng, R. Cheng, J. Feijen, et al., cRGD-functionalized reduction-sensitive shell-sheddable biodegradable micelles mediate enhanced doxorubicin delivery to human glioma xenografts in vivo, J. Control. Release 233 (2016) 29–38.
[224] H. Ko, S. Son, S. Bae, J.-H. Kim, G.-R. Yi, J.H. Park, Near-infrared light-triggered thermochemotherapy of cancer using a polymer–gold nanorod conjugate, Nanotechnology 27 (2016) 175102.
[225] J. Liu, C. Detrembleur, B. Grignard, M.-C. De Pauw-Gillet, S. Mornet, M. Treguer-Delapierre, et al., Gold nanorods with phase-changing polymer corona for remotely near-infrared-triggered drug release, Chem. Asian. J. 9 (2014) 275–288.
[226] S.M. Nikles, J.A. Nikles, J.S. Hudson, D.E. Nikles, Diblock copolymers for magnetically triggered drug delivery systems, JOSHUA 7 (2010) 35–39.
[227] A.L. Glover, J.B. Bennett, J.S. Pritchett, S.M. Nikles, D.E. Nikles, J.A. Nikles, et al., Magnetic heating of iron oxide nanoparticles and magnetic micelles for cancer therapy, IEEE Trans. Magn. 49 (2013) 231–235.
[228] F. Huang, J. Wang, A. Qu, L. Shen, J. Liu, J. Liu, et al., Maintenance of amyloid β peptide homeostasis by artificial chaperones based on mixed-shell polymeric micelles, Angew. Chem. Int. Ed. 53 (2014) 8985–8990.
[229] K. Miao, H. Liu, Y. Zhao, Thermo, pH and reduction responsive coaggregates comprising AB2C2 star terpolymers for multi-triggered release of doxorubicin, Polym. Chem. 5 (2014) 3335.
[230] J.H. Ryu, H. Koo, I.-C. Sun, S.H. Yuk, K. Choi, K. Kim, et al., Tumor-targeting multi-functional nanoparticles for theragnosis: new paradigm for cancer therapy, Adv. Drug Deliv. Rev. 64 (2012) 1447–1458.
[231] Y. Opoku-Damoah, R. Wang, J. Zhou, Y. Ding, Versatile nanosystem-based cancer theranostics: design inspiration and predetermined routing, Theranostics 6 (2016) 986–1003.
[232] J.T. Cole, N.B. Holland, Multifunctional nanoparticles for use in theranostic applications, Drug Deliv. Transl. Res. 5 (2015) 295–309.
[233] G. Lucignani, Nanoparticles for concurrent multimodality imaging and therapy: the dawn of new theragnostic synergies, Eur. J. Nucl. Med. Mol. Imaging 36 (2009) 869–874.
[234] G. Chen, I. Roy, C. Yang, P.N. Prasad, Nanochemistry and nanomedicine for nanoparticle-based diagnostics and therapy, Chem. Rev. 116 (2016) 2826–2885.
[235] M.A. Hahn, A.K. Singh, P. Sharma, S.C. Brown, B.M. Moudgil, Nanoparticles as contrast agents for in-vivo bioimaging: current status and future perspectives, Anal. Bioanal. Chem. 399 (2011) 3–27.
[236] P. Huang, J. Lin, W. Li, P. Rong, Z. Wang, S. Wang, et al., Biodegradable gold nanovesicles with an ultrastrong plasmonic coupling effect for photoacoustic imaging and photothermal therapy, Angew. Chem. Int. Ed. 52 (2013) 13958–13964.
[237] S. Huang, P.K. Upputuri, H. Liu, M. Pramanik, M. Wang, A dual-functional benzobisthiadiazole derivative as an effective theranostic agent for near-infrared photoacoustic imaging and photothermal therapy, J. Mater. Chem. B 4 (2016) 1696–1703.
[238] J.-X. Zhou, Ren-Xu, J.-X. Zhou, Folate-targeted polymeric micelles loaded with ultrasmall superparamagnetic iron oxide: combined small size and high MRI sensitivity, Int. J. Nanomedicine (2012) 2863–2872.
[239] G. Hong, R. Yuan, B. Liang, J. Shen, X. Yang, X. Shuai, Folate-functionalized polymeric micelle as hepatic carcinoma-targeted, MRI-ultrasensitive delivery system of antitumor drugs, Biomed. Microdevices 10 (2008) 693–700.
[240] T. Endres, M. Zheng, A. Kılıç, A. Turowska, M. Beck-Broichsitter, H. Renz, et al., Amphiphilic biodegradable PEG-PCL-PEI triblock copolymers for FRET-capable *in vitro* and *in vivo* delivery of siRNA and quantum dots, Mol. Pharm. 11 (2014) 1273–1281.
[241] T.K. Endres, M. Beck-Broichsitter, O. Samsonova, T. Renette, T.H. Kissel, Self-assembled biodegradable amphiphilic PEG–PCL–lPEI triblock copolymers at the borderline between micelles and nanoparticles designed for drug and gene delivery, Biomaterials 32 (2011) 7721–7731.
[242] T. Endres, M. Zheng, M. Beck-Broichsitter, T. Kissel, Lyophilised ready-to-use formulations of PEG-PCL-PEI nano-carriers for siRNA delivery, Int. J. Pharm. 428 (2012) 121–124.
[243] Y. Wu, Y. Zhang, W. Zhang, C. Sun, J. Wu, J. Tang, Reversing of multidrug resistance breast cancer by co-delivery of P-gp siRNA and doxorubicin via folic acid-modified core-shell nanomicelles, Colloids Surf. B: Biointerfaces 138 (2016) 60–69.
[244] S.-Y. Lee, C.-Y. Yang, C.-L. Peng, M.-F. Wei, K.-C. Chen, C.-J. Yao, et al., A theranostic micelleplex co-delivering SN-38 and VEGF siRNA for colorectal cancer therapy, Biomaterials 86 (2016) 92–105.
[245] Y. (Chezy) Barenholz, Doxil® — the first FDA-approved nano-drug: lessons learned, J. Control. Release 160 (2012) 117–134.
[246] J.I. Hare, T. Lammers, M.B. Ashford, S. Puri, G. Storm, S.T. Barry, Challenges and strategies in anti-cancer nanomedicine development: an industry perspective, Adv. Drug Deliv. Rev. 108 (2016) 25–38.
[247] P. Satalkar, B.S. Elger, P. Hunziker, D. Shaw, Challenges of clinical translation in nanomedicine: a qualitative study, Nanomedicine Nanotechnol. Biol. Med. 12 (2016) 893–900.
[248] M. Ukawala, T. Rajyaguru, K. Chaudhari, A.S. Manjappa, S. Pimple, A.K. Babbar, et al., Investigation on design of stable etoposide-loaded PEG-PCL micelles: effect of molecular weight of PEG-PCL diblock copolymer on the *in vitro* and *in vivo* performance of micelles, Drug Deliv. 19 (2012) 155–167.
[249] N. Dubey, R. Varshney, J. Shukla, A. Ganeshpurkar, P.P. Hazari, G.P. Bandopadhaya, et al., Synthesis and evaluation of biodegradable PCL/PEG nanoparticles for neuroendocrine tumor targeted delivery of somatostatin analog, Drug Deliv. 19 (2012) 132–142.
[250] W.-L.L. Suen, Y. Chau, Specific uptake of folate-decorated triamcinolone-encapsulating nanoparticles by retinal pigment epithelium cells enhances and prolongs antiangiogenic activity, J. Control. Release 167 (2013) 21–28.
[251] J. Yang, X. Sun, W. Mao, M. Sui, J. Tang, Y. Shen, Conjugate of Pt(IV)–histone deacetylase inhibitor as a prodrug for cancer chemotherapy, Mol. Pharm. 9 (2012) 2793–2800.
[252] Q. Li, W. Xiong, L. Peng, H. Chen, Surface modification of MPEG-b-PCL-based nanoparticles via oxidative self-polymerization of dopamine for malignant melanoma therapy, Int. J. Nanomedicine 2985 (2015).
[253] X. Yang, W. Deng, L. Fu, E. Blanco, J. Gao, D. Quan, et al., Folate-functionalized polymeric micelles for tumor targeted delivery of a potent multidrug-resistance modulator FG020326, J. Biomed. Mater. Res. A 86A (2008) 48–60.
[254] E.K. Park, S.Y. Kim, S.B. Lee, Y.M. Lee, Folate-conjugated methoxy poly(ethylene glycol)/poly(ε-caprolactone) amphiphilic block copolymeric micelles for tumor-targeted drug delivery, J. Control. Release 109 (2005) 158–168.

CHAPTER II

Biodegradable PEG-PCL Micelles as Long-Circulating Drug Carriers

Grossen P, Detampel P, Sieber S, Hartmann Z, Witzigmann D, Québatte G, Huwyler J

Manuscript: Ready for submission

Highlights: While successful therapeutic options are available for many diseases, cancer remains a leading cause of death worldwide. Long-circulating drug delivery system may increase the performance of established drug therapies and decrease the high attrition rate of new chemical entities for the treatment of cancer entering clinical trials. In this study, a nanoparticulate drug delivery system based on PEG-PCL was developed and used for the delivery of doxorubicin. Therapeutic effects were analyzed *in vitro* and accumulation of doxorubicin at its site of action was studied. To assess the potential of doxorubicin-loaded PEG-PCL micelles for passive tumor targeting, PK properties and tissue distribution were analyzed in a high-trough put-screening model (i.e. zebrafish embryos) and in rats. Results were compared to doxorubicin administered as free drug and encapsulated in PEG-liposomes, the gold standard for long circulating NPs.

Biodegradable PEG-PCL Micelles as Long-Circulating Drug Carriers

[1] Grossen P, [1] Sieber S, [1] Detampel P, [1] Witzigmann D, [1] Québatte G,

°[1] Huwyler J

[1] Division of Pharmaceutical Technology, Department of Pharmaceutical Sciences, University of Basel, Basel, Switzerland

° Corresponding author:

Klingelbergstrasse 50, CH-4056 Basel, Switzerland

E-Mail: joerg.huwyler@unibas.ch

Phone: +41 (0)61 207 15 13

Abstract

The use of nanomedicines for delivery of anti-cancer drugs is a promising strategy to increase the therapeutic efficiency of these compounds. Whereas PEGylated liposomes (PEG-liposomes) are gold standards for long-circulating drug carriers, other systems such as polymeric micelles are promising alternatives.

In this study, doxorubicin-loaded poly(ethylene glycol)-*b*-poly(ε-caprolactone) (PEG-PCL) micelles were compared to doxorubicin-loaded PEG-liposomes. Dox-PEG-PCL micelles were characterized by similar pharmacological effects as compared to doxorubicin administered as free drug or encapsulated in PEG-liposomes. Biodistribution studies in an *in vivo* screening tool (i.e. zebrafish embryos) revealed long circulating properties of PEG-PCL micelles. To further confirm these findings, pharmacokinetics of doxorubicin as free drug or encapsulated in PEG-liposomes or PEG-PCL micelles was assessed *in vivo*. Whereas free doxorubicin was rapidly cleared form the blood circulation, encapsulation in PEG-PCL micelles dramatically increased the area under the plasma concentration curve and decreased the systemic volume of distribution. These results highlight the long-circulating properties of doxorubicin-loaded PEG-PCL micelles and thus their potential application for the delivery of anti-cancer drugs via passive tumor targeting.

Introduction

Despite great progress in the understanding of cancer biology, this group of diseases still remains a leading cause of death. With the discovery of novel potential drug targets, a variety of promising new chemical entities entered

preclinical and clinical research. Nevertheless, attrition during clinical development of oncology drugs is high: Less than one out of ten compounds receives market approval after reaching Phase-I clinical trials [1]. Major causes of failure are lack in clinical safety and non-favorable pharmacokinetics of the investigational compounds [2,3]. Nanocarriers can increase drug solubility, protect metabolically labile drugs, improve the pharmacokinetics of their drug payload (i.e. prolong the blood-circulation time), and by this reduce off-target effects, increase therapeutic efficiency, and improve drug safety [4]. They can therefore be used to implement drug delivery strategies of highly potent drugs lacking in drug-like properties to cancer cells. Moreover, some solid tumors are characterized by fenestrated blood vessels and reduced lymphatic drainage. Long-circulating nanoparticles (NPs) can therefore extravasate and passively accumulate in the tumor tissue, a phenomenon called the enhanced permeability and retention (EPR) effect [5]. The efficiency of passive tumor targeting mainly depends on tumor biology (e.g. blood flow and pore size of the fenestration) as well as particle-related features such as size and surface charge [6,7]. Doxorubicin entrapped in PEG-liposomes, for example, remain in the plasma for hours and accumulates in solid tumors when injected i.v., whereas free drug is rapidly cleared from the central blood compartment [8–10]. Although PEG-liposomes remain the most advanced nanocarriers (i.e. gold standard for long-circulating drug carriers), they are not suitable for all therapeutic strategies. Therefore, a big arsenal of NPs was developed using various building materials during the last decades. Some showed encouraging preclinical results and successfully proceeded to clinical trials [11]. Genexol-PM™, a polymeric micelle encapsulating paclitaxel reached market

approval in 2007 [12]. Micelles consisting of FDA approved, biodegradable PEG-PCL block copolymers are promising candidates for the delivery of anti-cancer drugs [13–15]. The hydrophobic PCL core can serve as a reservoir for drugs, the hydrophilic PEG corona sterically stabilizes the micelle, minimizes protein opsonization, and by this, prolongs the blood circulation-time of the drug carrier [16–19]. They can easily be chemically modified, are biodegradable, and non-toxic. When paclitaxel was entrapped in PEG-PCL micelles, a high tumor accumulation was observed and mean survival time of xenograft-bearing animals was prolonged 1.5-fold as compared to animals treated with an approved paclitaxel formulation (Taxol^{TM}) [14]. The aim of this experiment was to produce PEG-PCL micelles loaded with the model drug doxorubicin. Pharmacological effects of doxorubicin were analyzed *in vitro* on the hepatocellular carcinoma (HCC)-derived cell line HepG2. Cellular uptake and nuclear translocation of doxorubicin was analyzed using confocal microscopy. To assess the potential of PEG-PCL micelles for passive drug targeting, the pharmacokinetic profile of doxorubicin as free drug and encapsulated in PEG-liposomes or PEG-PCL micelles was assessed *in vivo*. To the best of our knowledge this is the first time that PEG-PLC micelles are compared to PEG-liposomes in the same experimental setting.

Results

Physico-chemical characterization of doxorubicin-loaded nanoparticles

PEG-PCL micelles were prepared and loaded with doxorubicin using a modified cosolvent method [20]. PEG-PCL micelles had a mean hydrodynamic diameter of 73.4 ± 4.2 nm and a monodisperse size distribution (PDI

0.083 ± 0.029) as determined by DLS ($n = 3$) (Table 1). TEM analysis showed spherical particles with a diameter of 77.3 ± 20.9 nm ($n = 50$) as shown in Figure 1. PEG-PCL micelles were stable over 2 months as indicated by constant size and size distribution (data not shown). A drug loading content (DLC) of 1.9 ± 0.04% [w/w] was achieved with a drug loading efficiency (DLC) of 5.0 ± 0.1%. Drug release at 37 °C was analyzed with PBS (pH 7.4, 3% BSA) as a receiver medium. A slow release of doxorubicin was observed. Only 5.1 % of the initial drug content was detected in the receiver medium after 24 hours (Fig. 2). Similar results were obtained for Dox-PEG-liposomes (Table 1 and Fig. 2)

***In vitro* characterization of doxorubicin-loaded nanoparticles**

A cell viability assay was used to study the pharmacological effect of Dox-PEG-PCL micelles. A human HCC-derived cell line (HepG2) was incubated with equal concentrations of free doxorubicin or doxorubicin encapsulated in PEG-liposomes or PEG-PCL micelles. Cell viability was then determined using the MTT assay (Fig. 3B). A similar decrease in cell viability was detected in cells incubated with doxorubicin administered as free drug or encapsulated in PEG-liposomes or PEG-PCL micelles. In addition, cellular uptake and intracellular distribution of doxorubicin was analyzed qualitatively using confocal microscopy. After 24 hours of incubation with either free drug or doxorubicin encapsulated in PEG-PCL micelles, doxorubicin fluorescence (red) merged with stained nuclei (blue) as shown in Figure 3A. However, a slower uptake of doxorubicin was observed when encapsulated in PEG-PCL micelles as indicated by lower intracellular red fluorescence after 2 hours of incubation

(data not shown). In addition to qualitative analysis, Pearson's Correlation Coefficients (PCC) were calculated. Free doxorubicin showed a high correlation with stained nuclei after 2 hours (PCC 0.853) whereas doxorubicin encapsulated in PEG-PCL micelles showed a low correlation (PCC 0.165). After 24 hours, both formulations showed similar PCCs with values of 0.536 for free doxorubicin and 0.657 for doxorubicin encapsulated in PEG-PCL micelles.

Biodistribution in zebrafish embryos

The biodistribution and blood circulation of fluorescently labeled PEG-PCL micelles and PEG-liposomes were tested in zebrafish embryos. Formulations were injected in the duct of cuvier using a micromanipulator device. For both formulations, DiI (carbocyanine dye) fluorescence was found evenly distributed in tail vein areas without signs of agglomeration or uptake by macrophages (Fig. 4)

***In vivo* pharmacokinetics and biodistribution**

Plasma concentration of free doxorubicin and doxorubicin encapsulated in PEG-liposomes or PEG-PCL micelles was analyzed after i.v. injection using a jugular vein catheter. To prevent adsorption and loss of doxorubicin to plastic tubing during preparation and injection, free drug formulation was prepared using 0.1% BSA. The area under the plasma concentration curve (AUC_0^{∞}) increased significantly (Table 2 and Fig. 5) when doxorubicin was encapsulated in PEG-liposomes (16-fold) or PEG-PCL micelles (14-fold). From these data, the systemic volume of distribution at steady state (V_D) and the plasma clearance were calculated (Table 2). As described previously, a

pronounced difference was revealed for PEG-liposomes as compared to free drug [21,22]. Free doxorubicin disappeared rapidly from the plasma compartment with a plasma clearance of 44.5 ± 10.5 mL/min/kg and a high V_D of 1182.0 ± 311.9 mL/kg. Encapsulation of doxorubicin in PEG-liposomes decreased plasma clearance 90-fold (0.5 ± 0.1 mL/min/kg). A similar effect on the plasma clearance was obtained when doxorubicin was entrapped in PEG-PCL micelles (0.6 ± 0.2 mL/min/kg). V_D of doxorubicin was decreased dramatically when encapsulated in PEG-liposomes (44.0 ± 8.9 mL/kg) or PEG-PCL micelles (77.0 ± 9.1 mL/kg). In addition to the plasma concentration over time, recovery of doxorubicin from liver, spleen, kidneys, lung, and heart after 60 min was analyzed (Fig. 6). Encapsulation of doxorubicin in PEG-liposomes and PEG-PCL micelles significantly reduced accumulation in kidneys.

Discussion

Physico-chemical characterization of doxorubicin-loaded nanoparticles

PEG-PCL micelles used in this study were characterized by a monodisperse size distribution, a hydrodynamic diameter below 100 nm, and a slightly negative zeta potential (Table 1). Ideally, long-circulating nanocarriers should be within a size range of 10-500 nm to avoid renal filtration and uptake by mononuclear macrophage system (MPS) [23–25]. Doxorubicin was stably incorporated in PEG-PCL micelles as indicated by a slow drug release profile (Fig. 2). Stable drug incorporation is important regarding two issues. First, premature drug release may reverse the positive effects of NP encapsulation

on the drug. It was shown that the release rate of doxorubicin from liposomes negatively correlates with intratumoral accumulation and therapeutic activity [26]. Second, stable encapsulation is a prerequisite for further *in vivo* testing of PEG-PCL micelles using doxorubicin as model drug. Total recovery of doxorubicin after 72 hours was 79.3 ± 8.8%. A high affinity of doxorubicin to plastic devices (e.g. polypropylene) was described previously [27]. Although 3% BSA was added to the receiver medium, adsorption of doxorubicin to plastic could thus reduce the total recovery obtained in the release experiments.

***In vitro* characterization of doxorubicin-loaded nanoparticles**

The pharmacological effect of doxorubicin encapsulated in PEG-PCL micelles was analyzed on HepG2 cells. Similar therapeutic effects (i.e. decrease in cell viability) were obtained when cells were incubated with doxorubicin as free drug or encapsulated in PEG-liposomes or PEG-PCL micelles (Fig. 3B). These results indicate that although doxorubicin was stably encapsulated in PEG-PCL micelles, cellular uptake results in efficient release of the drug from its carrier. These findings were further supported qualitatively by confocal microscopy. One mode of action that was described for doxorubicin is the intercalation with DNA and disturbance of DNA repair mechanisms [28]. Thus, to induce its pharmacological effects, doxorubicin needs to enter the cell nucleus. After 2 hours of incubation, doxorubicin fluorescence was observed as condensed spots in the cytoplasm, indicating uptake of doxorubicin incorporated in PEG-PCL micelles (PCC 0.165). In contrast, doxorubicin fluorescence was observed in the cell nucleus when doxorubicin was

administered as free drug (PCC 0.853). After 24 hours of incubation, doxorubicin fluorescence merged with stained cell nuclei in cells incubated with free drug (PCC 0.536) or Dox-PEG-PCL micelles (PCC 0.657) as shown in Fig. 3A. Higher fluorescence intensity for cells incubated with free drug as compared to cells incubated with Dox-PEG-PCL micelles indicates slower cellular uptake due to stealth properties of PEG-PCL micelles. Decrease in PCC for free doxorubicin may be explained due to morphological changes such as blebbing of incubated cells due to initiation of apoptosis as described previously [29].

Biodistribution in zebrafish embryos

Invertebrate models such as zebrafish embryos are valuable screening tools to predict *in vivo* behavior of nanomedicines as shown previously [30]. In comparison with mammalian *in vivo* models, these screening models (i.e. zebrafish embryos) have several advantages. They can be used in 96-well formats and thus are prawn to high-trough put screening, they are transparent and allow fluorescent imaging, and they are cheap. Additionally, there are major benefits on animal welfar. Whereas non-circulating particles are rapidly removed from the central blood compartment, fluorescence of long-circulating NPs remains in the blood compartment for hours [30]. One hour after injection into the duct of cuvier, both formulations tested in this work showed evenly distributed fluorescence signals in the vasculature (Fig. 4). No agglomerations or extravascular signal were detected indicating the long-circulating properties of PEG-PCL micelles, comparable to PEG-liposomes.

In vivo pharmacokinetics and biodistribution

The goal of this study was to assess the potential of PEG-PCL micelles as long circulating drug delivery system using the model drug doxorubicin. Although the pharmacokinetic profile of PEG-PCL micelles was analyzed previously [31–33], factors such as polymer composition and NP preparation may influence the *in vivo* faith of NPs. In addition, parameters related to the *in vivo* model and study design (e.g. choice of analytics, dose, and animal species) can highly influence the outcome of the experiment. Due to these reasons, the pharmacokinetic profiles of doxorubicin as free drug or encapsulated in PEG-liposomes or PEG-PCL micelles were analyzed in the same experimental setting. With this approach, PEG-PCL micelles can be compared to the gold standard of long circulating NPs, i.e. PEG-liposomes. Plasma concentration data were analyzed using PK solver [34]. A one (Dox-PEG-liposomes and Dox-PEG-PCL micelles) and two compartment model (free doxorubicin) were used for fitting and interpretation of data. The best model for each formulation was selected using the Akaike Information Criterion [35] and the Schwarz Criterion [36] as described previously [37]. To validate the experimental animal model, a design that was used in previous experiments using anthracyclines in combination with PEG-liposomes was chosen. Data obtained for doxorubicin as free drug or entrapped in PEG-liposomes were comparable to the reference data indicating the validity of the experimental procedure used in this study [21,22]. Encapsulation of doxorubicin in PEG-liposomes or in PEG-PCL micelles reduced the total clearance from plasma compartment dramatically. Both formulations increased the AUC_0^{∞} (16-fold increase vs. 14-fold increase) and the plasma clearance (89-fold decrease vs. 74-fold

decrease) of doxorubicin (Table 2). However, the V_D of doxorubicin encapsulated in PEG-PCL micelles was almost 2-fold higher as compared to PEG-liposomes. Several reasons could account for this difference. First, traces of non-encapsulated doxorubicin characterized by a high V_D could influence the experimental outcome. Second, differences in NP characteristics could result in differences in tissue distribution as it was shown for lipid NPs [38]. Indeed, slightly higher doses of doxorubicin were recovered from liver and kidneys when encapsulated in Dox-PEG-PCL micelles as compared to PEG-liposomes (Fig. 6).

Conclusion

PEG-PCL micelles prepared in this study are characterized by physico-chemical properties that are favorable for long-circulating drug carriers. Using a powerful screening tool for the biodistribution and blood circulation (i.e. zebrafish embryos), a long plasma half-life of PEG-PCL micelles was predicted. These results were further confirmed in experimental animals (i.e. rats). PEG-PCL micelles were compared to PEG-liposomes, the gold standard for long circulating NPs, in the same experimental setting. PEG-PCL micelles remained in the central blood compartment for hours and reduced the accumulation of doxorubicin in off-target tissue such as the liver and kidney. Thus, PEG-PCL micelles are suitable carriers for anti-cancer drugs and can be used to increase the therapeutic performance drugs that lack in drug-like properties and that are characterized by unfavorable pharmacokinetics.

Acknowledgements

The authors would like to thank Karin Hinni (Head of Biozentrum Safety, University of Basel, Basel, Switzerland) for her support with liquid scintillation counting. The authors would like to thank Prof. Dr. Markus Affolter (Biozentrum, University of Basel, Basel, Switzerland) for the kdrl:GFP zebrafish.

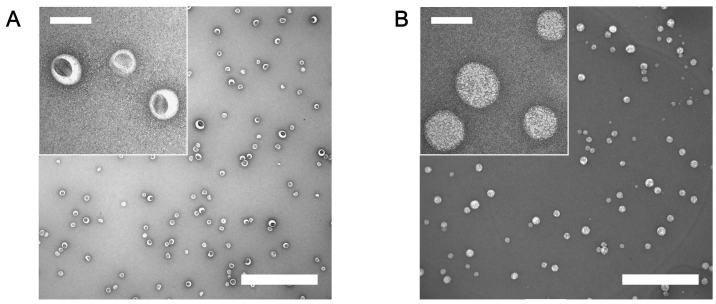

Figure 1 Transmission electron micrographs of doxorubicin-loaded (A) PEG-liposomes and (B) PEG-PCL micelles. Nanoparticles were negatively stained using uranyl acetate. Scale bar: 500 nm; Insert: 100 nm.

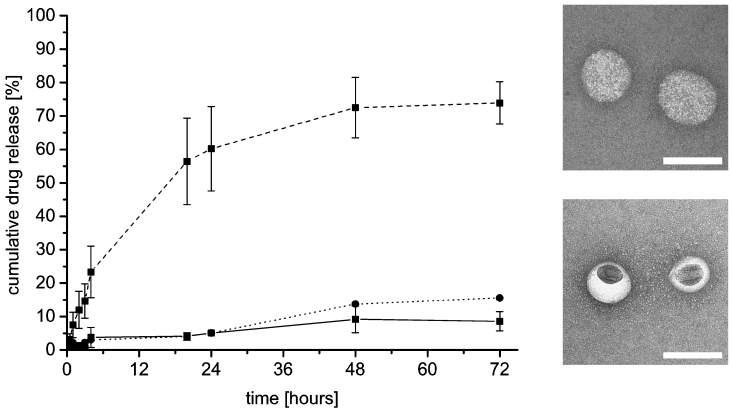

Figure 2 Cumulative drug release. Release of doxorubicin as free drug (dashed line, black squares), incorporated in PEG-liposomes (dotted line, black dots), or PEG-PCL micelles (solid line, black squares) was analyzed by dialysis against PBS (pH 7.4, BSA 3%, 37°C). For free doxorubicin and PEG-PCL micelles values represent means ± S.D. of $n = 3$ experiments. Transmission electron micrographs of Dox-PEG-PCL micelles and Dox-PEG-liposomes after drug release (72 hours). Scale bare: 100 nm.

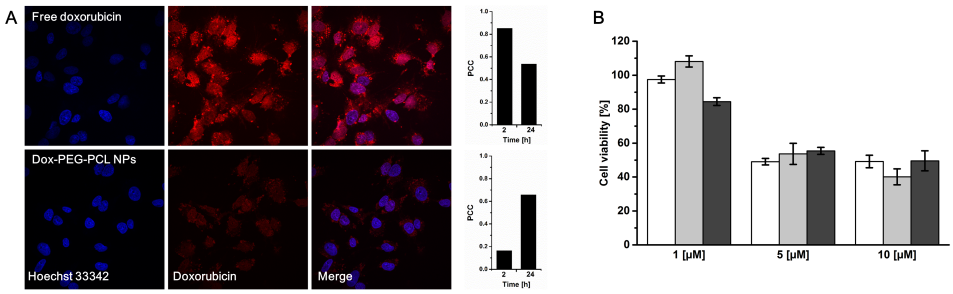

Figure 3 *In vitro* characterization of Dox-PEG-PCL micelles. (A) Cellular uptake and nuclear localization of doxorubicin in HepG2 after incubation for 24 hours as free drug or encapsulated in PEG-PCL micelles. Red: doxorubicin; Blue: cell nuclei (Hoechst 33342). Pearson's correlation coefficients (PCC) for doxorubicin and Hoechst 33342 after 2 hours and 24 hours are shown. (B) Cell viability assay of HepG2 cells 24 hours after incubation with free drug (white) or doxorubicin encapsulated in PEG-liposomes (grey), or PEG-PCL micelles (black). Values represent means ± S.D. of $n = 3$ experiments.

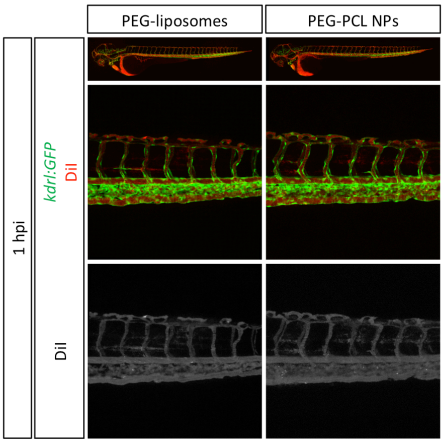

Figure 4 Circulation behavior of fluorescently labeled PEG-liposomes and PEG-PCL micelles in zebrafish embryos was analyzed one hour post infection (hpi). Upper panel: 10 x; lower panels: 20 x. Green: GFP signal in vasculature; Red: DiI; Grey; DiI.

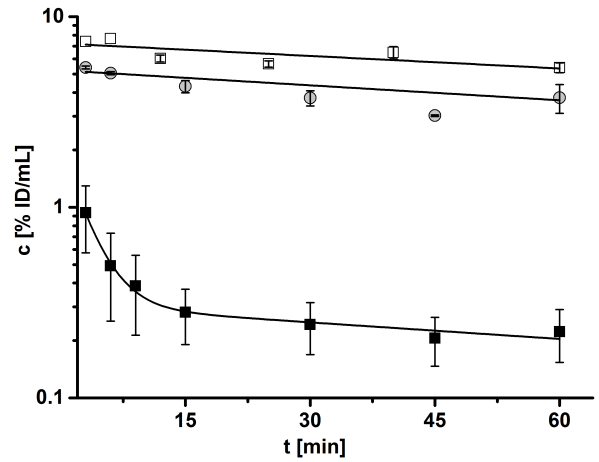

Figure 5 Plasma-concentration curve of doxorubicin after injection of free drug (black squares), drug incorporated in PEG-liposomes (white squares) and PEG-PCL micelles (grey dots). Results represent means ± S.D. of $n = 3$ experiments.

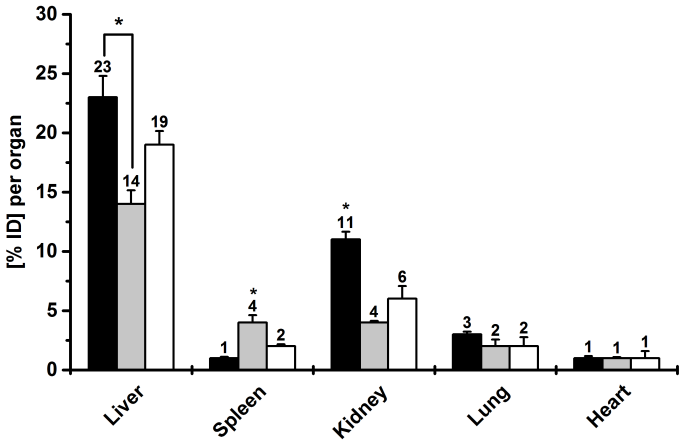

Figure 6 Tissue distribution of doxorubicin as free drug (black), drug incorporated in PEG-liposomes (grey) and PEG-PCL micelles (white) analyzed at 60 minutes after injection. Values represent means ± S.D. of $n = 3$ experiments. Statistical significance was tested using one-way analysis of variance (ANOVA) followed by Tukey's *post hoc* test at a level if significance of $p < 0.05$ (*).

15

Table 1 Physico-chemical characterization of Dox-PEG-PCL micelles and Dox-PEG-Liposomes.

	Dox-PEG-PCL micelles	**Dox-PEG-Liposomes**
Hydrodynamic diameter [nm][a]	73.4 ± 4.2	85.1 ± 2.6
Polydispersity index (PDI)[a]	0.08 ± 0.03	0.13 ± 0.03
Diameter [nm][b]	77.3 ± 20.9	72.2 ± 15.6
Morphology[c]	Solid spheres	Hollow spheres

[a] Determined by dynamic light scattering. Values represent means ± S.D. of $n = 3$ experiments.

[b] Determined by transmission electron microscopy (TEM). Values represent means ± S.D. of $n = 50$ counts.

[c] Determined by SLS and Cyro-EM.

Table 2 Plasma clearance, systemic volume of distribution (V_D), and area under the plasma concentration curve (AUC) of doxorubicin after injection of free drug or drug incorporated in PEG-liposomes or PEG-PCL micelles.

	Clearance [mL/min/kg][a]	**V_D** [mL/kg][a]	**AUC_0^t** [%ID/mL*min][a]	**AUC_0^∞** [%ID/mL*min][a]
Doxorubicin HCl	44.5 ± 10.5	1182.0 ± 311.9	21.1 ± 5.3	59.2 ± 19.9
Dox-PEG-liposomes	0.5 ± 0.1	44.0 ± 8.9	405.9 ± 24.9	970.3 ± 310.8
Dox-PEG-PCL micelles	0.6 ± 0.2	77.0 ± 9.1	256.6 ± 26.6	818.0 ± 260.0

[a] Values represent means ± S.D. of $n = 3$ experiments.

Experimental section

Materials. PEG-b-PCL (PCL average M_n 13 000, PEG average M_n 5 000), anhydrous tetrahydrofuran (THF; ≥99.9%), triethylamine (TEA), cholesterol, anhydrous dimethyl sulfoxide (DMSO; ≥99.9%), ethyl 3-aminobenzoate methane sulfonate (tricaine), N-phenylthiourea (PTU), methylene blue, halocarbon oil 27, and hydrogen peroxide (35% [w/v]) were purchased from Sigma-Aldrich (Buchs, Switzerland). Thiazolyl blue (MTT reagent; ≥98%) was purchased from Carl Roth GmbH (Karlsruhe, Germany). 1,2-Distearoyl-sn-glycero-3-phosphocholine (DSPC) and 1,2-distearoyl-sn-glycero-3-phosphoethanolamine-N-(methoxy(polyethylene glycol)-2000) (DSPE-PEG-2000) were purchased from Avanti Polar-Lipids (Alabaster, AL, USA). Amicon Ultra-4 centrifugal filter units (100 kDa MWCO) were purchased from Merck Millipore (Darmstadt, Germany). Regenerated cellulose dialysis membrane tubing (6-8 kDa MWCO) was purchased from Spectrum Laboratories Inc. (Rancho Dominguez, CA, USA). Tritium-labeled Dox ([3H]-Dox; 0.5-3 Ci/mmol, in EtOH) was purchased from Campro Scientific GmbH (Berlin, Germany). Econo-Pac 10DG desalting columns and agarose standard low were purchased from BioRad (Hercules, CA, USA). Ultima-Gold XR and Solvable were purchased from PerkinElmer (Schwerzenbach, Switzerland). Doxorubicin (Doxorubicin Sandoz eco, 2 mg/mL in NaCl 0.9%) and doxorubicin-loaded PEG-liposomes (Caelyx™) were purchased in a public pharmacy. Tg(kdrl:EGFP) zebrafish were kindly provided by Prof. Dr. Markus Affolter (Biozentrum, University of Basel, Basel, Switzerland).

Preparation of doxorubicin loaded PEG-PCL micelles. Doxorubicin-loaded PEG-PCL micelles were prepared using a modified cosolvent method [20]. PEG-PCL (5 mg) was dissolved in THF (50 µL). Doxorubicin (1 mL; 2 mg/mL) was mixed with an equivalent molar ratio of TEA and was added dropwise to the polymer solution under constant stirring (700 rpm). After overnight stirring at room temperature, free doxorubicin was removed by gel filtration chromatography using a Superose 6 Prep column eluting with PBS (0.01 M, 0.15 M NaCl, pH 7.4). Samples were concentrated using Amicon Ultra-4 centrifugal filter units (100 kDa MWCO).

Preparation of [^{3}H]-doxorubicin-loaded PEG-PCL micelles. For pharmacokinetic experiments, tritium-labeled PEG-PCL micelles were prepared. Therefore, [^{3}H]-doxorubicin (30 µCi) in EtOH was placed in a glass vial and EtOH was evaporated under nitrogen. [^{3}H]-doxorubicin was dissolved in THF (50 µL) and mixed with a 1:1 molar ratio of TEA. PEG-PCL (3 mg) was added. MiliQ water (1 mL) was added dropwise under constant stirring at 700 rpm. After 2 horus, free [^{3}H]-doxorubicin was removed by gel filtration chromatography using Econo-Pac® 10DG desalting columns eluting with PBS (0.001 M, 0.15 M NaCl, pH 7.4). Fractions containing [^{3}H]-doxorubicin-loaded PEG-PCL micelles were concentrated using Amicon Ultra-4 centrifugal filter units (100 kDa MWCO).

Preparation of fluorescently labeled PEG-PCL micelles. Fluorescently labeled PEG-PCL micelles were prepared as described previously [20]. In brief, PEG-PCL (5 mg) was dissolved in THF (50 µL) and DiI (10 µg) was added. The mixture was stirred at 700 rpm and room temperature. PBS (0.01 M, pH 7.4, 0.15 M NaCl; 1 mL) was added dropwise under constant stirring at 700 rpm. The mixture was stirred for 24 h at room temperature. Free DiI was removed by gel filtration chromatography using Superose 6 prep column eluting with PBS (0.01 M, 0.15 M NaCl, pH 7.4). Samples were concentrated using Amicon Ultra-4 centrifugal filter units (100 kDa MWCO).

Preparation of [^{3}H]-doxorubicin-loaded PEG-liposomes. PEG-liposomes were prepared using a microfluidics device (NanoAssemblr Benchtop, Precision Nanosystems, Vancouver, BC, Canada). A lipid mix (20 mM tot) containing DSPC (10.45 mM), cholesterol (8.55 mM) and DSPE-PEG (1 mM) in EtOH was prepared. Lipids in EtOH were mixed with acetate buffer (0.3 M, pH 4.0) at a flow-rate ratio (FRR) of 2.5:1 and a total flow rate (TFR) of 6 mL/min. PEG-liposomes were dialyzed over night against PBS (0.01 M, 0.15 M NaCl, pH 7.8). PEG-liposomes were loaded with [^{3}H]-doxorubicin using a remote loading strategy (i.e. pH gradient) as described previously [21]. In brief, [^{3}H]-doxorubicin was placed in a glass vial and EtOH was removed under nitrogen. [^{3}H]-doxorubicin was reconstituted in 20 µL of MiliQ water. PEG-liposomes were added and the mixture was incubated at 60°C for 10 min. Excess of

[^{3}H]-doxorubicin was removed by gel filtration chromatography using Econo-Pac® 10DG desalting columns eluting with PBS (0.001 M, 0.15 M NaCl, pH 7.4). Fractions containing [^{3}H]-doxorubicin-loaded PEG-liposomes were concentrated using Amicon Ultra-4 centrifugal filter units (100 kDa MWCO). For the preparation of DiI-labeled PEG-liposomes, DiI was added to lipids (1% [mol/mol]) and PEG-liposomes were prepared and purified as described above.

Physico-chemical characterization. PEG-PCL micelles and PEG-liposomes were characterized using transmission electron microscopy (TEM) and dynamic light scattering (DLS). For TEM analysis, 5 µL of the NP suspension were mounted on a copper-carbon grid (400 mesh per grid) and negatively stained with a 2% uranyl acetate solution. Samples were then analyzed using a Philips Morgagni 268D transmission electron microscope. Average nanoparticle size was determined by dynamic using a Delsa Nano C (Beckman Coulter, Nyon, Switzerland). The laser was adjusted to 658 nm and scattered light was detected at a 165° angle. Data was converted using CONTIN particle size distribution analysis.

Determination of the drug loading content and drug loading efficiency. Doxorubicin content was determined by absorption measurement. In brief, a calibration curve of doxorubicin in PBS/DMSO (1:1 v/v) was prepared and absorbance was measured at a wavelength of 493 nm using a Spectrramax M2 microplate reader (Molecular Devices, Sunnyvale, CA, USA). Doxorubicin-loaded PEG-PCL micelles were mixed with DMSO at a ratio of 1:1 [v/v] and the doxorubicin content was determined. Drug loading content was calculated as percentage [m/m] of doxorubicin to PEG-PCL. Drug loading efficiency was calculated as percantage of the initial doxorubicin concentration (i.e. before purification). Concentration of [^{3}H]-doxorubicin was determined by liquid scintillation counting.

Analysis of drug release. Drug release was measured by dialysis. Either 1 mL of doxorubicin as free drug and encapsulated in PEG-liposomes or PEG-PCL micelles was placed in dialysis membrane tubing (6-8 kDa MWCO) and dialyzed against 10 mL of PBS (pH 7.4, 3% BSA) at 37 °C. Samples were taken at time points indicated from the recipient

medium and replaced by fresh medium. Doxorubicin concetration in receiver medium was determined using absorbance measurments as described above. Total recovery was calculated by measuring the remaining doxorubicin concetration in the donor medium at the end of the release experiment and is expressed as percentage of the initial doxorubicin concentration.

Cell culture. The human hepatoma cell line HepG2 was kindly provided by Prof. Dr. Dietrich von Schweinitz (University Hospital of Basel, Basel, Switzerland). Cells were cultured in Dulbecco's modified eagle medium (DMEM, Sigma-Aldrich, Buchs, Switzerland; glucose 4500 g/L) supplemented with 10% fetal calf serum (FCS, Amimed BioConcept, Allschwil, Switzerland), 100 U/mL penicillin (Sigma-Aldrich, Buchs, Switzerland), and 100 mg/mL streptomycin (Sigma-Aldrich, Buchs, Switzerland).

***In vitro* cell viability studies**. *In vitro* cell viability was determined using a modified MTT assay as described previously [39]. In brief, HepG2 cells were seeded at a density of 1 x 10^4 cells/well in a 96-well plate (TPP, Trasadingen, Switzerland) coated with poly-D lysine (0.04 mg/mL; Sigma-Aldrich, Buchs, Switzerland). Cells were allowed to adhere over night and were washed twice with Dulbecco's phosphate-buffered saline (DPBS). Then, doxorubicin as free drug, encapsulated in PEG-liposomes, or PEG-PCL micelles was added at 1-10 µM. DMEM was used as negative control, terfenadine (20 µM) as positive control. After 24 hours of incubation, cells were washed three times with DPBS and MTT working solution (100 µL, thiazolyl blue 5 mg/mL) was added. MTT working solution was aspirated after 2-3 hours of incubation at 37 °C and formazan crystals were solubilized with acidified isopropyl alcohol (100 µL) and SDS (3%, 20 µL) for 2 hours at room temperatue under light protection. Absorption was read at 570 nm and 670 nm using a Spectrramax M2 microplate reader (Molecular Devices, Sunnyvale, CA, USA). Cell viability is expressed as relative cell viability compared to control cells (DMEM only). Experiments were performed in triplicates and statistical analysis was performed as described below.

***In vitro* cell uptake**. *In vitro* uptake of doxorubicin as free drug or encapsulated in PEG-PCL micelles by HepG2 cells was analyzed by confocal laser scanning microscopy (CLSM). Glass coverslips (♯1.5, Menzel, Braunschweig, Germany) were coated with poly-D lysine (0.4 mg/mL) and placed in a 12-well plate (TPP, Trasadingen, Switzerland). HepG2 cells were seeded at a density of 2.5 x 10^4 cells/cm^2 and were allowed to adhere over night. Cells were then washed twice with DPBS and were incubated with free doxorubicin or doxorubicin encapsulated in PEG-PCL micelles for indicated times. To stain cell nuclei, Hoechst 33342 dye (0.2 µg/mL; Eugene, OR, USA) was added 10 min prior to end of incubation time. Cells were then washed three times with ice-cold DPBS and were fixed with paraformaldehyde (4%) for 15 min at 4 °C. Paraformaldehyde was removed and cell were washed three times with ice-cold DPBS. Coverslips were mounted with Prolong Gold (Thermo Fisher Scientific, Waltham, MA, USA). Cells were analyzed using an Olympus FV 1000 inverted laser scanning microscope equiped with a 40x (NA 1.30) and a 60x (NA 1.40) oil immersion objective (Olympus, Tokyo, Japan). Doxorubicin was excited at 488 nm and emitted signal was detected using a 530/30 bandpass filter. Colocalization of Hoechst 33342 and doxorubicin was calculated was determined by Pearson's Correlation Coefficient (PCC) using ImagJ 1.46 software (National Institutes of Health).

Zebrafish biodistribution studies. All experiments using zebrafish were performed in accordance with Swiss animal welfare regulations. Experiments were performed as described previously [30]. In brief, zebrafish embryo (ZFE) culture medium at pH 7.4 was prepared at final concentrations of sodium chloride (5 mM), potassium chloride (0.25 mM), magnesium sulfate (0.5 mM), potassium dihydrogen phosphate (0.15 mM), sodium phosphate dibasic (0.05 mM), calcium chloride (0.5 mM), sodium bicarbonate (0.71 mM), and methylene blue (0.001% w/v). Zebrafish eggs of Tg(kdrl:EGFP) zebrafishes were incubated at 28°C in ZFE culture medium and bleached 1-day post fertilization (dpf) using PTU (0.03 mg/mL). ZFE were anesthetized using tricaine (0.01% w/v) and immobilized using agarose (0.3% w/v) containing the same amount of tricaine. DiI labelled PEG-liposomes and PEG-PCL micelles were injected at 2 dpf via the duct of cuvier using a micromanipulator (Wagner Instrumentenbau KG,

Schöffengrund, Germany), a pneumatic Pico Pump PV830 (WPI, Sarasota, FL), and a Leica S8AP0 microscope (Leica, Wetzlar, Germany) according to an adapted protocol [40]. Injection volumes were calibrated to 1 nL using halocarbon oil. Fluorescence imaging of injected ZFE was performed 1-hour post injection using an Olympus FV1000 confocal microscope (Olympus, Tokyo, Jpaan) equiped with a 10x water immersion objective (NA 0.4; Tokyo, Japan). Samples were excited at 488 and 520 nm and fluorescence was detected at 559 and 569 nm.

***In vivo* pharmacokinetic studies**. Pharmacokinetic profiles of [^{3}H]-doxorubicin as free drug and encapsulated in PEG-liposomes or PEG-PCL micelles were determined in female wistar rats (250-280 g) as described previously [21,22]. The protocol for animal experiments was approved by Swiss animal welfare authorities and experiments were performed in accordance with Swiss animal welfare regulations. In brief, rats were anesthetized by isoflurane (2-5%) and the jugular vein was cannulated. [^{3}H]-doxorubicin (4 µCi) was injected as free drug, encapsulated in PEG-liposomes, or PEG-PCL micelles. Blood samples (200 µL) were collected at indicated time points, mixed with EDTA (0.5 M, 10 uL), and centrifuged for 5 min at 1 000 rcf and 4 °C to seperate plasma. The blood volume collected was replaced by sterile normal saline containing heparin (100 U/mL). After 1 hour, animals were sacrificed and organs (liver, kidney, spleen, heart, and lung) were removed. Plasma aliquots (40 µL) and tissue samples (50-100 mg) were mixed with Solvable (1 mL) and solubilized according to the manufacturers protocol. Tissue samples were bleached with hydrogen peroxide (30%, 200 µL). Samples were then mixed with 10 mL of Ultima-Gold XR scintillation cocktail and activity was determined using liquid scintillation counting. Plasma-concentration time data were analyzed using PK Solver software [34]. One or two compartmental models were used to fit the data. Statistical significance of tissue distribution was determined by performing one-way analysis of variance (ANOVA) followed by Tukey's post hoc test using OriginPro (Version 9.1.0, OriginLab Corporation, Northampton, MA, USA).

References

[1] M. Hay, D.W. Thomas, J.L. Craighead, C. Economides, J. Rosenthal, Clinical development success rates for investigational drugs, Nat. Biotechnol. 32 (2014) 40–51. doi:10.1038/nbt.2786.

[2] S. Basavaraj, G.V. Betageri, Can formulation and drug delivery reduce attrition during drug discovery and development—review of feasibility, benefits and challenges, Acta Pharm. Sin. B. 4 (2014) 3–17. doi:10.1016/j.apsb.2013.12.003.

[3] M.J. Waring, J. Arrowsmith, A.R. Leach, P.D. Leeson, S. Mandrell, R.M. Owen, G. Pairaudeau, W.D. Pennie, S.D. Pickett, J. Wang, O. Wallace, A. Weir, An analysis of the attrition of drug candidates from four major pharmaceutical companies, Nat. Rev. Drug Discov. 14 (2015) 475–486. doi:10.1038/nrd4609.

[4] V.P. Torchilin, Micellar Nanocarriers: Pharmaceutical Perspectives, Pharm. Res. 24 (2006) 1–16. doi:10.1007/s11095-006-9132-0.

[5] Y. Matsumura, H. Maeda, A new concept for macromolecular therapeutics in cancer chemotherapy: mechanism of tumoritropic accumulation of proteins and the antitumor agent smancs, Cancer Res. 46 (1986) 6387–6392.

[6] S.K. Hobbs, W.L. Monsky, F. Yuan, W.G. Roberts, L. Griffith, V.P. Torchilin, R.K. Jain, Regulation of transport pathways in tumor vessels: role of tumor type and microenvironment, Proc. Natl. Acad. Sci. 95 (1998) 4607–4612.

[7] S.M. Moghimi, A.C. Hunter, J.C. Murray, Long-Circulating and Target-Specific Nanoparticles: Theory to Practice, Pharmacol. Rev. 53 (2001) 283–318.

[8] A. Gabizon, R. Catane, B. Uziely, B. Kaufman, T. Safra, R. Cohen, F. Martin, A. Huang, Y. Barenholz, Prolonged circulation time and enhanced accumulation in malignant exudates of doxorubicin encapsulated in polyethylene-glycol coated liposomes, Cancer Res. 54 (1994) 987–992.

[9] A. Gabizon, H. Shmeeda, Y. Barenholz, Pharmacokinetics of pegylated liposomal doxorubicin, Clin. Pharmacokinet. 42 (2003) 419–436. doi:10.2165/00003088-200342050-00002.

[10] D. Papahadjopoulos, T.M. Allen, A.A. Gabizon, E. Mayhew, K. Matthay, S.K. Huang, K.-D. Lee, M.C. Woodle, D.D. Lasic, C. Redemann, F.J. Martin, Sterically stabilized liposomes: Improvements in pharmacokinetics and antitumor therapeutic efficacy, Proc. Natl. Acad. Sci. 88 (1991) 11460–11464.

[11] A. Wicki, D. Witzigmann, V. Balasubramanian, J. Huwyler, Nanomedicine in cancer therapy: Challenges, opportunities, and clinical applications, J. Controlled Release. 200 (2015) 138–157. doi:10.1016/j.jconrel.2014.12.030.

[12] K.S. Lee, H.C. Chung, S.A. Im, Y.H. Park, C.S. Kim, S.-B. Kim, S.Y. Rha, M.Y. Lee, J. Ro, Multicenter phase II trial of Genexol-PM, a Cremophor-free, polymeric micelle formulation of paclitaxel, in patients with metastatic breast cancer, Breast Cancer Res. Treat. 108 (2008) 241–250. doi:10.1007/s10549-007-9591-y.

[13] Z. Ma, A. Haddadi, O. Molavi, A. Lavasanifar, R. Lai, J. Samuel, Micelles of poly(ethylene oxide)- *b* -poly(ε-caprolactone) as vehicles for the solubilization, stabilization, and controlled delivery of curcumin, J. Biomed. Mater. Res. A. 86A (2008) 300–310. doi:10.1002/jbm.a.31584.

[14] H. Xin, L. Chen, J. Gu, X. Ren, Z. wei, J. Luo, Y. Chen, X. Jiang, X. Sha, X. Fang, Enhanced anti-glioblastoma efficacy by PTX-loaded PEGylated poly(ε-

caprolactone) nanoparticles: In vitro and in vivo evaluation, Int. J. Pharm. 402 (2010) 238–247. doi:10.1016/j.ijpharm.2010.10.005.
[15] A.K. Yadav, P. Mishra, S. Jain, P. Mishra, A.K. Mishra, G.P. Agrawal, Preparation and characterization of HA–PEG–PCL intelligent core–corona nanoparticles for delivery of doxorubicin, J. Drug Target. 16 (2008) 464–478. doi:10.1080/10611860802095494.
[16] G. Gaucher, M.-H. Dufresne, V.P. Sant, N. Kang, D. Maysinger, J.-C. Leroux, Block copolymer micelles: preparation, characterization and application in drug delivery, J. Controlled Release. 109 (2005) 169–188. doi:10.1016/j.jconrel.2005.09.034.
[17] X. Ke, V.W.L. Ng, R.J. Ono, J.M.W. Chan, S. Krishnamurthy, Y. Wang, J.L. Hedrick, Y.Y. Yang, Role of non-covalent and covalent interactions in cargo loading capacity and stability of polymeric micelles, J. Controlled Release. 193 (2014) 9–26. doi:10.1016/j.jconrel.2014.06.061.
[18] A.L. Klibanov, K. Maruyama, V.P. Torchilin, L. Huang, Amphipathic polyethyleneglycols effectively prolong the circulation time of liposomes, FEBS Lett. 268 (1990) 235–237.
[19] V.P. Torchilin, Structure and design of polymeric surfactant-based drug delivery systems, J. Controlled Release. 73 (2001) 137–172. doi:10.1016/S0168-3659(01)00299-1.
[20] P. Grossen, G. Québatte, D. Witzigmann, C. Prescianotto-Baschong, L.-H. Dieu, J. Huwyler, Functionalized Solid-Sphere PEG-b-PCL Nanoparticles to Target Brain Capillary Endothelial Cells In Vitro, J. Nanomater. 2016 (2016) 1–13. doi:10.1155/2016/7818501.
[21] J. Huwyler, D. Wu, W.M. Pardridge, Brain drug delivery of small molecules using immunoliposomes, Proc. Natl. Acad. Sci. 93 (1996) 14164–14169.
[22] J. Huwyler, J. Yang, W.M. Pardridge, Receptor mediated delivery of daunomycin using immunoliposomes: pharmacokinetics and tissue distribution in the rat, J. Pharmacol. Exp. Ther. 282 (1997) 1541–1546.
[23] F. Alexis, E. Pridgen, L.K. Molnar, O.C. Farokhzad, Factors Affecting the Clearance and Biodistribution of Polymeric Nanoparticles, Mol. Pharm. 5 (2008) 505–515. doi:10.1021/mp800051m.
[24] H. Kobayashi, B. Turkbey, R. Watanabe, P.L. Choyke, Cancer Drug Delivery: Considerations in the Rational Design of Nanosized Bioconjugates, Bioconjug. Chem. 25 (2014) 2093–2100. doi:10.1021/bc500481x.
[25] J. Huwyler, H. Kettiger, A. Schipanski, P. Wick, Engineered nanomaterial uptake and tissue distribution: from cell to organism, Int. J. Nanomedicine. (2013) 3255–3269. doi:10.2147/IJN.S49770.
[26] G.J.. Charrois, T.M. Allen, Drug release rate influences the pharmacokinetics, biodistribution, therapeutic activity, and toxicity of pegylated liposomal doxorubicin formulations in murine breast cancer, Biochim. Biophys. Acta BBA - Biomembr. 1663 (2004) 167–177. doi:10.1016/j.bbamem.2004.03.006.
[27] D.C. Wu, C.M. Ofner, Adsorption and Degradation of Doxorubicin from Aqueous Solution in Polypropylene Containers, AAPS PharmSciTech. 14 (2013) 74–77. doi:10.1208/s12249-012-9885-1.
[28] C.F. Thorn, C. Oshiro, S. Marsh, T. Hernandez-Boussard, H. McLeod, T.E. Klein, R.B. Altman, Doxorubicin pathways: pharmacodynamics and adverse effects, Pharmacogenet. Genomics. 21 (2011) 440–446. doi:10.1097/FPC.0b013e32833ffb56.

[29] Y. Negishi, N. Hamano, D. Omata, A. Fujisawa, M. Manandhar, M. Nomizu, Y. Aramaki, Effects of doxorubicin-encapsulating AG73 peptide-modified liposomes on tumor selectivity and cytotoxicity, Results Pharma Sci. 1 (2011) 68–75. doi:10.1016/j.rinphs.2011.10.001.
[30] S. Sieber, D. Witzigmann, P. Grossen, P. Detampel, S. Siegfried, J. Huwyler, Zebrafish as early in vivo screening tool for liposome formulation optimization, (2017).
[31] H.M. Aliabadi, D.R. Brocks, P. Mahdipoor, A. Lavasanifar, A novel use of an in vitro method to predict the in vivo stability of block copolymer based nano-containers, J. Controlled Release. 122 (2007) 63–70. doi:10.1016/j.jconrel.2007.06.008.
[32] Z. Pang, W. Lu, H. Gao, K. Hu, J. Chen, C. Zhang, X. Gao, X. Jiang, C. Zhu, Preparation and brain delivery property of biodegradable polymersomes conjugated with OX26, J. Controlled Release. 128 (2008) 120–127. doi:10.1016/j.jconrel.2008.03.007.
[33] K.S. Shalaby, M.E. Soliman, G. Bonacucina, M. Cespi, G.F. Palmieri, O.A. Sammour, A.A. El Shamy, L. Illum, L. Casettari, Nanoparticles Based on Linear and Star-Shaped Poly(Ethylene Glycol)-Poly(ε-Caprolactone) Copolymers for the Delivery of Antitubulin Drug, Pharm. Res. 33 (2016) 2010–2024. doi:10.1007/s11095-016-1939-8.
[34] Y. Zhang, M. Huo, J. Zhou, S. Xie, PKSolver: An add-in program for pharmacokinetic and pharmacodynamic data analysis in Microsoft Excel, Comput. Methods Programs Biomed. 99 (2010) 306–314. doi:10.1016/j.cmpb.2010.01.007.
[35] H. Akaike, A new look at the statistical model identification, IEEE Trans. Autom. Control. 19 (1974) 716–723.
[36] G. Schwarz, Estimating the Dimension of a Model, Ann. Stat. 6 (1978) 461–464.
[37] T.M. Ludden, S.L. Beal, L.B. Sheiner, Comparison of the Akaike Information Criterion, the Schwarz criterion and the F test as guides to model selection, J. Pharmacokinet. Biopharm. 22 (1994) 431–445.
[38] S. Hirsjärvi, L. Sancey, S. Dufort, C. Belloche, C. Vanpouille-Box, E. Garcion, J.-L. Coll, F. Hindré, J.-P. Benoît, Effect of particle size on the biodistribution of lipid nanocapsules: Comparison between nuclear and fluorescence imaging and counting, Int. J. Pharm. 453 (2013) 594–600. doi:10.1016/j.ijpharm.2013.05.057.
[39] H. Kettiger, D. Sen Karaman, L. Schiesser, J.M. Rosenholm, J. Huwyler, Comparative safety evaluation of silica-based particles, Toxicol. In Vitro. 30 (2015) 355–363. doi:10.1016/j.tiv.2015.09.030.
[40] B.M. Weinstein, D.L. Stemple, W. Driever, M.C. Fishman, Gridlock, a localized heritable vascular patterning defect in the zebrafish, Nat. Med. 1 (1995) 1143–1147.

CHAPTER III

Formation of lipid and polymer based gold nanohybrids using a nanoreactor approach

Witzigmann D, Sieber S, Porta F, Grossen P, Bieri A, Strelnikova N, Pfohl T, Prescianotto-Baschong C, Huwyler J

Manuscript: Published in RSC Adv. 5 (2015) 74320–74328.
DOI: 10.1039/c5ra13967h

Highlights: To further understand uptake mechanisms of NPs and to analyze intracellular trafficking after cellular uptake, labeling techniques are of great interest. This article highlights the development of gold-nanohybrids using a novel strategy that is applicable to a broad range of engineered nanomaterials (i.e. lipids and polymers) and that is highly reproducible. These gold-nanohybrids exert unique physico-chemical properties and can be visualized in complex biological scaffolds such as mammalian cells using electron microscopy. This technique is a promising tool for the analysis of cellular uptake mechanisms and intracellular trafficking and may further be used for diagnostic purposes.

RSC Advances

PAPER

View Article Online
View Journal | View Issue

Cite this: *RSC Adv.*, 2015, **5**, 74320

Formation of lipid and polymer based gold nanohybrids using a nanoreactor approach†

Dominik Witzigmann,[a] Sandro Sieber,[a] Fabiola Porta,[a] Philip Grossen,[a] Andrej Bieri,[b] Natalja Strelnikova,[c] Thomas Pfohl,[c] Cristina Prescianotto-Baschong[d] and Jörg Huwyler*[a]

Received 15th July 2015
Accepted 24th August 2015

DOI: 10.1039/c5ra13967h

www.rsc.org/advances

Nanocarriers encapsulating gold nanoparticles (AuNPs) hold tremendous promise for numerous biomedical applications. So far only a few fabrication strategies have been investigated and efficient processes for the manufacturing of gold nanohybrids (AuNHybs) are still missing. We encapsulated a tetrachloroaurate/citrate mixture within nanocarriers and initiated the AuNP formation after self-assembly of the nanomaterial by a temperature shift. This nanoreactor approach was successfully combined with the film-rehydration, nanoprecipitation, or microfluidics method. Different nanomaterials were validated including phospholipids and copolymers and the process was optimized towards encapsulation efficiency and physico-chemical homogeneity of AuNHybs. Our nanoreactor technology is versatile, efficient, and highly reproducible. Dynamic light scattering and electron microscopy techniques confirmed that generated lipid and polymer based AuNHybs were of uniform size below 130 nm and contained a single AuNP. The AuNHyb solutions had a deep-red color and exhibited the specific surface plasmon absorption of AuNPs. The unique optical properties of AuNHybs were used to visualize cellular uptake of nanocarriers *in vitro* demonstrating the promising applicability of AuNHybs as a bioimaging tool.

1. Introduction

Gold nanoparticles (AuNPs) have attracted great interest since Michael Faraday first described them in 1857.[1,2] The application of AuNPs in the field of imaging and therapy were based on their unique properties, which include; (I) advantageous physico-chemical characteristics, (II) non-toxic and inert properties, (III) facile preparation of monodisperse AuNPs, and (IV) various modification options.[3–5] Different methods for the synthesis of AuNPs have been described.[6,7] The most widely used approach is the chemical reduction of gold salt (Au^{3+}) such as tetrachloroaurate ($HAuCl_4$) to metallic gold (Au^0) using the Turkevich[8,9] or Brust-Schiffrin[10] method. Moreover, synthesis methods using microwaves, UV irradiation, microfluidics, or biologic approaches were examined.[3,11] Ultimately, AuNPs have to be modified with capping agents to avoid aggregation, provide solubility in aqueous media, and improve stability.[12]

Encapsulation of AuNPs into different nanocarriers such as liposomes or polymeric nanoparticles is an interesting option for a wide range of applications such as smart drug delivery, imaging, or photothermal therapy.[13–18] In recent decades, great progress has been made in the field of hybrid nanocarriers using AuNPs and several strategies for their synthesis have been investigated. For example, lipid based gold nanohybrids (lipid-AuNHybs) have been prepared using the following methods: improved cholate dialysis,[19] incorporation of hydrophobic AuNPs,[20–22] physical absorption,[23,24] or precipitation of gold within liposomes using either, glycerol including formation or reverse-phase evaporation.[25,26]

However, these strategies exhibited marked variability in homogeneity, reproducibility, size distribution, and morphology of gold nanohybrids (AuNHybs). To overcome these challenges, we developed a novel and versatile strategy to encapsulate AuNPs into different nanocarriers with high reproducibility using a nanoreactor approach. The goal of the present study was, (I) the encapsulation of a tetrachloroaurate/citrate mixture within nanocarriers and (II) the initiation of AuNP formation after self-assembly of the nanomaterial. Selected nanomaterials (*i.e.* lipid and polymer based) were validated and the encapsulation efficiency, homogeneity, and robustness of our approach were optimized. Nanocarriers loaded with AuNPs were prepared by three different methods depending on the physico-chemical properties of the nanocarrier material.

[a]*Division of Pharmaceutical Technology, Department of Pharmaceutical Sciences, University of Basel, Klingelbergstrasse 50, Basel CH-4056, Switzerland. E-mail: joerg.huwyler@unibas.ch*

[b]*Center for Cellular Imaging and NanoAnalytics (C-CINA), Biozentrum, University of Basel, Mattenstrasse 26, Basel CH-4058, Switzerland*

[c]*Department of Chemistry, University of Basel, Klingelbergstrasse 80, Basel CH-4056, Switzerland*

[d]*Biozentrum, University of Basel, Klingelbergstrasse 70, Basel CH-4056, Switzerland*

† Electronic supplementary information (ESI) available. See DOI: 10.1039/c5ra13967h

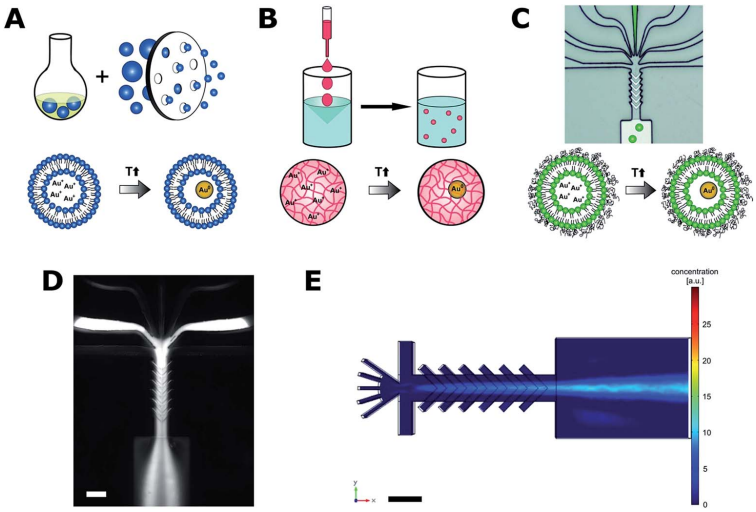

Fig. 1 Different methods for the preparation of gold nanohybrids. Schematic representation of the, (A) film-rehydration–extrusion method for lipids with T_m < room temperature (RT), (B) nanoprecipitation method for the di-block copolymer PEG–PCL, and (C) microfluidics platform for lipids with T_m > RT. The formation of gold nanoparticles inside the nanocarriers was initiated by temperature increase after self-assembly. (C) The microfluidics device had seven inlet channels converging to a single staggered herringbone micromixer. (D) Microfluidic streams were visualized using the fluorescence dye fluorescein. (E) Computational fluid dynamics simulation of concentration gradients (in a.u.) in the microfluidics device. Scale bars indicate 100 μm.

The film-rehydration–extrusion method[27] was used for conventional (non-PEGylated) liposomes, the nanoprecipitation method[28] was used for di-block copolymer nanoparticles, and the microfluidics method[29,30] was used for PEGylated (sterically stabilized) liposomes (Fig. 1). The most important feature of our nanoreactor approach is the production of nanocarriers at room temperature (RT), which avoids the formation of AuNPs before self-assembly. AuNP formation is subsequently initiated by a temperature shift. The applicability of the AuNHybs as bioimaging tool was demonstrated *in vitro* using HepG2 human hepatocellular carcinoma cells.

2. Experimental section

2.1 AuNP synthesis

AuNPs were synthesized following a modified Turkevich method.[7] Optimization of AuNP synthesis using a 2^3 full factorial design of experiment (DoE) [Stavex 5.2, Aicos Technologies, Basel, Switzerland] is described in detail in the ESI (Table S1†). Briefly, ddH_2O with 1 mM tetrachloroaurate (Sigma-Aldrich, Buchs, Switzerland) were heated to 70 °C for 20 min under vigorous stirring. To start the formation of AuNPs, citrate solution (170 mM; 50 mg mL^{-1}) was added as a reducing and capping reagent. The $HAuCl_4$/citrate gold reaction mixture (AuR-solution) was stirred at 70 °C for 10 min until the solution had a deep-red color.

2.2 AuNHyb formation using film rehydration

The film rehydration method was used for lipids with a transition temperature (T_m) below RT with modifications described elsewhere.[31] Liposomes were produced at a temperature which inhibits the AuNP formation. In brief, 1-palmitoyl-2-oleoyl-*sn-glycero*-3-phosphocholine (15 μmol) [POPC] (Avanti Polar-Lipids, Alabaster, USA) and 1-palmitoyl-2-oleoyl-*sn-glycero*-3-phospho-1′-*rac*-glycerol (5 μmol) [POPG] (Avanti Polar-Lipids, Alabaster, USA) were dissolved in chloroform/methanol (2 : 1, v/v) and a homogenous dry lipid film was prepared using a Rotavapor A-134 (Büchi, Flawil, Switzerland). The lipid film was rehydrated with a freshly prepared AuR-solution ($HAuCl_4$: citrate ratio – 1 : 4) at RT and 120 rpm for 10 min with 3 g glass beads (diameter 5 mm). Different lipid (20 mM) to AuR-solution ratios were tested starting from 1 mM $HAuCl_4$/4.1 mM citrate up to 8 mM $HAuCl_4$/32.8 mM citrate.

The resulting multilamellar vesicles were subjected to three freeze–thaw cycles and extruded through polycarbonate membranes with two different pore sizes using a barrel extruder (Lipex; Northern Lipids, Vancouver; Canada). Liposomes were extruded at RT 3 times through a 200 nm polycarbonate membrane and 11 times through a membrane with a pore size of 100 nm (VWR International, Dietikon, Switzerland). AuNPs, which were formed during the extrusion procedure, bind to the filter membranes. Finally, the unilamellar liposomes were heated to 70 °C for 10 min to start the formation of AuNPs. To separate liposomes from free AuNPs, the sample was purified by FPLC using a Superose 6 prep column (GE Healthcare,

Glattbrugg, Switzerland) eluting with 0.01 M phosphate buffered saline (PBS) containing 150 mM sodium chloride, pH 7.4 (Sigma-Aldrich, Buchs, Switzerland).

2.3 AuNHyb formation using nanoprecipitation

A nanoprecipitation method was used for the di-block copolymer polyethyleneglycol–polycaprolactone [PEG–PCL] (Sigma-Aldrich, Buchs, Switzerland). The polymer (5 mg) was dissolved in THF (50 μL) [Sigma-Aldrich, Buchs, Switzerland] under constant stirring with a magnetic bar (750 rpm). The AuR-solution ($HAuCl_4$: citrate ratio – 1 : 4) was added dropwise (one drop per five seconds). The mixture was stirred for 10 min at 750 rpm followed by 10 min on a thermomixer at 70 °C and 300 rpm. Different polymer to AuR-solution ratios were tested starting from 1 mM $HAuCl_4$/4.1 mM citrate up to 8 mM $HAuCl_4$/32.8 mM citrate. To separate the PEG–PCL–AuNHybs from free AuNPs, a FPLC purification step was used (see above).

2.4 Microfluidics device design and fabrication

The microfluidics device was fabricated with 0.05 mm thick polystyrene foil (GoodFellow, Huntingdon, UK) and NOA 81 (Norland, Cranberry, USA) using standard soft-lithography techniques according to the procedure described previously.[32,33] The microfluidics device had seven inlet channels converging to a single staggered herringbone micromixer. The rectangular cross-section had dimensions of 468 μm length, 80 μm width, and 40 μm/200 μm height (Fig. 1C). Detailed experimental procedures are given in the ESI.†

2.5 Flow visualization and computational fluid dynamics simulation

Detailed experimental procedures are given in the ESI.†

2.6 AuNHyb formation using microfluidics

The microfluidics method was used for lipids with a transition temperature above RT (55 °C). Therefore, the AuNP formation during the liposome production was hampered due to decreased temperature. 1,2-Distearoyl-*sn-glycero*-3-phosphocholine (DSPC) [5.75 μmol] (Avanti Polar-Lipids, Alabaster, USA), cholesterol [4 μmol] (Sigma-Aldrich, Buchs, Switzerland), and 1,2-distearoyl-*sn-glycero*-3-phosphoethanolamine-*N*-(methoxy(polyethylene glycol)-2000) (DSPE-PEG2000) [0.25 μmol] (Avanti Polar-Lipids, Alabaster, USA) were dissolved in ethanol. The microfluidics device was primed with water for the outer streams and with ethanol for the central inlet (1 μL s^{-1}) using syringe pumps.

Afterwards four different syringes were connected: (I) double-distilled water, (II) citrate solution (4.1 mM–32.8 mM), and (III) tetrachloroaurate ($HAuCl_4$) solution (1 mM–8 mM) were connected to the outer streams (always with a $HAuCl_4$: citrate ratio of 1 : 4) and (IV) lipids in ethanol (5 mM) were connected to the central inlet. The speed was set to 4 μL s^{-1} for syringe I, 2 μL s^{-1} for syringe II/III and 1 μL s^{-1} for syringe IV. The sample was collected at the outlet. Finally, the liposomes were heated to 70 °C for 10 min to start the formation of AuNPs. To separate lipid-AuNHybs from free AuNPs, the sample was purified by FPLC using a Superose 6 prep column eluting with 0.01 M PBS pH 7.4.

2.7 Size analysis using dynamic light scattering

Dynamic light scattering (DLS) measurements of AuNPs and all lipid- and polymer-AuNHybs were conducted using a Delsa Nano C Particle Analyzer (Beckman Coulter, Nyon, Switzerland). The laser was adjusted to 658 nm and scattered light was detected at a 165° angle. Data was converted using CONTIN particle size distribution analysis. The AuNHyb size was analyzed three times in PBS at RT.

2.8 UV-Vis and fluorescence measurements

Ultraviolet-visible (UV-Vis) absorption from 260 nm to 750 nm (step size one nm) of different samples was measured using a SpectraMax M2 (Molecular Devices, Sunnyvale, USA). Fluorescence of lipid-AuNHybs containing rhodamine labelled phospholipids (Rho-PE) [Avanti Polar-Lipids, Alabaster, USA] was analyzed by excitation at 560 nm and detection between 572 nm to 750 nm.

2.9 Transmission electron microscopy of gold nanohybrids

Size and shape of the AuNPs and AuNHybs were analyzed by transmission electron microscopy (TEM) using a CM-100 (Philips, Eindhoven, Netherlands) operating at 80 kV. Samples were prepared by deposition onto a 400-mesh carbon-coated copper grid (Polysciences Inc., Eppelheim, Germany). Prior to sample deposition, the grid was exposed to plasma for 10 seconds to increase sample binding. Grids were washed with double-distilled water to prevent precipitation of uranyl salts by phosphate ions. Then the samples were negatively stained using a 2% uranylacetate solution (Sigma-Aldrich, Buchs, Switzerland), the excess of uranylacetate was removed using filter paper, and the samples were dried at RT overnight. Nanocarrier integrity was preserved by this procedure as confirmed by Cryo-EM analysis using sample vitrification (see below). To characterize the size of AuNPs inside of AuNHybs, the diameter of at least 100 AuNPs was determined.

2.10 Cryo-TEM of gold nanohybrids

Aliquots (4 μL) of AuNHybs were adsorbed onto holey-carbon supported grids (Quantifoil, Glossloebichau, Germany), blotted with Whatman 1 filter papers, and vitrified in liquid nitrogen-cooled liquid ethane using a Vitrobot IV (FEI Company, Eindhoven, Netherland). Cryo-electron imaging was performed with a Philips CM200-FEG electron microscope operated at an acceleration voltage of 200 kV. Micrographs were recorded with a 4k × 4k TemCam-F416 CMOS camera (TVIPS, Gauting, Germany).

2.11 Preparation of fluorescent lipid based AuNHybs

Detailed experimental procedures are given in the ESI.†

2.12 Passive uptake of AuNPs and AuNHybs in HepG2 cells

HepG2 cells were seeded on a 10 cm plate and cultured in 10 mL Dulbecco's modified Eagle's culture medium high glucose supplemented with 10% fetal calf serum (FCS), 100 units mL^{-1} penicillin, and 100 μg mL^{-1} of streptomycin (DMEM comp). All cell culture media components were purchased from Sigma-Aldrich (Buchs, Switzerland). Cells were allowed to adhere for 24 h before the AuNPs or AuNHybs were added. After incubation at 37 °C for 18 h, the tissue culture plate was washed three times with DMEM comp (37 °C). Afterwards, the cells were fixed with DMEM containing 3% formaldehyde (Sigma-Aldrich, Buchs, Switzerland) and 0.3% glutaraldehyde (Sigma-Aldrich, Buchs, Switzerland) for two hours at RT and stored overnight at 4 °C. The following day, cells were scraped, pelleted, and washed three times with water, and then incubated with 2% uranylacetate for two hours at 4 °C in the dark. The sample was washed, dehydrated by series of methanol, and infiltrated with LR-gold resin (London Resin, London, UK) according to the manufacturer's instructions. Polymerization was performed at −10 °C by UV light for one day. Sections of about 70 nm were collected on carbon-coated Formvar-Ni-grids (EMS, Hatfield, USA) and stained for 15 min with 4% uranylacetate followed by two minutes in Reynolds lead citrate solution. Sections were viewed using a Phillips CM-100 electron microscope.

3. Results and discussion

3.1 Film rehydration (conventional liposomes)

For the preparation of AuNP loaded liposomes, the most direct approach is the rehydration of a lipid film with presynthesized AuNPs. The well-characterized method developed by Turkevich and Frens is ideal to synthesize AuNPs with diameters of approximately 20 nm (see ESI† for experimental details).[7,34,35] However, the AuNP encapsulation approach has several issues. The AuNPs often form aggregates up to several hundred nanometers (Fig. 2A), which results in low encapsulation efficiency (Fig. 2D) and renders extrusion impossible due to blocked filter membranes. Therefore, we developed an alternative strategy and combined the film-rehydration method with a 'nanoreactor approach'. We rehydrated the lipid film with the Turkevich reaction mixture consisting of tetrachloroaurate and citrate. Then the formation of AuNPs was initiated inside the core of preassembled liposomes by a shift in temperature [70 °C, 10 min] (Fig. 1A).

To prevent the formation of AuNPs during the preparation of liposomes, we selected lipids that are characterized by a low transition temperature (T_m). The lipid composition consisted of POPC and POPG, which provides a T_m of −2 °C. The lipid film was rehydrated with a tetrachloroaurate and citrate reaction solution in different ratios and the liposomes were extruded at RT before initiation of AuNP formation. The final AuNHyb sample exhibited the characteristic ruby-red color resulting from the surface plasmon resonance of encapsulated AuNPs.[36] To test if the temperature affected the efficiency of the process, the entire procedure was also carried out at 4 °C. However, there was no difference between AuNHybs prepared at RT or at lower temperatures. TEM showed that the AuNPs were encapsulated inside the AuNHybs (Fig. 2B). Encapsulation efficiency (*i.e.* the ratio between liposomes encapsulating AuNPs and liposomes that were empty) was significantly higher using the nanoreactor approach compared with either extrusion at high temperature (data not shown) or use of preformed AuNPs (Fig. 2D). The latter condition lead to the formation of AuNP aggregates in the medium surrounding the liposomes (Fig. 2D). In contrast, the nanoreactor approach resulted in the encapsulation of a single AuNP in the inner liposomal core.

POPC/POPG–AuNHybs were also analyzed by Cryo-TEM (Fig. 2C). Under these conditions, the native, hydrated state of the lipid formulation is presented.[37] Cryo-TEM showed that lipid-AuNHybs were spherical, mainly unilamellar, and efficiently loaded with AuNPs (Fig. 2C). AuNPs were located in the hydrophilic core of the liposomes (Fig. 2C), consistent with TEM analysis (Fig. 2B). Interestingly, some AuNPs were located in close proximity to the lipid bilayer. This could be either an artefact from the drying process during the TEM grid preparation or an interaction of the AuNPs with one of the phospholipids. The number of AuNPs encapsulated was dependent on the concentration of the AuR-solution. The highest AuNP encapsulation efficiency was achieved with 4 mM tetrachloroaurate, 16.3 mM citrate, and 20 mM lipids. Higher AuR-solution to lipid ratios resulted in the formation of AuNP agglomerates outside of the liposomes. On the other hand, lower AuR-solution to lipid ratios led to a significant amount of empty nanocarriers. Interestingly, TEM analysis revealed that the AuNPs, which were synthesized inside liposomes were significantly smaller than AuNPs synthesized without lipids (approximately 12.0 nm *vs.* 21.5 nm) (Fig. 2A *vs.* Fig. 2B). It is tempting to speculate that the limited amount of tetrachloroaurate and citrate available inside the nanocarriers is limiting the maximum size of the AuNPs. The POPC/POPG–AuNHybs were analyzed by DLS. The size of POPC/POPG–AuNHybs (104.7 nm ± 5.2 nm) was similar to the size of empty liposomes (Fig. 3A). Thus, AuNPs did not influence the nanocarrier diameter. In Fig. 4A, the absorption spectra of empty POPC/POPG liposomes (negative control), AuNPs (positive control), and POPC/POPG–AuNHybs are compared. As expected no absorption maximum was observed for empty POPC/POPG liposomes in the wavelength range from 500 nm to 600 nm. In contrast, AuNPs and POPC/POPG–AuNHybs showed a distinct surface plasmon absorbance peak at 525 nm. This indicates the successful encapsulation of AuNPs inside POPC/POPG liposomes.

3.2 Nanoprecipitation (di-block copolymer nanoparticles)

To demonstrate the broad applicability of our nanoreactor approach, we investigated the formation of polymer-AuNHybs using nanoprecipitation (Fig. 1B). For this method, the AuR-solution was added dropwise to the di-block copolymer PEG–PCL dissolved in THF (see ESI† for experimental details). Similar to the lipid-AuNHybs, the addition of preformed AuNPs to the polymer resulted in low encapsulation efficiency (Fig. S1A†). In contrast, high encapsulation efficiency with one

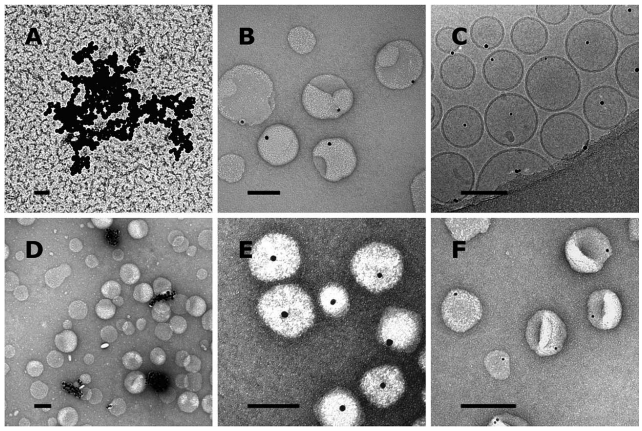

Fig. 2 Characterization of gold nanoparticles (AuNPs) and gold nanohybrids (AuNHybs). Representative transmission electron microscopy (TEM) (A/B, D–F) and Cryo-TEM (C) images are shown. (A) AuNPs were synthesized using a modified Turkevich method. (B) POPC/POPG–AuNHybs were analyzed by TEM and (C) Cryo-TEM. (D) The film-rehydration method for a lipid formulation with preformed AuNPs resulted in agglomerates. (E) PEG–PCL–AuNHybs prepared by nanoprecipitation and (F) PEG–liposome–AuNHybs after microfluidics platform preparation contain a single AuNP. Scale bars indicate 100 nm.

AuNP per polymeric nanocarrier was achieved using the nanoreactor approach (Fig. 2E). Cryo-TEM analysis confirmed that AuNPs with a size of 14.1 nm ± 3.1 nm were located inside the polymer-AuNHybs (Fig. S1B†).

Polymer-AuNHybs consisting of PEG–PCL presented a spherical morphology in which polymer chains self-assemble as solid polymeric nanoparticles. Thus, the hydrophilic parts of the di-block copolymer are exposed towards the outer buffer environment (Fig. S1B†). Recently, this was also shown for other polymeric nanoparticles.[38] DLS analysis showed a monodisperse formulation of polymer-AuNHybs (polydispersity index = 0.088) with a diameter of 77.5 nm ± 3.9 nm (Fig. 3B). Additionally, the polymer-AuNHybs showed a characteristic surface plasmon band at 527 nm due to the unique optical properties of AuNPs (Fig. 4B).

3.3 Microfluidics (PEGylated liposomes)

Recently, it has been demonstrated that rapid microfluidic mixing offers a controlled method to produce lipid nanocarriers.[39] Defined interfacial forces between the nanomaterial components result in a controllable and highly reproducible self-assembly process.[40] To facilitate the production of AuNP loaded PEGylated liposomes, we developed a microfluidics platform for the preparation of lipid-AuNHybs using lipids with a transition temperature above RT. Briefly, PEGylated lipid based gold nanohybrids (PEG–Lipo–AuNHybs) were synthesized by rapid mixing of an ethanolic lipid solution (5 mM, consisting of DSPC, cholesterol, and DSPE-PEG2000) and the aqueous Turkevich AuR-solution. In the last step of the process, the PEGylated liposomes were heated to 70 °C to start the formation of the AuNPs inside the liposomes.

In more detail, our microfluidics device consisted of seven inlet channels which converged into a single staggered-herringbone micromixer (see ESI†). At the junction of the inlets, the center stream was hydrodynamically focused to improve the mixing. To illustrate the nanomanufacturing process, we simulated the flow patterns and visualized them with a fluorescent dye (Fig. 1D/E; ESI Fig. S2†). Liposomes are formed at the interface between the hydrodynamically focused lipid stream and the AuR-solution. The mechanism of controlled, focused, and rapid mixing[41] is visible both in the experimental setting (Fig. 1D) and the computer simulation (Fig. 1E). The central inlet was used for the model ethanolic lipid solution [5 mM] (Fig. S2B†). The other six, outer inlets were used for tetrachloroaurate (Fig. S2C†), citrate (Fig. S2D†), and water (two inlets for each solution). Syringe pumps were used with flow rates up to 4 $\mu L\ s^{-1}$. The reagents were supplied by separate inlets because the use of tetrachloroaurate and citrate in the same inlet resulted in premature AuNP formation in the herringbone micromixer (Fig. S3D†).[40] In addition, the use of preformed AuNPs resulted in a low encapsulation efficiency, as observed for the film-rehydration and nanoprecipitation method with preformed AuNPs (Fig. S3E†). Therefore, the best results were achieved using a microfluidics platform with seven different inlets (Fig. 1C–E).

Water (4 $\mu L\ s^{-1}$) was used to improve the hydrodynamic flow focusing of the lipid stream and to decrease the final ethanol concentration. Furthermore, we used a higher flow rate for the outer inlets to increase the water to ethanol ratio. This is important to prevent the destabilization of liposomes caused by elevated ethanol concentrations.[42] Microfluidics parameters were adjusted to optimize encapsulation efficiency and size distribution. A continuous and efficient production was achieved with 2 mM tetrachloroaurate/8.2 mM citrate solution

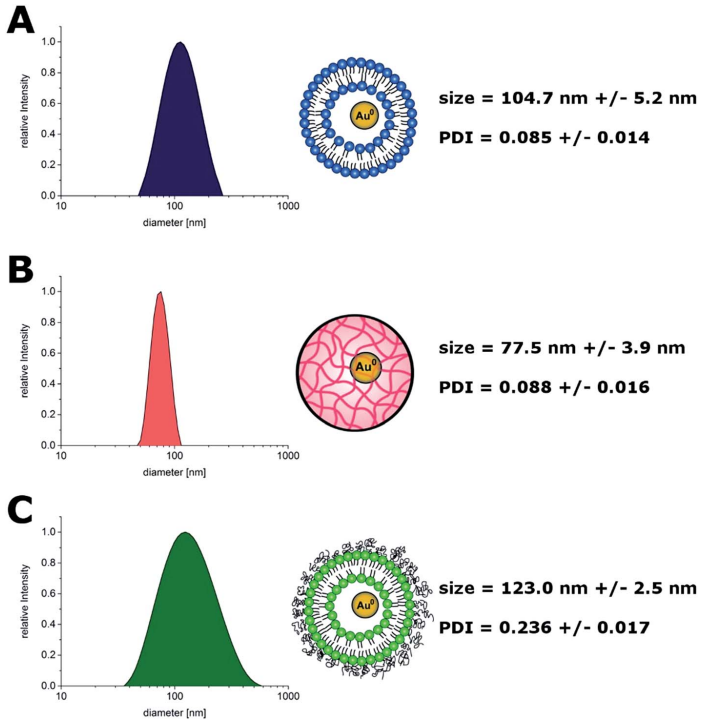

Fig. 3 Dynamic light scattering analysis of gold nanohybrids (AuNHybs). Intensity distribution of (A) POPC/POPG–AuNHyb, (B) PEG–PCL–AuNHyb, and (C) PEGylated liposome–AuNHyb. Mean values of size and polydispersity index (PDI) are given ± SD ($n = 5$).

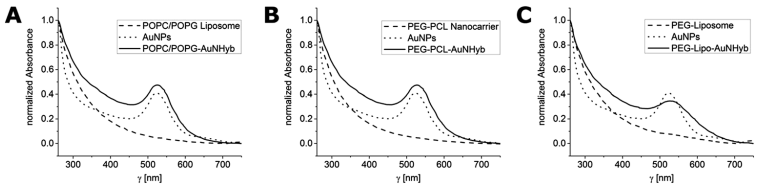

Fig. 4 UV spectra of empty nanocarriers, gold nanoparticles (AuNPs), and gold nanohybrids (AuNHybs). Relative UV-Vis absorption from 260 nm to 750 nm (step size one nm) was measured for (A) POPC/POPG, (B) PEG–PCL, and (C) PEG–lipid based nanocarriers. Spectra were normalized to an OD_{260} of 1.0. All AuNHybs showed a characteristic surface plasmon band at approximately 525 nm.

(for 5 mM lipids); and flow rates of 2 μL s^{-1} for the AuR-solutions, and 1 μL s^{-1} for the lipid solution. The absolute production speed was 420 μL min^{-1} (Fig. S2A†). Increasing the concentration of the AuR-solution for the microfluidics manufacturing resulted in an increased number of encapsulated AuNPs per AuNHyb (Fig. S3A–C†) until agglomerates were observed. AuNHybs with several encapsulated AuNPs mostly resulted in Janus-like vesicle structures (*i.e.* asymmetrical loading) as recently shown for Janus magnetic liposomes.[43] DLS and TEM showed that the size of PEG–Lipo–AuNHybs was similar to that of empty PEGylated liposomes (Fig. 2F and 3C). PEG–Lipo–AuNHybs with a mean hydrodynamic diameter of 123 nm ± 2.5 nm (*Z*-average) and a monodisperse size distribution were obtained (Fig. 3C). Each liposome incorporated one AuNP with a diameter of 6.8 nm ± 1.5 nm as shown by TEM (Fig. 2F). A characteristic plasmon absorption at 525 nm was observed using UV-Vis spectroscopy (Fig. 4C).

3.4 Characterization of nanoreactor approach

We showed that our nanoreactor approach is applicable for a wide range of nanomaterials, as well as different preparation methods. The film rehydration method can be used for lipids

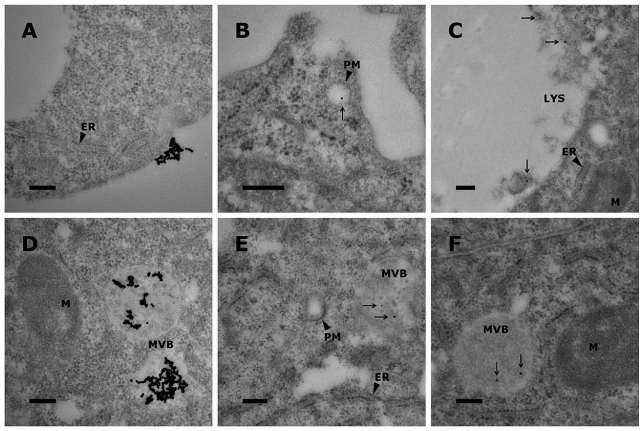

Fig. 5 Uptake experiments of gold nanoparticles (AuNPs) and gold nanohybrids (AuNHybs) in HepG2 cells. (A) AuNPs localized at the cell surface or (D) inside the cell. Representative uptake images of (B/E) POPC/POPG–AuNHybs and (C/F) PEG–PCL–AuNHybs (arrows). ER = endoplasmatic reticulum; LYS = lysosome; M = mitochondria; MVB = multi vesicular body; PM = plasma membrane. Scale bars indicate 200 nm.

with a transition temperature below RT, whereas the nanoprecipitation method is suitable for several polymer nanomaterials.[28,44] The microfluidics method is especially designed for lipids with a transition temperature above RT. However, this technique is suitable for all nanomaterials, that need highly controlled nanomanufacturing.[40]

The most important step of our nanoreactor approach is the speed of the nanocarrier production. The nanocarrier formation needs to be faster than AuNP aggregate formation. Therefore, the AuNP formation inside the nanocarriers is initiated by a temperature shift after self-assembly. AuNP aggregates formed outside of the self-assembled nanocarrier are removed by size exclusion chromatography. During this step, the outer buffer can be exchanged to a physiological compatible medium such as PBS. Several publications have shown that a difference in tonicity between the nanocarrier lumen and the outer buffer environment is not affecting the stability or morphology of nanocarriers.[45–47]

All tested combinations resulted in efficient and reproducible formation of AuNHybs. Moreover, DLS, TEM, and Cryo-TEM analysis showed that the final AuNHybs preserved the initial dimensions of the empty nanocarriers. Four distinct observations indicate that the AuNPs were encapsulated inside the nanocarriers. Firstly, the AuNHybs passed easily through the size exclusion chromatography medium (Superose 6 prep) whereas non-encapsulated AuNPs showed a high affinity for the chromatography medium, which was recently also shown for quantum dots.[48] Secondly, the AuNHybs exhibited an improved stability in PBS and aggregation was prevented as compared to free AuNPs. Thirdly, electron microscopy analysis showed a single AuNP entrapped per nanocarrier and no clusters of AuNPs were observed. Finally, the deep-red AuNHyb solutions exhibited a specific surface plasmon absorption peak at 525 nm, and a low 650 nm/530 nm ratio, which is characteristic for non-agglomerated AuNPs.[49]

3.5 Cellular uptake experiments

To demonstrate the use of AuNHybs for bioimaging, we performed uptake experiments with the AuNHybs in HepG2 cells exploiting the unique optical properties of AuNPs. The electron-density of AuNPs was used for further TEM analysis of cells (Fig. 5) as shown recently for surface-modified AuNPs.[50] Due to the high quality and uniform size of AuNPs, TEM observations were possible without silver enhancement. Using this approach, fundamental insights about nanocarrier uptake and intracellular fate can be obtained. For example, proteins covering the surface of nanocarriers after administration to biological medium can influence cellular uptake. However, formation of a protein corona and opsonisation can be minimized using PEGylated nanocarriers (*i.e.* PEG–PCL nanoparticles or PEGylated liposomes).[51,52] It remains to be elucidated to which degree protein adsorption onto non-modified nanocarriers such as conventional liposomes has to be taken into account for biomedical applications.[53,54]

The interaction of free AuNPs with HepG2 cells is shown in Fig. 5A and D. Free AuNPs formed aggregates which were located on the cellular plasma membrane (Fig. 5A) or taken up into the cell (Fig. 5D). These observations are in agreement with published results.[50,55] Fig. 5 shows the interaction with cells of lipid (panel B/E) or polymer based AuNHybs (panel C/F). In contrast to the uptake of free AuNPs, no AuNP aggregates were detected using AuNHybs. Different internalization steps were observed. An early stage in the cellular uptake mechanism was indicated by parts of the cellular plasma membrane around endosomes located near the cellular membrane (Fig. 5B). Compartments filled with more than one AuNP are most likely caused during maturation of different AuNHyb-filled vesicles (Fig. 5E/F).

AuNHybs could thus be used to examine nanoparticle–cell-interactions and the intracellular fate of the nanocarriers

inside the cells using TEM, a technique which offers greater resolution compared to confocal microscopy. It should be noted that liposomes encapsulating AuNPs can act simultaneously as a carrier for fluorescent dyes (see ESI† for experimental details). For example rhodamine labelled phospholipids (Rho-PE) can be used to fluorescence label AuNHybs (Fig. S4b†). This offers the possibility to image fluorescent AuNHybs by confocal fluorescence microscopy or to quantify them with flow cytometry analysis.

4. Conclusions

In conclusion, we have developed a novel strategy for the preparation of lipid and polymer based AuNHybs. After encapsulation of the required reagents inside nanocarriers, formation of AuNPs was triggered by a temperature shift. In future, a similar approach could be used for the preparation of alternative metal nanohybrids such as silver nanoparticles. Different preparation techniques were used in combination with various nanomaterials. To the best of our knowledge, this nanoreactor approach is unique and was not used previously. The high reproducibility and versatility of our nanoreactor approach is unprecedented and makes this technology suitable for many nanomaterials. Microfluidics offers the possibility for an efficient and large scale production.

The produced AuNHybs have a size of 70 nm to 130 nm, which makes them ideal for bioimaging applications.[56] In addition, AuNHybs can be stored over a prolonged period of time (*i.e.* >3 months/4 °C) maintaining their initial size and monodispersity.

In order to target specific cells or tissues, AuNHybs can be easily modified using surface-conjugated receptor ligands.[57] Our nanoreactor approach will be instrumental to develop a better understanding of cellular uptake and intracellular trafficking of targeted nanocarriers.

Acknowledgements

The authors declare no conflicting financial interest. Funding of the Stiftung zur Förderung des pharmazeutischen Nachwuchses in Basel is acknowledged. C. P.-B. was supported by the Swiss National Science Foundation (31003A-125423). D. W. thanks Lisa Stoltenburg for her support during this project. The authors thank Dr Adam Lister for editorial and Andrea Fehrenbach for graphical assistance. In addition, we thank Dr Susanne H. Schenk for her feedback on the manuscript, Dr Timothy Sharpe for his scientific input, and Prof. Henning Stahlberg (Director of C-CINA, Centre for Cellular Imaging and NanoAnalytics) and the Microscopy Center of the Biozentrum Basel for their support with electron microscopy techniques.

Notes and references

1 A. S. Thakor, J. Jokerst, C. Zavaleta, T. F. Massoud and S. S. Gambhir, *Nano Lett.*, 2011, **11**, 4029–4036.
2 D. F. Moyano, B. Duncan and V. M. Rotello, *Methods Mol. Biol.*, 2013, **1025**, 3–8.
3 D. Kumar, N. Saini, N. Jain, R. Sareen and V. Pandit, *Expert Opin. Drug Delivery*, 2013, **10**, 397–409.
4 R. Cao-Milán and L. M. Liz-Marzán, *Expert Opin. Drug Delivery*, 2014, **11**, 741–752.
5 L. C. Kennedy, L. R. Bickford, N. A. Lewinski, A. J. Coughlin, Y. Hu, E. S. Day, J. L. West and R. A. Drezek, *Small*, 2011, **7**, 169–183.
6 E. Oh, K. Susumu, R. Goswami and H. Mattoussi, *Langmuir*, 2010, **26**, 7604–7613.
7 C. Li, D. Li, G. Wan, J. Xu and W. Hou, *Nanoscale Res. Lett.*, 2011, **6**, 440.
8 S. K. Sivaraman, S. Kumar and V. Santhanam, *J. Colloid Interface Sci.*, 2011, **361**, 543–547.
9 J. Kimling, M. Maier, B. Okenve, V. Kotaidis, H. Ballot and A. Plech, *J. Phys. Chem. B*, 2006, **110**, 15700–15707.
10 P. J. G. Goulet and R. B. Lennox, *J. Am. Chem. Soc.*, 2010, **132**, 9582–9584.
11 L. L. Lazarus, A. S.-J. Yang, S. Chu, R. L. Brutchey and N. Malmstadt, *Lab Chip*, 2010, **10**, 3377–3379.
12 W. Wang, Q.-Q. Wei, J. Wang, B.-C. Wang, S. Zhang and Z. Yuan, *J. Colloid Interface Sci.*, 2013, **404**, 223–229.
13 D. Pornpattananangkul, S. Olson, S. Aryal, M. Sartor, C.-M. Huang, K. Vecchio and L. Zhang, *ACS Nano*, 2010, **4**, 1935–1942.
14 D. V. Volodkin, A. G. Skirtach and H. Möhwald, *Angew. Chem., Int. Ed. Engl.*, 2009, **48**, 1807–1809.
15 M. R. Preiss and G. D. Bothun, *Expert Opin. Drug Delivery*, 2011, **8**, 1025–1040.
16 A. K. Rengan, M. Jagtap, A. de, R. Banerjee and R. Srivastava, *Nanoscale*, 2014, **6**, 916–923.
17 G. von White, Y. Chen, J. Roder-Hanna, G. D. Bothun and C. L. Kitchens, *ACS Nano*, 2012, **6**, 4678–4685.
18 J. Nam, Y. S. Ha, S. Hwang, W. Lee, J. Song, J. Yoo and S. Kim, *Nanoscale*, 2013, **5**, 10175–10178.
19 H. Minematsu, T. Otani, T. Oohashi, M. Hirai, K. Oie, K. Igarashi and A. Ohtsuka, *J. Electron Microsc.*, 2011, **60**, 95–99.
20 M. R. Rasch, E. Rossinyol, J. L. Hueso, B. W. Goodfellow, J. Arbiol and B. A. Korgel, *Nano Lett.*, 2010, **10**, 3733–3739.
21 S.-H. Park, S.-G. Oh, J.-Y. Mun and S.-S. Han, *Colloids Surf., B*, 2006, **48**, 112–118.
22 L. Paasonen, T. Sipilä, A. Subrizi, P. Laurinmäki, S. J. Butcher, M. Rappolt, A. Yaghmur, A. Urtti and M. Yliperttula, *J. Controlled Release*, 2010, **147**, 136–143.
23 C. Kojima, Y. Hirano, E. Yuba, A. Harada and K. Kono, *Colloids Surf., B*, 2008, **66**, 246–252.
24 T. K. Sau, A. S. Urban, S. K. Dondapati, M. Fedoruk, M. R. Horton, A. L. Rogach, F. D. Stefani, J. O. Rädler and J. Feldmann, *Colloids Surf., A*, 2009, **342**, 92–96.
25 R. Genç, G. Clergeaud, M. Ortiz and C. K. O'Sullivan, *Langmuir*, 2011, **27**, 10894–10900.
26 K. Hong, D. S. Friend, C. G. Glabe and D. Papahadjopoulos, *Biochim. Biophys. Acta*, 1983, **732**, 320–323.
27 J. Huwyler, D. Wu and W. M. Pardridge, *Proc. Natl. Acad. Sci. U. S. A.*, 1996, **93**, 14164–14169.
28 T. Govender, S. Stolnik, M. C. Garnett, L. Illum and S. S. Davis, *J. Controlled Release*, 1999, **57**, 171–185.

29 Y. Kim, B. Lee Chung, M. Ma, W. J. M. Mulder, Z. A. Fayad, O. C. Farokhzad and R. Langer, *Nano Lett.*, 2012, **12**, 3587–3591.
30 L. Y. Yeo, H.-C. Chang, P. P. Y. Chan and J. R. Friend, *Small*, 2011, **7**, 12–48.
31 P. Detampel, D. Witzigmann, S. Krähenbühl and J. Huwyler, *J. Drug Targeting*, 2013, **22**, 232–241.
32 S. Deshpande and T. Pfohl, *Biomicrofluidics*, 2012, **6**, 34120.
33 M. E. Brennich, J.-F. Nolting, C. Dammann, B. Nöding, S. Bauch, H. Herrmann, T. Pfohl and S. Köster, *Lab Chip*, 2011, **11**, 708–716.
34 J. Turkevich, P. C. Stevenson and J. Hillier, *Discuss. Faraday Soc.*, 1951, **11**, 55–75.
35 G. Frens, *Nature (London), Phys. Sci.*, 1973, **241**, 20–22.
36 E. Casals, T. Pfaller, A. Duschl, G. J. Oostingh and V. Puntes, *ACS Nano*, 2010, **4**, 3623–3632.
37 S. Mornet, O. Lambert, E. Duguet and A. Brisson, *Nano Lett.*, 2005, **5**, 281–285.
38 E. Jäger, A. Jäger, T. Etrych, F. C. Giacomelli, P. Chytil, A. Jigounov, J.-L. Putaux, B. Říhová, K. Ulbrich and P. Štěpánek, *Soft Matter*, 2012, **8**, 9563–9575.
39 I. V. Zhigaltsev, N. Belliveau, I. Hafez, A. K. K. Leung, J. Huft, C. Hansen and P. R. Cullis, *Langmuir*, 2012, **28**, 3633–3640.
40 A. Jahn, W. N. Vreeland, M. Gaitan and L. E. Locascio, *J. Am. Chem. Soc.*, 2004, **126**, 2674–2675.
41 P. M. Valencia, P. A. Basto, L. Zhang, M. Rhee, R. Langer, O. C. Farokhzad and R. Karnik, *ACS Nano*, 2010, **4**, 1671–1679.
42 N. Maurer, K. F. Wong, H. Stark, L. Louie, D. McIntosh, T. Wong, P. Scherrer, S. C. Semple and P. R. Cullis, *Biophys. J.*, 2001, **80**, 2310–2326.
43 C. Bonnaud, C. A. Monnier, D. Demurtas, C. Jud, D. Vanhecke, X. Montet, R. Hovius, M. Lattuada, B. Rothen-Rutishauser and A. Petri-Fink, *ACS Nano*, 2014, **8**, 3451–3460.
44 U. Bilati, E. Allémann and E. Doelker, *Eur. J. Pharm. Sci.*, 2005, **24**, 67–75.
45 D. D. Lasic, B. Ceh, M. C. Stuart, L. Guo, P. M. Frederik and Y. Barenholz, *Biochim. Biophys. Acta*, 1995, **1239**, 145–156.
46 B. Ceh and D. D. Lasic, *J. Colloid Interface Sci.*, 1997, **185**, 9–18.
47 A. Fritze, F. Hens, A. Kimpfler, R. Schubert and R. Peschka-Süss, *Biochim. Biophys. Acta, Biomembr.*, 2006, **1758**, 1633–1640.
48 M. Camblin, P. Detampel, H. Kettiger, D. Wu, V. Balasubramanian and J. Huwyler, *Int. J. Nanomed.*, 2014, **9**, 2287–2298.
49 C.-C. Huang, Y.-F. Huang, Z. Cao, W. Tan and H.-T. Chang, *Anal. Chem.*, 2005, **77**, 5735–5741.
50 P. Nativo, I. A. Prior and M. Brust, *ACS Nano*, 2008, **2**, 1639–1644.
51 D. Pozzi, V. Colapicchioni, G. Caracciolo, S. Piovesana, A. L. Capriotti, S. Palchetti, S. D. Grossi, A. Riccioli, H. Amenitsch and A. Laganà, *Nanoscale*, 2014, **6**, 2782–2792.
52 M. Lundqvist, J. Stigler, T. Cedervall, T. Berggård, M. B. Flanagan, I. Lynch, G. Elia and K. Dawson, *ACS Nano*, 2011, **5**, 7503–7509.
53 M. Lundqvist, J. Stigler, G. Elia, I. Lynch, T. Cedervall and K. A. Dawson, *Proc. Natl. Acad. Sci. U. S. A.*, 2008, **105**, 14265–14270.
54 M. Hadjidemetriou, Z. Al-Ahmady, M. Mazza, R. F. Collins, K. Dawson and K. Kostarelos, *ACS Nano*, 2015, **9**, 8142–8156.
55 B. D. Chithrani, A. A. Ghazani and W. C. W. Chan, *Nano Lett.*, 2006, **6**, 662–668.
56 H. Kettiger, A. Schipanski, P. Wick and J. Huwyler, *Int. J. Nanomed.*, 2013, **8**, 3255–3269.
57 A. Wicki, D. Witzigmann, V. Balasubramanian and J. Huwyler, *J. Controlled Release*, 2015, **200**, 138–157.

RSC Advances

Supplementary Information

Formation of Lipid and Polymer Based Gold Nanohybrids Using a Nanoreactor Approach

Dominik Witzigmann, Sandro Sieber, Fabiola Porta, Philip Grossen, Andrej Bieri, Natalja Strelnikova, Thomas Pfohl, Cristina Prescianotto-Baschong, Jörg Huwyler *

** Author for correspondence:*
Prof. Dr. Jörg Huwyler
Phone: +41 (0)61 267 15 13
E-mail: joerg.huwyler@unibas.ch

1. Supplementary Information Experimental Section

1.1 Gold nanoparticle (AuNP) synthesis

The AuNP synthesis was optimized using a 2^3 full factorial design of experiment (DoE) [Stavex 5.2, Aicos Technologies, Basel, Switzerland]. Variables are listed in Table S1. All glass equipment was cleaned with aqua regia to prevent the formation of gold seeds. The best condition (smallest AuNPs and mild reaction condition) from our screening was used for further AuNHyb preparations (1.0 mM $HAuCl_4$ / 4.1 mM citrate; 1:4 molar ratio).

Table S1: AuNP synthesis screening using Turkevich method. Variations of citrate or tetrachloroaurate concentration, pH, and temperature.

Sample	c ($HAuCl_4$) [mM]	c (Citrate) [mM]	c (NaOH) [mM]	T [°C]	Size [nm]
Factorial Design (Mild Conditions)					
A	0.5	2.0	-	70	20.2
B	1.0	2.0	-	70	24.3
C	0.5	4.1	-	70	43.1
D	1.0	4.1	-	70	16.6
E	0.5	2.0	-	85	20.8
F	1.0	2.0	-	85	19.8
G	0.5	4.1	-	85	17.0
H	1.0	4.1	-	85	17.8
Other Approaches [1–4]					
I	0.5	2.0	-	boiling	18.7
K	1.0	4.1	-	boiling	19.3
L	2.5	5.1	5.0	70	26.6
M	2.5	5.1	6.6	85	19.6

1.2 Microfluidics device design and fabrication

For the master fabrication, SU8 (Microchem, Newton, USA) spin coated silicon wafers (Si-Mat, Kaufering, Germany) were used. To produce a master with a staggered herringbone micromixer, multi-layer photolithography was carried out using appropriate photomasks (JD Pho-tools, Oldham, UK) and a MJB4 mask aligner (SUSS MicroTec AG, Garching, Germany).
The first layer was made of SU8-3025 and the second one of SU8-3050 negative photoresists. PDMS and cross-linker (Sylgard 184, Dow Corning GmbH, Wiesbaden, Germany) were mixed in the mass ratio of 10:1, degassed, and poured on the masters followed by overnight curing. Cured PDMS stamp was peeled off from the wafer.
To prepare a 3D channel device, two sides (bottom side and top side) of polystyrene foil/NOA 81 were prepared as follows. A drop of NOA 81 was pipetted onto the structure of the PDMS stamp. Then a piece of polystyrene foil was placed on the NOA 81 and pressed down until the polystyrene foil touches elevated channel on the PDMS stamp that the channels were only laterally defined by NOA 81. NOA 81 was cured under UV-light for 3 min (366 nm, 2 x 8 W, Camag, Muttenz, Switzerland). The second side of the device was prepared the same way. Additionally, 0.75 mm holes were punched for tubing connection (Harris Unicore). Both polystyrene foil/NOA 81 sides were aligned, gently pressed, and cured under UV-light for 10 min.

1.3 Flow visualization

Deionized water, ethanol, and a fluorescein solution were used to visualize the flow patterns of the microfluidics device (Figure 1D). Images were taken using an Olympus IX81 inverted microscope (Olympus, Tokyo, Japan) equipped with fluorescence illumination (X-Cite Series 120 Q).

1.4 Computational Fluid Dynamics Simulation

For the numerical computational fluid dynamics (CFD) simulations we used the CFD module of the software COMSOL 4.3a (COMSOL Inc, Burlington, USA). The microfluidics device was modeled in 3D using 792,779 finite elements solving the incompressible Navier-Stokes-equation and advection-diffusion equation. The stationary flow field was calculated and in a second step the material transport of the diluted species were calculated using the beforehand-obtained stationary flow fields. We assumed a Newtonian fluid having the properties of water at room temperature.[5] Flow rates and inflow concentrations were specified at the seven inlets and the following diffusion coefficients were assumed: $D_{lipids} = 5 \cdot 10^{-11}$ m^2 s^{-1}, $D_{citrate} = 8.9 \cdot 10^{-10}$ m^2 s^{-1} and $D_{AuCL4} = 5.6 \cdot 10^{-10}$ m^2 s^{-1}.

1.5 Preparation of fluorescent lipid based gold nanohybrids (AuNHybs)

To broaden the application spectrum of AuNHybs for bioimaging purposes, we introduced an additional fluorescence marker, namely Rho-PE (Avanti Polar-Lipids, Alabaster, USA), into lipid based nanocarriers. Rho-PE was post inserted into preformed 75mol% POPC, 25mol% POPG liposomes as described elsewhere.[6] The modified liposomes possessed specific absorption properties based on the encapsulated AuNPs and an additional fluorescence based on the post-insertion of Rho-PE. The non-Rho-PE liposomes showed neither an absorption peak between 260 nm and 750 nm, nor a fluorescence after excitation at 560 nm. In contrast, the Rho-PE containing liposomes possessed a strong fluorescence with a maximum at 596 nm after they were excited near their absorption maximum at 560 nm. Compared with lipid-AuNHybs, the Rho-PE containing AuNHybs showed an additional absorption peak and were fluorescent after they were excited at 560 nm.

2. Supplementary Information Figures

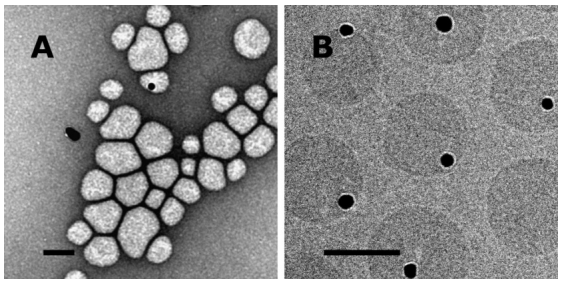

Figure S1. Electron microscopy analysis of PEG-PCL-gold nanohybrids (AuNHybs). Representative transmission electron microscopy (TEM) and Cryo-TEM images of solid polymeric nanoparticles are shown. (A) Preparation of PEG-PCL-AuNHybs using preformed AuNPs results in low encapsulation efficiency. (B) Cryo-TEM analysis of PEG-PCL-AuNHybs prepared via nanoreactor approach. Scale bars indicate 50 nm.

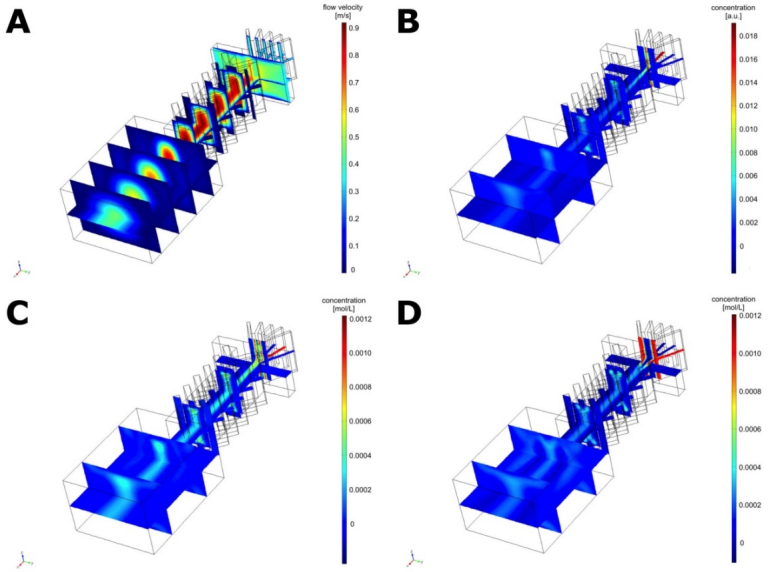

Figure S2. Computational fluid dynamics (CFD) simulations. (A) CFD simulation of the flow rate (m/s) of all seven inlet channels converging to a single micromixer is shown. Simulation of concentration gradients of (B) ethanol (in a.u.), (C) tetrachloroaurate (in mol/L), and (D) citrate (in mol/L) solution are presented.

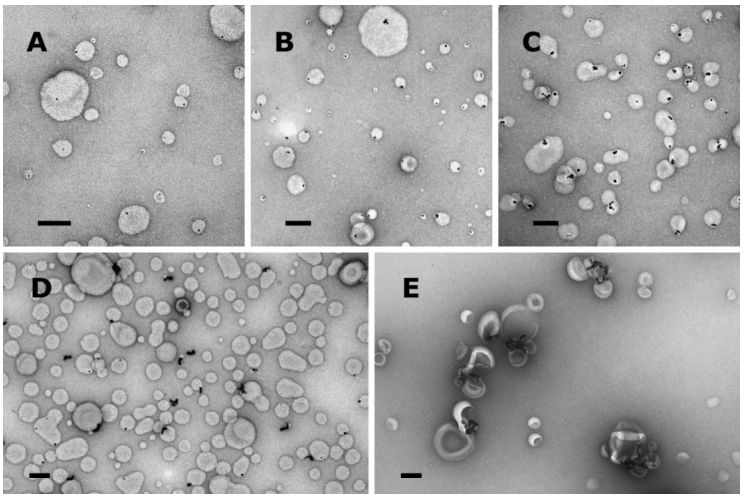

Figure S3. Preparation of gold nanohybrids (AuNHybs) using microfluidics. Representative transmission electron microscopy (TEM) images are shown. Increasing concentration of the reaction solutions (1x = 1 mM $HAuCl_4$ / 4.1 mM citrate) for the nanoreactor approach resulted in an increased number of AuNPs per nanocarrier. (A) 2x, (B) 4x, and (C) 8x reaction solutions were used. (D) Preparation of AuNHybs with one combined reaction solution in the same inlet resulted in AuNP formation during microfluidics procedure. (E) Direct use of AuNPs resulted in agglomerates and low encapsulation efficiency. Scale bars indicate 100 nm.

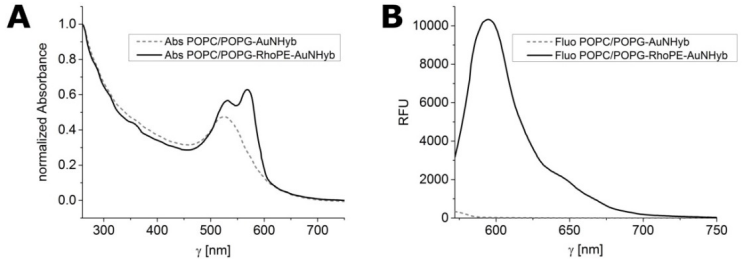

Figure S4. UV-Vis and fluorescence spectra of gold nanohybrids (AuNHybs) with and without fluorescent lipid (Rho-PE). (A) UV-Vis absorption from 260 nm to 750 nm (step size one nm) was measured. Spectra were normalized to an OD_{260} of 1.0. Fluorescently labelled AuNHybs showed two absorbance maxima, i.e. characteristic surface plasmon band and absorbance maximum of Rho-PE. (B) Fluorescence spectra of AuNHybs between 572 nm to 750 nm after excitation at 560 nm. POPC/POPG-RhoPE-AuNHybs showed strong fluorescence (RFU = relative fluorescence units), whereas POPC/POPG-AuNHybs were not fluorescent.

Supplementary Information References

1 E. Oh, K. Susumu, R. Goswami and H. Mattoussi, *Langmuir*, 2010, **26**, 7604–7613.
2 C. Li, D. Li, G. Wan, J. Xu and W. Hou, *Nanoscale Res. Lett.*, 2011, **6**, 440.
3 S. K. Sivaraman, S. Kumar and V. Santhanam, *J. Colloid Interface Sci.*, 2011, **361**, 543–547.
4 J. Kimling, M. Maier, B. Okenve, V. Kotaidis, H. Ballot and A. Plech, *J. Phys. Chem. B*, 2006, **110**, 15700–15707.
5 Y. Kim, B. Lee Chung, M. Ma, W. J. M. Mulder, Z. A. Fayad, O. C. Farokhzad and R. Langer, *Nano Lett.*, 2012, **12**, 3587–3591.
6 T. M. Allen, P. Sapra and E. Moase, *Cell. Mol. Biol. Lett.*, 2002, **7**, 889–894.

CHAPTER IV

Functionalized Solid-Sphere PEG-b-PCL Nanoparticles to Target Brain Capillary Endothelial Cells In Vitro

Grossen P, Québatte G, Witzigmann D, Prescianotto-Baschong C, Dieu L-H, Huwyler J

Manuscript: Published in J. Nanomater. 2016 (2016) 1–13.
DOI: 10.1155/2016/7818501

Highlights: Active drug targeting strategies hold promising potential to specifically deliver drugs to their target cells. In this work, a drug delivery platform based on PEG-PCL micelles was evaluated to target human blood-brain barrier (BBB) endothelial cells. A monoclonal antibody directed towards the human insulin receptor (83-14 mAb) was therefore conjugated to PEG-PCL micelles. Functionalized micelles were characterized physico-chemically using state-of-the-art methods and their interaction with an *in vitro* model of the BBB was studied. The gold nanohybrid strategy described in **Chapter III** was further used to analyze the intracellular fate of targeted PEG-PCL micelles.

Hindawi Publishing Corporation
Journal of Nanomaterials
Volume 2016, Article ID 7818501, 13 pages
http://dx.doi.org/10.1155/2016/7818501

Research Article

Functionalized Solid-Sphere PEG-*b*-PCL Nanoparticles to Target Brain Capillary Endothelial Cells *In Vitro*

Philip Grossen,[1] Gabriela Québatte,[1] Dominik Witzigmann,[1] Cristina Prescianotto-Baschong,[2] Le-Ha Dieu,[1] and Jörg Huwyler[1]

[1]*Division of Pharmaceutical Technology, Department of Pharmaceutical Sciences, University of Basel, 4056 Basel, Switzerland*
[2]*Biozentrum University of Basel, 4056 Basel, Switzerland*

Correspondence should be addressed to Jörg Huwyler; joerg.huwyler@unibas.ch

Received 23 February 2016; Revised 4 May 2016; Accepted 12 May 2016

Academic Editor: Jean M. Greneche

Nanoparticles are increasingly used to implement drug targeting strategies. In the present study, solid-sphere nanoparticles (SNPs) made of poly(ethylene glycol)-*b*-poly(ε-caprolactone) (PEG-*b*-PCL) were covalently linked to a monoclonal antibody (83-14 mAb) targeted against the human insulin receptor that is highly expressed on human brain microvascular endothelial cells. Resulting targeted SNPs were characterized using transmission electron microscopy (TEM), cryo-TEM, dynamic light scattering, and fluorescence correlation spectroscopy. The critical aggregation concentration was determined using a fluorescence approach. Interaction with a well-characterized human *in vitro* model of the blood-brain barrier (hCMEC/D3) was analysed using an array of methods (flow cytometry, confocal laser scanning microscopy, and TEM). The toxicity on hCMEC/D3 cells and in addition on the human liver cell line HepG2 was assessed using the MTT assay. SNPs with a diameter of 80 nm and a homogeneous size distribution were obtained. Successful conjugation of 83-14 mAb using a heterobifunctional linker resulted in 5-6 molecules of fluorescently labeled 83-14 mAb per SNP. Functionalized SNPs were taken up by hCMEC/D3 cells efficiently without showing a significant toxic effect on cells of the blood-brain barrier and HepG2 cells. These results indicate that functionalized PEG-*b*-PCL SNPs are a promising candidate to deliver drugs to the CNS.

1. Introduction

Despite the presence of potent active pharmaceutical ingredients (API), efficient treatment of central nervous system- (CNS-) related diseases remains a major challenge in pharmacotherapy. The blood-brain barrier (BBB) that maintains the homeostasis of the brain excludes many small and large molecule drugs from the CNS [1, 2]. To reach therapeutic concentrations of systemic administered drugs in the CNS, high doses are often required. This is linked with an increased risk for toxic side effects. Therefore, different strategies for effective drug transfer across the BBB are currently under investigation [3]. Besides chemical optimization of the API and invasive delivery techniques, targeting of transporters and receptors expressed on BBB endothelial cells is a promising way to specifically deliver drugs to the CNS [3]. Endogenous macromolecules can cross the BBB by receptor-mediated transport and thus reach the brain despite their size as shown for insulin [4, 5] and transferrin [6]. Antibodies can mimic these endogenous ligands and transport bound drugs, macromolecules, or nanoparticles across the BBB *in vivo*. For example, the enzyme N-sulfoglucosamine sulfohydrolase (SGSH) was conjugated to a monoclonal antibody (mAb) directed against the human insulin receptor (HIR). Recombinant SGSH was not able to cross the BBB. However, it was possible to reach therapeutic concentrations in the brain after injection of the mAb fusion protein in Rhesus monkeys [7]. While antibody drug conjugates (ADCs) provide specific targeting to a distinctive tissue or cell type, their drug carrying capacity is very limited. Nanocarriers can exceed the drug payload of ADCs by three to four orders of magnitude [8]. Within these nanocarriers, self-assembled micelles consisting of biodegradable diblock copolymers are extensively studied as drug delivery systems (DDS) [9]. Their hydrophobic core serves as a reservoir for poorly soluble drugs, sterically stabilized by a hydrophilic corona [10]. Polymeric micelles

can prevent premature drug degradation, reduce off-target effects, and increase bioavailability. In addition, these systems can be directed towards specific organs, tissues, or cells by coupling targeting moieties onto their surface [11]. In recent years, various approaches were investigated to combine NPs with BBB targeting mAbs. The neuropeptide NK-1900, for example, improved scopolamine-induced learning impairments and memory deficits in rats by i.v. administration of NK-1900-loaded polymersomes conjugated to an antitransferrin receptor mAb (OX-26) [12]. Previous studies by our group showed that polymersomes consisting of poly(dimethylsiloxane)-*b*-poly(2-methyloxazoline) (PDMS-*b*-PMOXA) modified with 83-14 mAb were taken up specifically by human brain capillary endothelial cells *in vitro* [13]. With K_D of 0.45 ± 0.10 nM, 83-14 mAb has a strong affinity to the α-subunit of the insulin receptor expressed on human brain capillary endothelial cells (hBMEC). Its binding to the HIR was shown to trigger receptor-mediated endocytosis *in vivo* and 83-14 mAb was shown to cross the primate BBB 10x more efficiently as compared to an antitransferrin receptor mAb [14, 15].

With respect to polymer-based NPs, however, the question arises if these particles can be safely degraded after delivering their drug payload, since accumulation and persistence within the target tissue are of potential safety concern. For example, PDMS-*b*-PMOXA vesicles used in our previous studies are characterized by a high chemical and mechanical stability [16]. Polyacrylamide-based nanocarriers used previously to implement drug targeting strategies could give rise to potential toxicity due to degradation products [17]. Polylactic acid-based NPs have been shown to be readily degradable but lactic acid, a major degradation product, can lead to acidification of the metabolizing cell and organ [18–20].

To address these potential issues, this study aimed to design and use PEG-*b*-PCL SNPs ([PP-SNP]) as a safe alternative to existing technologies. This polymer is already approved by regulatory authorities such as the US Food and Drug Administration (FDA) for tissue engineering and drug delivery. PEG-*b*-PCL is known to be biocompatible and biodegradable and was therefore used to implement an active targeting strategy to the brain [21]. 83-14 mAb was covalently conjugated to the surface of [PP-SNP] by a PEG-spaced heterobifunctional linker. Resulting [PP-SNP]-[mAb] was then analysed using an array of analytical methods (i.e., TEM, cryo-TEM, dynamic light scattering [DLS], pyrene encapsulation, and fluorescence correlation spectroscopy [FCS]). Interactions with eukaryotic cells and potential toxic effects were studied in a well-characterized *in vitro* BBB model (hCMEC/D3) and the human hepatocellular carcinoma cell line HepG2 [13, 22].

2. Materials and Methods

2.1. Materials. PEG-*b*-PCL (PCL average $M_n \approx 13\,000$, PEG average $M_n \approx 5000$, stored at 4°C under argon atmosphere, batch number. MKBR7365V), pyrene (≥99%), anhydrous tetrahydrofuran (THF; ≥99.9%), anhydrous dimethyl sulfoxide (DMSO; ≥99.9%), 2-iminothiolane hydrochloride (Traut's reagent; ≥98%), 1,1′-dioctadecyl-3,3,3′,3′-tetramethylindocarbocyanine perchlorate (DiI; ≥98%) gold(III) chloride trihydrate, sodium citrate dihydrate (≥99%), and anti-mouse IgG (whole molecule) gold antibody (5 nm colloidal gold) were purchased from Sigma-Aldrich (Schnelldorf, Germany). NH_2-PEG-*b*-PCL (PCL average $M_n \approx 15\,500$, PEG average $M_n \approx 5000$, batch number. P18343-NH2EGCL) was purchased from Polymer Source (Montreal, Canada). $SM(PEG)_{24}$ and DyLight 488 NHS ester were purchased from Thermo Fisher Scientific (Waltham, MA, USA). Thiazolyl Blue (MTT reagent; ≥98%) was purchased from Carl Roth GmbH (Karlsruhe, Germany). Amicon Ultra-4 centrifugal filter units (10 kDa NMWL, 30 kDa NMWL) were purchased from Merck Millipore (Darmstadt, Germany). The hybridoma cell line producing 83-14 mAb was kindly provided by Professor Ken Siddle (Department of Clinical Biochemistry, University of Cambridge, UK). Cell culture reagents and chemicals are listed below.

2.2. Preparation of [PP-SNP]. [PP-SNP] composed of a mixture of amphiphilic diblock copolymers (95% mol/mol PEG-*b*-PCL and 5% mol/mol NH_2-PEG-*b*-PCL) was prepared using the cosolvent method, also called the solvent displacement method [23]. In brief, the block copolymer (5.3 mg) was dissolved in THF (50 μL) and stirred at 700 rpm. Phosphate-buffered saline (PBS; 157 mM Na, 140 mM Cl) EDTA 5 mM, pH 7.4 (1 mL) was added dropwise under constant stirring. The mixture was stirred at room temperature (RT) overnight. THF was removed by two consecutive steps: THF was allowed to evaporate during overnight stirring [24]. Buffer was subsequently exchanged by gel filtration chromatography using Superose 6 Prep column eluting with PBS, pH 7.4 [25]. DiI-loaded [PP-SNP] ([PP-SNP-DiI]) was produced by adding 1 μg DiI per mg of PEG-*b*-PCL to THF and particles were produced using the same protocol as described above.

2.3. Fluorescent Labeling of 83-14 mAb. 83-14 mAb (1 mg/mL in PBS, pH 8.0) was incubated with a 5x molar excess of NHS ester functionalized DyLight 488 for 1 h at RT ([mAb-DL]). The sample was purified using an Amicon Ultra-4 centrifugal filter unit (MWCO 10 kDa).

2.4. Conjugation of 83-14 mAb to SNPs. A heterobifunctional linker ($SM(PEG)_{24}$) was used to conjugate 83-14 mAb or 83-14 mAb DL to [PP-SNP] giving rise to [PP-SNP]-[mAb], [PP-SNP-DiI]-[mAb], [PP-SNP-Au]-[mAb], or [PP-SNP]-[mAb-DL], respectively. SNPs were prepared as described above and incubated with a 20x molar excess of linker for 1 h at RT in PBS EDTA 5 mM, pH 7.0. Unbound linker was removed using an Amicon Ultra-4 centrifugal filter unit (MWCO 30 kDa). In parallel, a 2x molar excess of fluorescently labeled 83-14 mAb in sodium borate 0.1 M pH 8.5 was thiolated using Traut's reagent, that is, 100x molar excess of 2-iminothiolane. After incubation for 1 h at RT, thiolated 83-14 mAb was purified by using an Amicon Ultra-4 centrifugal filter unit (MWCO 10 kDa). SNPs and thiolated 83-14 mAb DL were mixed and incubated at RT overnight. Unbound 83-14 mAb was separated by gel filtration chromatography (Superose 6

Prep, PBS pH 7.4). For all experiments, modified SNPs were used immediately after preparation.

2.5. Gold-Nanohybrid SNP Formation. To visualize [PP-SNP] in TEM, gold-nanohybrids [PP-SNP-Au] were prepared as described recently [26]. In brief, 5.3 mg of PEG-*b*-PCL was dissolved in THF (50 μL) and stirred at 700 rpm. The AuR-solution (1 mM $HAuCl_4$, 4.1 mM citrate) was added dropwise under constant stirring. The mixture was heated to 70°C under constant agitation at 300 rpm on the thermomixer (Thermomixer Comfort; Eppendorf, Hamburg, Germany). Free gold NPs were separated by gel filtration chromatography (Superose 6 Prep) using PBS pH 7.4 as an eluent. Free gold particles did not elute during gel filtration chromatography. They had a high affinity for the stationary phase and were retained in the chromatography column [26]. [PP-SNP-Au] and [PP-SNP-Au]-[mAb] were collected after 8–12 min using a column volume of 30 mL and a flow rate of 1 mL/min.

2.6. Characterization of [PP-SNP]. Morphology and size distribution of [PP-SNP] were analysed using TEM, cryo-TEM, and DLS. For TEM analysis, 5 μL of nonconjugated and conjugated SNPs was mounted on a carbon-coated copper grid, negatively stained with 2% uranyl acetate solution, and dried overnight. Samples were visualized using a Philips Morgagni 268D transmission microscope. Mean SNP size was determined based on $n = 50$ particles. For cryo-TEM analysis, 4 μL of the polymer suspension was adsorbed onto glow-discharged holey carbon-coated grid (Quantifoil, Großlöbichau, Germany), blotted with Whatman filter paper, and vitrified into liquid ethane at −178°C using a vitrobot (FEI Company, Eindhoven, Netherlands). Frozen grids were transferred onto a Philips CM200-FEG electron microscope using a Gatan 626 cryoholder. Electron micrographs were recorded at an accelerating voltage of 200 kV and a nominal magnification of 50 000x, using a low-dose system (10 $e^-/Å^2$) and keeping the sample at −175°C. Defocus values were −4 μm. Micrographs were recorded at 4 K × 4 K CMOS camera (TVIPS, Gauting, Germany). DLS measurements were performed using a Delsa Nano C Particle Sizer (Beckman Coulter, Brea, CA, USA) operated in back scattering mode (165° angle).

2.7. Critical Aggregation Concentration (CAC). To assess the stability of [PP-SNP] upon dilution, the CAC of PEG-*b*-PCL was determined. Pyrene was used as a fluorescent probe as described previously [27, 28]. Pyrene in acetone (0.5 mL, 2.4 × 10^{-6} M) was mixed with 2 mL of Milli-Q water and 0.05, 0.5, 5, 50, or 500 μg/mL of PEG-*b*-PCL. The mixtures were heated to 60°C for 1 h and allowed to cool down to RT. After degasing with N_2, the fluorescence of pyrene was measured (Spectramax M2 plate reader, Molecular Devices, Sunnyvale, CA, USA; excitation: λ_{ex} 332 nm; emission: λ_{em1} 373 nm, λ_{em2} 384 nm). The ratio of $\lambda_{em2}/\lambda_{em1}$ was plotted against the logarithm of the PEG-*b*-PCL concentration to determine the CAC.

2.8. Density Measurements and Specific Volume Calculations. Density of particle suspension was measured at 20°C using an Anton Paar Density Meter DMA 4500 M (Anton Paar GmbH, Graz, Austria). The measured density (g/cm^3) of a suspension containing nanoparticles was used to calculate the apparent specific volume (cm^3/g) of the nanoparticles ($v_{PP\text{-}SNP}$) according to [29]

$$v_{PP\text{-}SNP} = \left(\frac{1}{c_{polymer}}\right)\left(\frac{1}{\rho_{suspension}}\right) - \left(\frac{1 - c_{polymer}}{c_{polymer}}\right)\left(\frac{1}{\rho_{blank}}\right), \quad (1)$$

where $\rho_{suspension}$ is the measured density of the suspension, ρ_{blank} is the measured density of the buffer, and $c_{polymer}$ is the weight fraction of the polymer. The apparent volume (cm^3) of one polymer molecule in the assembled state was calculated according to

$$v_{polymer} \approx \frac{M_w \times v_{PP\text{-}SNP}}{N_A}, \quad (2)$$

where M_w is the molecular weight of the polymer and N_A is the Avogadro constant. The aggregation number (N_{agg}) was then calculated according to

$$N_{agg} \approx \frac{V_{PP\text{-}SNP}}{v_{polymer}} = \frac{(4/3) \times \pi \times (D/2)^3}{v_{polymer}}, \quad (3)$$

where $v_{polymer}$ is the apparent volume of one polymer molecule and $V_{PP\text{-}SNP}$ is the volume of one solid-sphere nanoparticle ([PP-SNP]) and D is the nanoparticle diameter as determined by DLS or TEM measurements.

2.9. Gold Labeling of 83-14 mAb. To visualize conjugated 83-14 mAb, antibodies were stained using an anti-mouse IgG-gold antibody. In brief, 0.25 mg of [PP-SNP]-[mAb] was incubated with 50 μL of the anti-mouse IgG-gold antibody for 1 h at RT. Free anti-mouse IgG-gold antibodies were separated by gel filtration chromatography (Superose 6 prep) eluting with PBS pH 7.4. Samples were negatively stained as described above and were analysed by TEM. To exclude unspecific binding of the anti-mouse IgG-gold antibody, [PP-SNP] was stained using the same protocol.

2.10. Fluorescence Correlation Spectroscopy (FCS). Fluorescence correlation spectroscopy (FCS) was used to determine the number of fluorescently labeled 83-14 mAb per [PP-SNP]-[mAb-DL]. Measurements were performed with an inverted confocal fluorescence laser scanning microscope (Zeiss LSM 510-META/ConfoCor 2; Carl Zeiss AG, Oberkochen, Germany) equipped with an argon laser (488 nm) and a 40x water immersion objective lens (Zeiss C-Apochromat 40x, NA 1.2). 15 μL of sample was measured on a cover glass (Huber & Co AG, Reinach, Switzerland) at RT. Fluorescence intensity fluctuations were analysed in terms of an autocorrelation function. Autocorrelation curves were obtained by taking the average of 10 measurements over 30 s. Diffusion times for free DyLight 488 and DyLight 88-labeled antibodies were independently measured and fixed in the fitting procedure

in order to reduce the number of free fitting parameters. Molecular brightness measurements were used to calculate the number of fluorescently labeled antibodies per [PP-SNP]-[mAb-DL].

2.11. Cell Culture. Immortalized human brain capillary endothelial cells, hCMEC/D3 cells, were obtained under license from the Institut National de la Santé et de la Recherche Médicale, Paris, France. hCMEC/D3 cells were grown in culture flasks coated with 0.1 mg/mL rat tail collagen type I (BD Bioscience, San Jose, CA, USA) and cultured in endothelial cell basal medium (Provitro GmbH, Berlin, Germany) supplemented with 5% fetal bovine serum (FBS; Amimed BioConcept, Allschwil, Switzerland), 1 ng/mL basic fibroblast growth factor (PeproTech, Hamburg, Germany), 5 μg/mL ascorbic acid, 1.4 μM hydrocortisone (Sigma-Aldrich, Schnelldorf, Germany), 10 μL/mL chemically defined lipid concentrate (Gibco Life Technologies, Carlsbad, CA, US), 10 mM HEPES (Sigma-Aldrich, Schnelldorf, Germany), 2 mM GlutaMAX (Gibco Life Technologies, Carlsbad, CA, US), 100 U/mL penicillin, and 100 mg/mL streptomycin (Sigma-Aldrich, Schnelldorf, Germany). Only passages 29 to 35 were used for experiments. Human liver HepG2 cells were kindly provided by Professor Doctor Dietrich von Schweinitz (University Hospital of Basel, Basel, Switzerland). HepG2 cells were cultured in Dulbecco's modified eagle medium (DMEM; Sigma-Aldrich, Schnelldorf, Germany; glucose 4500 g/L) supplemented with 10% FBS, 100 U/mL penicillin, and 100 mg/mL streptomycin.

2.12. MTT Assay. Cell viability was determined using the MTT assay as described previously [22]. Toxicity of [PP-SNP] and [PP-SNP]-[mAb] was tested on the target cell line (hCMEC/D3). In addition, the well-characterized and frequently used human hepatocellular carcinoma cell line HepG2 was used to confirm cell viability results in another cell line and to rule out cell line specific effects. In brief, cells were seeded at a density of 2×10^4/well in a 96-well plate (TPP, Trasadingen, Switzerland) coated with collagen type I (10 μg/cm^2) or poly-D lysine (0.04 mg/mL), respectively. [PP-SNP] and [PP-SNP]-[mAb] were diluted with complete or serum-free culture medium to a final concentration of 0.01–1 mg/mL. PBS concentration was kept constant for all [PP-SNP] concentrations. Cells were washed twice with Dulbecco's phosphate-buffered saline (DPBS) and incubated with particle dilutions for 24 h in triplicate. Terfenadine (20 μM) was taken as positive controls. Cells were washed three times with DPBS and MTT working solution (100 μL, Thiazolyl Blue 5 mg/mL) was added. After 1.5–3 h, MTT working solution was aspirated and resulting formazan crystals were dissolved with DMSO (100 μL) protected from light for 15 min on an orbital shaker at RT. Absorption of dissolved formazan was measured at 570 nm and unspecific signals measured at 670 nm were subtracted (Spectramax M2 plate reader, Molecular Devices, Sunnyvale, CA, USA). Cell viability was expressed as percentage, whereas cell viability of untreated cells was defined as 100%. MTT assays were performed in triplicate and repeated three times. To determine statistical significance, one-way analysis of variance (ANOVA) followed by Tukey's *post hoc* test using OriginPro (Version 9.1.0, OriginLab Corporation, Northampton, MA, USA) was performed.

2.13. Flow Cytometry. To analyse uptake of [PP-SNP]-[mAb-DL] and [PP-SNP-DiI]-[mAb], flow cytometry was used. hCMEC/D3 cells were seeded at a density of 5×10^4 cells/cm^2 in a 12-well plate (TPP, Trasadingen, Switzerland). SNP formulations were diluted with culture medium to a final concentration of 0.1 mg/mL. Cells (80% confluency) were washed with DPBS and incubated with SNPs for 0.25, 0.5, 1, and 2 h. For competitive inhibition, cells were preincubated with a 100x excess of 83-14 mAb for 30 min at 37°C and washed twice with DPBS before incubating with SNPs. Washed cells were detached with 0.25% Trypsin-EDTA (Gibco Life Technologies, Carlsbad, CA, USA) for 3 min at 37°C and Trypsin-reaction was stopped by adding 1 mL of ice-cold DMEM supplemented with 10% FBS. The cell suspension of each well was collected, centrifuged at 200 g for 5 min (4°C), and washed three times with ice-cold DPBS. The pellets were resuspended in 500 μL of staining buffer (DPBS, 0.05% NaN_3, 1% FBS, EDTA 2.5 mM) and analysed by flow cytometry using a FACS Canto II flow cytometer (BD Bioscience, San Jose, CA, USA). Excitation wavelength was 488 nm and 561 nm. Cell doublets were excluded from analysis. The green fluorescence of DyLight 488 was detected using a 530/30 bandpass filter; the red fluorescence of DiI was detected using a 586/15 bandpass filter. Signals from 10 000–20 000 cells were normalised to max and analysed using FlowJo analysis software version V9/X (Tree-Star, Ashland, OR, USA). One-way analysis of variance (ANOVA) followed by Tukey's *post hoc* test using OriginPro (Version 9.1.0, OriginLab Corporation, Northampton, MA, USA) was performed to determine statistical significance.

2.14. Confocal Laser Scanning Microscopy (CLSM). Glass coverslips were placed in a 12-well plate and were coated with collagen (10 μg/cm^2). hCMEC/D3 cells were seeded at a density of 2.5×10^4 cells/cm^2 and allowed to adhere overnight. Level of confluency was 70–80%. Cells were washed with DPBS twice and incubated with [PP-SNP]-[mAb-DL], [PP-SNP-DiI], or [PP-SNP-DiI]-[mAb] (0.1 mg/mL) for 30 and 60 min at 37°C. Cell nuclei were stained by adding Hoechst 33342 dye (Eugene, OR, USA; 0.2 μg/mL) for 10 min. Cells were washed three times with ice-cold DPBS and fixed with freshly prepared paraformaldehyde (4%) for 15 min at 4°C. Paraformaldehyde was removed by washing three times with ice-cold DPBS; then cells were mounted with Prolong-Gold (Thermo Fisher Scientific, Waltham, MA, USA). Cells were analysed using an Olympus FV 1000 inverted laser scanning microscope and 40x (NA 1.30) and 60x (NA 1.40) oil immersion objectives (Olympus, Tokyo, Japan).

2.15. Transmission Electron Microscopy (TEM). Transwell polycarbonate membrane inserts (Corning, Baar, Switzerland; 0.4 μm pore size, 12 mm insert diameter) were coated with collagen type I (10 μg/cm^2) for 1 h at 37°C. Filters

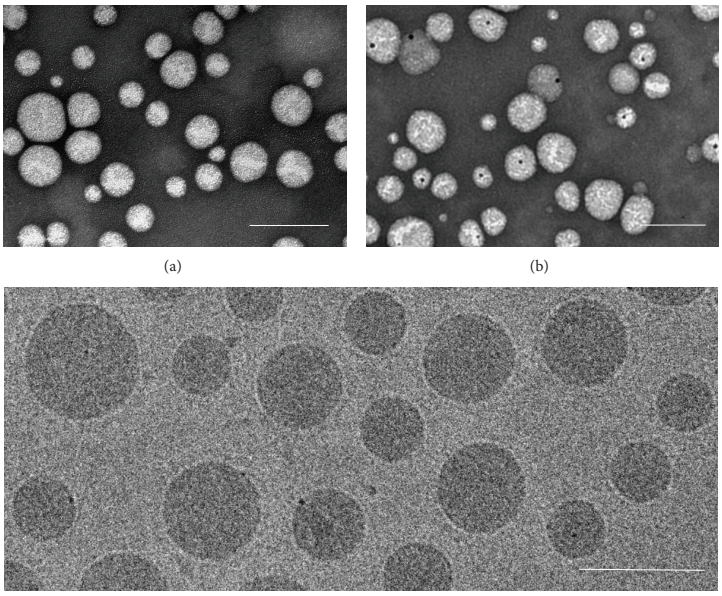

Figure 1: Transmission electron microscope (TEM) images of PEG-*b*-PCL nanoparticles ([PP-SNP]). (a) TEM images [PP-SNP]. Size bar: 200 nm. (b) TEM image of gold-nanohybrid [PP-SNP] ([PP-SNP-Au]). Size bar: 200 nm. (c) Cryo-TEM images of [PP-SNP]. Size bar: 100 nm.

were washed twice with DPBS and hCMECM/D3 cells were seeded at a density of 5×10^4 cells/cm^2. Cells were grown to confluency for 8 days; medium was exchanged at days 4 and 7. At day 8, hCMEC/D3 cells were incubated with colloidal gold-loaded [PP-SNP-Au]-[mAb] at a final concentration of 0.1 mg/mL on the apical side for 0.25, 0.5, 1, 2, and 4 h. Cells were incubated with fixing medium (3% formaldehyde, 0.3% glutaraldehyde) at 4°C overnight. Cells were carefully rinsed three times with Hepes buffer (0.5 M, pH 7.0) and dehydrated using methanol. hCMEC/D3 cells were infiltrated with LR-Gold (PolyScience, Warrington, PA, USA) according to the manufacturer's instructions. The filter membrane was removed from the transwell insert using a scalpel. Membrane cuts were placed on a polymerized drop of resin in a plastic flat embedding mold and covered with a fresh resin. Polymerization was induced by UV-light at −10°C for 24 h. Sections of 70 nm were cut and collected on a carbon-coated Ni-grids and stained with uranyl acetate (2%) for 15 min and with lead citrate (Reynold's solution) for 2 min. Sections were analysed using a Philips CM 100 TEM.

3. Results

3.1. Characterization. TEM micrographs of [PP-SNP] showed spherical particles with a homogenous size distribution (Figure 1(a)). Mean diameter of $n = 50$ particles determined by TEM was 67 ± 15 nm. Size and size distribution of [PP-SNP] were confirmed by DLS. A mean hydrodynamic diameter of 78.2 ± 1.7 nm and a narrow size distribution (0.069 ± 0.021) were determined (Table 1). The zeta potential was −4.13 ± 0.24 (Table 1). In buffer (PBS, pH 7.4, room temperature), [PP-SNP] was stable for at least 2 months as shown by a constant particle size and a PDI below 0.2. To characterize the core structure of the NPs, cryo-TEM was performed. In cryo-TEM, a well-defined membrane can be observed for polymersomes, while no such structure is visible in micelles and solid-sphere NPs [30]. No membrane was observed in micrographs of [PP-SNP] as shown in Figure 1(c), indicating the solid-sphere structure of [PP-SNP]. Therefore, these particles were

Table 1: Comparison of nonconjugated PEG-*b*-PCL SNPs ([PP-SNP]) and targeted [PP-SNP]-[mAb]. [PP-SNP] and [PP-SNP]-[mAb] were analysed and the hydrodynamic diameter, polydispersity index (PDI), zeta potential, morphology, and the number of antibodies per NP (mAb/NP ratio) were compared ($n = 3$ experiments; values are means ± S.E.M).

	[PP-SNP]	[PP-SNP]-[mAb]
Hydrodynamic diameter (nm)	78.2 ± 1.7	79.9 ± 2.4
PDI	0.069 ± 0.021	0.079 ± 0.021
Zeta potential (mV)	−4.13 ± 0.24	2.43 ± 0.16
Morphology	Spherical	Spherical
mAb/NP ratio	—	5

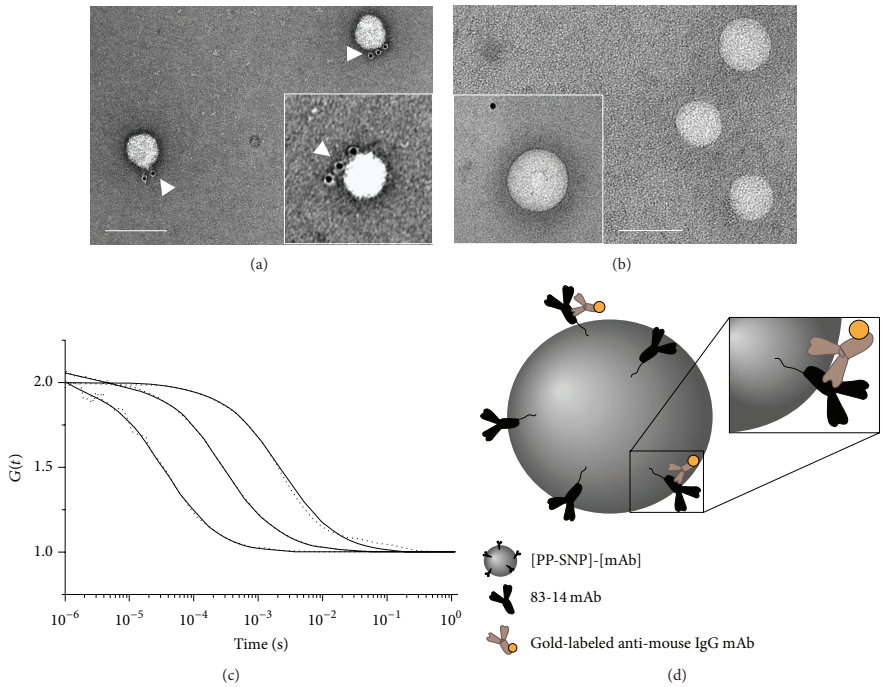

Figure 2: Determination of the mAb/NP ratio by transmission electron microsopy and fluorescence correlation spectroscopy. ((a) and (b)) Visualization of 83-14 mAb using a 5 nm colloidal gold-labeled anti-mouse IgG monoclonal antibody (white arrows). (a) PEG-*b*-PCL solid-sphere nanoparticles [PP-SNP] covalently conjugated to 83-14 mAb ([PP-SNP]-[mAb]). (b) Nonmodified [PP-SNP] after control incubation with gold-labeled anti-mouse IgG mAb (secondary mAb only). Size bar: 100 nm; insert: 2x magnification of a single NP and a noninteracting gold-labeled secondary antibody before purification. (c) FCS analysis of PEG-*b*-PCL SNPs conjugated to DyLight 488-labeled 83-14 mAb ([PP-SNP]-[mAb-DL]). Dotted line: free DyLight 488; dot-dashed line: DyLight 488-labeled 83-14 mAb; dashed line: [PP-SNP]-[mAb-DL]; solid lines: normalized autocorrelation curves. (d) Schematic drawing of [PP-SNP]-[mAb] incubated with colloidal gold-labeled anti-mouse IgG mAb.

classified as solid-sphere nanoparticles (SNPs). The CAC was determined using a hydrophobic fluorescent probe [27, 28]. By this technique, changes in fluorescence characteristics of fluorescent dyes, induced by their environment, are analysed. Thus, lipophilic dyes will be redistributed to the hydrophobic PCL-core of [PP-SNP] at concentrations above the CAC. The CAC of PEG-*b*-PCL determined by pyrene encapsulation during this study was 5 μg/mL (2.8×10^{-7} M). In this study, *in vitro* cell uptake experiments were always performed at 0.1 mg/mL, a concentration that is about 20 times higher than the determined CAC. The specific volume $v_{\text{PP-SNP}}$ of the [PP-SNP] suspension was determined to be 0.87 ± 0.01 cm^3/g.

3.2. Functionalization. To covalently conjugate 83-14 mAb to [PP-SNP], a PEG-spaced heterobifunctional linker was used. The linker was reactive towards primary amines (i.e., NH_2-PEG-*b*-PCL as a constituent of [PP-SNP]) and sulfhydryl groups (i.e., thiolated 83-14 mAb). FCS was used to quantify the number of fluorescently labeled antibodies per [PP-SNP]-[mAb-DL]. Figure 2(c) shows the normalized autocorrelation curves of free DyLight 488 dye, DyLight 488-labeled 83-14 mAb ([mAb-DL]), and [PP-SNP] conjugated to DyLight-labeled mAbs ([PP-SNP]-[mAb-DL]). Diffusion times for [mAb-DL] and [PP-SNP]-[mAb-DL] were 282 μs and 2594 μs. The increase in the diffusion times observed indicated the immobilization of [mAb-DL] on [PP-SNP]-[mAb-DL]. The mAb/NP ratio was determined by comparing the mean molecular brightness (CPM) of [PP-SNP]-[mAb-DL] (CPM = 85 kHz) to [mAb-DL] (CPM = 17 kHz). The CPM of [PP-SNP]-[mAb-DL] was 5x higher than the CPM of [mAb-DL]. Therefore, on average, 5 antibodies were conjugated to one [PP-SNP]-[mAb-DL]. Covalently attached 83-14 mAb to the surface of SNPs was furthermore visualised by TEM. Schematic drawing is shown in Figure 2(d). [PP-SNP]-[mAb] was incubated with a gold-labeled secondary mAb directed towards murine IgGs to visualize 83-14 mAb (Figure 2(a)). Gold particles were located in close proximity to the [PP-SNP]-[mAb] surface confirming 83-14 mAb presence

and accessibility. When nonfunctionalized [PP-SNP] was stained according to the same protocol, gold particles were not immobilized on SNP surface before (Figure 2(b) insert) and after purification using gel filtration chromatography (Figure 2(b)). This result indicates specific binding of the secondary mAb.

3.3. Toxicity. SNPs composed of the FDA-approved, biodegradable PEG-*b*-PCL show high biocompatibility [21, 31]. This is particularly important with respect to brain delivery of SNPs since accumulation of polymeric material could lead to toxic side effects within the CNS. To confirm these findings, hCMEC/D3 cells and a human hepatocellular carcinoma cell line (HepG2) were incubated with [PP-SNP] and [PP-SNP]-[mAb] (0.01–1 mg/mL) to analyse cell viability using the MTT assay. Even high polymer concentrations of up to 1 mg/mL caused only a slight decrease in cell viability. Uptake experiments were performed with 0.1 mg/mL PEG-*b*-PCL. This concentration does not show any significant cytotoxic effects on HepG2 and hCMEC/D3 cells.

3.4. Uptake. To study cellular uptake, hCMEC/D3 cells were incubated with [PP-SNP-DiI]-[mAb] or [PP-SNP-DiI] for 30 and 60 min and analysed using flow cytometry. Mean fluorescence intensity (MFI) increased in a time dependent manner (Figure 4). A representative flow cytometry graph is shown in Figure 5(b). For cells incubated with nonmodified [PP-SNP-DiI], increase in MFI of 7.7 ± 1.6 and 21.2 ± 4.3 was observed after 30 min and 1 h of incubation as compared to blank control cells. When cells were incubated with [PP-SNP-DiI]-[mAb], a significant increase in MFI was observed. A 2x increase in MFI was observed after 30 min (MFI = 16.3 ± 1.6) and 1 h (MFI = 38.9 ± 6.7) as compared to cells incubated with their nonmodified counterparts (Figure 4). [PP-SNP-DiI]-[mAb]-uptake could be inhibited competitively by preincubating the cells with an excess of free, unlabeled 83-14 mAb (MFI = 26.3 ± 4.8) as shown in Figures 4 and 5(b). To confirm these findings, the experiments were repeated using an alternative labeling method for the NPs. 83-14 mAb covalently labeled with DyLight 488 was conjugated to [PP-SNP] ([PP-SNP]-[mAb-DL]). Again, MFI decreased and was close to untreated control cells when cellular uptake was competitively inhibited (Figure 5(a)). In addition, SNP uptake by hCMEC/D3 cells was analysed using CLSM (Figure 5(c)). hCMEC/D3 cells were incubated with 0.1 mg/mL of [PP-SNP-DiI] or [PP-SNP-DiI]-[mAb] for 30 min. Distinct fluorescence signals (red dots) were observed close to the cell nuclei in the DiI-channel. Competitive inhibition reduced the [PP-SNP-DiI]-[mAb] signal. To study the intracellular localization of SNPs, gold-nanohybrids functionalized with 83-14 mAb ([PP-SNP-Au]-[mAb]) were prepared. Using such gold-nanohybrids, intracellular trafficking could be visualised by electron microscopy as a result of the high electron density of the Au-core whereas morphology, size, and PDI of [PP-SNP-Au] are similar to [PP-NP] (Figures 1(b) and 6(d)). Encapsulated gold NPs have a diameter of 14.1 ± 3.1 nm as shown previously [26]. Intracellular vesicles with [PP-SNP-Au]-[mAb] were observed after 15 min (Figures 6(a)–6(c)). After 60 min of incubation, [PP-SNP-Au]-[mAb] was detected in multivesicular bodies (MVBs; Figure 7).

4. Discussion

In this study, PEG-*b*-PCL diblock copolymer was used to produce a nanosized drug delivery system. SNPs were prepared using the cosolvent method at a final concentration of 5.3 mg/mL polymer. Particles assembled immediately after stirring at 700 rpm and adding PBS dropwise. This method is easy to handle, fast, and highly reproducible and uses no expensive or complex equipment. A fast preparation protocol is of huge advantage for different applications, for example, for scale-up or when radiolabeled NPs are prepared for pharmacokinetics studies. To target the NPs towards a specific tissue or cell type, ligands have to be attached to the NP surface. Different strategies can be used for such modifications. Since different classes of targeting moieties (e.g., mAbs, peptides, or small molecules) may require different conjugation strategies, a universal coupling tool is advantageous. Therefore, 5% mol/mol of amine-terminated PEG-*b*-PCL (NH_2-PEG-*b*-PCL) was used to covalently couple targeting moieties to [PP-SNP] by using the heterobifunctional linker $SM(PEG)_n$. $SM(PEG)_n$ contains an amine-reactive NHS ester functionality and maleimide that reacts to a metabolically stable thioether in the presence of sulfhydryl groups. A PEG-spacer of variable length links the two reactive groups. While a very low degree of functionalization was observed using $SM(PEG)_2$ with a spacer length of 17.6 Å, conjugation with 24 PEG-subunit long $SM(PEG)_{24}$ (spacer length: 95.2 Å) resulted in an increased mAb/NP ratio per [PP-SNP]-[mAb] using the same reaction conditions. Furthermore, PEG-spacers also can prevent the covalently attached mAb from being covered by particle-adsorbed biomolecules [32]. FCS was used to determine the mAb/NP ratio. On average, 5 molecules of fluorescently labeled 83-14 mAb were conjugated to the surface of one [PP-SNP]-[mAb-DL] (Figure 2(c)). FCS was used similarly in previous studies to determine the amount of fluorescently labeled molecules on SNPs [13, 33]. Radiolabeling, as typically used for the quantification of antibodies per NP, can be avoided by using FCS [34]. The number of targeting moieties on the NP surface influences the interaction with the target cell and can promote cellular uptake but may lead to increased clearance from the blood circulation [35]. In addition, a defined and narrow size distribution and the surface charge are important determinants for the fate of nanoparticles upon systemic exposure. NPs with a size below 6 nm can easily be excreted by renal filtration, while NPs with >300 nm in diameter or with a high surface charge will be recognized and removed by the reticuloendothelial system [36, 37]. Noncharged, pegylated NPs with a diameter below 200 nm show reduced protein opsonisation and remain in the systemic circulation for hours [38].

In cryo-TEM micrographs, no membrane was observed for [PP-SNP] indicating a solid-sphere structure of [PP-SNP] (Figure 1(c)). In comparison to low-molecular weight surfactants, SNPs show a low CAC, which is important for stability and drug retention. A high CAC can lead to a micelle collapse and subsequent burst release of the incorporated

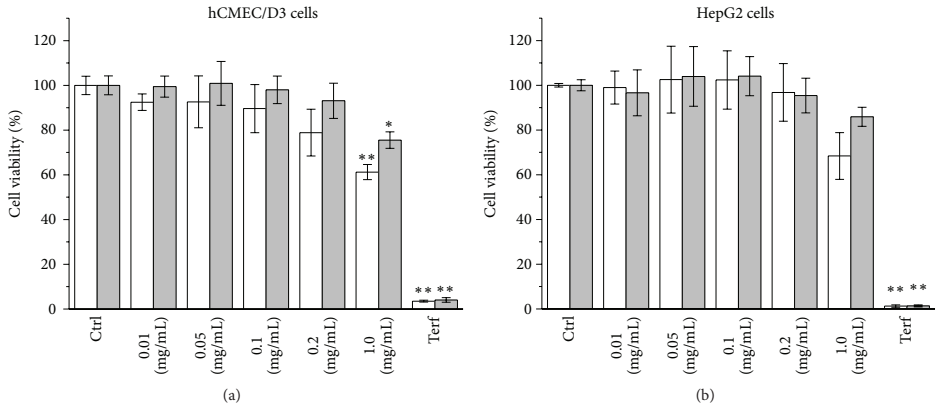

Figure 3: Cell viability of hCMEC/D3 and HepG2. hCMEC/D3 and HepG2 cells were incubated with 0.01–1.0 mg/mL PEG-*b*-PCL solid-sphere nanoparticles ([PP-SNP]) and 83-14 mAb modified [PP-SNP] ([PP-SNP]-[mAb]). Cell viability was analysed using the MTT assay 24 h after incubation. Cell viability is expressed as % viable cells compared to untreated control cells. Terfenadine (Terf) was used as positive control. White bars: [PP-SNP]-[mAb]; grey bars: [PP-SNP]. ANOVA and Tukey's *post hoc* means comparison was used to test for statistical significance ($n = 3$ experiments; $^{**}p < 0.05$; $^{*}p < 0.1$; S.E.M. is shown with error bars).

drug upon dilution in the blood compartment [10, 39]. Whereas typical low-molecular weight surfactants have CAC values in the range of 10^{-3}–10^{-4} M, CACs of diblock polymers can typically be found in range 10^{-6}–10^{-7} M. Additionally, the kinetic stability of the core structure of SNPs is high and thus the disassembly of SNPs after dilution below the CAC occurs slowly allowing an efficient retention of their drug payload [40]. The CAC of [PP-SNP] was determined using a fluorescent probe-based approach as described previously [28]. The CAC of PEG-*b*-PCL is 5 μg/mL (2.8×10^{-7} M), comparable to previously published data characterizing similar polymers [27].

The apparent specific volume $v_{\text{PP-SNP}}$ of the [PP-SNP] suspension was calculated from the measured density as described by Sommer et al. [29]. $v_{\text{PP-SNP}}$ was 0.87±0.01 cm^3/g, which is close to the specific volume determined for micelles formed by the PEG-derived nonionic surfactant "Brij" [29]. Using this result, one can calculate the apparent volume of a single PEG-*b*-PCL polymer molecule (v_{polymer}) according to (2). In our experiment, v_{polymer} was 51 nm^3. The aggregation number (N_{agg}) of [PP-SNP] can then be estimated according to (3). A similar approach using apparent volumes to calculate aggregation numbers was proposed previously to determine N_{agg} of NPs consisting of a cell-penetrating peptide [41]. Since this calculation depends on the diameter of the particle, N_{agg} covers a range of ~2200 to ~10 000 for [PP-SNP] with diameters of 60 to 100 nm, respectively. These numbers are higher than results obtained by, for example, static light scattering (SLS) or fluorescent techniques where typical N_{agg} for diblock copolymer micelles are lower than 1000 [42, 43].

Among the broad range of polymer-based DDS, NPs composed of the FDA-approved, biodegradable PEG-*b*-PCL show high biocompatibility [21, 31, 44]. This is an important advantage regarding organ delivery of NPs since accumulation of polymeric material might lead to toxic side effects, for example, in the CNS. Because toxic effects of polymeric NPs on cells are driven not only by the polymeric material but also by many other characteristics including particle size, charge, or impurities, each NP formulation needs to be tested [45]. Toxicity of [PP-SNP] and [PP-SNP]-[mAb] on hCMEC/D3 cells was tested using the MTT assay. [PP-SNP] induced only a slight decrease in cell viability on hCMEC/D3 cells if incubated in concentrations up to 0.2 mg/mL (Figure 3). Cells incubated with [PP-SNP]-[mAb] showed as well a high cell viability. Even at high concentrations of 1 mg/mL, more than 60% of the incubated cells were viable. For cellular uptake experiments performed in this work, a concentration of 0.1 mg/mL was used. At this concentration the decrease in cell viability was negligible. The MTT assay was repeated with a second cell line to confirm the biocompatibility of the nanoparticles and to rule out cell line specific effects. The human hepatocellular carcinoma derived cell line HepG2 was used. Again, only a slight decrease in cell viability was observed (Figure 3). We conclude from these experiments that PEG-*b*-PCL SNPs are well tolerated within a typical dose range used in nanomedicine [22].

[PP-SNP-DiI]-[mAb] was taken up by hCMEC/D3 cells. These cells express similar HIR protein levels as freshly isolated hBMECs (1 fmol HIR/μg protein) and were therefore successfully used as an *in vitro* targeting model in previous studies [13, 46–48]. A time dependent increase in the fluorescence signal was observed (Figure 4). Conjugation with 83-14 mAb leads to an increase in MFI. Furthermore, uptake was specific and mediated by the 83-14 mAb since competition for the target receptor (HIR) with free mAb leads to a decrease of intracellular fluorescence (Figures 4

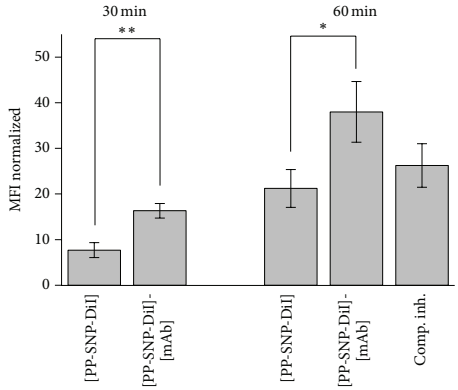

Figure 4: Uptake of PEG-*b*-PCL nanoparticles ([PP-SNP]) by hCMEC/D3 cells. Uptake of DiI-loaded PEG-*b*-PCL solid-sphere nanoparticles ([PP-SNP-DiI]) and 83-14 modified [PP-SNP-DiI] ([PP-SNP-DiI]-[mAb]) by hCMEC/D3 cells. Cells were incubated with SNPs for 30 min or 1 h and cellular uptake was analysed by flow cytometry. Mean fluorescence intensity (MFI) was normalized to untreated control cells. ANOVA and Tukey's *post hoc* means comparison was used to test for statistical significance ($n = 3$ experiments; $^{**}P < 0.05$; $^{*}P < 0.1$; S.E.M. is shown with error bars).

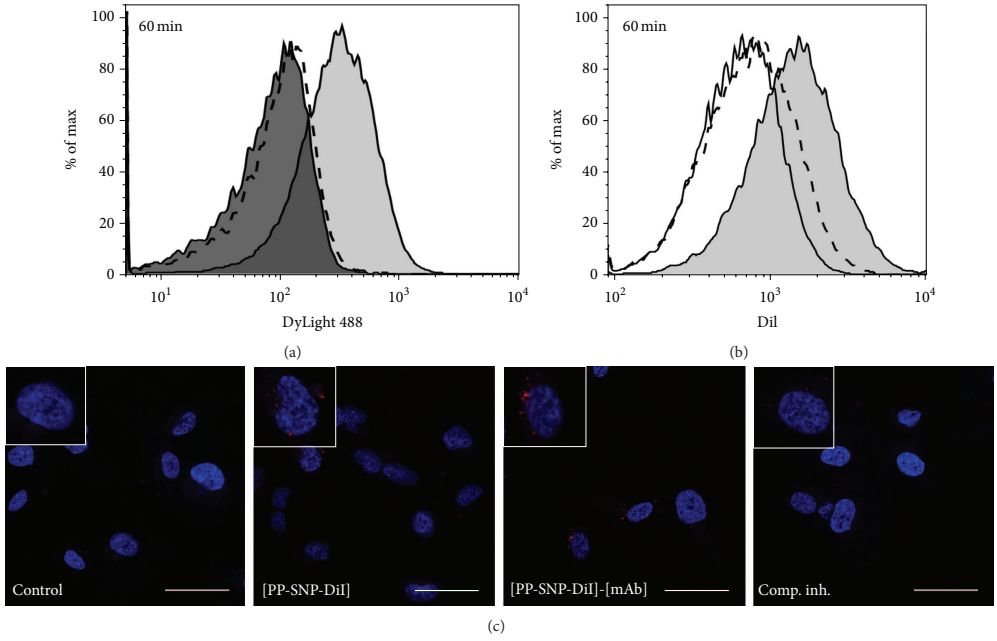

Figure 5: Cellular uptake of PEG-*b*-PCL nanoparticles ([PP-SNP]) analysed by flow cytometry and confocal laser scanning microscopy (CLSM). (a) Flow cytometry analysis of uptake of [PP-SNP] conjugated to DyLight 488-labeled 83-14 mAb ([PP-SNP]-[mAb-DL]) by hCMEC/D3 cells. Dark grey shaded: untreated cells; light grey shaded: cells incubated with [PP-SNP]-[mAb-DL] for 1 h; dashed line: cells incubated with [PP-SNP]-[mAb-DL] in the presence of a 100x excess of unlabeled 83-14 mAb. (b) Flow cytometry analysis of cellular uptake (hCMEC/D3) of DiI-loaded [PP-SNP] ([PP-SNP-DiI]) and 83-14 mAb modified [PP-SNP-DiI] ([PP-SNP-DiI]-[mAb]) after 1 h of incubation. Solid line: [PP-SNP-DiI]; dashed line: cells incubated with [PP-SNP-DiI]-[mAb] in the presence of a 100x excess of unlabeled 83-14 mAb; light grey shaded: [PP-SNP-DiI]-[mAb]. (c) Cellular uptake of [PP-SNP-DiI] and [PP-SNP-DiI]-[mAb] analysed by confocal laser scanning microscopy. Blue: nuclei stained with Hoechst 33342; red: [PP-SNP-DiI]-[mAb]. Size bar: 40 μm. Single-cell inserts: 2x magnification.

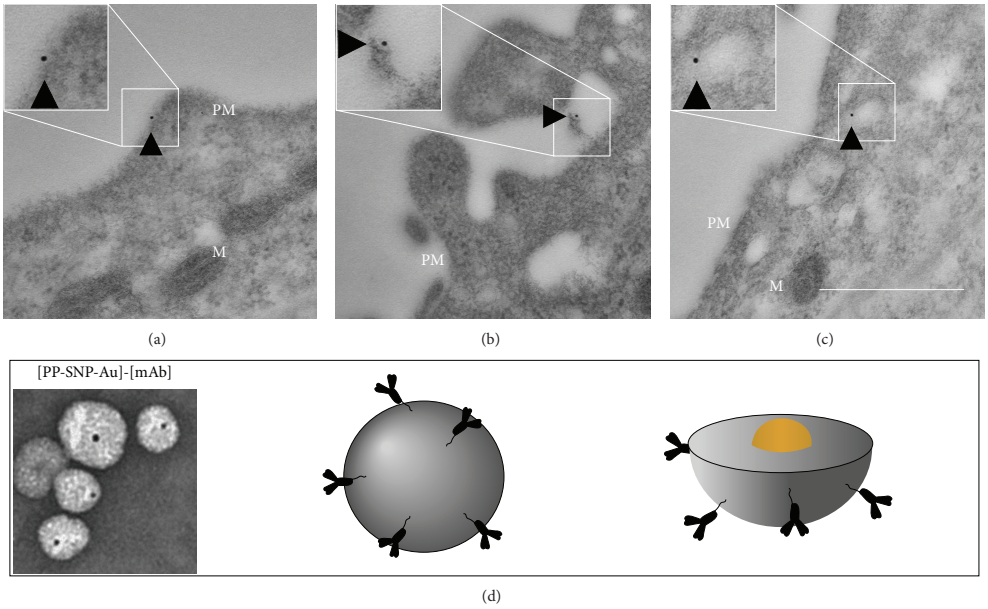

Figure 6: Uptake of gold-nanohybrid PEG-*b*-PCL nanoparticles conjugated to 83-14 mAb ([PP-SNP-Au]-[mAb]). ((a)–(c)) hCMEC/D3 cells were incubated with [PP-SNP-Au]-[mAb] for 15 min. Black arrows: gold particles; PM: plasma membrane; M: mitochondria. Size bar: 500 nm. (d) TEM image and schematic drawing of [PP-SNP-Au]-[mAb].

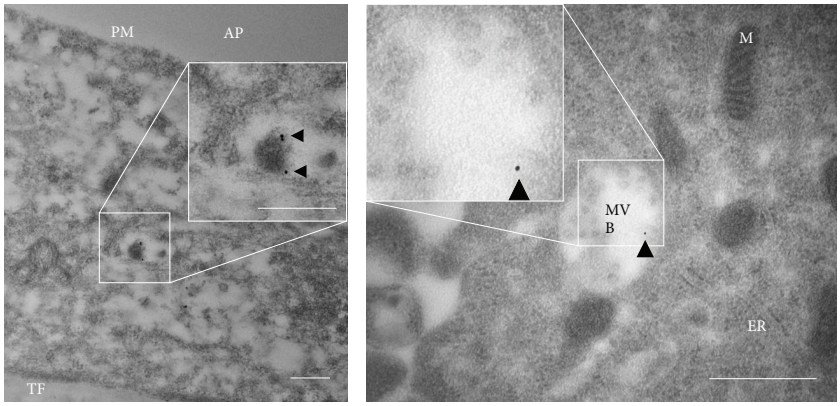

Figure 7: Intracellular localization of gold-nanohybrid PEG-*b*-PCL SNPs conjugated to 83-14 mAb ([PP-SNP-Au]-[mAb]). hCMEC/D3 cells were incubated with [PP-SNP-Au]-[mAb] for 60 min. (a) Cross section of a cell grown on a transwell insert. Size bar: 250 nm. Black arrows: gold particles. (b) [PP-SNP-Au]-[mAb] localized within a multivesicular body (MVB). Black arrows: gold particles; AP: apical compartment; PM: plasma membrane; TF: transwell filter membrane; M: mitochondria; ER: endoplasmic reticulum; MVB: multivesicular body. Size bar: 500 nm.

and 5). Immunoelectron transmission microscopy was used to study the subcellular localization of [PP-SNP-Au]-[mAb]. SNPs were visualized by a preembedding staining technique. To this end, a protocol to prepare gold-nanohybrids ([PP-SNP-Au]) was developed by our group [26]. This opens attractive possibilities to monitor intracellular trafficking of SNPs. hCMEC/D3 cells were grown on transwell inserts for 8 days as it was reported that hCMEC/D3 cells grown under these conditions show BBB characteristics and develop cell polarity [49]. This was furthermore demonstrated by their use for quantitative drug transport studies and qualitative analysis of albumin-gold-conjugates by TEM [50, 51]. [PP-SNP-Au]-[mAb] targeting the HIR was found in intracellular vesicles after 15 min of incubation at 37°C (Figure 6(c)). Accumulation in multivesicular bodies (MVBs) was detected after 60 min of incubation (Figure 7). Cellular uptake of gold-labeled insulin was studied previously using retinal vascular endothelial cells. It was shown that insulin was taken up fast and efficiently and accumulated in MVBs after 30 min of incubation [52]. However, cellular uptake of insulin seems to be faster and more efficient as compared to [PP-SNP-Au]-[mAb]. Similarly, previous studies using OX-26-immunoliposomes targeting the transferrin receptor showed that size is a crucial factor with respect to cellular uptake kinetics and efficiency. The permeability surface area product, a factor describing the BBB permeability, of the free OX-26 mAb was significantly higher as compared to the immunoliposomes *in vivo* [53]. In the present study, single colloidal gold particles were detected at all time-points, indicating that gold particles were taken up while incorporated into [PP-SNP-Au]-[mAb]. Free colloidal gold particles prepared without PEG-*b*-PCL agglomerated very fast and were found as clusters of particles when analysed by TEM [26]. To the best of our knowledge, this is the first study using gold-loaded targeted polymeric SNPs to visualize their uptake in a cell-based model. Further experiments such as quantitative *in vitro* transport studies and colocalization studies by fluorescent imaging, as performed previously, could help to identify the uptake mechanism of 83-14 modified SNPs [13, 54–56].

5. Conclusion

SNPs of the biodegradable diblock copolymer PEG-*b*-PCL were prepared and characterized *in vitro*. Our SNPs are characterized by a hydrodynamic diameter of 79.6 nm, a homogeneous size distribution, a slightly negative zeta potential, and a low CAC in the submicromolar range. In second step, [PP-SNP] was conjugated to anti-HIR mAb to enhance the cellular uptake by hCMEC/D3 cells. This resulted in targeted [PP-SNP]-[mAb] decorated with 5 molecules of mAb per SNP. [PP-SNP]-[mAb] was taken up by human BBB endothelial cells *in vitro* as shown by confocal microscopy and flow cytometry. Furthermore, the intracellular localization of gold-nanohybrids [PP-SNP-Au]-[mAb] in hCMEC/D3 cells grown on transwell inserts was analysed by TEM. Accumulation in multivesicular bodies of target cells was observed after 60 min of incubation. A similar behaviour was described for gold-labeled insulin [52]. Our *in vitro* data suggest that SNPs consisting of PEG-*b*-PCL are well tolerated. They are promising candidates for the implementation of a targeted drug delivery strategy. Further experiments will be needed to explore their potential in experimental animals.

Competing Interests

The authors report no conflicts of interest.

Acknowledgments

The authors wish to acknowledge Dr. Mohamed Chami and C-CINA (Center for Cellular Imaging and NanoAnalytics; Biozentrum, University of Basel) for acquiring cryo-TEM micrographs of [PP-SNP]; Dr. Timothy Sharpe (Head of Biophysics Facility, Biozentrum University of Basel) for his scientific advices; Dr. Susanne Schenk (Department of Pharmaceutical Sciences, University of Basel) for her scientific input during the project; and the Microscopy Center of the University of Basel for their support with electron microscopy. Cristina Prescianotto-Baschong received support from Grant 31003A-125423, awarded to Professor Dr. Martin Spiess (Biozentrum University of Basel) by the Swiss National Science Foundation.

References

[1] D. J. Begley, "Delivery of therapeutic agents to the central nervous system: the problems and the possibilities," *Pharmacology & Therapeutics*, vol. 104, no. 1, pp. 29–45, 2004.

[2] W. M. Pardridge, "Drug targeting to the brain," *Pharmaceutical Research*, vol. 24, no. 9, pp. 1733–1744, 2007.

[3] C.-T. Lu, Y.-Z. Zhao, H. L. Wong, J. Cai, L. Peng, and X.-Q. Tian, "Current approaches to enhance CNS delivery of drugs across the brain barriers," *International Journal of Nanomedicine*, vol. 9, no. 1, pp. 2241–2257, 2014.

[4] K. R. Duffy and W. M. Pardridge, "Blood-brain barrier transcytosis of insulin in developing rabbits," *Brain Research*, vol. 420, no. 1, pp. 32–38, 1987.

[5] W. M. Pardridge, J. Eisenberg, and J. Yang, "Human blood—brain barrier insulin receptor," *Journal of Neurochemistry*, vol. 44, no. 6, pp. 1771–1778, 1985.

[6] W. M. Pardridge, J. Eisenberg, and J. Yang, "Human blood-brain barrier transferrin receptor," *Metabolism*, vol. 36, no. 9, pp. 892–895, 1987.

[7] R. J. Boado, J. Z. Lu, E. K.-W. Hui, and W. M. Pardridge, "Insulin receptor antibody-sulfamidase fusion protein penetrates the primate blood-brain barrier and reduces glycosoaminoglycans in sanfilippo type A cells," *Molecular Pharmaceutics*, vol. 11, no. 8, pp. 2928–2934, 2014.

[8] A. Wicki, D. Witzigmann, V. Balasubramanian, and J. Huwyler, "Nanomedicine in cancer therapy: challenges, opportunities, and clinical applications," *Journal of Controlled Release*, vol. 200, pp. 138–157, 2015.

[9] W. Chen, F. Meng, R. Cheng, C. Deng, J. Feijen, and Z. Zhong, "Advanced drug and gene delivery systems based on functional biodegradable polycarbonates and copolymers," *Journal of Controlled Release*, vol. 190, pp. 398–414, 2014.

[10] G. Gaucher, M.-H. Dufresne, V. P. Sant, N. Kang, D. Maysinger, and J.-C. Leroux, "Block copolymer micelles: preparation,

characterization and application in drug delivery," *Journal of Controlled Release*, vol. 109, no. 1–3, pp. 169–188, 2005.

[11] V. P. Torchilin, "Polymer-coated long-circulating microparticulate pharmaceuticals," *Journal of Microencapsulation*, vol. 15, no. 1, pp. 1–19, 1998.

[12] Z. Pang, W. Lu, H. Gao et al., "Preparation and brain delivery property of biodegradable polymersomes conjugated with OX26," *Journal of Controlled Release*, vol. 128, no. 2, pp. 120–127, 2008.

[13] L.-H. Dieu, D. Wu, C. G. Palivan, V. Balasubramanian, and J. Huwyler, "Polymersomes conjugated to 83-14 monoclonal antibodies: *in vitro* targeting of brain capillary endothelial cells," *European Journal of Pharmaceutics and Biopharmaceutics*, vol. 88, no. 2, pp. 316–324, 2014.

[14] L. R. Walus, W. M. Pardridge, R. M. Starzyk, and P. M. Friden, "Enhanced uptake of rsCD4 across the rodent and primate blood-brain barrier after conjugation to anti-transferrin receptor antibodies," *Journal of Pharmacology and Experimental Therapeutics*, vol. 277, no. 2, pp. 1067–1075, 1996.

[15] D. Wu, J. Yang, and W. M. Pardridge, "Drug targeting of a peptide radiopharmaceutical through the primate blood-brain barrier in vivo with a monoclonal antibody to the human insulin receptor," *The Journal of Clinical Investigation*, vol. 100, no. 7, pp. 1804–1812, 1997.

[16] C. Nardin, M. Winterhalter, and W. Meier, "Giant free-standing ABA triblock copolymer membranes," *Langmuir*, vol. 16, no. 20, pp. 7708–7712, 2000.

[17] C.-Y. Huang and Y.-D. Lee, "Core-shell type of nanoparticles composed of poly[(n-butyl cyanoacrylate)-co-(2-octyl cyanoacrylate)] copolymers for drug delivery application: synthesis, characterization and *in vitro* degradation," *International Journal of Pharmaceutics*, vol. 325, no. 1-2, pp. 132–139, 2006.

[18] H. Liu, E. B. Slamovich, and T. J. Webster, "Less harmful acidic degradation of poly (lactic-co-glycolic acid) bone tissue engineering scaffolds through titania nanoparticle addition," *International Journal of Nanomedicine*, vol. 1, no. 4, pp. 541–545, 2006.

[19] G. C. Baltazar, S. Guha, W. Lu et al., "Acidic nanoparticles are trafficked to lysosomes and restore an acidic lysosomal pH and degradative function to compromised ARPE-19 cells," *PLoS ONE*, vol. 7, no. 12, Article ID e49635, 2012.

[20] F. Danhier, E. Ansorena, J. M. Silva, R. Coco, A. Le Breton, and V. Préat, "PLGA-based nanoparticles: an overview of biomedical applications," *Journal of Controlled Release*, vol. 161, no. 2, pp. 505–522, 2012.

[21] X. Wei, C. Gong, M. Gou et al., "Biodegradable poly(ε-caprolactone)-poly(ethylene glycol) copolymers as drug delivery system," *International Journal of Pharmaceutics*, vol. 381, no. 1, pp. 1–18, 2009.

[22] H. Kettiger, D. Sen Karaman, L. Schiesser, J. M. Rosenholm, and J. Huwyler, "Comparative safety evaluation of silica-based particles," *Toxicology in Vitro*, vol. 30, no. 1, pp. 355–363, 2015.

[23] R. Bleul, R. Thiermann, and M. Maskos, "Techniques to control polymersome size," *Macromolecules*, vol. 48, no. 20, pp. 7396–7409, 2015.

[24] X. Shuai, H. Ai, N. Nasongkla, S. Kim, and J. Gao, "Micellar carriers based on block copolymers of poly(ε-caprolactone) and poly(ethylene glycol) for doxorubicin delivery," *Journal of Controlled Release*, vol. 98, no. 3, pp. 415–426, 2004.

[25] I. Kim, S. A. Mckenna, E. V. Puglisi, and J. D. Puglisi, "Rapid purification of RNAs using fast performance liquid chromatography (FPLC)," *RNA*, vol. 13, no. 2, pp. 289–294, 2007.

[26] D. Witzigmann, S. Sieber, F. Porta et al., "Formation of lipid and polymer based gold nanohybrids using a nanoreactor approach," *RSC Advances*, vol. 5, no. 91, pp. 74320–74328, 2015.

[27] H. M. Aliabadi, A. Mahmud, A. D. Sharifabadi, and A. Lavasanifar, "Micelles of methoxy poly(ethylene oxide)-*b*-poly(ε-caprolactone) as vehicles for the solubilization and controlled delivery of cyclosporine A," *Journal of Controlled Release*, vol. 104, no. 2, pp. 301–311, 2005.

[28] E. D. Goddard, N. J. Turro, P. L. Kuo, and K. P. Ananthapadmanabhan, "Fluorescence probes for critical micelle concentration determination," *Langmuir*, vol. 1, no. 3, pp. 352–355, 1985.

[29] C. Sommer, J. S. Pedersen, and P. C. Stein, "Apparent specific volume measurements of poly(ethylene oxide), poly(butylene oxide), poly(propylene oxide), and octadecyl chains in the micellar state as a function of temperature," *Journal of Physical Chemistry B*, vol. 108, no. 20, pp. 6242–6249, 2004.

[30] S. A. Meeuwissen, S. M. C. Bruekers, Y. Chen, D. J. Pochan, and J. C. M. van Hest, "Spontaneous shape changes in polymersomes via polymer/polymer segregation," *Polymer Chemistry*, vol. 5, no. 2, pp. 489–501, 2014.

[31] T. Ameller, V. Marsaud, P. Legrand, R. Gref, and J.-M. Renoir, "Pure antiestrogen RU 58668—loaded nanospheres: morphology, cell activity and toxicity studies," *European Journal of Pharmaceutical Sciences*, vol. 21, no. 2-3, pp. 361–370, 2004.

[32] E. Mahon, A. Salvati, F. Baldelli Bombelli, I. Lynch, and K. A. Dawson, "Designing the nanoparticle-biomolecule interface for 'targeting and therapeutic delivery'," *Journal of Controlled Release*, vol. 161, no. 2, pp. 164–174, 2012.

[33] T. Einfalt, R. Goers, I. A. Dinu et al., "Stimuli-triggered activity of nanoreactors by biomimetic engineering polymer membranes," *Nano Letters*, vol. 15, no. 11, pp. 7596–7603, 2015.

[34] E. M. Cornford, S. Hyman, M. E. Cornford et al., "Non-invasive gene targeting to the fetal brain after intravenous administration and transplacental transfer of plasmid DNA using PEGylated immunoliposomes," *Journal of Drug Targeting*, vol. 24, no. 1, pp. 58–67, 2015.

[35] J. Huwyler, D. Wu, and W. M. Pardridge, "Brain drug delivery of small molecules using immunoliposomes," *Proceedings of the National Academy of Sciences of the United States of America*, vol. 93, no. 24, pp. 14164–14169, 1996.

[36] M. Hamidi, A. Azadi, and P. Rafiei, "Pharmacokinetic consequences of pegylation," *Drug Delivery*, vol. 13, no. 6, pp. 399–409, 2006.

[37] H. Kobayashi, B. Turkbey, R. Watanabe, and P. L. Choyke, "Cancer drug delivery: considerations in the rational design of nanosized bioconjugates," *Bioconjugate Chemistry*, vol. 25, no. 12, pp. 2093–2100, 2014.

[38] F. Alexis, E. Pridgen, L. K. Molnar, and O. C. Farokhzad, "Factors affecting the clearance and biodistribution of polymeric nanoparticles," *Molecular Pharmaceutics*, vol. 5, no. 4, pp. 505–515, 2008.

[39] V. P. Torchilin, "Structure and design of polymeric surfactant-based drug delivery systems," *Journal of Controlled Release*, vol. 73, no. 2-3, pp. 137–172, 2001.

[40] W. Xu, P. Ling, and T. Zhang, "Polymeric micelles, a promising drug delivery system to enhance bioavailability of poorly water-soluble drugs," *Journal of Drug Delivery*, vol. 2013, Article ID 340315, 15 pages, 2013.

[41] G. Québatte, E. Kitas, and J. Seelig, "RiDOM, a cell-penetrating peptide. Interaction with DNA and heparan sulfate," *Journal of Physical Chemistry B*, vol. 117, no. 37, pp. 10807–10817, 2013.

[42] X. Ye, J. Fei, K. Xu, and R. Bai, "Effect of polystyrene-*b*-poly(ethylene oxide) on self-assembly of polystyrene-*b*-poly(*N*-isopropylacrylamide) in aqueous solution," *Journal of Polymer Science Part B: Polymer Physics*, vol. 48, no. 11, pp. 1168–1174, 2010.

[43] L. Yang, X. Qi, P. Liu, A. El Ghzaoui, and S. Li, "Aggregation behavior of self-assembling polylactide/poly(ethylene glycol) micelles for sustained drug delivery," *International Journal of Pharmaceutics*, vol. 394, no. 1-2, pp. 43–49, 2010.

[44] S. Li, H. Garreau, B. Pauvert, J. McGrath, A. Toniolo, and M. Vert, "Enzymatic degradation of block copolymerase prepared from ε-caprolactone and poly(ethylene glycol)," *Biomacromolecules*, vol. 3, no. 3, pp. 525–530, 2002.

[45] L. Shang, K. Nienhaus, and G. U. Nienhaus, "Engineered nanoparticles interacting with cells: size matters," *Journal of Nanobiotechnology*, vol. 12, article 5, 2014.

[46] S. Ohtsuki, C. Ikeda, Y. Uchida et al., "Quantitative targeted absolute proteomic analysis of transporters, receptors and junction proteins for validation of human cerebral microvascular endothelial cell line hCMEC/D3 as a human blood-brain barrier model," *Molecular Pharmaceutics*, vol. 10, no. 1, pp. 289–296, 2013.

[47] Y. Uchida, S. Ohtsuki, Y. Katsukura et al., "Quantitative targeted absolute proteomics of human blood-brain barrier transporters and receptors," *Journal of Neurochemistry*, vol. 117, no. 2, pp. 333–345, 2011.

[48] D. Chirio, M. Gallarate, E. Peira et al., "Positive-charged solid lipid nanoparticles as paclitaxel drug delivery system in glioblastoma treatment," *European Journal of Pharmaceutics and Biopharmaceutics*, vol. 88, no. 3, pp. 746–758, 2014.

[49] B. B. Weksler, "Blood-brain barrier-specific properties of a human adult brain endothelial cell line," *The FASEB Journal*, vol. 19, no. 13, pp. 1872–1874, 2005.

[50] L. D. Simmler, T. A. Buser, M. Donzelli et al., "Pharmacological characterization of designer cathinones *in vitro*," *British Journal of Pharmacology*, vol. 168, no. 2, pp. 458–470, 2013.

[51] D. Ye, K. A. Dawson, and I. Lynch, "A TEM protocol for quality assurance of in vitro cellular barrier models and its application to the assessment of nanoparticle transport mechanisms across barriers," *The Analyst*, vol. 140, no. 1, pp. 83–97, 2015.

[52] A. W. Stitt, H. R. Anderson, T. A. Gardiner, J. R. Bailie, and D. B. Archer, "Receptor-mediated endocytosis and intracellular trafficking of insulin and low-density lipoprotein by retinal vascular endothelial cells," *Investigative Ophthalmology and Visual Science*, vol. 35, no. 9, pp. 3384–3392, 1994.

[53] A. Cerletti, J. Drewe, G. Fricker, A. N. Eberle, and J. Huwyler, "Endocytosis and transcytosis of an immunoliposome-based brain drug delivery system," *Journal of Drug Targeting*, vol. 8, no. 6, pp. 435–446, 2000.

[54] A. Grover, A. Hirani, Y. Pathak, and V. Sutariya, "Brain-targeted delivery of docetaxel by glutathione-coated nanoparticles for brain cancer," *Ageing International*, vol. 15, no. 6, pp. 1562–1568, 2014.

[55] A. R. Neves, J. F. Queiroz, B. Weksler, I. A. Romero, P. Couraud, and S. Reis, "Solid lipid nanoparticles as a vehicle for brain-targeted drug delivery: two new strategies of functionalization with apolipoprotein E," *Nanotechnology*, vol. 26, no. 49, Article ID 495103, 2015.

[56] X. Tian, S. Nyberg, P. S. Sharp et al., "LRP-1-mediated intracellular antibody delivery to the Central Nervous System," *Scientific Reports*, vol. 5, Article ID 11990, 2015.

CHAPTER V

Non-viral gene delivery of a parvovirus-derived anticancer gene for therapy of hepatocellular carcinoma

*Grossen P, *Witzigmann D, Englinger B, Quintavalle C, Gruenig D, Tran X-T, Quagliata L, Schenk SH, Van Schoonhoven S, Berger W, Terragiano LM, Krähenbühl S, Rommelaere J, Nuesch J, Huwyler J

*contributed equally

Manuscript: First draft

Highlights: In this study, the large non-structural protein NS1 of the H-1PV was used to implement a therapeutic strategy for the treatment of liver cancer. Lipid NPs were used to deliver pDNA coding for NS1 to a set of liver cancer cells and protein expression as well as pharmacological effects were studied *in vitro*. To show that this therapeutic approach is specific to cancer cells, primary human hepatocytes were used as control. Various *in vitro* assays were used to analyze NS1-induced cell death in detail. In addition, a biomarker for the sensitivity to NS1 therapy was evaluated. In a last step, safety and toxicity of this novel therapeutic approach was tested in mice after single and multiple dosing.

Non-viral gene delivery of a parvovirus-derived anticancer gene for the treatment of hepatocellular carcinoma

*[1]Grossen P, *[1]Witzigmann D, [2]Englinger B, [3]Quintavalle C, [4]Gruenig D, [1]Tran X-T, [3]Quagliata L, [1]Schenk SH, [2]Van Schoonhoven S, [2]Berger W, [3]Terragiano LM, [4]Krähenbühl S, [5]Rommelaere J, [5]Nüesch J, °[1]Huwyler J

***Contributed equally**

[1]Division of Pharmaceutical Technology, Department of Pharmaceutical Sciences, University of Basel, Basel, Switzerland

[2]Applied and Experimental Oncology, Medical University of Vienna, Vienna, Austria

[3]Institute of Pathology, Molecular Pathology Division, University Hospital of Basel, Basel, Switzerland

[4]Division of Clinical Pharmacology and Toxicology, University Hospital of Basel, Basel, Switzerland

[5]Infection and Cancer Program, Division of Tumor Virology, German Cancer Research Center (DKFZ), Heidelberg, Germany

°Corresponding author:

Klingelbergstrasse 50, CH-4056 Basel, Switzerland

E-Mail: joerg.huwyler@unibas.ch

Phone: +41 (0)61 207 15 13.

Abstract

Hepatocellular carcinoma (HCC) is still lacking of adequate therapeutic options resulting in poor prognosis. Thus, novel treatment strategies are urgently needed. Here, we report a novel therapeutic approach using a virus-derived anticancer gene (large-non structural protein 1, NS1) delivered using lipoplex nanoparticles (LNPs). We used a set of established HCC-derived cell lines to study cellular LNP internalization, subsequent gene expression, and to analyze oncotoxic effects mediated by our anticancer protein. We achieved high gene delivery efficiencies *in vitro* in liver cancer-derived cell lines and were able to induce multimodal cell death. Expression of NS1 resulted in superoxide induction, reduced intracellular ATP levels, promoted morphological alterations, and subsequently induced apoptosis and necrosis. Notably, we show that healthy primary human hepatocytes are not affected by NS1 gene delivery. Furthermore, we validated a prognostic marker for the sensitivity to NS1-mediated therapy and we were able to render non-susceptible cells sensitive by expression of a constitutive active isoform of phosphoinositide-dependent kinase 1 (PDK1). Our therapeutic approach was well tolerated *in vivo* after multiple dosing indicated by a constant weight and a good overall health condition of treated mice. Our data suggest that NS1 can be efficiently delivered using LNPs and that this anticancer gene is a promising therapeutic option for HCC.

Introduction

Recently, anticancer genes and their proteins that selectively induce cell death in cancer cells have gained much attention [1]. This class of drugs allows efficient killing of cancer cells whereas healthy tissue stays unaffected. Apoptin, for example, a 14 kDa protein from the Chicken anemia virus (CAV), was tested on various human tumor cell lines and efficiently induced apoptosis [2,3]. In contrast, no or only minor effects were observed in healthy cells such as primary hepatocytes [4]. Another candidate is derived from the rat parvovirus (H-1PV). This virus showed promising results in the treatment of various tumors in a preclinical setting and was recently tested in a clinical Phase-I/IIa trial in patients suffering from glioma [5]. The major effector protein of H-1PV is NS1 consisting of 672 amino acids (i.e. 83 kDa) [6]. NS1 is essential for viral replication [7] and interestingly, the expression of NS1 without other viral components is sufficient to kill cancer cells [8,9]. NS1 can induce multimodal cell death via apoptosis, necrosis, lysosomal-like programmed cell death, and cytolysis exclusively in neoplastically transformed (i.e. tumor) cells [6,10,11]. These oncotoxic effects result from physical interaction with cellular proteins rather than own enzymatic functions of NS1 [12,13]. For example, NS1 recruits components of cellular DNA replication and repair machineries for viral DNA transcription and replication [14–18] and can interact with other cellular proteins such as the catalytic subunit of casein kinase II (CKIIα) [12]. Pivotal for NS1 functions is the regulation of NS1 by cellular kinases: Activation of the PDK1/PKC/PKB signaling pathway was shown to be a prerequisite for H-1PV-mediated oncotoxicity and oncotropism (i.e. specificity) [19].

For the first time, we report the use of plasmid DNA (pDNA)-loaded lipoplex nanoparticles (LNPs) encoding the sequence of the oncotoxic protein NS1 for the treatment of HCC (Fig. 1A). We observed selectively induced cell death in HCC cells

in vitro without toxic effects on healthy liver cells. Detailed analysis of cell death mechanisms revealed contribution of apoptotic and necrotic pathways. We were able to render non-permissive cells susceptible for NS1-mediated cell death by activating PDK1 and therefore propose PDK1 activity as prognostic marker for the sensitivity to NS1 in HCC therapy. *In vivo*, NS1-LNP constructs were well tolerated after single or multiple administrations.

Results

Development of LNPs for efficient pDNA delivery to human liver cancer cells

To analyze expression of NS1, we generated plasmid DNA (pDNA) constructs coding for NS1 under control of the cytomegalovirus (CMV) promoter (Fig. 1A). This promoter can be used in a broad range of cell types with a very high activity and is therefore frequently used in mammalian expression plasmids [20]. To analyze the expression of NS1 in liver cancer-derived cell lines, we additionally generated an NS1-green fluorescence protein (GFP) fusion protein (NS1-GFP). NS1-GFP had the correct size (see below) and GFP did not alter the subcellular distribution (see below) or intrinsic toxicity of NS1 (data not shown). We therefore used NS1 or NS1-GFP (i.e. fluorescent marker) for further experiments. For gene delivery assays, pDNA was rapidly mixed with lipid nanoparticles to induce spontaneous LNP formation. We characterized LNPs by Nanoparticle Tracking Analysis (NTA), electrophoretic light scattering, and transmission electron microscopy (TEM). LNPs had an average size of 101.0 ± 2.6 nm (Fig. 1B) and were characterized by a positive zeta potential (11.6 ± 1.0 mV) that is typical for lipoplexes [21]. To obtain additional information about LNP morphology, we analyzed electron micrographs of LNPs and found spherical particles with an average diameter of 81.8 ± 27.0 nm (n = 100) and a monodisperse size distribution (Fig. 1C) corresponding to a polydispersity index

(PDI) of 0.109. Size, shape, and zeta potential did not change significantly for LNPs containing pDNA coding for GFP, NS1, NS1-GFP, or empty vector control (data not shown).

In a first step, we analyzed the interaction of LNPs with a set of 9 established immortalized HCC cell lines. To assess the cellular uptake of LNPs, we fluorescently labeled pDNA using a carbocyanine dye and analyzed intracellular fluorescence after LNP incubation by confocal microscopy (CLSM). A time-dependent increase of intracellular fluorescence was observed in all cell lines already after 60 min (Fig. 1D and Supplementary Fig. 1A). In sharp contrast, we observed significantly lower fluorescence signals when cells were incubated with naked pDNA. In a next step, we analyzed NS1-GFP gene delivery efficiency qualitatively and quantitatively by CLSM and flow cytometry respectively. We used a final pDNA concentration of 0.1 ng per cell and used complete culture medium containing fetal calf serum (FCS). All cell lines tested showed a high NS1-GFP expression after 24 h of incubation with expression levels up to 85% NS1-positive cells (Fig. 1E/F). LNPs were therefore deemed as suitable non-viral vectors for NS1 gene delivery for further experiments. The NS1 expression level in NS1 positive cells was strongly depending on the cell line: A high variability in NS1-GFP expression (88-fold to 2994-fold increase in mean fluorescence intensity, MFI) was observed (Fig. 1F). Subsequently, expression of NS1 was analyzed by western blotting. We observed a typical NS1 signal (i.e. double band) at 80 kDa (Fig. 1G). Similar results were observed in cells infected with H-1PV previously [19]. We furthermore quantified expression levels of NS1 and normalized the results to the expression of β-actin. We again found pronounced differences in NS1 levels between different cell lines (Supplementary Fig. 1B). NS1-GFP showed an increase in the apparent molecular weight and was detected above 100 kDa confirming the presence of a GFP (27 kDa) fusion protein (Supplementary Fig. 1C). A

fluorescence signal that overlapped with NS1-GFP western blot bands was detected when acrylamide gels loaded with non-denaturized proteins were illuminated at 488 nm (data not shown).

Recently, it was reported that during viral infection, a distinct intracellular distribution pattern of NS1 can be observed with a preferential localization in the cell nucleus [22]. However, the contribution of other viral proteins to the redistribution of NS1 is not completely revealed yet. Therefore, we were interested, if this phenomenon can be observed without other viral components present. We analyzed NS1-GFP expression over time by CLSM and compared the distribution of the fluorescence signal to the expression of GFP. Indeed, we found nuclear accumulation of NS1-GFP already after 4 h of LNP uptake (Fig. 1H) whereas GFP was evenly distributed inside the cell (Fig. 1E). Since it was reported that GFP may have an inherent nuclear accumulation [23], we repeated the experiment using immunohistochemistry (IHC) in cells expressing NS1. Confirming our results using the NS1-GFP fusion protein, we found a nuclear accumulation of NS1 (Supplementary Fig. 1E).

Effect of NS1 expression on human liver cancer-derived cell lines

Recent work has revealed that parvovirus infection induces apoptosis, necrosis, and lysosomal-like programmed cell death in cancer cells [9,24,25]. As major effector for these oncotoxic effects NS1 was identified [6,8,9] (Fig. 1A). However, little is known about the therapeutic use of NS1 uncoupled from H-1PV infection.

To address this question, we analyzed NS1-induced changes in cell viability in 9 HCC cell lines 72 h after LNP uptake. We normalized results to cells incubated with LNPs containing empty plasmid vector (Fig. 2A) or pDNA coding for GFP. Not all of the 9 HCC cell lines tested were susceptible for NS1-mediated toxicity. Whereas in some cell lines a significant decrease in cell viability of more than 60% was observed

(e.g. Hep3B), others did not show a significant response (less than 10%) to NS1 (e.g. HepT1). Thus, we categorized the HCC cells into strong, medium, weak, and non-responders (Fig. 2A). A huge advantage of parvovirus therapy is the oncotropism of this virus that renders the treatment selective for transformed cells whereas their healthy counterparts stay unaffected [10,11]. To show that our therapeutic approach using LNP-mediated NS1 gene delivery is still selective to tumor cells (i.e. oncotropism), we transfected freshly isolated primary human hepatocytes (PHH) and HepaRG cells. It should be noted that HepaRG cells share features with PHH and are used as an alternative to *ex vivo* cultured hepatocytes [26]. Importantly, PHH and HepaRG cells were not affected by the expression of NS1 and did not show a decrease in cell viability as compared to vector-treated control cells (Fig. 2A). For all further experiments, we selected a weak (HepG2), a medium (HuH7), and a strong responding cell line (Hep3B). First, we analyzed NS1 expression over time and analyzed effects on cell morphology. GFP and NS1-GFP fluorescence was detected already starting 4 h post LNP uptake. The gene expression increased over time with a maximum after 24 h (Fig. 2B). As described above, NS1 preferentially accumulated in cell nuclei. Interestingly, NS1 induced morphological alterations: Cells shrinked in size and nuclei became fragmented whereas GFP expressing cells rendered their morphology up to 72 h after gene delivery (Fig. 2B). We were further interested in the dynamics of NS1-induced cell death. Cell viability, induction of apoptosis, and necrosis were analyzed using fluorescence and luminescence-based assays [27]. Cell viability of HuH7 and Hep3B cells decreased over time with a maximal decrease 72 h after LNP uptake (Fig. 2C). We observed no change in cell viability for HepG2 cells (Fig. 2C). Consequently, we found a strong induction of apoptosis in strong responding Hep3B cells with a maximum after 72 h (5.40 ± 1.51-fold increase) with only minor effects on HepG2 (1.15 ± 0.38) and HuH7 (0.99 ± 0.03) cells (Fig. 2D). A

similar behavior was observed for the induction of necrosis (Fig. 2E). We further used propium iodide (PI) to stain dead cells and to quantify cytotoxic effects of NS1-GFP (Fig. 2F). A significant increase in PI positive cells was observed in all cell lines ranging from an 1.75 ± 0.46-fold increase ($p < 0.05$) for weak responding HepG2 cells up to a 2.91 ± 0.56-fold increase ($p < 0.01$) for strong responding Hep3B cells. In summary, the kinetic experiments confirmed the findings of the initial cell viability screening using a HCC cell panel as described above (Fig. 2A).

***In vivo* safety evaluation**

NS1 did not induced any toxic effects in PHH and HepaRG cells as shown above. Furthermore, we were interested if our therapeutic approach is well tolerated *in vivo* after single or multiple dosing. For multiple dosing, we weekly injected LNPs containing pDNA coding for NS1 or empty vector control i.p. for 4 weeks (i.e. 4 injections). Weight of mice was monitored and compared to the initial body weight at day zero (start of the experiment). At day 31, mice were sacrificed and spleens were resected, weighted, and compared to vector treated control mice.

Body weight decreased the day after the treatment. However, animals recovered two days post injection and body weight did not alter significantly as compared to non-treated mice (Fig. 3A) or vector-treated control mice (Fig. 3B). We additionally found no increase in spleen weight after NS1 therapy as compared to vector-treated control animals (Fig. 3C). Thus, our non-viral gene delivery approach of NS1 well tolerated after single or multiple dosing.

Mechanisms of NS1-induced cell death

Whereas some anticancer genes selectively induce apoptosis [28], H-1PV infection was reported to induce various cytotoxic effects [6]. Therefore, we were again

interested whether the expression of NS1 independent from H-1PV infection is sufficient for multimodal killing of HCC cells.

To identify the contribution of apoptotic and necrotic cell death upon NS1 expression, we used Annexin V/PI staining and subsequent analysis by flow cytometry. Results were normalized to control cells incubated with medium. Representative flow cytometry contour plots for Hep3B cells are shown in Figure 4B. Measurements revealed a significant increase ($p < 0.05$) in apoptosis in Hep3B (29.58 ± 1.75% of total cells) and HuH7 (12.19 ± 2.99% of total cells) cells expressing NS1, whereas the fraction of apoptotic cells was comparable to vector treatment in weak responding HepG2 cells (Fig. 4A). We observed similar trends for the analysis of necrosis (Fig. 4A). Since apoptosis seems to play a major role in NS1-induced cell death, we took a closer look to the induction of apoptosis. Thus, we were interested in cleavage of pro-apoptotic caspases 9 and 3 as well as cleavage of poly(ADP-ribose) polymerase (PARP). For this we used western blot analysis to detect cleaved and non-cleaved protein species in cells after NS1 treatment. We found a strong increase in cleaved caspases 9/3 and PARP in Hep3B and HuH7 cells indicating an apoptotic cell death induction 48 h (Supplementary Fig. 2A/B) and 72 h after LNP uptake (Fig. 4C). Conforming our results that HepG2 cells are less susceptible for NS1 treatment, no increase in cleaved caspase 9/3 and PARP was observed as compared to vector-treated control cells (Fig. 4C). A representative western blot of Hep3B cells 72 h after LNP uptake is shown in Figure 4D. We further analyzed activity of caspases 3 and 7 using a luminescence-based assay. Notably, NS1 expression increased caspase 3 and 7 activity in strong-responding Hep3B and medium-responding HuH7 cells in a time dependent manner. Caspase activity rapidly increased within 24 h after gene delivery and reached a maximum after 48 h (Fig. 4E). In HepG2 cells, the caspase activity was close to vector-treated control

cells (Fig. 4E). Intracellular ATP levels were reported to serve as a switch between apoptosis and necrosis [29] and may be used as marker for disruption of mitochondrial function [30]. We therefore used a luminescence-based assay to determine NS1-induced decrease of intracellular ATP levels compared to vector-treated control cells. All three cell lines analyzed showed significantly ($p < 0.05$) reduced ATP levels (Fig. 4F). Recently, it was shown that induction of reactive oxygen species (ROS)-accumulation is a major mechanism for NS1-mediated apoptosis [31]. To address this question, we analyzed NS1-induced increase in intracellular superoxide levels using flow cytometry. Indeed, expression of NS1 was sufficient to elevate intracellular superoxide levels in responding cells. An increase in superoxide levels by a factor of 2.12 ± 0.32 and 1.63 ± 0.34 was observed in Hep3B and HuH7 cells, respectively, as compared to vector treated control cells (Fig. 4G). HepG2 cells showed only a minor increase (1.43 ± 0.58-fold) in superoxide levels (Fig. 4G). Importantly, gating of Hep3B cells revealed that only NS1-expressing cells showed an increase in superoxide levels, whereas GFP-expressing or non-transfected cells did not show an induced superoxide production (Fig. 4H). We made similar findings when we subsequently visualized stained cells by CLSM. A strong increase in superoxide was observed in NS1-GFP expressing Hep3B cells whereas cells treated with empty vector of GFP showed only minor increase (Fig. 4I).

Regulation of NS1 toxicity and prognostic biomarker

As described previously, our non-viral gene delivery of NS1 was not efficient to treat all HCC cell lines. Notably, there was no overall correlation between these findings and transfection efficiencies. Thus, we evaluated the biomarkers that allow identification of susceptible cells reported previously for parvovirus treatment. Activation of the PDK1/PKC/PKB signaling pathway was revealed as prognostic

marker for H-1PV toxicity in previous studies: Constitutive activation of PDK1 was sufficient to render non-susceptible cells responsive for H-1PV-induced cell death [19].

PDK1 was expressed in all HCC-derived cell lines tested (data not shown). However, PDK1 activity rather than overall PDK1 expression will lead to activation of NS1. We therefore expressed a PDK1 isoform (PDK1:S138E) that is constitutively active [19] in HCC cells using recombinant adeno-assicoated viruses (rAAV). Subsequently, we incubated transduced cells with LNPs for gene delivery of GFP or NS1-GFP and stained dead cells using PI. In weak-responding HepG2 cells, activation of the PDK1 signaling pathway resulted in a significant increase ($p < 0.05$) in dead cells (Fig. 5A) when NS1-GFP was expressed (1.39 ± 0.05-fold). In contrast, no additional therapeutic benefit was observed (Fig. 5A) in strong-responding Hep3B cells (1.00 ± 0.04-fold). No difference in the percentage of PI-positive cells was observed when only GFP was expressed (Fig. 5A). We performed a similar experiment using a dominant negative variant of PDK1. PDK1 is a master kinase with essential functions for proliferation and survival, thus inactivation of PDK1 induces severe side-effects [32]. Expression of a dominant negative PDK1 (i.e. functional knock-out, PDK1:K204M) was toxic for all three HCC cells analyzed (data not shown) and thus, we were not able to correlate changes in PI-positive cells with NS1-GFP expression. It was shown that NS1 is phosphorylated by PKC isoforms (e.g. PKCη) rather than direct regulation by PDK1 [33,34]. PKCη was detected in all HCC cell lines tested (data not shown). Due to the interaction of PKCη and NS1, nuclear translocation of PKCη during parvovirus infection was observed [35]. To see if this redistribution of PKCη can be triggered by non-viral gene delivery of NS1, we performed an immunofluorescence staining of NS1 and PKCη 24 h after LNP internalization. Whereas PKCη showed a diffuse distribution pattern in vector control treated cells,

we observed a pronounced accumulation of PKCη in the cell nucleus when NS1-GFP was expressed (Fig. 5B and Supplementary Figure 1E).

Discussion

Oncotoxic viruses such as the rodent parvovirus H-1PV are promising candidates for the treatment of cancer. This therapeutic strategy has several advantages over conventional cancer chemotherapies: (i) rodent parvoviruses selectively induce cell death in cancer cells [6,10,11] and (ii) a low resistance to H-1PV treatment is expected due to multimodal killing [6]. However, there are several issues including concerns about the safety of viral therapies [36–38] and a restriction to specific cancer types for some onctoxic viruses.

In this study, we therefore wanted to develop a therapeutic approach that is distinct from previous studies and virus-based strategies. For the first time, we uncoupled NS1 for therapy of HCC from the virus: We generated pDNA vectors coding for the virus-derived anticancer gene (NS1) and prepared LNPs for non-viral gene delivery. We achieved high transfection efficiencies (Fig. 1E/F) in a set of 9 established HCC cell lines and confirmed expression of NS1 by western blot analysis (Fig. 1G). NS1 is a multifunctional protein that is endowed with various functional domains [39] including a nuclear localization signal [40] (NLS): After H-1PV infection, a nuclear accumulation of NS1 was reported. Moreover, a distinct distribution pattern in cell nuclei was described. Both, an accumulation in nuclear bodies, so-called H-1PV-associated replication bodies (PAR), and a diffuse distribution in the nucleoplasm were observed [22]. However, NS1 was absent in nucleoli of infected cells [22]. We made similar findings when we used our non-viral gene delivery approach in HCC cells (Fig. 1I and Fig. 2B). NS1-GFP accumulated in the cell nucleus already 4 h after LNP uptake: Fluorescence signals were found in distinct nuclear foci and distributed

in the nucleoplasm, whereas no signal was detected in nucleoli (Supplementary Fig. 1D). Recently, a similar approach using a fluorescent canine parvovirus (CPV) NS1 fusion protein (NS1-EYFP) revealed comparable results [41]. Over time, we observed strong morphological alterations due to NS1-GFP expression whereas GFP expression induced no changes in cell morphology (Fig. 2B). Morphological alterations (i.e. cytopathic effects) of host cells during H-1PV life cycle were described previously and were attributed to rearrangement and degradation of micro- and intermediate filaments of the cytoskeleton [24]. We observed increased cytotoxic effects over time starting 24 h after LNP uptake with a maximal therapeutic effect after 72 h (Fig. 2C-E). We found an early onset of necrotic cell death starting 24 h after gene delivery (Fig. 2C) followed by the induction of apoptosis after 48 h in highly susceptible Hep3B cells (Fig. 2D). Interestingly, we observed increased activity of caspases 3/7 within 24 h after LNP uptake (Fig. 4E) and found cleaved caspases 9/3 and PARP after 48 h and 72 h (Fig. 4C/D). Intracellular ATP levels were already decreased 24 h after gene delivery (Fig. 4F). Importantly, we found no complete intracellular ATP depletion that would prevent cells to enter apoptotic pathways [29]. Thus, the multimodal killing described for H-1PV can be achieved via non-viral gene delivery of NS1 as shown in this study. Conventional chemotherapies are often directed towards single cellular targets and mutation of these can result in rapid development of acquired therapy resistances [42,43]. In contrast, NS1 targets multiple cellular pathways and can therefore bypass such acquired mutations and minimize the risk for therapy resistances. Furthermore, NS1 is able to kill cells that are resistant to apoptosis-inducers (e.g. cisplatin) and may therefore serve as an important therapeutic alternative for pre-treated patients [25]. Besides direct killing of tumor cells (i.e. oncolytic effect), a major contribution of the immune system is attributed to the overall oncotoxic effect of H-1PV. H-1PV infection stimulates natural

killer (NK) [44] and dendritic cells [45]. Release of viral and cellular immunogenic signals (e.g. heat shock protein HSP72) during cell lysis was observed [46]. Furthermore, vesicular egress of virus progenitors can increase the exposure of tumor-associated and viral antigens [13,47]. Notably, NS1 activity is required for vesicular viral egress [47]. We found accumulation of NS1 in cellular structures close to nuclei (Fig. 1H) that could be structures of the endoplasmic reticulum (ER). Therefore, the question whether NS1 is transported to the cell surface and may initiate an anti-tumor immune response should be addressed in future experiments. It should be noted that not all HCC cells tested in this study were susceptible for NS1 gene therapy. We therefore asked the question whether decrease in cell viability correlates with transfection efficiency or protein expression levels. However, we did not find an overall correlation between efficiency of gene delivery (i.e. transfection efficiency, MFI, and protein expression levels) and cytotoxic effects. It was shown previously, that expression of oncogenes and cell transformation render resistant cells sensitive for parvovirus-induced cell death [10,11]. Therefore, we focused on the intracellular activation pathway of NS1. NS1 is a “prodrug” that needs intracellular activation prior to its pharmacological function. Mutation at distinctive PKC phosphorylation sites interfered with NS1 function and resulted in reduced toxic effects upon parvovirus infection [48]. PKC isoforms were shown to phosphorylate NS1 *in vivo* and co-localize with NS1 in cell nuclei [35,49]. We observed similar results when NS1 was expressed using our non-viral gene delivery approach (Fig. 5B). We were therefore interested if PKCη can be used to modify NS1 toxicity. However, expression of PKCη using rAAV transduction was not sufficient to increase NS1-mediated toxicity (data not shown) as it was described previously for H-1PV therapy [50]. Activation of PKCη by e.g. the master kinase PDK1 [51,52] seems thus to be a prerequisite for NS1 phosphorylation. Indeed, expression of a constitutive

active PDK1 isoform (PDK1:S138E) [19] was sufficient to render NS1 resistant HCC cells susceptible for NS1 therapy (Fig. 4B). However, besides the constitutive active PDK1 isoform that was proposed as marker in glioma therapy [19], alternative PDK1 activation mechanisms have to be considered for HCC treatment [53,54]. Conclusively, PDK1 activity seems to be a valid prognostic marker. It is tempting to speculate that this marker can further be used to stratify patient subpopulations for personalized HCC therapy. In addition, activation of NS1 by cellular proteins that are preferentially overexpressed in transformed cells is an important key factor for H-1PV selectivity to cancer cells (i.e. oncotropism). We were interested, if our therapeutic approach renders this tumor specificity and we therefore tested the effect of NS1 expression in PHH and the model cell line for *ex vivo* cultured hepatocytes HepaRG. We observed no toxic effects and PHH as well as HepaRG cells were unaffected by NS1 (Fig. 2A). Furthermore, we analyzed the toxicity of our non-viral gene delivery approach of NS1 *in vivo* after single or multiple i.p. injection. Notably, single or weekly-administered non-viral gene delivery of NS1 was well tolerated by female SCID mice (Fig. 3A/B).

In summary, our work demonstrates the potential of non-viral gene delivery of NS1 in tumor therapy. We provide a detailed insight into NS1 expression, intracellular distribution, and NS1-mediated cytotoxicity. Moreover, we show that our therapeutic approach is selective for tumor cells without affecting healthy cells *in vitro* and *in vivo* and we propose a biomarker that can be used to stratify HCC patient populations and thus for personalized HCC treatment.

Outlook

Further experiments will help to understand the oncotoxicity and the oncotropism of NS1 in more detail. First, a targeted RNA sequencing in NS1-treated and vector-

treated control cells is ongoing. Using this approach, we hope to identify further cellular pathways that are involved in NS1-mediated cell death in susceptible cells over time. Second, an *in vivo* proof-of-concept study in mice (Hep3B xenograft) is ongoing. Mice are treated weekly for 4 weeks (i.e. 4 injections): This scheme was already tested in our safety study and was well tolerated (Fig. 5A/B). The therapeutic effect of NS1 and the expression pattern of NS1 in tumor and healthy tissue will be analyzed and compared to vector-treated control animals. Third, a tissue microarray in human HCC tissue samples is ongoing. As shown previously [19] and as further confirmed in this study, PDK1 activity is a potent biomarker for susceptibility of NS1 (and H-1PV) treatment. We therefore aim to characterize total PDK1 levels, PDK1 activation (staining of PDK1phosphoS241), and the constitutive active PDK1 isoform (PDK1phosphoS135) that was described in human glioma patients. With these results, we will be able to identify patient subpopulations that are susceptible for NS1-mediated therapy: PDK1 activity could potentially be tested prior to therapy to allow patient stratification and personalized treatment of HCC patients. In addition, these results could help to understand HCC development and progression. For example, total PDK1 expression levels correlate with prognosis of HCC patients [55].

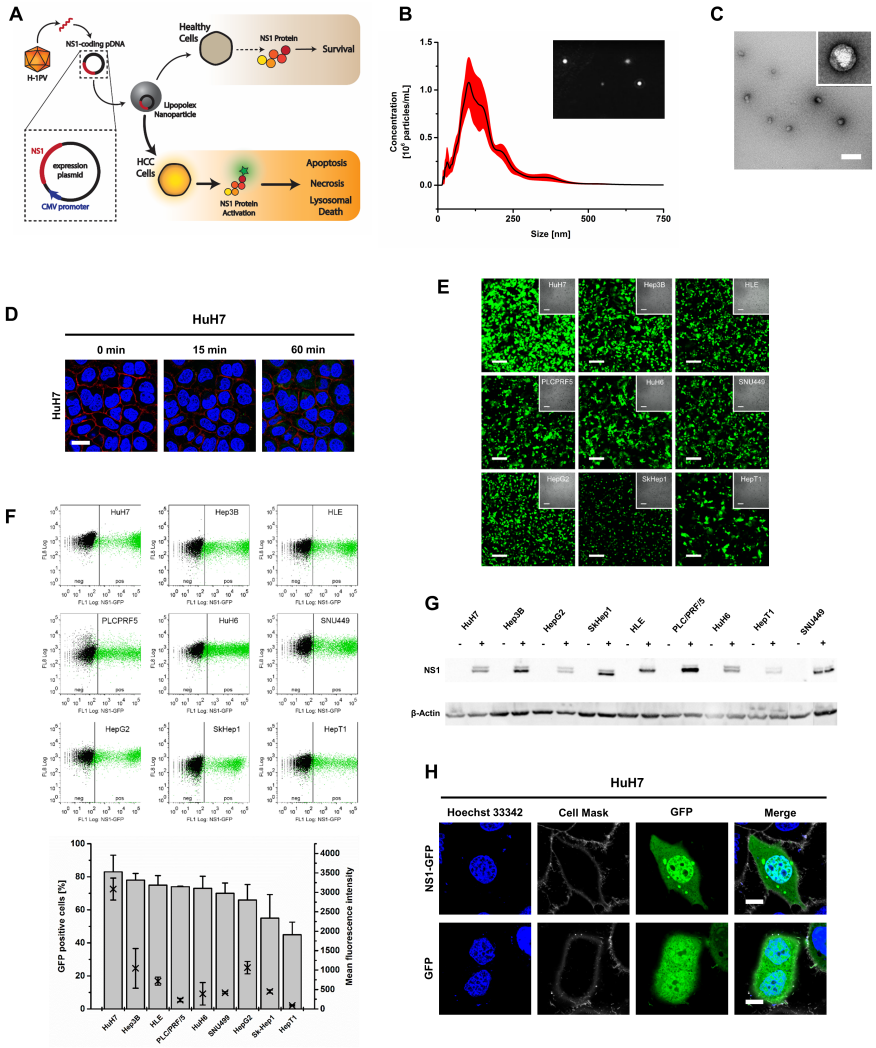

Figure 1 Characterization of lipoplex nanoparticles (LNPs), cellular LNP internalization, and expression of the large non-structural protein 1 (NS1) in hepatocellular carcinoma (HCC) cells. HCC cells were incubated with LNPs containing plasmid DNA (pDNA) coding for an NS1-green fluorescence protein (GFP) fusion protein (NS1-GFP) at a final pDNA concentration of 0.1 ng/cell. (A) Schematic overview of the therapeutic approach developed in this study. The sequence of H-1 parvoviral NS1 was cloned on a pDNA vector and delivered via LNPs to healthy cells and HCC cells.

(B) Characterization of LNPs by Nanoparticle Tracking Analysis (NTA). The average mode size distribution is plotted against the LNP concentration (black line) ± S.D. of *n* = 4 measurements. Insert: representative video frame obtained by NTA. (C) Transmission electron micrograph (TEM image) of spherical LNPs after uranyl-acetate negative staining. Scale bar: 200 nm. (D) Uptake of fluorescently labeled LNPs by HuH7 cells after 0, 15, and 60 min of incubation analyzed by confocal microscopy. Blue: cell nuclei (Hoechst 33342); red: plasma membrane (Cell Mask); green: pDNA (DiYO-1). Scale bar: 20 µm. (E) Expression of NS1-GFP in a set of 9 HCC cell lines 24 h after LNP uptake analyzed by confocal microscopy with corresponding bright field image (insert). Green: NS1-GFP. Scale bar: 150 µm. (F) Analysis of NS1-GFP expression in 9 HCC cell lines by flow cytometry 24 h after LNP uptake. A representative flow cytometry dot blot for each cell line is shown. Black: vector-treated control cells, green: NS1-GFP. Quantification of NS1-GFP positive cells, expressed as percentage of total cells (bar) and shift in relative mean fluorescence intensity (cross). Results represent means ± S.D. of *n* = 3 experiments. (G) Western blot analysis of NS1 expression 24 h after LNP uptake. NS1 (+) was visualized using a polyclonal anti-NS1 antibody[19], empty vector (-) was used as control. β-actin was used as protein loading control. (H) Expression and nuclear localization of NS1-GFP and GFP in HuH7 cells 24 h after LNP uptake analyzed by confocal microscopy. Blue: cell nuclei (Hoechst 33324); white: plasma membrane (Cell Mask); green: GFP or NS1-GFP. Scale bar: 10 µm.

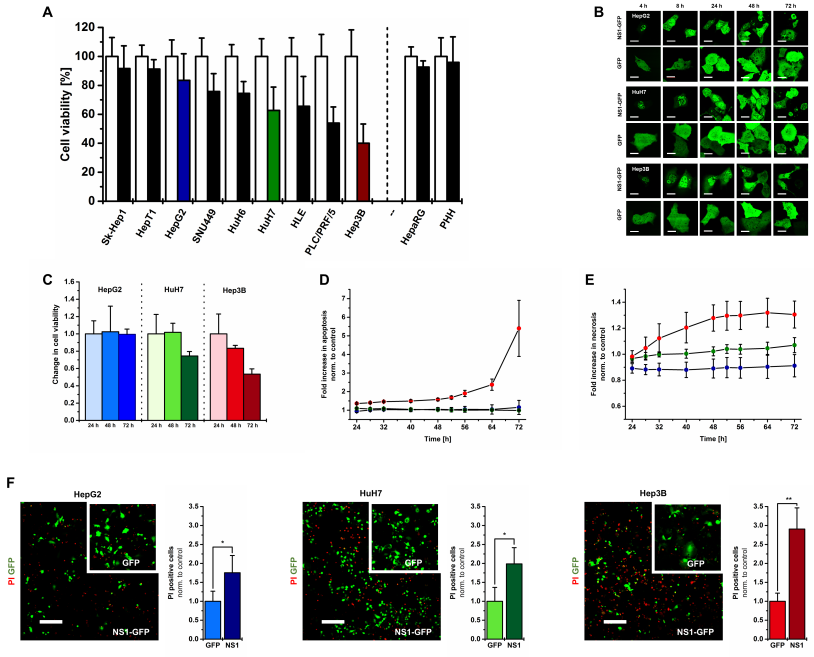

Figure 2 Pharmacological effects of NS1 expression in HCC cells. HCC cells were incubated with LNPs containing pDNA (0.1 ng/cell) coding for an NS1-green fluorescence protein (GFP) fusion protein (NS1-GFP), GFP, or empty vector control. (A) Analysis of cell viability 72 h after LNP uptake using the MTT assay. Results are expressed as relative cell viability normalized to vector-treated control cells. Results represent mean ± S.D. of *n* = 4 experiments. (B) Analysis of NS1-GFP and GFP expression over time by confocal microscopy. Green: GFP or NS1-GFP. Scale bar: 20 µm. (C) Change in cell viability over time analyzed 24, 48, and 72 h after LNP uptake. Relative cell viability normalized to vector-treated control cells is expressed as fold change. Values represent mean ± S.D of *n* = 3 experiments. (D, E) Induction of apoptosis and necrosis over time after NS1 gene delivery analyzed by fluorescence and luminescence-based kinetic assays. Results were normalized to vector-treated control cells and represent mean ± S.D. of *n* = 3 experiments. (F) Staining of dead cells using propium iodide (PI) 24 h after LNP uptake. Red: dead cells (PI), green: GFP (insert) or NS1-GFP. Scale bar: 200 µm. Fluorescence was quantified and normalized to GFP control cells (insert) and is presented as mean ± S.D. of *n* = 4 experiments.

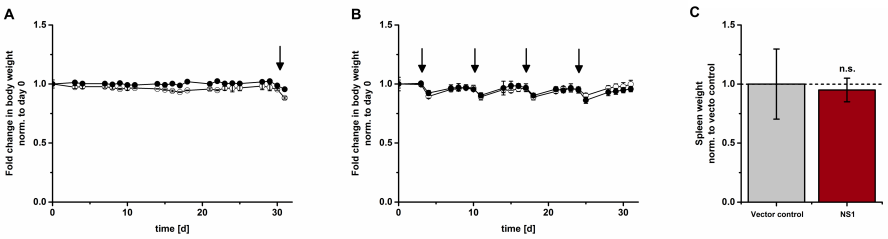

Figure 3 Toxicity of non-viral gene delivery of NS1 *in vivo*. LNPs containing pDNA coding for NS1 or empty vector control were administered i.p. in mice as (A) single dose or (B) weekly over a period of 4 weeks. Body weight was measured and normalized to day zero (start of the experiment). Treatment days are indicated with black arrows. (C) Spleens were resected after 4 weeks of weekly administration of LNPs, were weighted, and mean weight normalized to vector-treated control mice. Results are shown as mean ± S.D. of *n* = 4 experiments. Grey: vector-treated control mice, red: NS1-treated mice.

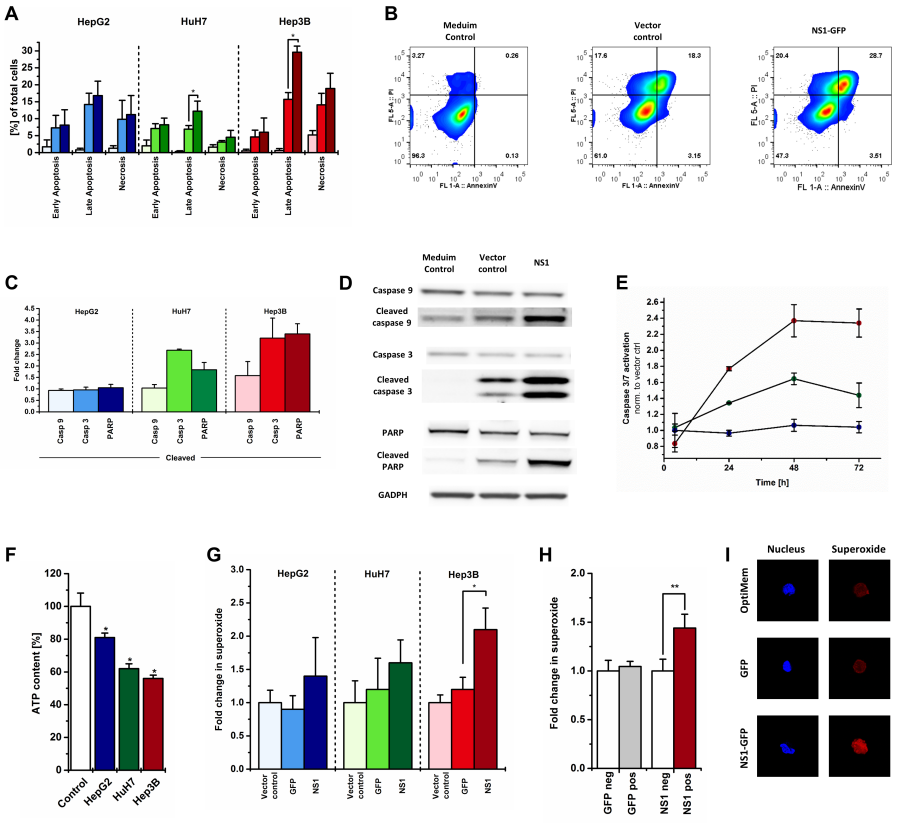

Figure 4 Induction of apoptosis and necrosis after NS1 expression. Cells were incubated with LNPs containing pDNA (0.1 ng/cell) coding for NS1-GFP, GFP, or empty vector control. (A) Percentage of cells in apoptosis and necrosis determined by Annexin V/PI staining analyzed by flow cytometry 72 h after LNP uptake: medium control (left panel, light color), vector control (middle panel, medium color), and NS1-GFP (right panel, dark color). Results normalized to medium control are expressed as mean ± S.D. of *n* = 3 experiments ($p < 0.05$). (B) Representative density plot of Annexin V/PI stained Hep3B cells. (C) Analysis of native and cleaved caspases 9/3 and PARP by western blot 72 h after LNP uptake. Ratios of cleaved vs. non-cleaved caspases 9/3 and PARP normalized to vector-treated control cells are shown as mean ± S.D. of *n* = 3 experiments. GADPH was used as protein loading control. (D) Representative western blot of apoptotic proteins form (C) of Hep3B cells. (E) Analysis of caspase 3/7 activity over time after LNP uptake using a luminescence-based assay. Normalized results (vector control) are shown as mean ± S.D. of *n* = 3 experiments. Red: Hep3B; green: HuH7;

blue: HepG2. (F) Intracellular ATP content 24 h after LNP uptake. Results normalized to vector-treated control cells represent mean ± S.D. of $n = 3$ experiments ($p < 0.01$). (G) Induction of superoxide accumulation 24 h after LNP uptake analyzed by flow cytometry. Results normalized to vector-treated control cells represent mean ± S.D. of $n = 3$ experiments ($p < 0.05$). (H) Representative confocal microscopy image of Hep3B cells. Blue: nucleus (Hoechst 33342), red: superoxide (Superoxide detection reagent).

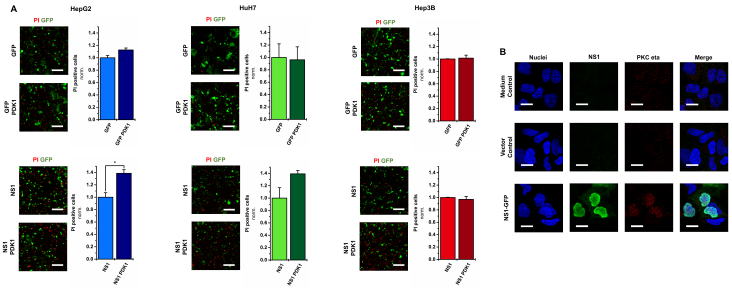

Figure 5 Biomarker for NS1 therapy. (A) Influence of constitutive active PDK1 (PDK1:S138E) on NS1 toxicity after non-viral gene delivery. PDK1:S138E was expressed using recombinant adeno-associated viruses (rAAVs) and GFP or NS1-GFP was subsequently delivered using LNPs (0.1 ng pDNA/cell). Propium iodide staining was used 72 h post LNP uptake to visualize dead cells. Red: dead cells (PI), green: GFP or NS1-GFP. Quantified PI signal was normalized to non-transduced cells. Values represent mean ± S.D. of $n = 4$ experiments ($p < 0.05$). Scale bar: 150 µm. (B) Intracellular localization of PKCη. HuH7 cells analyzed 24 h after LNP uptake. Blue: cell nuclei (Hoechst 33342), green: NS1-GFP, red: PKCη (sc-136036). Scale bar: 20 µm.

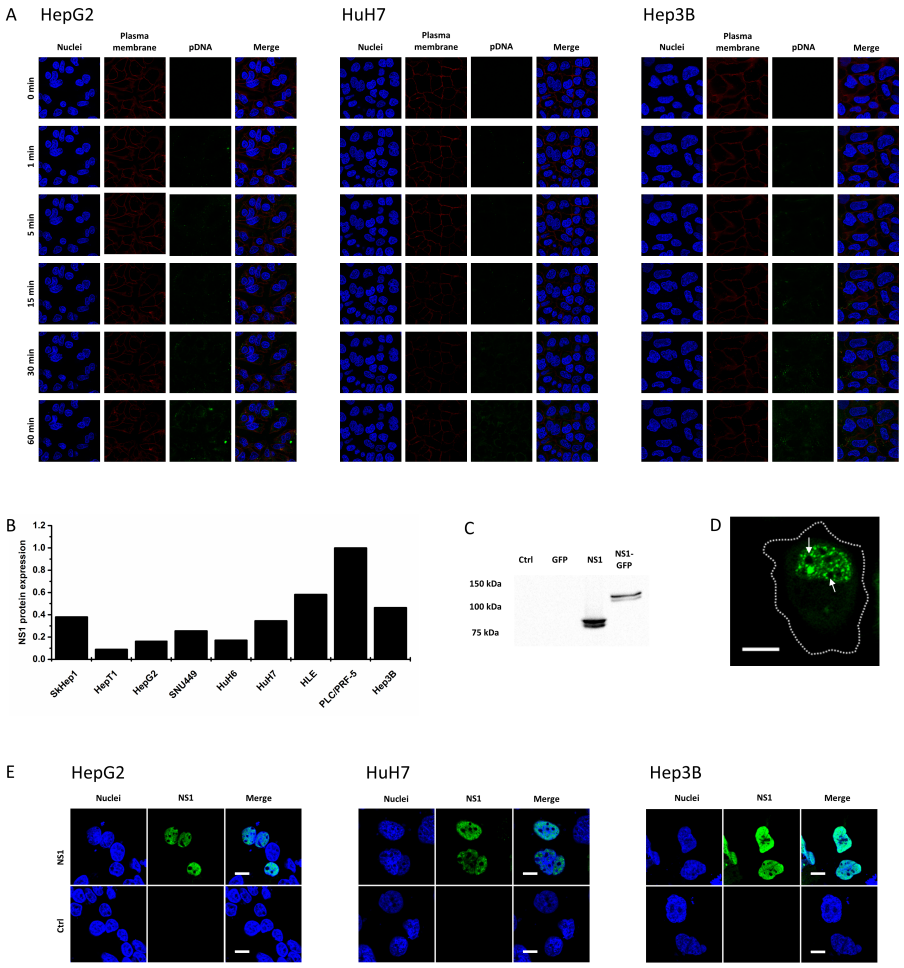

Supplementary Figure S1 (A) Uptake of LNPs by the three selected cell lines after 0, 1, 5, 15, 30, and 60 min of incubation analyzed by confocal microscopy. Blue: cell nuclei (Hoechst 33342); Red: plasma membrane (Cell Mask); Green: pDNA (DiYO-1). (B) Quantification of NS1 expression by western blotting 24 h after LNP uptake. (C) Western blot analysis of NS1 and the NS1-GFP fusion protein 24 h after LNP uptake. (D) Nuclear localization of NS1-GFP in HuH7 cells 4 h after LNP uptake analyzed by confocal microscopy. Cell morphology is outlined (dashed line), nucleoli are indicated by white arrows. Scale bar: 10 µm. (E) Nuclear localization of NS1 after non-viral gene delivery analyzed

by confocal microscopy 24 h after LNP uptake. Blue: cell nuclei (Hoechst 33342); green: NS1 (polyclonal anti-NS1 antibody). Scale bar: 10 µm.

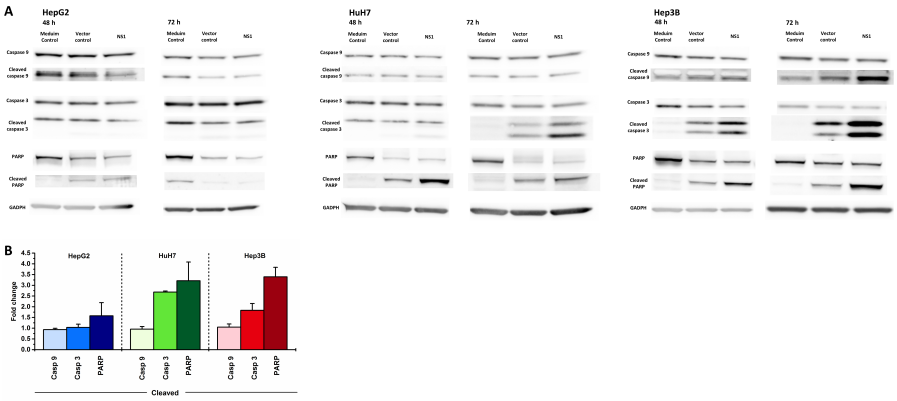

Supplementary Figure S2 (A) Analysis of native and cleaved caspases 9/3 and PARP by western blot 48 and 72 h after LNP uptake. Representative western blots of non-cleaved and cleaved caspases 9/3 and PARP. GADPH was used as protein loading control. (B) Quantification of (A) 48 h after LNP uptake. The ratio of cleaved versus non-cleaved (native) caspases 9/3 and PARP normalized to vector-treated control cells represented as mean ± S.D. of *n* = 3 experiments.

Experimental section

Lipoplex preparation and characterization

DNA-Lipoplex Preparation. pDNA lipid nanoparticles (LNPs) were produced according to the manufacturers recommendation. In brief, pDNA was diluted in OptiMEM, mixed thoroughly, and p3000 reagent was added. Lipofectamine was diluted with OptiMEM, mixed with the pDNA mixture, and vortexed. After 5 min of incubation at room temperature, LNP were used for further experiments. For *in vivo* experiments, OptiMEM transfection medium was replaced by sterile glucose solution (5% w/v).

Nanoparticle Tracking Analysis. LNP size and size distribution was determined by Nanoparticle Tracking Analysis (NTA) using a Nanosight NS200, LM20 (Malvern Instruments Ltd., Malvern, United Kingdom) equipped with a 405 nm laser as described previously[56]. In brief, the chamber was cleaned before measurements using 0.02 µm filtered (Anotop 25, Whatman, Glattbrugg, Switzerland) water and absence of particles was confirmed. LNPs were prepared as described above and were injected using a 1 mL sterile syringe (Norm-Ject, HSW, Tuttlingen, Germany). Four videos of 90 s were recorded using replenished sample for each measurement. Settings for video recording were set to obtain clear and sharp images. NTA 2.2 software was used for capturing and analysis of average particle size and size distribution. In order to obtain statistically reliance, a minimum of 300 completed tracks was required. Results are expressed as mean ± S.D. of n = 4 experiments.

Zeta Potential Measurement. The zeta potential of LNPs was determined using the Delsa Nano C Particle Analyser (Beckman Coulter, Nyon, Switzerland). Samples were analyzed using a laser wavelength of 685 nm operated in an angle of 15° and converted according to the Smoluchowski equation.

Transmission Electron Microscopy. LNPs were visualized by transmission electron microscopy (TEM) after negative staining. In brief, 5 µL of the LNP suspensions were mounted on a carbon-coated copper grid, negatively stained with uranyl acetate (2%), and dried overnight. Samples were then analyzed using a CM-100 transmission microscope (Philips, Eindhoven, Netherlands) at an accelerating voltage of 80 kV. Size was determined by measuring n = 100 particles and results are depicted as mean ± S.D.

Cloning of plasmids

Cloning of plasmids. pcDNA3.1$^+$ was obtained from Invitrogen (Zug, Switzerland) and pTagGFP-N was purchased from Evrogen (Moscow, Russia). pdB-H-1PVwt (German Cancer

Research Center DKFZ, Heidelberg, Germany) was used as template for NS1 and extracted by polymerase chain reaction (PCR) using primers 1 and 2 (pcDNA3.1-NS1) and primers 1 and 3 (pTag-NS1-GFP) [Supplementary experimental section]. Phusion® High-Fidelity DNA Polymerase (New England Biolabs, Ipswich, MA, USA) was used according to the manufacturers recommendation. DNA was initially denaturated at 98 °C for 30 sec followed by 35 cycles of denaturating (98 °C, 10 sec), annealing (67 °C, and elongation (72 °C, 45 sec). DNA was extended finally at 72 °C for 10 min. Subsequently, the PCR product was digested and ligated into the expression plasmids pcDNA3.1$^+$ (pcDNA3.1-NS1 using BamHI and NotI sites) or pTagGFP-N (pTag-NS1-GFP using BamHi sites). The resulting plasmids were sequenced to confirm NS1 sequence and correct reading frame. Plasmids were then purified using the Plasmid Mini Kit (Qiagen, Hombrechtikon, Switzerland) in accordance with the manufacturers recommendations.

Cell culture

Cell culture. Human hepatoma cell lines (HepG2, Hep3B, HuH7, HuH6, SNU449, PLC/PRF-5, HepT1, HLE, SkHep1) were cultured in Dulbecco's modified Eagle's culture medium high glucose (DMEM) supplemented with 10% FCS, penicillin 100 U/mL, and streptomycin 100 µg/mL at 37 °C and 5% CO_2 and saturated humidity. Primary human hepatocytes (donor: BHum 16043) were obtained from QPS Hepatic Biosciences (Barcelona, Spain). Cells were maintained in Fresh Maintenance Medium (FMM, QPS Hepatic Biosciences, Barcelona, Spain) supplemented with dexamethasone according to the manufacturers recommendation at 37 °C and 5% CO_2 and saturated humidity. HepaRG cells were cultured as described previously [57,58].

Transfection of adherent cells. A standard transfection protocol was developed. Cells were seeded in complete culture medium at a density of 2.5 x 10^4 cells/cm^2 in poly-D-lysine coated (0.4 mg/mL) wells or slides and allowed to adhere over night. Plasmid DNA (pDNA) was added at a concentration 0.1 ng pDNA per cell (1 µg/mL) using freshly prepared LNP formulation (see above).

NS1-GFP expression analysis.

Confocal microscopy. Cells were seeded in a 24-well plate (TPP, Transadigen, Switzerland) and were transfected with GFP or NS1-GFP as described above. Expression of GFP and NS1-GFP fluorescence was analyzed using a FV1000 confocal microscope (Olympus, Tokyo, Japan) equipped with a 10x water immersion objective (NA 0.4; Olympus, Tokyo, Japan). Excitation and emission

wavelength were 488 nm and 516 nm, respectively. For live cell imaging, cells were seeded on glass bottom culture slides (µ-slide, Ibidi, Martiensried, Germany) and cultured in complete culture medium using phenol red-free DMEM.

Flow cytometry. To quantify the percentage of NS1-GFP expressing cells and the average expression level, transfected cells were analyzed by flow cytometry. Cells were detached at inidcated time points, washed once with D-PBS, centrifuged (400 x g, 5 min, 4 °C) and resuspended in FACS staining buffer (D-PBS supplemented with 0.05% NaN_3 and 1% FCS). Cells were then analyzed by flow cytometry using a FACS Canto II flow cytometer (Becton Dickinson, San Jose, CA, USA) exciting at 488 nm. Doublets were excluded and fluorescence signals were collected using FL1 (505LP-530/30). Results were analyzed using Flow Jo VX (TreeStar, Ashland, OR, USA) and percentage of NS1-GFP-positive cells was evaluated. Mean fluorescence intensities (MFI) were normalized to vector-treated control cells. Results are shown as mean ± S.D. of *n* = 3 experiments.

NS1 expression analysis.

NS1 staining and confocal microscopy. For analysis of NS1 expression in adherent cells, cells were seeded on a 254 mm^2 cover slip (Menzel Gläser, Braunschweig, Germany) coated with poly-D-lysine (0.4 mg/mL). At indicated time points post transfection, cells were washed three times with D-PBS (0.5 mM Ca^{2+}, 1 mM Mg^{2+}) and fixed using 4% PFA (30 min, RT). Cells were then incubated with D-PBS (50 mM NH_4Cl) for 6 min at RT and treated with Triton-X100 0.1% for 10 min at RT. Cells were then washed three times with D-PBS (0.5 mM Ca^{2+}, 1 mM Mg^{2+}) and incubated with FCS 10% for 30 min. After blocking, cells were incubated with primary antibody (*Dr. Jürg Nüesch, DKFZ, Heidelberg*) in FACS staining buffer for 2 h at RT. Cells were washed three times with D-PBS (0.5 mM Ca^{2+}, 1 mM Mg^{2+}) and incubated with secondary antibody (DILUTION) in FACS staining buffer for 60 min at RT under light protection. Hoechst 33342 was added at a final concentration of 0.1 µg/mL 10 min prior to the end of the staining procedure. Expression of GFP and NS1-GFP fluorescence was analyzed using a FV1000 confocal microscope (Olympus, Tokyo, Japan) using a 60x oil immersion objective (NA 1.4; Olympus, Tokyo, Japan). Excitation and emission wavelength were 488 nm and 516 nm, respectively. Emission wavelengths were 405 nm and 488 nm, fluorescence was collected at 425-575 nm and 500-545 nm, respectively.

Western blot analysis.

Extraction of proteins. Expression of NS1 and intracellular kinases was analyzed by western blotting. Collection of cellular proteins was performed on ice. At indicated time points, culture medium was collected and cells were detached in ice cold D-PBS using a pre-cooled cell scraper. Supernatant and cell suspension were centrifuged (590 x g, 5 min, 4 °C) and resuspended in 60 µL of IP-buffer (20 mM Hepes pH 7.5, 5 mM MgCl, 300 mM NaCl, 0.1% NP40) containing 1x protease and phosphatase inhibitor cocktail (Roche diagnostics, Indianapolis, USA). Cells were incubated on ice for 30 min and vortexed every 10 min. Cell extracts were used immediately after preparation or snap frozen in liquid nitrogen and stored at -80 °C. Total protein concentration was determined using the Pierce BCA Protein Assay Kit (Thermo Scientific, Zug, Switzerland) according to the manufacturers recommendation. For further analysis, samples were mixed with 4x sample buffer (140 mM SDS, 20% glycerol, 25% β-mercaptoethanol, bromphenol blue) and incubated at 96 °C for 5 min.

SDS Page. 7.5% acrylamide gels were casted manually according to the manufacturers recommendation. After completion of polymerization, slots were washed with water and gels were mounted in the gel running chamber. Running buffer (25 mM Tris, 0.19 mM glycine, 3.5 mM SDS) was added. Samples and protein standard (NAME) were loaded into the slots and proteins were separated at 120 V.

Western blotting. Proteins were blotted on cellulose or PVDF (Immobilon-P®) membranes using a semi-dry approach. In brief, 6 filter papers soaked in blotting buffer (48 mM Tris pH 9.2, 39 mM glycine, 1.3 mM SDS, 20% MeOH) were placed on the anode of the blotting chamber (XX,XX,XX). Pre-wetted membranes were placed on top and covered by SDS page gels. 6 pre-soaked filter papers were placed on top and proteins were blotted at 0.7 mA/cm^2 of membrane for 1.5 h.

Immuno-staining of proteins. Blotted membranes were blocked by 3% BSA, 10% skim milk, or 2% casein in TBS-T (20 mM Tris-HCl pH 7.5, 150 mM NaCl, 0.05% Tween 20) for 60 min at RT. Membranes were incubated with appropriate primary antibodies over night at 4 °C in TBS-T, washed three times with TBS-T, and incubated with horseradish-peroxidase-conjuagted secondary antibodies for 60 min at RT. After repetition of the washing procedure, Western ECL Blotting Substrates (Bio-Rad, Hercules, CA, USA) were added to produce luminescence. ANALYSIS

Subcellular localization of NS1

Live cell imaging of NS1-GFP. To analyze expression and subcellular localization of NS1-GFP, cells were seeded in poly-D-lysine coated glass bottom culture slides (µ-slide, Ibidi, Martiensried, Germany) and transfected as described above. At indicated time-points, images were captured by confocal laser scanning microscopy using a FV1000 microscope (Olympus, Tokyo, Japan) equipped with a 60x oil immersion objective (NA 1.4; Olympus, Tokyo, Japan). Samples were excited at 488 nm and fluorescence was collected at 500-545 nm. Due to changes in NS1-GFP expression, laser intensity was adjusted at each time point. In additional samples, cell nuclei and plasma membrane were stained 24 h post transfection using Hoechst 33342 and Cell Mask (manufacturer), respectively. Cells were incubated with Hoechst 33342 at a final concentration of 0.1 µg/mL for 10 min at 37 °C and washed three times with D-PBS. Then, 200 µL of Cell Mask staining solution (0.2 µL Cell Mask/400 µL culture medium) was added. Images were captured using a FV1000 microscope (Olympus, Tokyo, Japan) equipped with a 60x objective (NA 1.4; Olympus, Tokyo, Japan). Emission wavelengths were 405 nm, 488 nm, and 635 nm. Fluorescence was collected at 425-575 nm, 500-545 nm, and 655-755 nm, respectively.

Analysis of the pharmacological effect *in vitro*

Cell viability assay. *In vitro* cell viability was determined using the MTT assay. Cells were seeded in 250 µL of complete culture medium in poly-D-lysine coated 96-well plates (TPP, Transadigen, Switzerland). Terfenadine (20 µM) was used as positive control. After indicated time points, 100 µL of the culture medium was removed carefully and 100 µL of MTT working solution (Thiazolyl blue, 5 mg/mL) were added. Cells were incubated for 2-4 h at 37 °C. Then, medium was removed and formazan crystals were dissolved with acidified isopropyl alcohol (100 µL) and SDS (3%, 20 µL). Absorption was measured at 570 nm and unspecific signals measured at 670 nm were substracted (Spectramax M2 plate reader, Molecular Devices, Sunnyvale, CA, USA). Cell viability was expressed as percentage, whereas cells treated with empty vector (?) were defined as 100%. MTT assays were performed in triplicates and repeated three times and results are expressed as mean ± S.D.

Intracellular ATP content. Intracellular ATP content was analyzed using the CellTiter Glo Luminescent cell viability assay (Promega, Wallisellen, Switzerland) in accordance with the

manufacturers recommendation as described previously [30]. In brief, 100 µL of assay buffer were added to each 96-well containing 100 µL of complete culture medium. Samples were incubated for 12 min at RT under light protection and luminescence was measured using a XXX reader. Intracellular ATP content is normalized to vector-treated control cells. 0.1% Triton-X100 was used as positive control. Results are shown as mean ± S.D. of *n* = 3 experiments.

Kinetic cell viability assay. Cell viability over time was determined using the RealTime-Glo™ MT Cell Viability Assay (Promega, Madison, WI, USA) with modifications. In brief, cells were seeded in 96-well plates (TPP, Transadigen, Switzerland) and transfected as described above. 100 µL of culture medium were removed 8 h post transfection and MT Cell Viability Substrate and NanoLuc® Enzyme were added at a concentration of 1x at a total volume of 200 µL per well. At indicated time points, luminescence was collected with an integration time of 1000 ms using an Infinite 200Pro plate reader (Tecan, Männedorf, Switzerland) and cell viability was calculated. Values were normalized to vector-treated control cells. Experiments were performed in quadruplicates and results are expressed as mean ± S.D.

Kinetic apoptosis assay. Apoptosis induction over time was analyzed by using the prototype RealTime-Glo™ Annexin V Apoptosis Assay (Promega, Madison, WI, USA) with midifications. In brief, cells were seeded in 96-well plates (TPP, Transadigen, Switzerland) and transfected as described above. After 8 h of incubation with LNPs, 100 µL of culture medium were removed. Necrosis Detection Reagent, $CaCl_2$, Annexin V-SmBiT, Annexin V-LgBiT, and RT substrate were added at a concentration of 1x at a total volume of 200 µL. At indicated time points, luminescence (integration time: 1000 ms) and fluorescence (excitation at 488 nm, emission at 525 nm) were measured using a Infinite 200Pro plate reader (Tecan, Männedorf, Switzerland) and increase in apoptosis compared to vector-treated control cells was calculated. Experiments were performed in quadruplicates and results are expressed as mean ± S.D.

Kinetic cytotoxicity assay. Cytotoxicity over time was determined using the CellTox™ Green Cytotoxicity Assay (Promega, Madison, WI, USA) with modifications. Briefly, cells were seeded in 96-well plates (TPP, Transadigen, Switzerland) and transfected as described above. 100 µL of culture medium were removed 8 h post transfection and CellTox™ Green Dye was added at a final concentration of 1x at a total volume of 160 µL. At indicated time points, fluorescence was measured using a Infinite 200Pro (Tecan, Männedorf, Switzerland). Excitation wavelength was 513 nm, fluorescence was collected at an emission wavelength of 532 nm. Fold change in cytotoxicity as

compared to vector-treated control cells was calculated. Experiments were performed in quadruplicates and results are presented as mean ± S.D.

Propium iodide (PI) staining. Cells were seeded in a 96-well plate (TPP, Transadigen, Switzerland) and were transfected with GFP or NS1-GFP as described above. After 72 h, PI was added at a final concentration of 500 nM for 5 min and cells were washed carefully with D-PBS. Fluorescence was analyzed using a FV1000 confocal microscope (Olympus, Tokyo, Japan) using a 10x water immersion objective (NA 0.4; Olympus, Tokyo, Japan). Excitation wavelengths were 488 nm and 559 nm. Fluorescence was detected at 520 nm and 619 nm respectively. Fluorescence was quantified using ImageJ 1.46 software (National Institutes of Health). Lower particle threshold was set to 20 pixels. Percentage of PI positive cells was calculated by dividing counted particles in PI channel by the sum of particles counted in GFP and PI channel. Results are displayed as mean ± S.D of $n = 4$ experiments.

Apoptosis/Necrosis

Annexin V/PI staining. Apoptotic and necrotic cells were stained using the Dead Cell Apoptosis Kit (Thermo Scientific, Zug, Switzerland) with modifications. At indicated time points, cells were detached using 0.25% trypsin-EDTA, washed once, and centrifuged (400 x g, 5 min, 4 °C). Cell pellets were resuspended in 100 µL Annexin V staining buffer (5 µL Alexa Fluor® 488 Annexin V and 95 µL of 1x Annexin-binding buffer) and incubated for 15 min. Then, propium iodide was added to a final concentration of 0.7 µg/mL and cells were incubated for additional 15 min at RT. Fluorescence was then analyzed by flow cytometry using a FACS Canto II flow cytometer (Becton Dickinson, San Jose, CA, USA) exciting at 488 nm and 561 nm. Fluorescence was collected using FL1 (505LP – 530/30) and FL5 (586/15). To evaluate the percentage of apoptotic and necrotic cells, Flow Jo VX software (TreeStar, Ashland, OR, USA) was used. Results are expressed as mean ± S.D. of $n = 3$ experiments.

Caspase 3- and 7 activation assay. Caspase 3 and 7 activation was analyzed using Caspase-Glo 3/7 Assay (Promega, Wallisellen, Switzerland)in accordance with the manufacturers recommendation. Briefly, at indicated time points, 67 µL of freshly prepared Caspase-Glo 3/7 Reagent was added to each 96-well to a total volume of 135 µL. Plates were shaken carefully for 30 sec using a plate mixer and incubated for 60 min at RT. Luminescence was measured using an Infinite 200Pro plate reader (Tecan, Männedorf, Switzerland) with an integration time of 1000 ms. Results were

normalized to vector-treated control cells and are expressed as mean *fold* caspase activation ± S.D. of *n* = 3 experiments.

Detection of apoptosis in western blot. Cells were seeded in 6-well plates (TPP, Transadigen, Switzerland) and transfected as described above. A slightly modified protocol to the one described above was used. In brief, cells were washed with ice-cold D-PBS at indicated time points. Cells were lysed with RIPA buffer (50 nM Tris-HCL pH 7.4, 150 mM NaCl, 1% Triton X-100, 0.5% sodium deoxycholate, 0.1% sodium dodecylsulfate, and 1 mM EDTA) containing 1x protease inhibitor cocktail (Roche diagnostics, Indianapolis, USA) for 15 min under constant agitation. Proteins were collected by centrifugation (15700 x g, 10 min, 4 °C) and protein concentrations were determined by Pierce BCA Protein Assay Kit (Thermo Scientific, Zug, Switzerland) according to the manufacturers recommendation. 15 µg protein for 48 h-samples and 12.5 µg protein for 72 h-samples were separated on 4-12% bis-tris gradient gels using MOPS SDS running buffer (Invitrogen, Carlsbad, CA, U.S.A). After separation, proteins were transferred to nitrocellulose membranes using the Trans-Blot Turbo Transfer System from Bio-Rad (Hercules, CA, U.S.A). After transfer, the membranes were washed once with PBS-T for 5 min at 70 rpm on an orbital shaker and subsequently blocked with 5% skim milk for 1 h at 70 rpm. They then were washed 3 times for 5 min at 70 rpm with PBS Tween and incubated overnight with the indicated primary antibody in the cold room at 4 °C. Membranes were washed three times with PBS-T and were incubated with a HRP conjugated secondary antibody at room temperature for 1 h. Then, membranes were again washed three times with PBS-T before detection. Luminescence was produced using Western ECL Blotting Substrates (Bio-Rad, Hercules, CA, USA) and analyzed using the Fusion Pulse TS device from Vilber Lourmat (Oberschwaben, Germany). In order to incubate the membranes with another antibody, they were stripped for 15 min at 70 rpm with Restore™ PLUS Western Blot Stripping Buffer (Thermo Scientific, Waltham, MA, USA), washed three times with PBS-T, blocked for 1 h with 5% skim milk and washed again three times. Detection of GADPH was used to confirm uniform loading and for normalization.

Detection of superoxide

Analysis of intracellular superoxide. Real-time analysis of reactive oxygen species (ROS) and superoxide induction was performed using the total ROS/Superoxide detection kit (Enzo Life Sciences, Lausen, Switzerland) with modifications. Cells were seeded in 6-well plates (TPP, Transadigen, Switzerland) and transfected as described above. At indicated time points, cells were washed once

with D-PBS and were detached (0.25% trypsin/EDTA). Cells were resuspended in 1 mL of complete culture medium, centrifuged (400 x g, 5 min, RT), and washed once with 1x wash buffer. Cell suspensions were incubated with either 500 µL of oxidative stress detection reagent or superoxide detection reagent at a final concentration of 2 µM for 30 min at 37 °C under light protection. Cells were then analyzed by flow cytometry using a FACS Canto II flow cytometer (Becton Dickinson, San Jose, CA, USA) exciting at 488 nm and 561 nm. Fluorescence signals were collected using FL1 (505LP-530/30) and FL6 (600LP-610/10). Results were analyzed using Flow Jo VX (TreeStar, Ashland, OR, USA). Cells were subsequently analyzed using confocal microscopy. To stain cell nuclei, Hoechst 33342 at a final concentration of 0.1 µg/mL was added for 10 min at RT. Cells were then washed once with D-PBS, centrifuged (400 x g, 5 min, RT), and the pellet was resuspended in 20 µL of D-PBS. Cell suspensions were mounted on cover slips using ProLong Gold according to the manufacturers recommendation. Cells were analyzed using a FV1000 confocal laser scanning microscope (Olympus, Tokyo, Japan) equipped with a 60x oil immersion objective (NA 1.40). Emission wavelengths were 405 nm, 488 nm, and 559 nm, fluorescence was collected at 425-475 nm, 500-545 nm, and 575-620 nm, respectively. Results were normalized to vector-treated control cells. Results are expressed as mean ± S.D of *n* = 3 experiments.

Transduction of PDK1 and PKCη using recombinant adeno-associated viruses

Influence of PDK1 on NS1 toxicity. To study the influence of PDK1 activation on NS1 toxicity, cells were transduced with PDK1:S138E, dominant negative PDK1 (PDK1:K204M), PKCη, or dominant negative PKCη using recombinant adeno-asociated viruses (rAAV)[19]. It should be noted that PDK1:S138E mimics constitutive active PDK1phosphoS135 [19]. In brief, cells were seeded in 96-well plates as described above and transfected with rAAVs (10^4 genomes/cell). If indicated, cells were incubated 24 h post-transduction with LNPs for 72 h. PI at a final concentration of 500 nM was added for 5 min and cells were washed carefully with D-PBS. Fluorescence was analyzed using a FV1000 confocal microscope (Olympus, Tokyo, Japan). LASER. Fluorescence was quantified using ImageJ 1.46 software (National Institutes of Health). Lower particle threshold was set to 20 pixels. Percentage of PI positive cells was calculated by dividing counted particles in PI channel by the sum of particles counted in GFP and PI channel. Results are expressed as mean ± S.D of *n* = 4 experiments.

***In vivo* toxicity**

In vivo toxicity assessment. Animal experiments were authorized by the Ethics committee of the Medical University of Vienna and were performed according to the guidelines of the Federation of Laboratory Animal Science Association (FELASA) as well as the Arrive guidelines. To analyze toxicity of NS1 and empty vector gene delivery, 12 8-week-old female CB-17 scid/scid (SCID) mice were obtained from Harlan Laboratories (San Pietro al Natisone, Italy). Mice were divided into 4 groups. 4 animals received LNPs containing pDNA coding for empty vector or NS1 by weekly i.p. administration at a dose of 200 µg pDNA per injection. For single dose treatment, two animals received either NS1 or vector treatment administered as described above. Body weight was monitored constantly for 31 days. At day 31, mice were sacrificed and spleens were resected and weighted.

Statistical analysis

Statistical analysis. Statistical analysis was performed by one-way analysis of variance (ANOVA) followed by Tukey's *posthoc* test using OriginPro (Version 9.1.0, OriginLab Corporation, Northampton, MA, USA). Number of experiments (*n*) and level of significance are indicated at the respective experiments.

Supplementary experimental

Primers. The following primers were used for cloning of NS1 and NS1-GFP:

Primer 1: 5'-attggatccgcgatggctggaaacgcttactcc-3'

Primer 2: 5'-tattaatgcggccgcttagtccaaggtcagctcctcg-3'

Primer 3: 5'-aatggatccgcgtccaaggtcagctcctcg-3'

Antibodies. Monoclonal and polyclonal anti-NS1 antibodies were kindly provided by Dr. Jürg Nüesch (German Cancer Research Center DKFZ, Heidelberg, Germany). Anti-PDK1 antibody (mouse monoclonal, CP10363) was purchased from Cell Applications Inc. (San Diego, CA, USA). Anti-PKCη (rabbit polyclonal, sc-136036) and anti-GADPH (mouse monoclonal, sc-365062) antibodies were purchased from Santa Cruz Biotechnology (Dallas, TX, USA). Antibodies for detection of caspase 3 (rabbit polyclonal, ♯96655), caspase 9 (mouse monoclonal, ♯95085), and PARP (rabbit monoclonal, ♯95325) were purchased from Cell Signalling Technologies (Danvers, MA, USA).

References

[1] S. Grimm, Introduction, in: S. Grimm (Ed.), Anticancer Genes, Springer London, London, 2014: pp. 1–8. doi:10.1007/978-1-4471-6458-6_1.

[2] M. Los, S. Panigrahi, I. Rashedi, S. Mandal, J. Stetefeld, F. Essmann, K. Schulze-Osthoff, Apoptin, a tumor-selective killer, Biochim. Biophys. Acta BBA - Mol. Cell Res. 1793 (2009) 1335–1342. doi:10.1016/j.bbamcr.2009.04.002.

[3] M. Tavassoli, L. Guelen, B.A. Luxon, J. Gäken, Apoptin: Specific killer of tumor cells?, Apoptosis. 10 (2005) 717–724. doi:10.1007/s10495-005-0930-3.

[4] C. Backendorf, A.E. Visser, A.G. de Boer, R. Zimmerman, M. Visser, P. Voskamp, Y.-H. Zhang, M. Noteborn, Apoptin: Therapeutic Potential of an Early Sensor of Carcinogenic Transformation, Annu. Rev. Pharmacol. Toxicol. 48 (2008) 143–169. doi:10.1146/annurev.pharmtox.48.121806.154910.

[5] K. Geletneky, J. Huesing, J. Rommelaere, J.R. Schlehofer, B. Leuchs, M. Dahm, O. Krebs, M. von Knebel Doebritz, B. Huber, J. Hajda, Phase I/IIa study of intratumoral/intracerebral or intravenous/intracerebral administration of Parvovirus H-1 (ParvOryx) in patients with progressive primary or recurrent glioblastoma multiforme: ParvOryx01 protocol, BMC Cancer. 12 (2012) 1–9. doi:10.1186/1471-2407-12-99.

[6] J.P.F. Nüesch, J. Rommelaere, Tumor Suppressing Properties of Rodent Parvovirus NS1 Proteins and Their Derivatives, in: S. Grimm (Ed.), Anticancer Genes, Springer London, London, 2014: pp. 99–124. doi:10.1007/978-1-4471-6458-6_5.

[7] S.F. Cotmore, P. Tattersall, The Autonomously Replicating Parvovirus of Vertebrates, Adv. Virus Res. 33 (1987) 91–174.

[8] A. Op De Beeck, J. Sobczak-Thepot, H. Sirma, F. Bourgain, C. Brechot, P. Caillet-Fauquet, NS1- and Minute Virus of Mice-Induced Cell Cycle Arrest: Involvement of p53 and p21cip1, J. Virol. 75 (2001) 11071–11078. doi:10.1128/JVI.75.22.11071-11078.2001.

[9] A.O. De Beeck, P. Caillet-Fauquet, The NS1 protein of the autonomous parvovirus minute virus of mice blocks cellular DNA replication: a consequence of lesions to the chromatin?, J. Virol. 71 (1997) 5323–5329.

[10] S. Mousset, Y. Ouadrhiri, P. Caillet-Fauquet, J. Rommelaere, The cytotoxicity of the autonomous parvovirus minute virus of mice nonstructural proteins in FR3T3 rat cells depends on oncogene expression., J. Virol. 68 (1994) 6446–6453.

[11] C. Legrand, S. Mousset, N. Salome, J. Rommelaere, Cooperation of oncogenes in cell transformation and sensitization to killing by the parvovirus minute virus of mice, J. Gen. Virol. 73 (1992) 2003–2009.

[12] J.P.F. Nuesch, J. Rommelaere, NS1 Interaction with CKII : Novel Protein Complex Mediating Parvovirus-Induced Cytotoxicity, J. Virol. 80 (2006) 4729–4739. doi:10.1128/JVI.80.10.4729-4739.2006.

[13] J.P.F. Nuesch, J. Lacroix, A. Marchini, J. Rommelaere, Molecular Pathways: Rodent Parvoviruses--Mechanisms of Oncolysis and Prospects for Clinical Cancer Treatment, Clin. Cancer Res. 18 (2012) 3516–3523. doi:10.1158/1078-0432.CCR-11-2325.

[14] J. Christensen, P. Tattersall, Parvovirus Initiator Protein NS1 and RPA Coordinate Replication Fork Progression in a Reconstituted DNA Replication System, J. Virol. 76 (2002) 6518–6531. doi:10.1128/JVI.76.13.6518-6531.2002.

[15] R.O. Adeyemi, S. Landry, M.E. Davis, M.D. Weitzman, D.J. Pintel, Parvovirus Minute Virus of Mice Induces a DNA Damage Response That Facilitates Viral Replication, PLoS Pathog. 6 (2010) e1001141. doi:10.1371/journal.ppat.1001141.

[16] R.O. Adeyemi, D.J. Pintel, Replication of Minute Virus of Mice in Murine Cells Is Facilitated by Virally Induced Depletion of p21, J. Virol. 86 (2012) 8328–8332. doi:10.1128/JVI.00820-12.

[17] T. Bashir, J. Rommelaere, C. Cziepluch, In Vivo Accumulation of Cyclin A and Cellular Replication Factors in Autonomous Parvovirus Minute Virus of Mice-Associated Replication Bodies, J. Virol. 75 (2001) 4394–4398. doi:10.1128/JVI.75.9.4394-4398.2001.

[18] Z. Ruiz, I.S. Mihaylov, S.F. Cotmore, P. Tattersall, Recruitment of DNA replication and damage response proteins to viral replication centers during infection with NS2 mutants of Minute Virus of Mice (MVM), Virology. 410 (2011) 375–384. doi:10.1016/j.virol.2010.12.009.

[19] S. Bär, J. Rommelaere, J.P. Nüesch, PKCη/Rdx-driven phosphorylation of PDK1: a novel mechanism promoting cancer cell survival and permissiveness for parvovirus-induced lysis, PLoS Pathog. 11 (2015) 1–21. doi:0.1371/journal.ppat.1004703.

[20] M. Boshart, F. Weber, G. Jahn, K. Dorsch-H, B. Fleckenstein, W. Schaffner, others, A very strong enhancer is located upstream of an immediate early gene of human cytomegalovirus, Cell. 41 (1985) 521–530.

[21] A. Elouahabi, J.-M. Ruysschaert, Formation and Intracellular Trafficking of Lipoplexes and Polyplexes, Mol. Ther. 11 (2005) 336–347. doi:10.1016/j.ymthe.2004.12.006.

[22] C. Cziepluch, S. Lampel, A. Grewenig, C. Grund, P. Lichter, J. Rommelaere, H-1 Parvovirus-Associated Replication Bodies: a Distinct Virus-Induced Nuclear Structure, J. Virol. 74 (2000) 4807–4815. doi:10.1128/JVI.74.10.4807-4815.2000.

[23] N.M. Seibel, J. Eljouni, M.M. Nalaskowski, W. Hampe, Nuclear localization of enhanced green fluorescent protein homomultimers, Anal. Biochem. 368 (2007) 95–99. doi:10.1016/j.ab.2007.05.025.

[24] J.P.F. Nüesch, S. Lachmann, J. Rommelaere, Selective alterations of the host cell architecture upon infection with parvovirus minute virus of mice, Virology. 331 (2005) 159–174. doi:10.1016/j.virol.2004.10.019.

[25] M. Di Piazza, C. Mader, K. Geletneky, M. Herrero y Calle, E. Weber, J. Schlehofer, L. Deleu, J. Rommelaere, Cytosolic Activation of Cathepsins Mediates Parvovirus H-1-Induced Killing of Cisplatin and TRAIL-Resistant Glioma Cells, J. Virol. 81 (2007) 4186–4198. doi:10.1128/JVI.02601-06.

[26] M.-J. Marion, O. Hantz, D. Durantel, The HepaRG Cell Line: Biological Properties and Relevance as a Tool for Cell Biology, Drug Metabolism, and Virology Studies, in: P. Maurel (Ed.), Hepatocytes, Humana Press, Totowa, NJ, 2010: pp. 261–272. doi:10.1007/978-1-60761-688-7_13.

[27] S.J. Duellman, W. Zhou, P. Meisenheimer, G. Vidugiris, J.J. Cali, P. Gautam, K. Wennerberg, J. Vidugiriene, Bioluminescent, Nonlytic, Real-Time Cell Viability Assay and Use in Inhibitor Screening,

ASSAY Drug Dev. Technol. 13 (2015) 456–465. doi:10.1089/adt.2015.669.

[28] C. Backendorf, M.H.M. Noteborn, Apoptin Towards Safe and Efficient Anticancer Therapies, in: S. Grimm (Ed.), Anticancer Genes, Springer London, London, 2014: pp. 39–59. doi:10.1007/978-1-4471-6458-6_3.

[29] M. Leist, B. Single, A.F. Castoldi, S. Kühnle, P. Nicotera, Intracellular adenosine triphosphate (ATP) concentration: a switch in the decision between apoptosis and necrosis, J. Exp. Med. 185 (1997) 1481–1486.

[30] P. Haegler, D. Grünig, B. Berger, S. Krähenbühl, J. Bouitbir, Impaired mitochondrial function in HepG2 cells treated with hydroxy-cobalamin[c-lactam]: A cell model for idiosyncratic toxicity, Toxicology. 336 (2015) 48–58. doi:10.1016/j.tox.2015.07.015.

[31] G. Hristov, M. Kramer, J. Li, N. El-Andaloussi, R. Mora, L. Daeffler, H. Zentgraf, J. Rommelaere, A. Marchini, Through Its Nonstructural Protein NS1, Parvovirus H-1 Induces Apoptosis via Accumulation of Reactive Oxygen Species, J. Virol. 84 (2010) 5909–5922. doi:10.1128/JVI.01797-09.

[32] J. Du, M. Yang, S. Chen, D. Li, Z. Chang, Z. Dong, PDK1 promotes tumor growth and metastasis in a spontaneous breast cancer model, Oncogene. (2015). http://www.nature.com/onc/journal/vaop/ncurrent/full/onc2015393a.html (accessed April 18, 2017).

[33] J.P.F. Nüesch, R. Corbau, P. Tattersall, J. Rommelaere, Biochemical Activities of Minute Virus of Mice Nonstructural Protein NS1 Are Modulated In Vitro by the Phosphorylation State of the Polypeptide, J. Virol. 72 (1998) 8002–8012.

[34] J.P.F. Nüesch, S. Dettwiler, R. Corbau, J. Rommelaere, Replicative Functions of Minute Virus of Mice NS1 Protein Are Regulated In Vitro by Phosphorylation through Protein Kinase C, J. Virol. 72 (1998) 9966–9977.

[35] S. Lachmann, S. Bär, J. Rommelaere, J.P.F. Nüesch, Parvovirus interference with intracellular signalling: mechanism of PKCη activation in MVM-infected A9 fibroblasts, Cell. Microbiol. 10 (2008) 755–769. doi:10.1111/j.1462-5822.2007.01082.x.

[36] C.E. Thomas, A. Ehrhardt, M.A. Kay, Progress and problems with the use of viral vectors for gene therapy, Nat. Rev. Genet. 4 (2003) 346–358. doi:10.1038/nrg1066.

[37] Assessment of adenoviral vector safety and toxicity: report of the National Institutes of Health Recombinant DNA Advisory Committee, Hum. Gene Ther. 13 (2002) 3–13.

[38] D.W. Pack, A.S. Hoffman, S. Pun, P.S. Stayton, Design and development of polymers for gene delivery, Nat. Rev. Drug Discov. 4 (2005) 581–593. doi:10.1038/nrd1775.

[39] J.P.F. Nüesch, Regulation of non-structural protein functions by differential synthesis, modification and trafficking, in: J.R. Kerr, S.F. Cotmore, M.E. Bloom, M.R. Linden, C.R. Parrish (Eds.), The Parvoviruses, Taylor & Francis Group, Boca Raton, FL, 2006.

[40] J.P. Nüesch, P. Tattersall, Nuclear targeting of the parvoviral replicator molecule NS1: evidence for self association prior to nuclear transport, Virology. 196 (1993) 637–651.

[41] T.O. Ihalainen, E.A. Niskanen, J. Jylhävä, T. Turpeinen, J. Rinne, J. Timonen, M. Vihinen-Ranta, Dynamics and interactions of parvoviral NS1 protein in the nucleus, Cell. Microbiol. 9 (2007) 1946–1959. doi:10.1111/j.1462-5822.2007.00926.x.

[42] C. Holohan, S. Van Schaeybroeck, D.B. Longley, P.G. Johnston, Cancer drug resistance: an evolving paradigm, Nat. Rev. Cancer. 13 (2013) 714–726. doi:10.1038/nrc3599.

[43] G. Housman, S. Byler, S. Heerboth, K. Lapinska, M. Longacre, N. Snyder, S. Sarkar, Drug Resistance in Cancer: An Overview, Cancers. 6 (2014) 1769–1792. doi:10.3390/cancers6031769.

[44] R. Bhat, S. Dempe, C. Dinsart, J. Rommelaere, Enhancement of NK cell antitumor responses using an oncolytic parvovirus, Int. J. Cancer. 128 (2011) 908–919. doi:10.1002/ijc.25415.

[45] M.H. Moehler, M. Zeidler, V. Wilsberg, J.J. Cornelis, T. Woelfel, J. Rommelaere, P.R. Galle, M. Heike, Parvovirus H-1-induced tumor cell death enhances human immune response in vitro via increased phagocytosis, maturation, and cross-presentation by dendritic cells, Hum. Gene Ther. 16 (2005) 996–1005.

[46] M. Moehler, M. Zeidler, J. Schede, J. Rommelaere, P.R. Galle, J.J. Cornelis, M. Heike, Oncolytic parvovirus H1 induces release of heat-shock protein HSP72 in susceptible human tumor cells but may not affect primary immune cells, Cancer Gene Ther. 10 (2003) 477–480. doi:10.1038/sj.cgt.7700591.

[47] S. Bär, L. Daeffler, J. Rommelaere, J.P.F. Nüesch, Vesicular Egress of Non-Enveloped Lytic Parvoviruses Depends on Gelsolin Functioning, PLoS Pathog. 4 (2008) e1000126. doi:10.1371/journal.ppat.1000126.

[48] L. Daeffler, R. Horlein, J. Rommelaere, J.P.F. Nuesch, Modulation of Minute Virus of Mice Cytotoxic Activities through Site-Directed Mutagenesis within the NS Coding Region, J. Virol. 77 (2003) 12466–12478. doi:10.1128/JVI.77.23.12466-12478.2003.

[49] J.P.F. Nuesch, S. Lachmann, R. Corbau, J. Rommelaere, Regulation of Minute Virus of Mice NS1 Replicative Functions by Atypical PKC In Vivo, J. Virol. 77 (2003) 433–442. doi:10.1128/JVI.77.1.433-442.2003.

[50] P. Grossen, J.P.F. Nüesch, Second and third generation of oncolytic parvovirus therapy of cancer, 2012.

[51] D. Pal, S.P. Outram, A. Basu, Novel regulation of protein kinase C-η, Biochem. Biophys. Res. Commun. 425 (2012) 836–841. doi:10.1016/j.bbrc.2012.07.163.

[52] V. Cenni, H. Döppler, E.D. Sonnenburg, N. Maraldi, A.C. Newton, A. Toker, Regulation of novel protein kinase C ε by phosphorylation, Biochem. J. 363 (2002) 537–545.

[53] J. Downward, Mechanisms and consequences of activation of protein kinase B/Akt, Curr. Opin. Cell Biol. 10 (1998) 262–267.

[54] K.-J. Yang, S. Shin, L. Piao, E. Shin, Y. Li, K.A. Park, H.S. Byun, M. Won, J. Hong, G.R. Kweon, G.M. Hur, J.H. Seok, T. Chun, D.P. Brazil, B.A. Hemmings, J. Park, Regulation of 3-Phosphoinositide-dependent Protein Kinase-1 (PDK1) by Src Involves Tyrosine Phosphorylation of PDK1 and Src Homology 2 Domain Binding, J. Biol. Chem. 283 (2008) 1480–1491. doi:10.1074/jbc.M706361200.

[55] X. Wu, J. Wang, F. Liu, P. Ao, X. Li, H. Zheng, D. Wu, N. Zhang, J. She, J. Yuan, Correlation of PDK1 expression with clinicopathologic features and prognosis of hepatocellular carcinoma, OncoTargets Ther. Volume 9 (2016) 5597–5602. doi:10.2147/OTT.S110646.

[56] A. Ríos Quiroz, J. Lamerz, T. Da Cunha, A. Boillon, M. Adler, C. Finkler, J. Huwyler, R. Schmidt, H.-C. Mahler, A.V. Koulov, Factors Governing the Precision of Subvisible Particle Measurement Methods –

A Case Study with a Low-Concentration Therapeutic Protein Product in a Prefilled Syringe, Pharm. Res. 33 (2016) 450–461. doi:10.1007/s11095-015-1801-4.

[57] C. Aninat, EXPRESSION OF CYTOCHROMES P450, CONJUGATING ENZYMES AND NUCLEAR RECEPTORS IN HUMAN HEPATOMA HepaRG CELLS, Drug Metab. Dispos. 34 (2005) 75–83. doi:10.1124/dmd.105.006759.

[58] B. Berger, M. Donzelli, S. Maseneni, F. Boess, A. Roth, S. Krähenbühl, M. Haschke, Comparison of Liver Cell Models Using the Basel Phenotyping Cocktail, Front. Pharmacol. 7 (2016). doi:10.3389/fphar.2016.00443.

DISCUSSION

During the last decades, great progress in the field of nanomedicine was made. Various drug formulations were developed and tested in a preclinical and clinical setting. This PhD project focused on the development of nanoparticulate drug delivery systems for the treatment of cancer. In a first part (**Chapter II-IV**), a versatile drug delivery system for small molecular anticancer compounds was developed. In a second part (**Chapter V**), a novel gene therapy approach for the treatment of liver cancer was implemented. Nanomedicines for cancer therapy need to overcome several hurdles to reach their site of action: NPs need to **show a long blood circulation time**, **extravasate to the tumor microvascular environment** (TME), **penetrate the tumor**, **be internalized** by (preferentially) cancer cells, and **release the drug** at the site of action [153]. Many of these aspects were analyzed during this PhD project and are summarized in the following section.

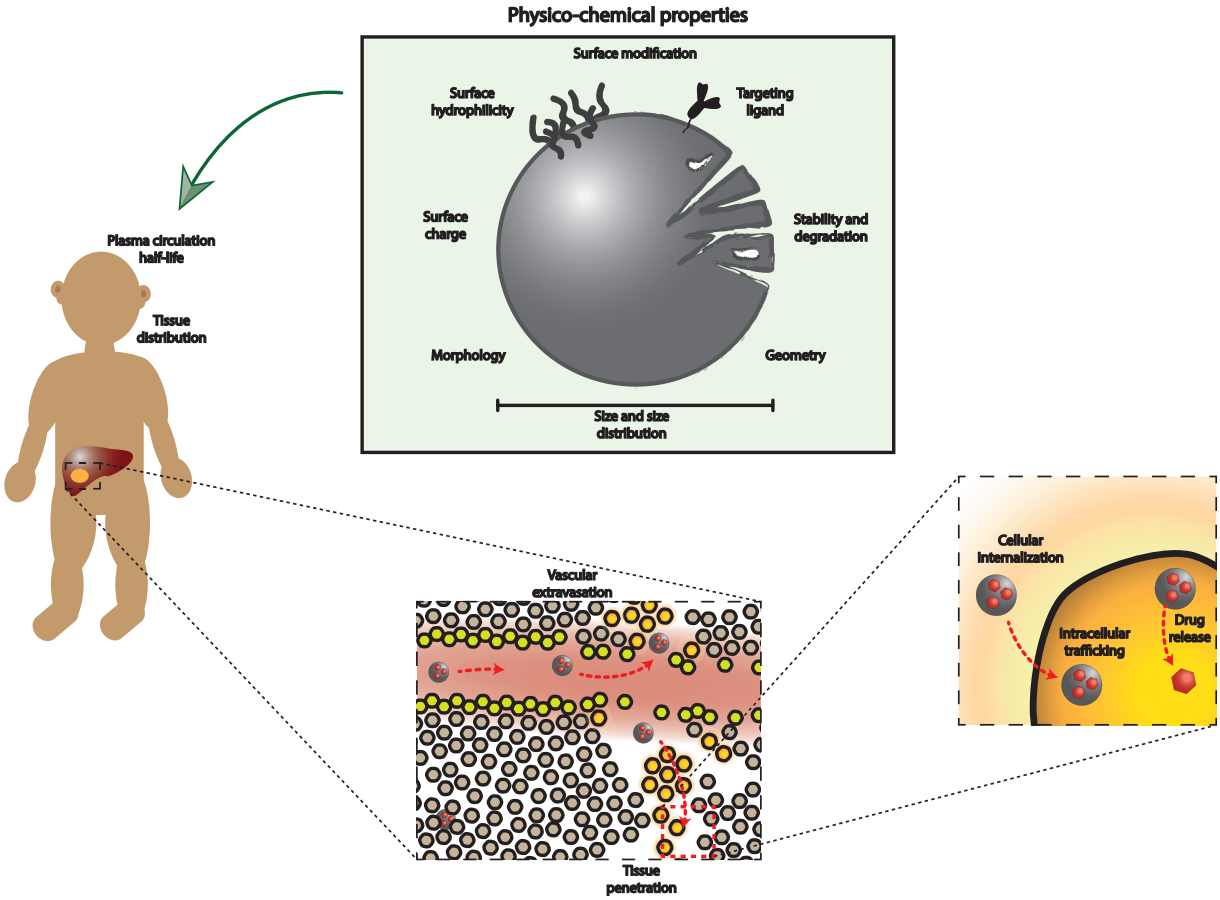

Figure 5 Physico-chemical characteristics of nanoparticles and hurdles in tumor targeting [154].

1 PHYSICO-CHEMICAL CHARACTERIZATION

PEG-PCL was chosen as biocompatible and biodegradable di-block copolymer. General aspects and advantages of this polymer are reviewed in **Chapter I**. In a first step, a preparation protocol for PEG-PCL micelles was developed. Resulting PEG-PCL micelles had a spherical shape, were

characterized by a solid-sphere (i.e. micelle-like) structure, and were below 100 nm in diameter (Table 1). In addition parameters such as the critical aggregation concentration (CAC) and the aggregation number (i.e. number of polymer unimers per micelle, N_{agg}) were determined.

Table 1 Summary of physico-chemical properties of PEG-PCL micelles and expert opinion on their impact for tumor targeting.

Characteristics	Method	Result	Impact
Critical aggregation concentration (CAC)	Pyrene encapsulation	2.8×10^{-7} M [155]	**(+)** Stability upon dilution (e.g. injection), **(+)** Prevention of burst relesae
	Langmuir	2.8×10^{-7} M [Fig. S3]	
Aggregation number	Specific volume	2200-10 000 [155]	
	Nanoparticle tracking analysis (NTA)	139 ± 17 [Fig. S1]	
Shape	Transmission electron microscopy (TEM)	Spherical [155,156]	**(+)** Efficient cellular uptake **(+)** Long blood-circulation time **(-)** High aspect ratio favorable for deep tumor penetration
Core morphology	Cryo-EM	Solid-spheres [155]	**(+)** Ideal for hydrophobic drugs **(-)** Delivery of hydrophilic drugs
	Static light scattering (SLS)	Solid-spheres	
Size (Diameter)	Dynamic light scattering (DLS)	78.2 ± 1.7 nm [155]	(+) Favorable PK properties (+) Passive tumor accumulation (+) Efficient cellular uptake (+) Size-dependent tumor penetration
	NTA	83.2 ± 19 nm [Fig. S1]	
	TEM	67 ± 15 nm [155]	
	Ultra small angle X-ray spectroscopy (U-SAXS)	109.4 [Fig. S2]	
Size distribution	DLS	PDI: 0.08 ± 0.03 [155]	**(+)** Monodisperse micelles
Zeta potential	Electrophoretic light scattering	-4.13 ± 0.24 mV [155]	**(+)** Decreased uptake by MPS **(+)** Reduced protein opsonation **(+)** Reduced unspecific uptake **(+)** Favorable PK properties
NP concentration	NTA	$2.44 \pm 0.28 \times 10^{14}$ NPs x g^{-1} PEG-PCL [Fig. S3]	

Extensive characterization of nanocarriers is of big importance regarding their further use. Physico-chemical properties of NPs determine their *in vivo* behavior such as PK properties and cellular

internalization (Figure 5) [154]. A summary of the physico-chemical characteristics of PEG-PCL micelles used in this PhD project is provided in Table 1 including an expert opinion commenting their importance for the implementation of nanoparticulate drug delivery systems for cancer therapy.

Table 2 Hurdles for nanomedicines in cancer therapy. Adapted from references [154,157–159]. PEG-PCL micelle characteristics were obtained in **Chapters II-IV**.

Factor	Ideal properties	Design consideration	PEG-PCL micelles
Pharmacokinetics	- Low interaction with serum proteins (opsonins) - Stable in circulation - High $t_{1/2}$	- Coating with hydrophilic polymers - Neutral or slightly negative zeta potential - NP size within 10-500 nm	(+) Ideal physico-chemical characteristics (+) Similar PK profile as gold-standard (PEG-liposomes) (?) Interaction with serum proteins (?) PK after multiple dosing
Biodistribution, extravasation and tumor accumulation	- Minimal peripheral (tissue) volume - Extravasation of leaky blood vessels - Low lymphatic clearance	- NP size < 200 nm - High NP concentration in plasma	**(+)** Low volume of distribution **(?)** Tumor extravasation
Tumor penetration	- Efficient and deep penetration of tumor	- Small size (< 200 nm)	**(+)** NP size **(?)** Test in a suitable tumor animal model or 3D cell culture model **(?)** Impact of aspect ratio (elongated NPs vs. spherical NPs)
Tumor cell uptake and intracellular trafficking	- Efficient uptake - Specific uptake	- Active targeting: Target/ligand Surface density	**(+)** Active drug targeting implemented **(?)** Choice of suitable target/ligand
Drug release	- High dose per NP - Efficient release at the site of action	- Active drug loading - Active drug release	**(+)** No burst release observed **(?)** Potent hydrophobic drug **(?)** *In vivo* drug release **(?)** Active drug release **(-)** Low encapsulation efficiency for doxorubicin

A set of “ideal properties” was defined, which is a prerequisite for NPs to be effective *in vivo* (Table 2) [153,157,158,160]. In addition, Table 2 provides information about PEG-PCL micelles used in the present study.

2 Drug Loading, Pharmacokinetics, and Tissue Distribution

In a second step, the model drug doxorubicin was encapsulated in PEG-PCL micelles. The anticancer drug doxorubicin was chosen due to several reasons. First, free doxorubicin is

characterized by unfavorable PK properties. After systemic administration, the drug is removed efficiently from the central plasma compartment [61,76]. Therefore, this drug may profit from advanced drug delivery systems. Consequently, the first nanoparticulate drug delivery system to reach market approval was a lipid-based nanocarrier of doxorubicin (Doxil®) [10]. Second, doxorubicin is characterized by an inherent fluorescence that can be used for imaging. Methods such as confocal laser scanning microscopy or flow cytometry offer the possibility to analyze the interaction of doxorubicin-loaded NPs and cancer cells without further labeling. Third, doxorubicin is a cytotoxic drug. Thus, its pharmacological effect can be studied using established cell viability or cytotoxicity assays. Fourth, tritium-labeled doxorubicin ([^{3}H]-doxorubicin) is commercially available. Liquid scintillation counting (LSC) can be used to determine [^{3}H]-doxorubicin concentrations: Having a sensitive analytical method is a prerequisite for *in vivo* experiments such as determination of PK parameters and tissue distribution. In addition to the methods described in **Chapter II**, [^{3}H]-doxorubicin was used to study the PK profile of liposomes consisting of lipids with different transition temperatures [161]. Fifth, various studies using doxorubicin in the field of oncology are available allowing direct comparison of different formulations: Therefore, the gold standard for long circulating NPs (PEG-liposomes) was used in this study.

Drug loading into PEG-PCL micelles was less efficient than drug loading into PEG-liposomes since an active encapsulation strategy was applied for PEG-liposomes using a pH gradient. The use of active (remote) loading strategies can dramatically increase the encapsulation efficiency [162]. Optimization of a protocol using transmembrane phosphate gradients for the encapsulation of doxorubicin in liposomes, for example, resulted in a 75-fold increase of the loading efficiency as compared to passive loading [163]. However, most active drug loading protocols using ion-gradients cannot be applied to micelles. Therefore, passive loading was used for PEG-PCL micelles resulting in a lower encapsulation efficiency as compared to PEG-liposomes. With respect to passive drug loading, PEG-PCL micelles may however be superior to liposomes for the delivery of highly lipophilic compounds such as paclitaxel, cyclosporine A, or the tyrosine-kinase inhibitor nintedanib. Whereas the loading capacity of the liposomal lipid bilayer is limited, the hydrophobic core of polymeric micelles serves as reservoir for such substances. It was, for example, shown the hydrophobic drug β-carotene (XLogP3: 13.5) was encapsulated efficiently in PEG-PCL micelles whereas a lower encapsulation efficiency and drug loading content was obtained with doxorubicin [164]. The core of polymeric micelles is in general characterized by a remarkable stability [165]. Consequently, doxorubicin was stably encapsulated in PEG-PCL micelles and a slow drug release was observed: Less than 20% of the initial drug content was released after 3 days.

In a next step, the pharmacological effect of doxorubicin was analyzed. Doxorubicin showed similar effects on cell viability and subcellular distribution when applied as free drug, encapsulated in PEG-liposomes, or PEG-PCL micelles. Thus, no benefit on the *in vitro* pharmacological effect of doxorubicin was obtained. Nevertheless, the use of PEG-PCL micelles for the delivery of doxorubicin may be beneficial regarding its *in vivo* performance: A major advantage of nanoparticulate drug delivery systems is the ability to change PK properties of drugs. As mentioned above, free doxorubicin is characterized by poor blood circulation properties and its use is therefore limited. In

addition, accumulation in off-target tissues such as the heart can be dose limiting. Cardiotoxicity is a serious issue related with doxorubicin therapy and is significantly reduced when long-circulating drug carriers are used as compared to administration of the free drug [166,167]. Although previous research was analyzing the PK profile of PEG-PCL NPs (summarized in **Chapter I**), variable particle characteristics such as size and size distribution, surface charge, and drug payload influence the PK profile. Therefore, new NP formulations need to be tested individually. In addition, the experimental procedure (e.g. route of injection, animal species, and anesthesia) and the analytics can strongly influence the experimental outcome of PK studies. To obtain valid results, an established protocol [61,76] using cannulated rats was chosen and the PK profile of PEG-PCL micelles was compared to free doxorubicin and the gold standard for long-circulating drug carriers (PEG-liposomes) in the same experimental setting. Encapsulation of doxorubicin in PEG-PCL micelles dramatically influenced its circulation half-life, plasma clearance, and tissue distribution. A similar behavior was observed for doxorubicin-loaded PEG-liposomes. Thus, the question arises, why alternatives to PEG-liposomes are of big interest? As mentioned above, PEG-PCL micelles show advantages regarding the loading efficiency of hardly soluble drugs. In addition, enhanced clearance of PEG-liposomes upon repeated administration was reported. This phenomenon is called accelerated blood-clearance (ABC) effect and is attributed to an immune response (e.g. anti-PEG-liposome IgM) [168]. The extent of this clearance depends on factors such as architecture and orientation of the PEG coating, type of nanocarrier, encapsulated drug, dose, and dose regimen [169,170]. Thus, chemically versatile PEG-PCL NPs depict an alternative if an immune response and subsequent ABC is observed in patients treated with PEG-liposomes. Importantly, previous studies in pretreated ABC animals showed that PEGylated micelles have a lower cross reactivity *in vivo* as compared to other PEGylated nanocarriers [171].

3 Extravasation, Tumor Accumulation, and Tissue Penetration

Long circulating drug delivery systems such as PEG-PCL micelles that remain in the blood compartment for hours can be used for passive targeting of solid tumors (EPR effect). As outlined in the **Introduction**, such tumors are often characterized by leaky vasculature and show reduced and inefficient lymphatic drainage [63–65,172,173]. As a result, NPs can extravasate from the blood circulation and accumulate at the tumor due to reduced and inefficient removal from the interstitial space. The extravasation to tumors strongly depends on physico-chemical properties of the nanomedicine, the tumor blood flow, the extend and size of the endothelial fenestration (i.e. leakiness), and the TME [174,175]. It has to be considered that tumor-related factors vary significantly within a tumor and between patient subpopulations. This heterogeneity and inadequate patient selection criteria in clinical trials is believed to be one of the main reasons for the poor translation of promising preclinical results into the clinical application [68]. Therefore, the use of diagnostic companion NPs or theranostics is an important consideration for future application of nanomedicines in cancer therapy [153]. In **Chapter III**, a protocol for the preparation of gold-nanohybrid NPs was developed. Encapsulation of gold NPs did not change the physico-chemical properties of the drug

carrier. The nanoreactor protocol was applicable to different types of nanomaterials (i.e. lipid- and polymer-based) and may therefore serve as a valuable strategy for the preparation of diagnostic or theranostic NPs. The protocol could further be adapted for the synthesis of iron oxide-nanohybrids that serve as contrast agents for MRI and PET [87,176,177]. PEG-PCL gold- and iron oxide-nanohybrids, for example, were used for imaging *in vivo* using MRI [176]. The use of PEG-PCL nanohybrids can thus help to identify patients that benefit from nanoparticulate drug delivery and drive the development of personalized treatment approaches. The extent of passive tumor accumulation of PEG-PCL micelles developed in this PhD project needs however to be tested in further experiments (see **Outlook**).

After extravasation and accumulation in the tumor, NPs need to reach the tumor cells. Notably, many solid tumors are characterized by necrotic areas that show a low blood supply and are therefore not accessible via the vascular route. Deep tumor penetration is therefore an important factor for successful treatment of solid tumors using NPs [153]. Several strategies such as modification of the TME or NP decoration with cell penetrating peptides were discussed to enhance the depth and uniformity of tumor penetration. It was shown that the size and shape of NPs strongly influence the extent of tumor penetration: Small NPs and NPs with an elongated shape (i.e. high aspect ratio) penetrate tumor tissue more efficiently and deeply as their spherical counterparts [178]. An adaptation of the preparation protocol for PEG-PCL micelles conducted in our group resulted in the formation of filomicelles (Supplementary Fig. S4) with a high aspect ratio of $\approx 5.2 \pm 1.9$ [179]. These elongated PEG-PCL micelles could therefore be used for the treatment of tumors that have large necrotic areas and are accessible via deep tumor penetration only.

4 Active Drug Targeting and Cellular Internalization

Many drugs that show efficiency in large tumors do not reach metastatic sites. In contrast to solid tumors that may show EPR and allow passive accumulation of long circulating nanomedicines, small tumors and metastases are often characterized by poor vascularization and are less susceptible for passive targeting [56,68,180]. Keeping in mind that the high mortality rate of cancer diseases is often correlated with secondary cancer (i.e. metastases) rather than primary solid tumors, the implementation of active drug targeting strategies that enable specific delivery of drugs to small tumors or metastases is needed. The use of novel high-throughput "-omics" technologies (e.g. proteomics) lead to the detection of surface antigens and receptors that are preferentially expressed on malignant cells. By using targeting moieties such as antibodies to decorate nanoparticulate drug delivery systems, enhanced cellular uptake can be achieved [181]. In **Chapter IV**, targeted PEG-PCL micelles were developed. As a model antibody which might have advantages for glioma therapy as described in the following section, 83-14 mAb was conjugated to PEG-PCL micelles. This antibody is directed against the human insulin receptor (HIR), a receptor that is highly expressed on endothelial cells of the blood-brain barrier (BBB) [182]. The BBB prevents transport of many drugs to the brain and is a major obstacle in the treatment of central nervous system (CNS)-related diseases [183]. Several strategies to overcome this barrier were therefore developed. A promising approach is the

use of so-called Trojan horses, i.e. the use of ligands or antibodies that bind specific receptors on the BBB and promote transport (i.e. transcytosis) of their cargo to the brain [184]. This strategy was used to ferry enzyme-antibody fusion proteins across the BBB with promising results in the treatment of e.g. lysosomal storage diseases [185–187]. The BBB also plays an important role in cancer progression and therapy. The BBB is, for example, a key factor for migration of cancer cells in the development of brain metastases [188]. Since CNS metastases often result in poor prognosis, targeting the BBB and inhibiting cancer cell migration into the brain may depict a promising therapeutic approach. In primary brain tumors, the BBB function is impaired in hypoxic areas of the tumor and can be considered to be leaky: Therefore, the term blood-brain tumor barrier (BBTB) was introduced [189]. This phenomenon can lead to the development of peritumoral edema and tumor-derived seizures [189]. However, in less aggressive and diffuse parts of brain tumors, the BBTB remains its protecting function and shows a high similarity with the intact BBB [190]. The transport of anticancer drugs to these parts of the tumor is therefore limited. Improving the delivery of small molecular drugs and biologics to CNS tumors is thus a prerequisite for efficient treatment of brain tumors and needs to be improved in future therapeutic approaches [191]. Whereas the drug carrying capacity for ADCs and antibody-fusion proteins is limited, NPs can transport a substantial number of drug molecules that exceed ADCs by three to four orders of magnitude [3]. Targeted PEG-PCL micelles developed in this work showed an increased cellular uptake by human brain microvascular endothelial cells. The gold-nanohybrid strategy described in **Chapter III** was used to analyze the intracellular fate of PEG-PCL micelles. An accumulation in multi-vesicular bodies (MVBs) after 60 min of incubation was observed. MVBs are intracellular sorting organs that contain intraluminal vesicles [192]. Interestingly, the endogenous substrate of the HIR, insulin, was found to accumulate in MVBs in a similar manner [193]. However, it needs to be elucidated if PEG-PCL-mediated transport can be translated into the *in vivo* situation. Whereas 83-14 mAb was shown to be transported across the BBB more efficiently than other ligands such as anti-transferrin receptor (TFR) antibodies [194], this promising targeting ligand shows some drawbacks with respect to preclinical testing: Only few species (i.e. primates) may be used for testing 83-14 mAb constructs *in vivo* [195]. Therefore, alternative anti-rodent insulin receptor antibodies such as the 29B4 antibody are of big interest to enable preclinical testing [196]. Alternatively, such targeting strategies may be adapted to other epitopes and receptors such as the TFR, the low-density lipoprotein receptor (LDLR), or the low-density lipoprotein receptor-related protein 1 (LRP1) [197–199].

5 NS1-Therapy for Hepatocellular Carcinoma

The use of anticancer genes and their proteins is a promising therapeutic concept [200,201]. In **Chapter V**, a novel therapeutic strategy to treat liver cancer was established using the H-1PV-derived anticancer gene coding for NS1. NS1 is a multifunctional protein that interacts with various cellular proteins and interferes with several cellular pathways resulting in a multimodal killing of cancer cells: NS1 (H-1PV infection) can promote apoptosis, necrosis, and lysosomal-like programmed cell death [138]. As outlined in the **Introduction**, most tumors do not depend on single

dysregulations and thus the paradigm to target various signaling pathways in cancer treatment was introduced [127,130,131]. The fast development of acquired therapy resistances due to mutation of single cellular targets can dramatically reduce the therapeutic success of anticancer drugs targeting single pathways [129,202]. In contrast, multimodal killing induced by NS1 has a lower risk of acquired resistances since mutation of a single cellular target will be bypassed by complementing toxic effects. In addition, NS1 can be used to treat pre-treated patients that already acquired resistances to chemotherapeutics and apoptosis-inducers such as cisplatin [203]. Furthermore, NS1 is a prodrug that needs to be activated prior to its pharmacological effect. Activation of the PDK1/PKC/PKB signaling pathway is pivotal for NS1 toxicity. As a consequence, NS1-mediated therapy is preferentially toxic for malignantly transformed cells since this signaling cascade frequently shows increased activity in cancer cells. Thus, this strategy has the potential to increase the therapeutic efficiency, to increase tumor specificity, minimizes the risk for development of resistances, and to serve as alternative therapeutic approach for patients suffering from resistances (i.e. bypass resistances) [128,129]. The anticancer gene NS1 and its protein product is therefore an ideal drug for the treatment of cancer. However, most approaches using NS1 in cancer therapy were limited to infection with H-1PV. The rat parvovirus H-1PV was well characterized in preclinical studies and successfully entered a Phase-I/IIa clinical trial for the treatment of patients suffering from recurrent glioblastoma multiforma [138,150,204]. As mentioned above, viral therapeutics may suffer form several drawbacks. Therefore, this project aimed to use non-viral gene delivery methods for the expression of NS1 and to further increase the therapeutic potential of this promising anticancer gene. Established lipoplex NPs (LNPs) were chosen to study non-viral NS1-based therapeutic approaches. LNPs were characterized by a size around 100 nm and a slightly positive zeta potential. LNPs were efficiently internalized by HCC cells *in vitro* and a high transfection efficiency with up to 85% of NS1-GFP positive cells was achieved. The use of positively charged drug delivery vehicles is however limited: After systemic administration, these drug carriers show a fast removal from the central blood compartment and accumulate in off-target tissue such as the lungs [205]. An ideal carrier for NS1 would show long circulating properties and allow targeted delivery to tumor cells while remaining the high transfection efficiency obtained in this study. A strategy to improve this drawback is outline in the **Outlook** of this thesis.

OUTLOOK AND FUTURE PERSPECTIVES

This PhD project aimed to implement nanoparticulate drug delivery systems and novel therapeutic strategies for the treatment of cancer. Several ongoing and future research projects and collaborations were initiated and will further contribute to the development of PEG-PCL micelles for cancer therapy.

1 SCALE-UP AND STORAGE STABILITY

Scale-up of nanoparticulate drug delivery systems remains difficult. Thus, innovative approaches for the formulation of such systems are of big need. Microfluidics (**Chapter III**) is a promising method that shows several advantages over bulk production. This method allows systematic optimization of NP formulations, especially when combined with design of experiments (DoE). In addition, microfluidics-assisted formulation of NPs is a promising tool for transfer of small research-scale batches to large-scale production in clinical research [206]. In a next step, a preparation protocol for PEG-PCL micelles using microfluidics will be established. In preliminary experiments, PEG-PCL micelles with a diameter below 100 nm were obtained using acetone as a solvent. This protocol can further be adapted for drug loading and/or labeling of PEG-PCL micelles.

Although PEG-PCL micelles prepared in this thesis were stable over month when stored in adequate buffer and at reduced temperatures, storage stability of NPs is an important issue. During a master thesis project, a DoE was therefore used for the optimization of freeze-drying of doxorubicin-loaded PEG-PCL micelles (Supplementary Fig. S5) [207]. Lyophilization dramatically improves the storage stability of NPs and allows production of large batches, a major advantage regarding the scale-up of NP formulations [208]. The influence of additives such as bulking agents and cryo-protectants on the parameters size, size distribution, and drug release after NP reconstitution was analyzed [207]. The optimized formulation contained a mix of trehalose and poloxamer 188. After reconstitution, Dox-PEG-PCL micelles showed less than 15% change in mean particle diameter and had a monodisperse size distribution (PDI below 0.2) [207].

2 PEG-PCL MICELLES FOR DELIVERY OF SMALL MOLECULAR DRUGS

Doxorubicin-loaded PEG-PCL micelles will be analyzed in a xenograft model for their capacity to passively accumulate at the tumor site. In a first step, biodistribution of PEG-PCL micelles can be followed by using near infrared dyes such as DiR that allow real-time *in vivo* imaging of small experimental animals. Labeling of PEG-PCL micelles using hydrophobic carbocyanine dyes (DiI) was already performed (**Chapter IV**) and was shown to be feasible. In a next step, concentrations of tritium-labeled doxorubicin in target (tumor) and off-target tissue can be analyzed *ex vivo* as shown in **Chapter II**. In a last step, therapeutic effects induced by doxorubicin encapsulated in PEG-PCL micelles will be analyzed by tracking of tumor volume and overall health status of tumor-bearing animals. In addition, staining of proliferating (Ki67) and apoptotic (TUNEL) tumor cells can be used. A similar approach was used in the preliminary *in vivo* proof-of-concept study of NS1 (**Chapter V**).

Since loading of doxorubicin was suffering from a low encapsulation efficiency and drug loading content, a more hydrophobic drug could be combined with PEG-PCL micelles in a next step. Inhibitors of fibroblast growth factor receptor 4 (FGFR4) are promising candidates for the treatment of liver cancer [209–211]. A couple of candidates are in ongoing clinical trials (e.g. the Novartis compound FGF401 in a Phase I/II clinical trial). The FDA approved FGRF4 (multi-tyrosine kinase) inhibitors nintedanib (BIBF 1120) and ponatinib were successfully used for the treatment of HCC. They showed similar or superior effects as compared to sunatinib, the gold-standard in HCC chemotherapy [209,212]. However, these compounds are characterized by severe side effects (e.g. liver toxicity) and suffer form low water solubility. Therefore, advanced delivery strategies are needed. In collaboration with the research group of Prof. Dr. Walter Berger (Cancer Research Center, Medical University of Vienna, Austria), delivery of FGFR4 inhibitors encapsulated in PEG-PCL micelles will be analyzed. This group has a great expertise in this class of therapeutics and the understanding of acquired resistances during cancer therapy.

3 PEG-PCL Micelles for Targeted Drug Delivery in Vivo

The strategy to develop targeted PEG-PCL micelles shown in **Chapter IV** can be further improved. In a next step, a targeting ligand that can be used for preclinical testing in experimental animals such as mice or rats will be used. For example, conjugation of antibodies directed against LRP1 is a promising approach. Such antibodies were developed by the group of Prof. Dr. Claus Pietrzik (Johannes zu Gutenburg-University, Mainz, Germany) to analyze the influence of LRP1 in BBB transport of Aβ peptides in Alzheimer's disease [213,214]. In addition, this group has developed powerful assays to analyze LRP1-mediated transport *in vitro* and has established an inducible knock-out mouse that is deficient of LRP1 in brain capillary endothelial cells [214]. These tools will allow testing targeted PEG-PCL micelles *in vitro* and *in vivo* for their use as drug delivery vehicles. In preliminary experiments, successful conjugation of these antibodies to PEG-PCL micelles and PEG-liposomes was achieved. These targeted PEG-PCL micelles will now be analyzed for their ability to enhance drug delivery to the brain. Fluorescence correlation spectroscopy (FCS) will further be used to determine and optimize the number of antibodies per PEG-PCL micelle. In addition, the use of gold-nanohybrids (**Chapter III**) will further help to understand the mechanisms of cell interaction and to track targeted micelles after cellular uptake. Besides the potential for treatment of Alzheimer's disease, LRP1 was successfully used for the treatment of brain tumors recently. Angiopep-2, a peptide ligand of LRP1 [215], was conjugated to paclitaxel (ANG1005) [216] or paclitaxel-loaded PEG-PCL NPs [217,218]. These constructs showed superior efficiency in treatment of CNS tumors as compared to free paclitaxel.

4 NS1-Therapy for Hepatocellular Carcinoma

H-1PV-derived NS1 was analyzed as therapeutic intervention for HCC (**Chapter V**). Expression of this oncotoxic protein resulted in specific induction of multimodal cell death in cancer cells whereas healthy primary human hepatocytes were unaffected. Activation of NS1 by cellular kinases

(PDK1/PKC/PKB pathway) that are dysregulated in cancer was found to be major reason for this oncotropism that was previously described for H-1PV in glioma therapy [149]. The analysis of PDK1 status in more than 400 HCC patients (i.e. tissue microarray) is ongoing and results are expected soon. This will give insight in HCC cancer progression and sensitivity of this cancer type to NS1-mediated therapy. In the future, this biomarker can be used for patient stratification and thus to allow personalized medicine. In addition, a targeted RNA sequencing is ongoing to reveal a more detailed mechanistic insight into NS1-induced cell death in liver cancer cells. Finally, a proof-of-concept study in HCC-bearing mice (Hep3B xenograft model) is ongoing to show the potential of NS1 *in vivo*.

The use of positively charged LNPs restricts the use of this therapeutic approach to tumors that are accessible via local delivery [205]. Whereas this may be feasible for cancers such as HCC (e.g. via catheter for chemo-embolization) or melanoma, therapy of delocalized tumors and metastases is not possible. Consequently, future experiments will focus on the development of delivery and targeting strategies. Chemically modified PEG-PCL will be used to prepare PEG-PCL pDNA micelles and to specifically deliver NS1 to cancer cells. As summarized in **Chapter I**, synthesis of PEG-PCL-PEI tri-block copolymers for the formulation of micelles is a promising strategy for systemic nucleic acid delivery. Whereas these polymeric micelles are able to efficiently complex pDNA, their PEG corona renders them long circulating and enables systemic delivery.

To further improve the therapeutic effect of NS1, several combination therapies with small molecules and other biologics were proposed. The simultaneous therapy with H-1PV and sub-toxic doses of valproic acid, for example, increased the therapeutic potential of H-1PV [219]. In another trial, the combination of oncolytic measles vaccine virus and another histone deacetylase (HDAC) inhibitor (resmonistat) with FDA *Orphan Drug* status for liver cancer showed promising results in the treatment of HCC [220]. However, as summarized in **Chapter I**, translating synergistic therapy regimens from the preclinical setup to the patient situation remains difficult. The use of a multi-component nanoparticulate drug carrier for the synchronized delivery of NS1 and a small molecular HDAC inhibitor such as resmonistat could improve the *in vivo* performance of this therapeutic approach. For example, a multi-component PEG-PCL-PEI micelle was used for the simultaneous delivery of siRNA to knock-down the expression of p-glycoprotein (P-gp) and doxorubicin [221]. Additionally, combination of NS1 with other viral proteins such as apoptin or the H-1PV structural (capsid) protein VP1 could further potentiate the toxic effects of NS1. It was shown that NS1 and apoptin can be combined to further enhance the therapeutic effect of NS1 [212]. Similar results were obtained when NS1 was combined with VP1: Combination of these two parvoviral proteins resulted in increased cytotoxicity and several strategies such as the parallel expression or the formation of a NS1 VP1 fusion protein were proposed [213].

CONCLUSION

The use of targeted nanomedicines for the delivery of small molecular drugs and nucleic acids is a promising alternative to conventional chemotherapies. By enhancing the ratio of toxicity in tumor versus non-target cells, these drug carriers can improve the therapeutic index of cancer therapy. Especially in small or delocalized (e.g. metastatic) tumors where radiotherapy and surgical removal are not applicable, there is an urgent need for the development of adequate chemotherapeutics and advanced drug delivery systems. Characterized by biodegradability and biocompatibility, PEG-PCL depicts a promising polymer for the development of such delivery systems. PEG-PCL micelles are long circulating, can be chemically modified to target specific cell types, PEG-PCL gold-nanohybrids can be used for imaging and diagnostics, and PEG-PCL variants are suitable for gene delivery. The proposed drug delivery and drug targeting strategies will be instrumental to implement PEG-PCL micelles for cancer therapy.

ABBREVIATIONS

AAV	Adeno-Associated Virus
ABC	Accelerated Blood-Clearance
ADC	Antibody Drug Conjugate
AUC	Area Under the Plasma Concentration Curve
BBB	Blood-Brain Barrier
BBTB	Blood-Brain Tumor Barrier
CAC	Critical Association Concentration
Cas9	CRISPR Associated Protein 9
CL	Plasma Clearance
CNS	Central Nervous System
CRISPR	Clustered Regularly Interspaced Short Palindromic Repeats
CT	Computer Tomography
DiI	1,1'-Dioctadecyl-3,3,3',3'-Tetramethylindocarbocyanine Perchlorate
DiR	1,1'-Dioctadecyl-3,3,3',3'-Tetramethylindotricarbocyanine Iodide
DLS	Dynamic Light Scattering
DMPK	Drug Metabolism and Pharmacokinetics
DNA	Deoxyribonucleic Acid
DoE	Design of Experiments
EGFR	Endothelial Growth Factor Receptor
ENM	Engineered Nanomaterials
EPR	Enhanced Permeability and Retention Effect
Fab'	Monoclonal Antibody **Fragment**
FDA	U S Food and Drug Administration
FGFR4	Fibroblast Growth Factor Receptor 4
GBM	Glioblastoma Multiforme
GFP	Green fluorescence protein
GM-CSF	Granulocyte-Monocyte Colony-Stimulating Factor
GNP	Gold Nanoparticle
H-1PV	H-1 Parvovirus
HCC	Hepatocellular Carcinoma
HDAC	Histone Deacetylase
HIR	Human Insulin Receptor
IFN	Interferon
IL-2	Interleukin-2
LDLR	Low-Density Lipoprotein Receptor
LNP	Lipoplex Nanoparticle
LRP1	Low-Density Lipoprotein Receptor-Related Protein 1
mRNA	Messenger RNA
miRNA	Micro RNA
MMP	Matrixmetalloprotease
MPS	Mononuclear Phagocyte System
MRI	Magnet Resonance Imaging
MVB	Multi-Vesicular Body
MVM	Minute Virus of Mice
N_{agg}	Aggregation Number
NIR	Near Infrared
NP	Nanoparticle
NS1	Large Non-Structural Protein 1
NTA	Nanoparticle Tracking Analysis
PC	Phosphatidylcholine
PCL	Poly(ε-caprolactone)
PDK1	Phosphoinositide-Dependent Kinase-1
pDNA	Plasmid DNA
PEG	Poly(ethylene glycol)
PEI	Poly(ethyleneimine)
PET	Positron Emission Tomography
PGA	Poly(glycolic acid)
P-gp	P-Glycoprotein
PK	Pharmacokinetics
PKB	Protein Kinase B
PKC	Protein Kinase C
PLA	Poly(lactic acid)
PLGA	Poly(lactide-co-glycolide)
PTEN	Phosphatase and Tensin Homolog Deleted on Chromosome 10

PV	Parvovirus
RNA	Ribonucleic Acid
siRNA	Small Interfering RNA
SLS	Static Light Scattering
ssDNA	Single Strand DNA
$t_{1/2}$	Plasma half-life
TEM	Transmission Electron Microscopy
TFR	Transferrin Receptor
TGF-β	Tumor Growth Factor β
TME	Tumor Microvascular Environment
TUNEL	TdT-Mediated dUTP-Biotin Nick End Labeling
U-SAXS	Ultra Small X-Ray Spectroscopy
V_D	Systemic Volume of Distribution
VEGFR-2	Vascular Endothelial Growth Factor Receptor 2
VP1	H-1 parvovirus structural protein 1
WHO	World Health Organization

BIBLIOGRAPHY

[1] P. Ehrlich, Experimental researches on specific therapy. On immunity with special relationship between distribution and action of antigens., (1908).

[2] C.L. Ventola, The Nanomedicine Revolution, Pharmcol Ther. 37 (2012) 512–517.

[3] A. Wicki, D. Witzigmann, V. Balasubramanian, J. Huwyler, Nanomedicine in cancer therapy: Challenges, opportunities, and clinical applications, J. Controlled Release. 200 (2015) 138–157. doi:10.1016/j.jconrel.2014.12.030.

[4] G. Gregoriadis, Liposome research in drug delivery: The early days: EDITORIAL, J. Drug Target. 16 (2008) 520–524. doi:10.1080/10611860802228350.

[5] A.D. Bangham, M.M. Standish, J.C. Watkins, Diffusion of Univalent Ions across the Lamellae of Swollen Phospholipids, J. Mol. Biol. 13 (1965) 238–252. doi:doi.org/10.1016/S0022-2836(65)80093-6.

[6] G. Gregoriadis, Drug entrapment in liposomes, FEBS Lett. 36 (1973) 292–296. doi:10.1016/0014-5793(73)80394-1.

[7] G. Gregoriadis, B.E. Ryman, Lysosomal localization of β-fructofuranosidase-containing liposomes injected into rats. Some implications in the treatment of genetic disorders, Biochem. J. 129 (1972) 123–133. doi:10.1042/bj1290123.

[8] G. Gregoriadis, P.D. Leathwood, B.E. Ryman, Enzyme entrapment in liposomes, FEBS Lett. 14 (1971) 95–99. doi:10.1016/0014-5793(71)80109-6.

[9] T.M. Allen, C. Hansen, F. Martin, C. Redemann, A. Yau-Young, Liposomes containing synthetic lipid derivatives of poly(ethylene glycol) show prolonged circulation half-lives in vivoLiposomes containing synthetic lipid derivatives of poly(ethylene glycol) show prolonged circulation half-lives in vivo, Biochim. Biophys. Acta BBA-Biomembr. (1991) 29–36. doi:10.1016/0005-2736(91)90246-5.

[10] Y. (Chezy) Barenholz, Doxil® — The first FDA-approved nano-drug: Lessons learned, J. Controlled Release. 160 (2012) 117–134. doi:10.1016/j.jconrel.2012.03.020.

[11] J.M. Barroso, COMMISSION DELEGATED REGULATION (EU) No 1363/2013, 2013.

[12] E.A.J. Bleeker, W.H. de Jong, R.E. Geertsma, M. Groenewold, E.H.W. Heugens, M. Koers-Jacquemijns, D. van de Meent, J.R. Popma, A.G. Rietveld, S.W.P. Wijnhoven, F.R. Cassee, A.G. Oomen, Considerations on the EU definition of a nanomaterial: Science to support policy making, Regul. Toxicol. Pharmacol. 65 (2013) 119–125. doi:10.1016/j.yrtph.2012.11.007.

[13] R. Liang, M. Wei, D.G. Evans, X. Duan, Inorganic nanomaterials for bioimaging, targeted drug delivery and therapeutics, Chem. Commun. 50 (2014) 14071–14081. doi:10.1039/c4cc03118k.

[14] J. Gautier, E. Allard-Vannier, K. Hervé-Aubert, M. Soucé, I. Chourpa, Design strategies of hybrid metallic nanoparticles for theragnostic applications, Nanotechnology. 24 (2013) 432002. doi:10.1088/0957-4484/24/43/432002.

[15] A.C. Anselmo, S. Mitragotri, A Review of Clinical Translation of Inorganic Nanoparticles, AAPS J. 17 (2015) 1041–1054. doi:10.1208/s12248-015-9780-2.

[16] P.D. Robbins, S.C. Ghivizzani, Viral vectors for gene therapy, Pharmacol. Ther. 80 (1998) 35–47. doi:10.1016/S0163-7258(98)00020-5.

[17] X. Zhang, W. Godbey, Viral vectors for gene delivery in tissue engineering☆, Adv. Drug Deliv. Rev. 58 (2006) 515–534. doi:10.1016/j.addr.2006.03.006.

[18] G.Y. Gillespie, J. Roth, G. Friedman, T. Smith, Oncolytic viral therapy: targeting cancer stem cells, Oncolytic Virotherapy. 3 (2014) 21–33. doi:10.2147/OV.S52749.

[19] H. Fukuhara, Y. Ino, T. Todo, Oncolytic virus therapy: A new era of cancer treatment at dawn, Cancer Sci. 107 (2016) 1373–1379. doi:10.1111/cas.13027.

[20] J.J. Nemunaitis, R.H. Andtbacka, M. Ross, T. Amatruda, J. Chesney, F.A. Collichio, K.J. Harrington, N.M. Steven, S. Fourie, L. Dreosti, A. Li, K. Liu, M. Shilkrut, R. Coffin, H. Kaufman, Results of the extension trial of Optim, a multicenter, randomized phase 3 trial of talimogene laherparepvec (T-Vec) vs GM-GSF for unresected stage IIIB-IV melanoma, Ann. Oncol. 25 (2014) 382–382. doi:10.1093/annonc/mdu344.18.

[21] S.V. Talluri, G. Kuppusamy, V.V.S.R. Karri, S. Tummala, S.V. Madhunapantula, Lipid-based nanocarriers for breast cancer treatment – comprehensive review, Drug Deliv. 23 (2016) 1291–1305. doi:10.3109/10717544.2015.1092183.

[22] P. Yingchoncharoen, D.S. Kalinowski, D.R. Richardson, Lipid-Based Drug Delivery Systems in Cancer Therapy: What Is Available and What Is Yet to Come, Pharmacol. Rev. 68 (2016) 701–787. doi:10.1124/pr.115.012070.
[23] P. van Hoogevest, A. Wendel, The use of natural and synthetic phospholipids as pharmaceutical excipients, Eur. J. Lipid Sci. Technol. 116 (2014) 1088–1107. doi:10.1002/ejlt.201400219.
[24] G. van Meer, D.R. Voelker, G.W. Feigenson, Membrane lipids: where they are and how they behave, Nat. Rev. Mol. Cell Biol. 9 (2008) 112–124. doi:10.1038/nrm2330.
[25] G. Bozzuto, A. Molinari, Liposomes as nanomedical devices, Int. J. Nanomedicine. 10 (2015) 975. doi:10.2147/IJN.S68861.
[26] A.O. Elzoghby, Gelatin-based nanoparticles as drug and gene delivery systems: Reviewing three decades of research, J. Controlled Release. 172 (2013) 1075–1091. doi:10.1016/j.jconrel.2013.09.019.
[27] Y. Kodama, T. Nakamura, T. Kurosaki, K. Egashira, T. Mine, H. Nakagawa, T. Muro, T. Kitahara, N. Higuchi, H. Sasaki, Biodegradable nanoparticles composed of dendrigraft poly-l-lysine for gene delivery, Eur. J. Pharm. Biopharm. 87 (2014) 472–479. doi:10.1016/j.ejpb.2014.04.013.
[28] P. Loyer, S. Cammas-Marion, Natural and synthetic poly(malic acid)-based derivates: a family of versatile biopolymers for the design of drug nanocarriers, J. Drug Target. 22 (2014) 556–575. doi:10.3109/1061186X.2014.936871.
[29] M.A. dos Santos, A. Grenha, Polysaccharide Nanoparticles for Protein and Peptide Delivery, in: Adv. Protein Chem. Struct. Biol., Elsevier, 2015: pp. 223–261. http://linkinghub.elsevier.com/retrieve/pii/S1876162314000339 (accessed September 19, 2016).
[30] E. Miele, G.P. Spinelli, E. Miele, F. Tomao, S. Tomao, Albumin-bound formulation of paclitaxel (Abraxane ABI-007) in the treatment of breast cancer, Int J Nanomedicine. 4 (2009) 99–105. doi:10.2147/IJN.S3061.
[31] T.E. Stinchcombe, M.A. Socinski, C.M. Walko, B.H. O'Neil, F.A. Collichio, A. Ivanova, H. Mu, M.J. Hawkins, R.M. Goldberg, C. Lindley, E. Claire Dees, Phase I and pharmacokinetic trial of carboplatin and albumin-bound paclitaxel, ABI-007 (Abraxane®) on three treatment schedules in patients with solid tumors, Cancer Chemother. Pharmacol. 60 (2007) 759–766. doi:10.1007/s00280-007-0423-x.
[32] L. Ducry, ed., Antibody-Drug Conjugates, Humana Press, Totowa, NJ, 2013. http://link.springer.com/10.1007/978-1-62703-541-5 (accessed October 20, 2015).
[33] M.D. Joshi, V. Patravale, R. Prabhu, Polymeric nanoparticles for targeted treatment in oncology: current insights, Int. J. Nanomedicine. 10 (2015) 1001–1018. doi:10.2147/IJN.S56932.
[34] T.K. Dash, V.B. Konkimalla, Poly-ϵ-caprolactone based formulations for drug delivery and tissue engineering: A review, J. Controlled Release. 158 (2012) 15–33. doi:10.1016/j.jconrel.2011.09.064.
[35] H. Liu, E.B. Slamovich, T.J. Webster, Less harmful acidic degradation of poly (lactic-co-glycolic acid) bone tissue engineering scaffolds through titania nanoparticle addition, Int. J. Nanomedicine. 1 (2006) 541–545.
[36] L.W. McKeen, Plastics Used in Medical Devices, in: Handb. Polym. Appl. Med. Med. Devices, Elsevier, 2014: pp. 21–53. http://linkinghub.elsevier.com/retrieve/pii/B9780323228053000037 (accessed September 19, 2016).
[37] M. Santoro, S.R. Shah, J.L. Walker, A.G. Mikos, Poly(lactic acid) nanofibrous scaffolds for tissue engineering, Adv. Drug Deliv. Rev. 107 (2016) 206–212. doi:10.1016/j.addr.2016.04.019.
[38] G.-Y. Liu, C.-J. Chen, J. Ji, Biocompatible and biodegradable polymersomes as delivery vehicles in biomedical applications, Soft Matter. 8 (2012) 8811–8821. doi:10.1039/c2sm25721a.
[39] V.P. Torchilin, Structure and design of polymeric surfactant-based drug delivery systems, J. Controlled Release. 73 (2001) 137–172. doi:10.1016/S0168-3659(01)00299-1.
[40] K.S. Lee, H.C. Chung, S.A. Im, Y.H. Park, C.S. Kim, S.-B. Kim, S.Y. Rha, M.Y. Lee, J. Ro, Multicenter phase II trial of Genexol-PM, a Cremophor-free, polymeric micelle formulation of paclitaxel, in patients with metastatic breast cancer, Breast Cancer Res. Treat. 108 (2008) 241–250. doi:10.1007/s10549-007-9591-y.
[41] R.L. Siegel, K.D. Miller, A. Jemal, Cancer statistics, 2015: Cancer Statistics, 2015, CA. Cancer J. Clin. 65 (2015) 5–29. doi:10.3322/caac.21254.
[42] A. Coates, S. Abraham, S.B. Kaye, T. Sowerbutts, C. Frewin, R.M. Fox, M.H.N. Tattersall, On the receiving end—patient perception of the side-effects of cancer chemotherapy, Eur. J. Cancer Clin. Oncol. 19 (1983) 203–208. doi:10.1016/0277-5379(83)90418-2.

[43] C.A. Lipinski, Drug-like properties and the causes of poor solubility and poor permeability, J. Pharmacol. Toxicol. Methods. 44 (2000) 235–249. doi:doi.org/10.1016/S1056-8719(00)00107-6.
[44] C.A. Lipinski, F. Lombardo, B.W. Dominy, P.J. Feeney, Experimental and computational approaches to estimate solubility and permeability in drug discovery and development settings, Adv. Drug Deliv. Rev. 23 (1997) 3–25. doi:doi.org/10.1016/S0169-409X(00)00129-0.
[45] M.R. Stratton, P.J. Campbell, P.A. Futreal, The cancer genome, Nature. 458 (2009) 719–724. doi:10.1038/nature07943.
[46] S. Valastyan, R.A. Weinberg, Tumor Metastasis: Molecular Insights and Evolving Paradigms, Cell. 147 (2011) 275–292. doi:10.1016/j.cell.2011.09.024.
[47] D. Hanahan, R.A. Weinberg, The hallmarks of cancer, Cell. 100 (2000) 57–70.
[48] D. Hanahan, R.A. Weinberg, Hallmarks of Cancer: The Next Generation, Cell. 144 (2011) 646–674. doi:10.1016/j.cell.2011.02.013.
[49] J. Luo, N.L. Solimini, S.J. Elledge, Principles of Cancer Therapy: Oncogene and Non-oncogene Addiction, Cell. 136 (2009) 823–837. doi:10.1016/j.cell.2009.02.024.
[50] D.J. Benjamin, The efficacy of surgical treatment of cancer, Med. Hypotheses. 40 (1993) 129–138. doi:doi.org/10.1016/0306-9877(93)90143-E.
[51] D.S. Shewach, R.D. Kuchta, Introduction to Cancer Chemotherapeutics, Chem. Rev. 109 (2009) 2859–2861. doi:10.1021/cr900208x.
[52] B.A. Chabner, T.G. Roberts, Chemotherapy and the war on cancer, Nat. Rev. Cancer. 5 (2005) 65–72. doi:10.1038/nrc1529.
[53] C.A. Lipinski, F. Lombardo, B.W. Dominy, P.J. Feeney, Experimental and computational approaches to estimate solubility and permeability in drug discovery and development settings, Adv. Drug Deliv. Rev. 64 (2012) 4–17. doi:doi.org/10.1016/S0169-409X(00)00129-0.
[54] A.K. Ghose, V.N. Viswanadhan, J.J. Wendoloski, A Knowledge-Based Approach in Designing Combinatorial or Medicinal Chemistry Libraries for Drug Discovery. 1. A Qualitative and Quantitative Characterization of Known Drug Databases, J. Comb. Chem. 1 (1999) 55–68. doi:10.1021/cc9800071.
[55] M.J. Waring, J. Arrowsmith, A.R. Leach, P.D. Leeson, S. Mandrell, R.M. Owen, G. Pairaudeau, W.D. Pennie, S.D. Pickett, J. Wang, O. Wallace, A. Weir, An analysis of the attrition of drug candidates from four major pharmaceutical companies, Nat. Rev. Drug Discov. 14 (2015) 475–486. doi:10.1038/nrd4609.
[56] T. Lammers, F. Kiessling, W.E. Hennink, G. Storm, Drug targeting to tumors: Principles, pitfalls and (pre-) clinical progress, J. Controlled Release. 161 (2012) 175–187. doi:10.1016/j.jconrel.2011.09.063.
[57] S. Basavaraj, G.V. Betageri, Can formulation and drug delivery reduce attrition during drug discovery and development—review of feasibility, benefits and challenges, Acta Pharm. Sin. B. 4 (2014) 3–17. doi:10.1016/j.apsb.2013.12.003.
[58] M. Hay, D.W. Thomas, J.L. Craighead, C. Economides, J. Rosenthal, Clinical development success rates for investigational drugs, Nat. Biotechnol. 32 (2014) 40–51. doi:10.1038/nbt.2786.
[59] T. Konno, J. Watanabe, K. Ishihara, Enhanced solubility of paclitaxel using water-soluble and biocompatible 2-methacryloyloxyethyl phosphorylcholine polymers, J. Biomed. Mater. Res. A. 65 (2003) 209–214. doi:10.1002/jbm.a.10481.
[60] S.C. Kim, D.W. Kim, Y.H. Shim, J.S. Bang, H.S. Oh, S.W. Kim, M.H. Seo, In vivo evaluation of polymeric micellar paclitaxel formulation: toxicity and efficacy, J. Controlled Release. 72 (2001) 191–202. doi:10.1016/S0168-3659(01)00275-9.
[61] J. Huwyler, J. Yang, W.M. Pardridge, Receptor mediated delivery of daunomycin using immunoliposomes: pharmacokinetics and tissue distribution in the rat, J. Pharmacol. Exp. Ther. 282 (1997) 1541–1546.
[62] A. Gabizon, H. Shmeeda, Y. Barenholz, Pharmacokinetics of pegylated liposomal doxorubicin, Clin. Pharmacokinet. 42 (2003) 419–436. doi:10.2165/00003088-200342050-00002.
[63] S.K. Hobbs, W.L. Monsky, F. Yuan, W.G. Roberts, L. Griffith, V.P. Torchilin, R.K. Jain, Regulation of transport pathways in tumor vessels: role of tumor type and microenvironment, Proc. Natl. Acad. Sci. 95 (1998) 4607–4612.
[64] J. Fang, H. Nakamura, H. Maeda, The EPR effect: Unique features of tumor blood vessels for drug delivery, factors involved, and limitations and augmentation of the effect, Adv. Drug Deliv. Rev. 63 (2011) 136–151. doi:10.1016/j.addr.2010.04.009.

[65] Y. Matsumura, H. Maeda, A new concept for macromolecular therapeutics in cancer chemotherapy: mechanism of tumoritropic accumulation of proteins and the antitumor agent smancs, Cancer Res. 46 (1986) 6387–6392.
[66] S. Unezaki, K. Maruyama, J.-I. Hosoda, I. Nagae, Y. Koyanagi, M. Nakata, O. Ishida, M. Iwatsuru, S. Tsuchiya, Direct measurement of the extravasation of polyethyleneglycol-coated liposomes into solid tumor tissue by in vivo fluorescence microscopy, Int. J. Pharm. 144 (1996) 11–17. doi:10.1016/S0378-5173(96)04674-1.
[67] S.M. Moghimi, A.C. Hunter, J.C. Murray, Long-Circulating and Target-Specific Nanoparticles: Theory to Practice, Pharmacol. Rev. 53 (2001) 283–318.
[68] J.I. Hare, T. Lammers, M.B. Ashford, S. Puri, G. Storm, S.T. Barry, Challenges and strategies in anti-cancer nanomedicine development: An industry perspective, Adv. Drug Deliv. Rev. 108 (2016) 25–38. doi:10.1016/j.addr.2016.04.025.
[69] A. Schädlich, H. Caysa, T. Mueller, F. Tenambergen, C. Rose, A. Göpferich, J. Kuntsche, K. Mäder, Tumor Accumulation of NIR Fluorescent PEG–PLA Nanoparticles: Impact of Particle Size and Human Xenograft Tumor Model, ACS Nano. 5 (2011) 8710–8720. doi:10.1021/nn2026353.
[70] D.L. Emerson, R. Bendele, E. Brown, S. Chiang, J.P. Desjardins, L.C. Dihel, S.C. Gill, M. Hamilton, J.D. LeRay, L. Moon-McDermott, others, Antitumor efficacy, pharmacokinetics, and biodistribution of NX 211: a low-clearance liposomal formulation of lurtotecan, Clin. Cancer Res. 6 (2000) 2903–2912.
[71] G.G. Dark, A.H. Calvert, R. Grimshaw, C. Poole, K. Swenerton, S. Kaye, R. Coleman, G. Jayson, T. Le, S. Ellard, M. Trudeau, P. Vasey, M. Hamilton, T. Cameron, E. Barrett, W. Walsh, L. McIntosh, E.A. Eisenhauer, Randomized Trial of Two Intravenous Schedules of the Topoisomerase I Inhibitor Liposomal Lurtotecan in Women With Relapsed Epithelial Ovarian Cancer: A Trial of the National Cancer Institute of Canada Clinical Trials Group, J. Clin. Oncol. 23 (2005) 1859–1866. doi:10.1200/JCO.2005.02.028.
[72] M.V. Seiden, F. Muggia, A. Astrow, U. Matulonis, S. Campos, M. Roche, J. Sivret, J. Rusk, E. Barrett, A phase II study of liposomal lurtotecan (OSI-211) in patients with topotecan resistant ovarian cancer, Gynecol. Oncol. 93 (2004) 229–232. doi:10.1016/j.ygyno.2003.12.037.
[73] E. Nogueira, A.C. Gomes, A. Preto, A. Cavaco-Paulo, Design of liposomal formulations for cell targeting, Colloids Surf. B Biointerfaces. 136 (2015) 514–526. doi:10.1016/j.colsurfb.2015.09.034.
[74] A.F. Sikorski, M. Toporkiewicz, J. Meissner, L. Matusewicz, A. Czogalla, Toward a magic or imaginary bullet? Ligands for drug targeting to cancer cells: principles, hopes, and challenges, Int. J. Nanomedicine. (2015) 1399–1414. doi:10.2147/IJN.S74514.
[75] J.T. Duskey, K.G. Rice, Nanoparticle Ligand Presentation for Targeting Solid Tumors, AAPS PharmSciTech. 15 (2014) 1345–1354. doi:10.1208/s12249-014-0143-6.
[76] J. Huwyler, D. Wu, W.M. Pardridge, Brain drug delivery of small molecules using immunoliposomes, Proc. Natl. Acad. Sci. 93 (1996) 14164–14169.
[77] C. Mamot, R. Ritschard, A. Wicki, W. Küng, J. Schuller, R. Herrmann, C. Rochlitz, Immunoliposomal delivery of doxorubicin can overcome multidrug resistance mechanisms in EGFR-overexpressing tumor cells, J. Drug Target. 20 (2012) 422–432. doi:10.3109/1061186X.2012.680960.
[78] C. Mamot, R. Ritschard, A. Wicki, G. Stehle, T. Dieterle, L. Bubendorf, C. Hilker, S. Deuster, R. Herrmann, C. Rochlitz, Tolerability, safety, pharmacokinetics, and efficacy of doxorubicin-loaded anti-EGFR immunoliposomes in advanced solid tumours: a phase 1 dose-escalation study, Lancet Oncol. 13 (2012) 1234–1241. doi:10.1016/ S1470-2045(12)70476-X.
[79] E. Manchado, S. Weissmueller, J.P. Morris, C.-C. Chen, R. Wullenkord, A. Lujambio, E. de Stanchina, J.T. Poirier, J.F. Gainor, R.B. Corcoran, J.A. Engelman, C.M. Rudin, N. Rosen, S.W. Lowe, A combinatorial strategy for treating KRAS-mutant lung cancer, Nature. 534 (2016) 647–651. doi:10.1038/nature18600.
[80] C.-M.J. Hu, L. Zhang, Nanoparticle-based combination therapy toward overcoming drug resistance in cancer, Biochem. Pharmacol. 83 (2012) 1104–1111. doi:10.1016/j.bcp.2012.01.008.
[81] S. Mignani, M. Bryszewska, B. Klajnert-Maculewicz, M. Zablocka, J.-P. Majoral, Advances in Combination Therapies Based on Nanoparticles for Efficacious Cancer Treatment: An Analytical Report, Biomacromolecules. 16 (2015) 1–27. doi:10.1021/bm501285t.
[82] J.E. Cortes, S.L. Goldberg, E.J. Feldman, D.A. Rizzeri, D.E. Hogge, M. Larson, A. Pigneux, C. Recher, G. Schiller, K. Warzocha, H. Kantarjian, A.C. Louie, J.E. Kolitz, Phase II, multicenter, randomized trial of CPX-351 (cytarabine:daunorubicin) liposome injection versus intensive

salvage therapy in adults with first relapse AML: CPX-351 in AML Patients in First Relapse, Cancer. 121 (2015) 234–242. doi:10.1002/cncr.28974.
[83] E.J. Feldman, J.E. Lancet, J.E. Kolitz, E.K. Ritchie, G.J. Roboz, A.F. List, S.L. Allen, E. Asatiani, L.D. Mayer, C. Swenson, A.C. Louie, First-In-Man Study of CPX-351: A Liposomal Carrier Containing Cytarabine and Daunorubicin in a Fixed 5:1 Molar Ratio for the Treatment of Relapsed and Refractory Acute Myeloid Leukemia, J. Clin. Oncol. 29 (2011) 979–985. doi:10.1200/JCO.2010.30.5961.
[84] P. Tardi, S. Johnstone, N. Harasym, S. Xie, T. Harasym, N. Zisman, P. Harvie, D. Bermudes, L. Mayer, In vivo maintenance of synergistic cytarabine:daunorubicin ratios greatly enhances therapeutic efficacy, Leuk. Res. 33 (2009) 129–139. doi:10.1016/j.leukres.2008.06.028.
[85] C.P. McCoy, C. Brady, J.F. Cowley, S.M. McGlinchey, N. McGoldrick, D.J. Kinnear, G.P. Andrews, D.S. Jones, Triggered drug delivery from biomaterials, Expert Opin. Drug Deliv. 7 (2010) 605–616. doi:10.1517/17425241003677731.
[86] H. Yu, J. Chen, S. Liu, Q. Lu, J. He, Z. Zhou, Y. Hu, Enzyme sensitive, surface engineered nanoparticles for enhanced delivery of camptothecin, J. Controlled Release. 216 (2015) 111–120. doi:10.1016/j.jconrel.2015.08.021.
[87] J.H. Ryu, H. Koo, I.-C. Sun, S.H. Yuk, K. Choi, K. Kim, I.C. Kwon, Tumor-targeting multi-functional nanoparticles for theragnosis: New paradigm for cancer therapy, Adv. Drug Deliv. Rev. 64 (2012) 1447–1458. doi:10.1016/j.addr.2012.06.012.
[88] G. Hong, R. Yuan, B. Liang, J. Shen, X. Yang, X. Shuai, Folate-functionalized polymeric micelle as hepatic carcinoma-targeted, MRI-ultrasensitive delivery system of antitumor drugs, Biomed. Microdevices. 10 (2008) 693–700. doi:10.1007/s10544-008-9180-9.
[89] P. Huang, J. Lin, W. Li, P. Rong, Z. Wang, S. Wang, X. Wang, X. Sun, M. Aronova, G. Niu, R.D. Leapman, Z. Nie, X. Chen, Biodegradable Gold Nanovesicles with an Ultrastrong Plasmonic Coupling Effect for Photoacoustic Imaging and Photothermal Therapy, Angew. Chem. Int. Ed. 52 (2013) 13958–13964. doi:10.1002/anie.201308986.
[90] S. Huang, P.K. Upputuri, H. Liu, M. Pramanik, M. Wang, A dual-functional benzobisthiadiazole derivative as an effective theranostic agent for near-infrared photoacoustic imaging and photothermal therapy, J Mater Chem B. 4 (2016) 1696–1703. doi:10.1039/C5TB02367J.
[91] J.-X. Zhou, Ren-xu, J.-X. Zhou, Folate-targeted polymeric micelles loaded with ultrasmall superparamagnetic iron oxide: combined small size and high MRI sensitivity, Int. J. Nanomedicine. (2012) 2863–2872. doi:10.2147/IJN.S25739.
[92] S. Mitragotri, P.A. Burke, R. Langer, Overcoming the challenges in administering biopharmaceuticals: formulation and delivery strategies, Nat. Rev. Drug Discov. 13 (2014) 655–672. doi:10.1038/nrd4363.
[93] Y. Lu, J. Yang, E. Sega, Issues related to targeted delivery of proteins and peptides, AAPS J. 8 (2006) 466–478. doi:10.1208/aapsj080355.
[94] B.S. Parker, J. Rautela, P.J. Hertzog, Antitumour actions of interferons: implications for cancer therapy, Nat. Rev. Cancer. 16 (2016) 131–144. doi:10.1038/nrc.2016.14.
[95] C. Dhalluin, A. Ross, L.-A. Leuthold, S. Foser, B. Gsell, F. Müller, H. Senn, Structural and Biophysical Characterization of the 40 kDa PEG-Interferon-alpha and Its Individual Positional Isomers, Bioconjug. Chem. 16 (2005) 504–517. doi:10.1021/bc049781.
[96] P. Mishra, B. Nayak, R.K. Dey, PEGylation in anti-cancer therapy: An overview, Asian J. Pharm. Sci. 11 (2016) 337–348. doi:10.1016/j.ajps.2015.08.011.
[97] N.C. Ton, G.J.M. Parker, A. Jackson, S. Mullamitha, G.A. Buonaccorsi, C. Roberts, Y. Watson, K. Davies, S. Cheung, L. Hope, F. Power, J. Lawrance, J. Valle, M. Saunders, R. Felix, J.A. Soranson, L. Rolfe, K. Zinkewich-Peotti, G.C. Jayson, Phase I Evaluation of CDP791, a PEGylated Di-Fab' Conjugate that Binds Vascular Endothelial Growth Factor Receptor 2, Clin. Cancer Res. 13 (2007) 7113–7118. doi:10.1158/1078-0432.CCR-07-1550.
[98] P.A. Dinndorf, J. Gootenberg, M.H. Cohen, P. Keegan, R. Pazdur, FDA Drug Approval Summary: Pegaspargase (Oncaspar(R)) for the First-Line Treatment of Children with Acute Lymphoblastic Leukemia (ALL), The Oncologist. 12 (2007) 991–998. doi:10.1634/theoncologist.12-8-991.
[99] V.I. Avramis, P.N. Tiwari, Asparaginase (native ASNase or pegylated ASNase) in the treatment of acute lymphoblastic leukemia, Int. J. Nanomedicine. 1 (2006) 214–254.
[100] V.I. Avramis, S. Sencer, A.P. Periclou, H. Sather, B.C. Bostrom, L.J. Cohen, A.G. Ettinger, L.J. Ettinger, J. Franklin, P.S. Gaynon, others, A randomized comparison of nativeEscherichia coli asparaginase and polyethylene glycol conjugated asparaginase for treatment of children with newly diagnosed standard-risk acute lymphoblastic leukemia: a Children's Cancer Group study, Blood. 99 (2002) 1986–1994. doi:10.1182/blood.V99.6.1986.

[101] A. Abuchowski, T. Van Es, N.C. Palczuk, F.F. Davis, Alteration of immunological properties of bovine serum albumin by covalent attachment of polyethylene glycol., J. Biol. Chem. 252 (1977) 3578–3581.
[102] K.D. Bagshawe, S.K. Sharma, P.J. Burke, R.G. Melton, R.J. Knox, Developments with targeted enzymes in cancer therapy, Curr. Opin. Immunol. 11 (1999) 579–583. doi:10.1016/S0952-7915(99)00004-7.
[103] P. Bailon, W. Berthold, Polyethylene glycol-conjugated pharmaceutical proteins, Pharm. Sci. Technol. Today. 1 (1998) 352–356. doi:10.1016/S1461-5347(98)00086-8.
[104] D. Bobo, K.J. Robinson, J. Islam, K.J. Thurecht, S.R. Corrie, Nanoparticle-Based Medicines: A Review of FDA-Approved Materials and Clinical Trials to Date, Pharm. Res. 33 (2016) 2373–2387. doi:10.1007/s11095-016-1958-5.
[105] J.M. Harris, N.E. Martin, M. Modi, Pegylation, Clin. Pharmacokinet. 40 (2001) 539–551. doi:10.2165/00003088-200140070-00005.
[106] H. Wada, I. Imamura, M. Sako, S. Katagiri, S. Tarui, H. Nishimura, Y. Inada, Antitumor Enzyme: Polyethylene Glycol–modified Asparaginase, Ann. N. Y. Acad. Sci. 613 (1990) 95–108. doi:10.1111/j.1749-6632.1990.tb18151.x.
[107] J. Park, S.H. Wrzesinski, E. Stern, M. Look, J. Criscione, R. Ragheb, S.M. Jay, S.L. Demento, A. Agawu, P. Licona Limon, A.F. Ferrandino, D. Gonzalez, A. Habermann, R.A. Flavell, T.M. Fahmy, Combination delivery of TGF-β inhibitor and IL-2 by nanoscale liposomal polymeric gels enhances tumour immunotherapy, Nat. Mater. 11 (2012) 895–905. doi:10.1038/nmat3355.
[108] S.A. Altınoğlu, M. Wang, K.Q. Li, Y. Li, Q. Xu, Intracellular delivery of the PTEN protein using cationic lipidoids for cancer therapy, Biomater Sci. 4 (2016) 1773–1780. doi:10.1039/C6BM00580B.
[109] P. Uhl, F. Helm, G. Hofhaus, S. Brings, C. Kaufman, K. Leotta, S. Urban, U. Haberkorn, W. Mier, G. Fricker, A liposomal formulation for the oral application of the investigational hepatitis B drug Myrcludex B, Eur. J. Pharm. Biopharm. 103 (2016) 159–166. doi:10.1016/j.ejpb.2016.03.031.
[110] J. Parmentier, B. Thewes, F. Gropp, G. Fricker, Oral peptide delivery by tetraether lipid liposomes, Int. J. Pharm. 415 (2011) 150–157. doi:10.1016/j.ijpharm.2011.05.066.
[111] A.-C. Jacobsen, S.M. Jensen, G. Fricker, M. Brandl, A.H. Treusch, Archaeal lipids in oral delivery of therapeutic peptides, Eur. J. Pharm. Sci. (2017). doi:10.1016/j.ejps.2016.12.036.
[112] E. Keles, Y. Song, D. Du, W.-J. Dong, Y. Lin, Recent progress in nanomaterials for gene delivery applications, Biomater Sci. 4 (2016) 1291–1309. doi:10.1039/C6BM00441E.
[113] M. Rezaee, R.K. Oskuee, H. Nassirli, B. Malaekeh-Nikouei, Progress in the development of lipopolyplexes as efficient non-viral gene delivery systems, J. Controlled Release. 236 (2016) 1–14. doi:10.1016/j.jconrel.2016.06.023.
[114] C.E. Thomas, A. Ehrhardt, M.A. Kay, Progress and problems with the use of viral vectors for gene therapy, Nat. Rev. Genet. 4 (2003) 346–358. doi:10.1038/nrg1066.
[115] C.J. Breitbach, J. Burke, D. Jonker, J. Stephenson, A.R. Haas, L.Q.M. Chow, J. Nieva, T.-H. Hwang, A. Moon, R. Patt, A. Pelusio, F. Le Boeuf, J. Burns, L. Evgin, N. De Silva, S. Cvancic, T. Robertson, J.-E. Je, Y.-S. Lee, K. Parato, J.-S. Diallo, A. Fenster, M. Daneshmand, J.C. Bell, D.H. Kirn, Intravenous delivery of a multi-mechanistic cancer-targeted oncolytic poxvirus in humans, Nature. 477 (2011) 99–102. doi:10.1038/nature10358.
[116] J. Heo, T. Reid, L. Ruo, C.J. Breitbach, S. Rose, M. Bloomston, M. Cho, H.Y. Lim, H.C. Chung, C.W. Kim, J. Burke, R. Lencioni, T. Hickman, A. Moon, Y.S. Lee, M.K. Kim, M. Daneshmand, K. Dubois, L. Longpre, M. Ngo, C. Rooney, J.C. Bell, B.-G. Rhee, R. Patt, T.-H. Hwang, D.H. Kirn, Randomized dose-finding clinical trial of oncolytic immunotherapeutic vaccinia JX-594 in liver cancer, Nat. Med. 19 (2013) 329–336. doi:10.1038/nm.3089.
[117] J.H. Kim, J.Y. Oh, B.H. Park, D.E. Lee, J.S. Kim, H.E. Park, M.S. Roh, J.E. Je, J.H. Yoon, S.H. Thorne, D. Kirn, T.H. Hwang, Systemic Armed Oncolytic and Immunologic Therapy for Cancer with JX-594, a Targeted Poxvirus Expressing GM-CSF, Mol. Ther. 14 (2006) 361–370. doi:10.1016/j.ymthe.2006.05.008.
[118] C. Breitbach, J.C. Bell, T.-H. Hwang, D. Kirn, J. Burke, The emerging therapeutic potential of the oncolytic immunotherapeutic Pexa-Vec (JX-594), Oncolytic Virotherapy. 4 (2015) 25–31. doi:10.2147/OV.S59640.
[119] Assessment of adenoviral vector safety and toxicity: report of the National Institutes of Health Recombinant DNA Advisory Committee, Hum. Gene Ther. 13 (2002) 3–13.
[120] D.W. Pack, A.S. Hoffman, S. Pun, P.S. Stayton, Design and development of polymers for gene delivery, Nat. Rev. Drug Discov. 4 (2005) 581–593. doi:10.1038/nrd1775.

[121] D.J. Glover, H.J. Lipps, D.A. Jans, Towards safe, non-viral therapeutic gene expression in humans, Nat. Rev. Genet. 6 (2005) 299–310. doi:10.1038/nrg1577.
[122] H. Yin, R.L. Kanasty, A.A. Eltoukhy, A.J. Vegas, J.R. Dorkin, D.G. Anderson, Non-viral vectors for gene-based therapy, Nat. Rev. Genet. 15 (2014) 541–555. doi:10.1038/nrg3763.
[123] P. Chollet, M.C. Favrot, A. Hurbin, J.-L. Coll, Side-effects of a systemic injection of linear polyethylenimine–DNA complexes, J. Gene Med. 4 (2002) 84–91. doi:10.1002/jgm.237.
[124] J.W. Wiseman, C.A. Goddard, D. McLelland, W.H. Colledge, A comparison of linear and branched polyethylenimine (PEI) with DCChol/DOPE liposomes for gene delivery to epithelial cells in vitro and in vivo, Gene Ther. 10 (2003) 1654–1662. doi:10.1038/sj.gt.3302050.
[125] T. Endres, M. Zheng, A. Kılıç, A. Turowska, M. Beck-Broichsitter, H. Renz, O.M. Merkel, T. Kissel, Amphiphilic Biodegradable PEG-PCL-PEI Triblock Copolymers for FRET-Capable *in Vitro* and *in Vivo* Delivery of siRNA and Quantum Dots, Mol. Pharm. 11 (2014) 1273–1281. doi:10.1021/mp400744a.
[126] L. Liu, M. Zheng, D. Librizzi, T. Renette, O.M. Merkel, T. Kissel, Efficient and Tumor Targeted siRNA Delivery by Polyethylenimine- *graft* -polycaprolactone- *block* -poly(ethylene glycol)-folate (PEI–PCL–PEG–Fol), Mol. Pharm. 13 (2016) 134–143. doi:10.1021/acs.molpharmaceut.5b00575.
[127] J. Cicenas, E. Cicenas, Multi-kinase inhibitors, AURKs and cancer, Med. Oncol. 33 (2016) 1–11. doi:10.1007/s12032-016-0758-4.
[128] M. Casás-Selves, J. DeGregori, How Cancer Shapes Evolution and How Evolution Shapes Cancer, Evol. Educ. Outreach. 4 (2011) 624–634. doi:10.1007/s12052-011-0373-y.
[129] C. Holohan, S. Van Schaeybroeck, D.B. Longley, P.G. Johnston, Cancer drug resistance: an evolving paradigm, Nat. Rev. Cancer. 13 (2013) 714–726. doi:10.1038/nrc3599.
[130]F. Broekman, Tyrosine kinase inhibitors: Multi-targeted or single-targeted?, World J. Clin. Oncol. 2 (2011) 80. doi:10.5306/wjco.v2.i2.80.
[131] L. Gossage, T. Eisen, Targeting Multiple Kinase Pathways: A Change In Paradigm, Clin. Cancer Res. 16 (2010) 1973–1978. doi:10.1158/1078-0432.CCR-09-3182.
[132] S. Felgner, D. Kocijancic, M. Frahm, S. Weiss, Bacteria in Cancer Therapy: Renaissance of an Old Concept, Int. J. Microbiol. 2016 (2016) 1–14. doi:10.1155/2016/8451728.
[133] E. Kelly, S.J. Russell, History of Oncolytic Viruses: Genesis to Genetic Engineering, Mol. Ther. 15 (2007) 651–659. doi:doi.org/10.1038/sj.mt.6300108.
[134] H. zur Hausen, E.-M. de Villiers, Reprint of: Cancer “Causation” by Infections—Individual Contributions and Synergistic Networks, Semin. Oncol. 42 (2015) 207–222. doi:10.1053/j.seminoncol.2015.02.019.
[135] P.R. Buijs, J.H. Verhagen, C.H. van Eijck, B.G. van den Hoogen, Oncolytic viruses: From bench to bedside with a focus on safety, Hum. Vaccines Immunother. 11 (2015) 1573–1584. doi:10.1080/21645515.2015.1037058.
[136] J.P.F. Nüesch, S. Bär, J. Rommelaere, Viral proteins killing tumor cells: New weapons in the fight against cancer, Cancer Biol. Ther. 7 (2008) 1374–1376. doi:10.4161/cbt.7.9.6743.
[137] S.Y. Yoo, B. Narayanasamy, J. Heo, Viruses as nanomedicine for cancer, Int. J. Nanomedicine. Volume 11 (2016) 4835–4847. doi:10.2147/IJN.S116447.
[138] J.P.F. Nüesch, J. Rommelaere, Tumor Suppressing Properties of Rodent Parvovirus NS1 Proteins and Their Derivatives, in: S. Grimm (Ed.), Anticancer Genes, Springer London, London, 2014: pp. 99–124. doi:10.1007/978-1-4471-6458-6_5.
[139]P. Tattersall, The evolution of parvoviral taxonomy, in: J.R. Kerr, S.F. Cotmore, M.E. Bloom, M.R. Linden, C.R. Parrish (Eds.), The Parvoviruses, Taylor & Francis Group, Boca Raton, FL, 2006.
[140] J.J. Weitzmann, The Parvovirus life cycle: an introduction to molecular interactions important for infection, in: J.R. Kerr, S.F. Cotmore, M.E. Bloom, M.R. Linden, C.R. Parrish (Eds.), The Parvoviruses, Taylor & Francis Group, Boca Raton, FL, 2006.
[141] J.P.F. Nüesch, Regulation of non-structural protein functions by differential synthesis, modification and trafficking, in: J.R. Kerr, S.F. Cotmore, M.E. Bloom, M.R. Linden, C.R. Parrish (Eds.), The Parvoviruses, Taylor & Francis Group, Boca Raton, FL, 2006.
[142] R. Corbau, N. Salomé, J. Rommelaere, J.P.F. Nüesch, Phosphorylation of the Viral Nonstructural Protein NS1 during MVMp Infection of A9 Cells, Virology. 2 (1999) 402–415. doi:10.1006/viro.1999.9786.
[143] L. Daeffler, R. Horlein, J. Rommelaere, J.P.F. Nuesch, Modulation of Minute Virus of Mice Cytotoxic Activities through Site-Directed Mutagenesis within the NS Coding Region, J. Virol. 77 (2003) 12466–12478. doi:10.1128/JVI.77.23.12466-12478.2003.

[144] R. Corbau, V. Duverger, J. Rommelaere, J.P.F. Nüesch, Regulation of MVM NS1 by Protein Kinase C: Impact of Mutagenesis at Consensus Phosphorylation Sites on Replicative Functions and Cytopathic Effects, Virology. 278 (2000) 151–167. doi:10.1006/viro.2000.0600.
[145] S. Dettwiler, J. Rommelaere, J.P. Nüesch, DNA unwinding functions of minute virus of mice NS1 protein are modulated specifically by the lambda isoform of protein kinase C, J. Virol. 73 (1999) 7410–7420.
[146] S. Lachmann, J. Rommeleare, J.P.F. Nuesch, Novel PKC Is Required To Activate Replicative Functions of the Major Nonstructural Protein NS1 of Minute Virus of Mice, J. Virol. 77 (2003) 8048–8060. doi:10.1128/JVI.77.14.8048-8060.2003.
[147] S. Lachmann, S. Bär, J. Rommelaere, J.P.F. Nüesch, Parvovirus interference with intracellular signalling: mechanism of PKCη activation in MVM-infected A9 fibroblasts, Cell. Microbiol. 10 (2008) 755–769. doi:10.1111/j.1462-5822.2007.01082.x.
[148] J.P.F. Nuesch, J. Christensen, J. Rommelaere, Initiation of Minute Virus of Mice DNA Replication Is Regulated at the Level of Origin Unwinding by Atypical Protein Kinase C Phosphorylation of NS1, J. Virol. 75 (2001) 5730–5739. doi:10.1128/JVI.75.13.5730-5739.2001.
[149] S. Bär, J. Rommelaere, J.P. Nüesch, PKCη/Rdx-driven phosphorylation of PDK1: a novel mechanism promoting cancer cell survival and permissiveness for parvovirus-induced lysis, PLoS Pathog. 11 (2015) 1–21. doi:0.1371/journal.ppat.1004703.
[150] A. Marchini, S. Bonifati, E.M. Scott, A.L. Angelova, J. Rommelaere, Oncolytic parvoviruses: from basic virology to clinical applications, Virol. J. 12 (2015) 1–16. doi:10.1186/s12985-014-0223-y.
[151] J.P.F. Nuesch, J. Lacroix, A. Marchini, J. Rommelaere, Molecular Pathways: Rodent Parvoviruses--Mechanisms of Oncolysis and Prospects for Clinical Cancer Treatment, Clin. Cancer Res. 18 (2012) 3516–3523. doi:10.1158/1078-0432.CCR-11-2325.
[152] T. Niidome, L. Huang, Gene Therapy Progress and Prospects: Nonviral vectors, Gene Ther. 9 (2002) 1647–1652. doi:10.1038/sj.gt.3301923.
[153] J. Shi, P.W. Kantoff, R. Wooster, O.C. Farokhzad, Cancer nanomedicine: progress, challenges and opportunities, Nat. Rev. Cancer. 17 (2016) 20–37. doi:10.1038/nrc.2016.108.
[154] J. Shi, P.W. Kantoff, R. Wooster, O.C. Farokhzad, Cancer nanomedicine: progress, challenges and opportunities, Nat. Rev. Cancer. 17 (2016) 20–37. doi:10.1038/nrc.2016.108.
[155] P. Grossen, G. Québatte, D. Witzigmann, C. Prescianotto-Baschong, L.-H. Dieu, J. Huwyler, Functionalized Solid-Sphere PEG-b-PCL Nanoparticles to Target Brain Capillary Endothelial Cells In Vitro, J. Nanomater. 2016 (2016) 1–13. doi:10.1155/2016/7818501.
[156] D. Witzigmann, S. Sieber, F. Porta, P. Grossen, A. Bieri, N. Strelnikova, T. Pfohl, C. Prescianotto-Baschong, J. Huwyler, Formation of lipid and polymer based gold nanohybrids using a nanoreactor approach, RSC Adv. 5 (2015) 74320–74328. doi:10.1039/C5RA13967H.
[157] T. Stylianopoulos, R.K. Jain, Design considerations for nanotherapeutics in oncology, Nanomedicine Nanotechnol. Biol. Med. 11 (2015) 1893–1907. doi:10.1016/j.nano.2015.07.015.
[158] C.M. Dawidczyk, C. Kim, J.H. Park, L.M. Russell, K.H. Lee, M.G. Pomper, P.C. Searson, State-of-the-art in design rules for drug delivery platforms: Lessons learned from FDA-approved nanomedicines, J. Controlled Release. 187 (2014) 133–144. doi:10.1016/j.jconrel.2014.05.036.
[159] J. Huwyler, H. Kettiger, A. Schipanski, P. Wick, Engineered nanomaterial uptake and tissue distribution: from cell to organism, Int. J. Nanomedicine. (2013) 3255–3269. doi:10.2147/IJN.S49770.
[160] T. Sun, Y.S. Zhang, B. Pang, D.C. Hyun, M. Yang, Y. Xia, Engineered Nanoparticles for Drug Delivery in Cancer Therapy, Angew. Chem. Int. Ed. (2014) 12320–12364. doi:10.1002/anie.201403036.
[161] S. Sieber, D. Witzigmann, P. Grossen, P. Detampel, S. Siegfried, J. Huwyler, Zebrafish as early in vivo screening tool for liposome formulation optimization, (2017).
[162] J. Gubernator, Active methods of drug loading into liposomes: recent strategies for stable drug entrapment and increased *in vivo* activity, Expert Opin. Drug Deliv. 8 (2011) 565–580. doi:10.1517/17425247.2011.566552.
[163] A. Fritze, F. Hens, A. Kimpfler, R. Schubert, R. Peschka-Süss, Remote loading of doxorubicin into liposomes driven by a transmembrane phosphate gradient, Biochim. Biophys. Acta BBA - Biomembr. 1758 (2006) 1633–1640. doi:10.1016/j.bbamem.2006.05.028.
[164] F. Cheng, X. Guan, H. Cao, T. Su, J. Cao, Y. Chen, M. Cai, B. He, Z. Gu, X. Luo, Characteristic of core materials in polymeric micelles effect on their micellar properties studied by experimental and dpd simulation methods, Int. J. Pharm. 492 (2015) 152–160. doi:10.1016/j.ijpharm.2015.07.031.

[165] M. Narvekar, H.Y. Xue, J.Y. Eoh, H.L. Wong, Nanocarrier for Poorly Water-Soluble Anticancer Drugs—Barriers of Translation and Solutions, AAPS PharmSciTech. 15 (2014) 822–833. doi:10.1208/s12249-014-0107-x.
[166] A.M. Rahman, S.W. Yusuf, M.S. Ewer, others, Anthracycline induced cardiotoxicity and cardiac-sparing effect of liposomal formulation, Int. J. Nanomedicine. 2 (2007) 567–583.
[167] S.M. Rafiyath, M. Rasul, B. Lee, G. Wei, G. Lamba, D. Liu, Comparison of safety and toxicity of liposomal doxorubicin vs. conventional anthracyclines: a meta-analysis, Exp. Hematol. Oncol. 1 (2012) 1–10. doi:10.1186/2162-3619-1-10.
[168] A.S. Abu Lila, H. Kiwada, T. Ishida, The accelerated blood clearance (ABC) phenomenon: Clinical challenge and approaches to manage, J. Controlled Release. 172 (2013) 38–47. doi:10.1016/j.jconrel.2013.07.026.
[169] T. Ishida, K. Atobe, X. Wang, H. Kiwada, Accelerated blood clearance of PEGylated liposomes upon repeated injections: Effect of doxorubicin-encapsulation and high-dose first injection, J. Controlled Release. 115 (2006) 251–258. doi:10.1016/j.jconrel.2006.08.017.
[170] T. Ishida, H. Kiwada, Accelerated blood clearance (ABC) phenomenon upon repeated injection of PEGylated liposomes, Int. J. Pharm. 354 (2008) 56–62. doi:10.1016/j.ijpharm.2007.11.005.
[171] Y. Deng, C. Wang, X. Cheng, Y. Su, Y. Pei, Y. Song, J. Jiao, Z. Huang, Y. Ma, Y. Dong, Y. Yao, J. Fan, H. Ta, X. Liu, H. Xu, Accelerated blood clearance phenomenon upon cross-administration of PEGylated nanocarriers in beagle dogs, Int. J. Nanomedicine. 10 (2015) 3533–3545. doi:10.2147/IJN.S82481.
[172] N. Bertrand, J. Wu, X. Xu, N. Kamaly, O.C. Farokhzad, Cancer nanotechnology: The impact of passive and active targeting in the era of modern cancer biology, Adv. Drug Deliv. Rev. 66 (2014) 2–25. doi:10.1016/j.addr.2013.11.009.
[173] V. Kumar Khanna, Targeted Delivery of Nanomedicines, ISRN Pharmacol. 2012 (2012) 1–9. doi:10.5402/2012/571394.
[174] H. Kobayashi, R. Watanabe, P.L. Choyke, Improving Conventional Enhanced Permeability and Retention (EPR) Effects; What Is the Appropriate Target?, Theranostics. 4 (2014) 81–89. doi:10.7150/thno.7193.
[175] Y. Nakamura, A. Mochida, P.L. Choyke, H. Kobayashi, Nanodrug Delivery: Is the Enhanced Permeability and Retention Effect Sufficient for Curing Cancer?, Bioconjug. Chem. 27 (2016) 2225–2238. doi:10.1021/acs.bioconjchem.6b00437.
[176] L. Sun, D.Y. Joh, A. Al-Zaki, M. Stangl, S. Murty, J.J. Davis, B.C. Baumann, M. Alonso-Basanta, G.D. Kao, A. Tsourkas, others, Theranostic Application of Mixed Gold and Superparamagnetic Iron Oxide Nanoparticle Micelles in Glioblastoma Multiforme, J. Biomed. Nanotechnol. 12 (2016) 347–356. doi:10.1166/jbn.2016.2173.
[177] G. Lucignani, Nanoparticles for concurrent multimodality imaging and therapy: The dawn of new theragnostic synergies, Eur. J. Nucl. Med. Mol. Imaging. 36 (2009) 869–874. doi:10.1007/s00259-009-1104-2.
[178] V.P. Chauhan, Z. Popović, O. Chen, J. Cui, D. Fukumura, M.G. Bawendi, R.K. Jain, Fluorescent Nanorods and Nanospheres for Real-Time In Vivo Probing of Nanoparticle Shape-Dependent Tumor Penetration, Angew. Chem. Int. Ed. 50 (2011) 11417–11420. doi:10.1002/anie.201104449.
[179]C. Minder, An investigation on self-assembly behaviour of amphiphilic block copolymers, (2013).
[180] A. Schroeder, D.A. Heller, M.M. Winslow, J.E. Dahlman, G.W. Pratt, R. Langer, T. Jacks, D.G. Anderson, Treating metastatic cancer with nanotechnology, Nat. Rev. Cancer. 12 (2011) 39–50. doi:10.1038/nrc3180.
[181] T.M. Allen, Ligand-targeted therapeutics in anticancer therapy, Nat. Rev. Cancer. 2 (2002) 750–763. doi:10.1038/nrc903.
[182] W.M. Pardridge, J. Eisenberg, J. Yang, Human blood—brain barrier insulin receptor, J. Neurochem. 44 (1985) 1771–1778. doi:10.1111/j.1471-4159.1985.tb07167.x.
[183] W.M. Pardridge, Drug Targeting to the Brain, Pharm. Res. 24 (2007) 1733–1744. doi:10.1007/s11095-007-9324-2.
[184] W. Pardridge, Molecular Trojan horses for blood–brain barrier drug delivery, Curr. Opin. Pharmacol. 6 (2006) 494–500. doi:10.1016/j.coph.2006.06.001.
[185] R.J. Boado, Y. Zhang, Y. Zhang, Y. Wang, W.M. Pardridge, GDNF fusion protein for targeted-drug delivery across the human blood–brain barrier, Biotechnol. Bioeng. 100 (2008) 387–396. doi:10.1002/bit.21764.
[186] R.J. Boado, Q.-H. Zhou, J.Z. Lu, E.K.-W. Hui, W.M. Pardridge, Pharmacokinetics and Brain Uptake of a Genetically Engineered Bifunctional Fusion Antibody Targeting the Mouse Transferrin Receptor, Mol. Pharm. 7 (2010) 237–244. doi:10.1021/mp900235k.

[187] R.J. Boado, J.Z. Lu, E.K.-W. Hui, W.M. Pardridge, Insulin Receptor Antibody–Sulfamidase Fusion Protein Penetrates the Primate Blood–Brain Barrier and Reduces Glycosoaminoglycans in Sanfilippo Type A Cells, Mol. Pharm. 11 (2014) 2928–2934. doi:10.1021/mp500258p.
[188] F. Arshad, L. Wang, C. Sy, S. Avraham, H.K. Avraham, Blood-Brain Barrier Integrity and Breast Cancer Metastasis to the Brain, Pathol. Res. Int. 2011 (2011) 1–12. doi:10.4061/2011/920509.
[189] L.G. Dubois, L. Campanati, C. Righy, I. Dâ€™Andrea-Meira, T.C.L. de S. e Spohr, I. Porto-Carreiro, C.M. Pereira, J. BalÃ§a-Silva, S.A. Kahn, M.F. DosSantos, M. de A.R. Oliveira, A. Ximenes-da-Silva, M.C. Lopes, E. Faveret, E.L. Gasparetto, V. Moura-Neto, Gliomas and the vascular fragility of the blood brain barrier, Front. Cell. Neurosci. 8 (2014) 1–13. doi:10.3389/fncel.2014.00418.
[190] O. van Tellingen, B. Yetkin-Arik, M.C. de Gooijer, P. Wesseling, T. Wurdinger, H.E. de Vries, Overcoming the blood–brain tumor barrier for effective glioblastoma treatment, Drug Resist. Updat. 19 (2015) 1–12. doi:10.1016/j.drup.2015.02.002.
[191] U.H. Weidle, J. Niewöhner, G. Tiefenthaler, The Blood–Brain Barrier Challenge for the Treatment of Brain Cancer, Secondary Brain Metastases, and Neurological Diseases, Cancer Genomics-Proteomics. 12 (2015) 167–177.
[192] P.I. Hanson, A. Cashikar, Multivesicular Body Morphogenesis, Annu. Rev. Cell Dev. Biol. 28 (2012) 337–362. doi:10.1146/annurev-cellbio-092910-154152.
[193] A.W. Stitt, H.R. Anderson, T.A. Gardiner, J.R. Bailie, D.B. Archer, Receptor-mediated endocytosis and intracellular trafficking of insulin and low-density lipoprotein by retinal vascular endothelial cells., Invest. Ophthalmol. Vis. Sci. 35 (1994) 3384–3392.
[194] D. Wu, J. Yang, W.M. Pardridge, Drug targeting of a peptide radiopharmaceutical through the primate blood-brain barrier in vivo with a monoclonal antibody to the human insulin receptor., J. Clin. Invest. 100 (1997) 1804–1812. doi:10.1172/JCI119708.
[195] W.M. Pardridge, Y.-S. Kang, J.L. Buciak, J. Yang, Human Insulin Receptor Monocloncal Antibody Undergoes Affinity Binding to Human Brain Capillaries in Vitro and Rapid Transcytosis Through the Blood-Brain Barrier in Vivo in the Primate, Pharm. Res. 12 (1995) 807–816. doi:10.1023/A:1016244500596.
[196] K. Ulbrich, T. Knobloch, J. Kreuter, Targeting the insulin receptor: nanoparticles for drug delivery across the blood–brain barrier (BBB), J. Drug Target. 19 (2011) 125–132. doi:10.3109/10611861003734001.
[197] E.M. Cornford, S. Hyman, M.E. Cornford, G. Chytrova, J. Rhee, T. Suzuki, T. Yamagata, K. Yamakawa, M.L. Penichet, W.M. Pardridge, Non-invasive gene targeting to the fetal brain after intravenous administration and transplacental transfer of plasmid DNA using PEGylated immunoliposomes, J. Drug Target. 24 (2016) 58–67. doi:10.3109/1061186X.2015.1055569.
[198] H. Gao, Progress and perspectives on targeting nanoparticles for brain drug delivery, Acta Pharm. Sin. B. 6 (2016) 268–286. doi:10.1016/j.apsb.2016.05.013.
[199] J. Georgieva, D. Hoekstra, I. Zuhorn, Smuggling Drugs into the Brain: An Overview of Ligands Targeting Transcytosis for Drug Delivery across the Blood–Brain Barrier, Pharmaceutics. 6 (2014) 557–583. doi:10.3390/pharmaceutics6040557.
[200] S. Grimm, Introduction, in: S. Grimm (Ed.), Anticancer Genes, Springer London, London, 2014: pp. 1–8. doi:10.1007/978-1-4471-6458-6_1.
[201] C. Backendorf, M.H.M. Noteborn, Apoptin Towards Safe and Efficient Anticancer Therapies, in: S. Grimm (Ed.), Anticancer Genes, Springer London, London, 2014: pp. 39–59. doi:10.1007/978-1-4471-6458-6_3.
[202] G. Housman, S. Byler, S. Heerboth, K. Lapinska, M. Longacre, N. Snyder, S. Sarkar, Drug Resistance in Cancer: An Overview, Cancers. 6 (2014) 1769–1792. doi:10.3390/cancers6031769.
[203] M. Di Piazza, C. Mader, K. Geletneky, M. Herrero y Calle, E. Weber, J. Schlehofer, L. Deleu, J. Rommelaere, Cytosolic Activation of Cathepsins Mediates Parvovirus H-1-Induced Killing of Cisplatin and TRAIL-Resistant Glioma Cells, J. Virol. 81 (2007) 4186–4198. doi:10.1128/JVI.02601-06.
[204] K. Geletneky, J. Huesing, J. Rommelaere, J.R. Schlehofer, B. Leuchs, M. Dahm, O. Krebs, M. von Knebel Doebritz, B. Huber, J. Hajda, Phase I/IIa study of intratumoral/intracerebral or intravenous/intracerebral administration of Parvovirus H-1 (ParvOryx) in patients with progressive primary or recurrent glioblastoma multiforme: ParvOryx01 protocol, BMC Cancer. 12 (2012) 1–9. doi:10.1186/1471-2407-12-99.
[205] E. Blanco, H. Shen, M. Ferrari, Principles of nanoparticle design for overcoming biological barriers to drug delivery, Nat. Biotechnol. 33 (2015) 941–951. doi:10.1038/nbt.3330.

[206] G.T. Vladisavljević, N. Khalid, M.A. Neves, T. Kuroiwa, M. Nakajima, K. Uemura, S. Ichikawa, I. Kobayashi, Industrial lab-on-a-chip: Design, applications and scale-up for drug discovery and delivery, Adv. Drug Deliv. Rev. 65 (2013) 1626–1663. doi:10.1016/j.addr.2013.07.017.
[207] Z. Hartmann, In Vitro Evaluation of Doxorubicin Loaded PEG-b-PCL Micelles as Alternatives to Pegylated Liposomal Doxorubicin Formulations, (2015).
[208] A.-M. Layre, P. Couvreur, J. Richard, D. Requier, N. Eddine Ghermani, R. Gref, Freeze-Drying of Composite Core-Shell Nanoparticles, Drug Dev. Ind. Pharm. 32 (2006) 839–846. doi:10.1080/03639040600685134.
[209] N. Awasthi, R. Schwarz, Profile of nintedanib in the treatment of solid tumors: the evidence to date, OncoTargets Ther. (2015) 3691–3701. doi:10.2147/OTT.S78805.
[210] M. Hagel, C. Miduturu, M. Sheets, N. Rubin, W. Weng, N. Stransky, N. Bifulco, J.L. Kim, B. Hodous, N. Brooijmans, A. Shutes, C. Winter, C. Lengauer, N.E. Kohl, T. Guzi, First Selective Small Molecule Inhibitor of FGFR4 for the Treatment of Hepatocellular Carcinomas with an Activated FGFR4 Signaling Pathway, Cancer Discov. 5 (2015) 424–437. doi:10.1158/2159-8290.CD-14-1029.
[211] W.-T. Tai, C.-W. Shiau, Y.-S. Li, C.-W. Chang, J.-W. Huang, T.-T. Hsueh, H.-C. Yu, K.-F. Chen, Nintedanib (BIBF-1120) inhibits hepatocellular carcinoma growth independent of angiokinase activity, J. Hepatol. 61 (2014) 89–97. doi:10.1016/j.jhep.2014.03.017.
[212] T. Okusaka, T. Otsuka, H. Ueno, S. Mitsunaga, R. Sugimoto, K. Muro, I. Saito, Y. Tadayasu, K. Inoue, A.-B. Loembé, M. Ikeda, Phase I study of nintedanib in Japanese patients with advanced hepatocellular carcinoma and liver impairment, Cancer Sci. 107 (2016) 1791–1799. doi:10.1111/cas.13077.
[213] T. Pflanzner, M.C. Janko, B. André-Dohmen, S. Reuss, S. Weggen, A.J.M. Roebroek, C.R.W. Kuhlmann, C.U. Pietrzik, LRP1 mediates bidirectional transcytosis of amyloid-β across the blood-brain barrier, Neurobiol. Aging. 32 (2011) 1–11. doi:10.1016/j.neurobiolaging.2010.05.025.
[214] S.E. Storck, S. Meister, J. Nahrath, J.N. Meißner, N. Schubert, A. Di Spiezio, S. Baches, R.E. Vandenbroucke, Y. Bouter, I. Prikulis, C. Korth, S. Weggen, A. Heimann, M. Schwaninger, T.A. Bayer, C.U. Pietrzik, Endothelial LRP1 transports amyloid-β1–42 across the blood-brain barrier, J. Clin. Invest. 126 (2015) 123–136. doi:10.1172/JCI81108.
[215] M. Demeule, J.-C. Currie, Y. Bertrand, C. Ché, T. Nguyen, A. Régina, R. Gabathuler, J.-P. Castaigne, R. Béliveau, Involvement of the low-density lipoprotein receptor-related protein in the transcytosis of the brain delivery vector Angiopep-2, J. Neurochem. 106 (2008) 1534–1544. doi:10.1111/j.1471-4159.2008.05492.x.
[216] Y. Bertrand, J.-C. Currie, J. Poirier, M. Demeule, A. Abulrob, D. Fatehi, D. Stanimirovic, H. Sartelet, J.-P. Castaigne, R. Béliveau, Influence of glioma tumour microenvironment on the transport of ANG1005 via low-density lipoprotein receptor-related protein 1, Br. J. Cancer. 105 (2011) 1697–1707. doi:10.1038/bjc.2011.427.
[217] H. Xin, X. Jiang, J. Gu, X. Sha, L. Chen, K. Law, Y. Chen, X. Wang, Y. Jiang, X. Fang, Angiopep-conjugated poly(ethylene glycol)-co-poly(ε-caprolactone) nanoparticles as dual-targeting drug delivery system for brain glioma, Biomaterials. 32 (2011) 4293–4305. doi:10.1016/j.biomaterials.2011.02.044.
[218] H. Xin, X. Sha, X. Jiang, W. Zhang, L. Chen, X. Fang, Anti-glioblastoma efficacy and safety of paclitaxel-loading Angiopep-conjugated dual targeting PEG-PCL nanoparticles, Biomaterials. 33 (2012) 8167–8176. doi:10.1016/j.biomaterials.2012.07.046.
[219] J. Li, S. Bonifati, G. Hristov, T. Marttila, S. Valmary-Degano, S. Stanzel, M. Schnölzer, C. Mougin, M. Aprahamian, S.P. Grekova, Z. Raykov, J. Rommelaere, A. Marchini, Synergistic combination of valproic acid and oncolytic parvovirus H-1PV as a potential therapy against cervical and pancreatic carcinomas: VPA enhances H-1PV oncotoxicity, EMBO Mol. Med. 5 (2013) 1537–1555. doi:10.1002/emmm.201302796.
[220]B. Ruf, S. Berchtold, S. Venturelli, M. Burkard, I. Smirnow, T. Prenzel, S.W. Henning, U.M. Lauer, Combination of the oral histone deacetylase inhibitor resminostat with oncolytic measles vaccine virus as a new option for epi-virotherapeutic treatment of hepatocellular carcinoma, Mol. Ther. - Oncolytics. 2 (2015) 1–11. doi:10.1038/mto.2015.19.
[221] Y. Wu, Y. Zhang, W. Zhang, C. Sun, J. Wu, J. Tang, Reversing of multidrug resistance breast cancer by co-delivery of P-gp siRNA and doxorubicin via folic acid-modified core-shell nanomicelles, Colloids Surf. B Biointerfaces. 138 (2016) 60–69. doi:10.1016/j.colsurfb.2015.11.041.
[222] P. Fromherz, Instrumentation of handling monomolecular films at an air-water interface., Rev Sci Instrum. 46 (1975) 1380–1385.

ACKNOWLEDGMENT

A great thank you to all the people that supported my during my PhD project!

I would like to thank my doctoral advisor Prof. Dr. Jörg Huwyler for the opportunity to carry out my PhD studies in his guidance during the past years. I would like to thank him for inspiring discussions, the freedom to bring in own project ideas, and the motivation that he gave to me when projects were not working as planned. I'm looking forward for the chance to collaborate in future projects.

I would like to thank to Prof. Dr. Gert Fricker for his co-referee and the good advice that he gave me. In addition, I would like to thank him for the organization of the "Bad Herrenalber Transportertage" where I met a lot of interesting people and was able to initiate research collaborations.

I would like to thank Dr. Jürg Nüesch for being expert in my PhD committee and for his supervision during my master thesis in Heidelberg. It was a pleasant experience working together with him and I'm thankful for the great collaboration we had during my PhD thesis.

I would like to thank my supervisor Dr. Gabriela Quèbatte. It was great working together with her on several projects, to discuss scientific topics, and to talk about weekends, holidays, and other important things in live. I wish you and your family all the best in the future.

A big thank you goes to Dr. Dominik Witzigmann. I'm thankful for his scientific advices, inputs, and for the projects we we're working on together. Moreover I would like to thank him for the nice time that we had during the past years. I hope you will have a great time in Canada with your family!

I would like to thank all the members of the research group of pharmaceutical technology. I'm thankful for the great time I had while working on my PhD project! In particular I would like to thank Jonas Buck, Emre Cörek, Roger Roth, Andreas Schittny, Sandro Sieber, Stefan Siegrist, Dr. Dominik Witzigmann, the "Thirsty Thursday Club", for nice discussions, cold beers to cool down smoking heads, and the support during the thesis. I would like to thank Dr. Pascal Detampel, Dr. Le-Ha Dieu, Dr. Maxim Puchkov, and Dr. Susanne Schenk for their help during my PhD project, scientific advice, and the time that I was able to spend with them. In addition I would like to thank Darryl Borland, Dominique Ditter, Tim Dreckmann, Tomaz Einfalt, Marzia Farzal, Christina Häuser, Klara Kiene, Jana Kovac, Julia Riede, Denise Ruoff, Jessica Schulz, Mahsa Sedighi, and Leonie Wagner-Hattler for their support during my PhD thesis, the funny moments during the student practicals, and the nice "Glühwein sessions".

I would like to thank the Zoe Hartmann, Anne-Kathrin Julen, and Xue-Ting Tran for the chance to supervise their master thesis projects. It was a great experience working together with them.

I would like to thank all the collaborators that contributed to this thesis. In particular I would like to thank Prof. Dr. Walter Berger and Sushilla van Schoonhoven from the Medical University of Vienna; Prof. Dr. Claus Pietrzik and Dr. Steffen Storck from the Medical University of Mainz; Cristina Prescianotto-Baschong, Dr. Moussin Oufir, and Dr. Timothy Sharpe from the University of Basel; Prof. Dr. Andreas Wicki, Dr. Luca Quagliate, Dr. Cristina Quintavalle, and David Grünig form the University Hospital of Basel; and Prof. Dr. Jean Rommelaere from the German Cancer Research Center (DKFZ) in Heidelberg. I would like to thank them for their open-minded attitude that allowed fruitful collaborations and that was expanding my horizon. A special thank you goes to Bernhard Englinger. It was great working together with him in Heidelberg during my master thesis and to collaborate during my PhD project. But besides the scientific collaborations, I would like to thank him for nice bike trips, holidays, and bar tours.

I would like to thank my family, Anne and Beat Ruckstuhl, Rebecca Grossen and Wilma Mengel as well as Johannes, Barbara, Peter, Anne-Sophie, Marie-Luise, Matthias, and Milène Grossen for their support during my studies and PhD project. Without their help, this would have never been possible!

I would like to thank Simone Candel for her support during the past years. I would like to thank her for her patience and motivating words!

I would like to thank my friends from the “Langenthaler Hochwasser Beer Brewery”, my band “The Late Night Show”, “Mac Dähler and the Bacon”, my Handball Team (HVL), the “Straffer-Hendrik Pikett Team”, the “Megadüdlers” and “Mhmm Raclette isch fein” group, and all my other friends. I’m looking forward for many years to come.

SUPPLEMENTARY INFORMATION

S1. Nanoparticle Tracking Analysis

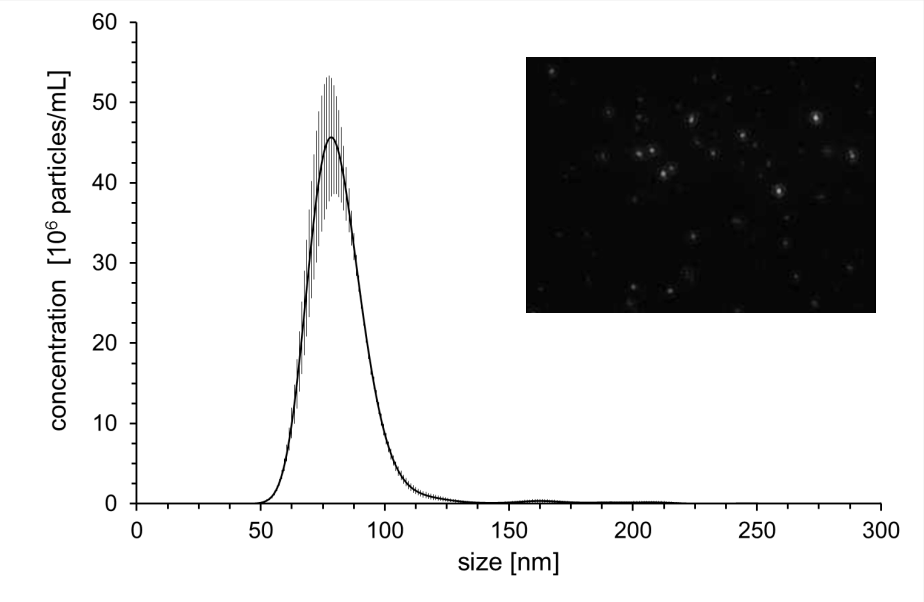

Figure S1 Nanoparticle Tracking Analysis of of PEG-PCL micelles. Size distribution represents mean ± S.D. of $n = 5$ measurements. Insert: representative video frame.

Table S1 Nanoparticle Tracking Analysis of PEG-PCL micelles. Values represent means ± S.D. of $n = 5$ experiments.

	PEG-PCL-NPs
Mean [nm] ± SE	83.2 ± 0.9
Mode [nm] ± SE	78.8 ± 1.5
D10 [nm] ± SE	67.1 ± 0.8
D90 [nm] ± SE	95.9 ± 1.1
Conc [NPs/mL] ± SE	$1.22 \times 10^9 \pm 1.44 \times 10^8$

Experimental section.

NTA analysis of NP size and size distribution was performed using the Nanosight NS300 equipped with a 405 nm laser (Malvern Instruments Ltd, Instrumat AG, Switzerland). In brief, the chamber was cleaned with fresh PBS (Sigma-Aldrich, PBS, D8537) and analyzed to confirm the absence of any particles. The PEG-PCL micelle suspensions were diluted 1:1000 in PBS and injected using 1 mL sterile syringes. For the video recording the syringe pump speed was set to 50. The temperature was kept between 25.7°C ± 0.1, the camera level was set to 11 and detection threshold was set to 2. A total number of 1498 frames were recorded using a sCMOS camera and analyzed using the NTA 3.1 Build 3.1.54 software. Five video recordings of each sample were performed. Aggregation number (N_{agg}) of PEG-PCL micelles was calculated using the particle concentration obtained in NTA analysis. The number of PEG-PCL unimers per mL was therefore divided by the particle concentration that was measured by NTA.

S2. Ultra-small angle X-ray scattering analysis

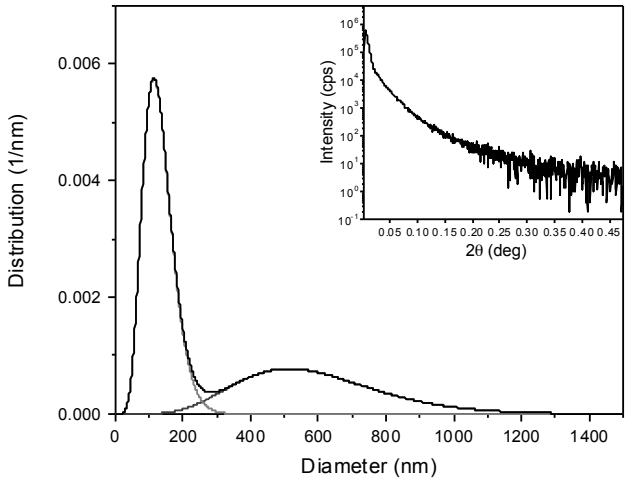

Figure S2 Ultra-small angle X-ray scattering analysis of PEG-PCL micelles.

Table S2 Ultra-small angle X-ray scattering analysis of PEG-PCL micelles.

		PEG-PCL-NPs
Distribution 1	**Mean [nm]**	**109.4**
	Max. probability [nm]	**100**
	Volume [%]	**49.47**
Distribution 2	Mean [nm]	497.1
	Max. probability [nm]	381.6
	Volume [%]	50.53
Average (1+2)	Mean [nm]	305.3
	R-factor	0.0373

Experimental section.

Ultra small-angle X-ray scattering (U-SAXS) measurements were performed on Rigaku SmartLab diffractometer equipped with 9kW rotating anode generator, 2-bounce Ge (220) monochromator and high resolution U-SAXS 2-bounce channel crystal analyser (Rigaku Corporation, Tokyo, Japan). The samples (~50 mg/mL in miliQ water) were filled in glass capillaries (0.9 mm diameter, 0.01 mm wall thickness, Hilgenberg, Malsfeld, Germany) and exposed to X-rays of Cu wavelength (1.541 Å). Scattered X-rays were recorded on SC-70S scintillation counter detector (Rigaku Corporation, Tokyo, Japan) in range of 0 – 0.5 2θ scattering angle. Sample to detector distance was 300 mm. The optics were set as follow: parallel beam slit, 2-bounce Ge (220) monochromator, incident parallel open soller slit, 1 mm incident slit, 10 mm length limiting slit on the incident arm of the goniometer and 2 mm receiving slit #1, U-SAXS analyser, receiving parallel 5.0 deg soller slit, 20 mm receiving slit #2 on the receiving arm of the goniometer. Recorded data were analysed with Particle-/Pore-size Analysis Software NANO-Solver 3.7 (Rigaku Corporation, Tokyo, Japan). Results are shown of $n = 1$ experiments.

S3. Langmuir through

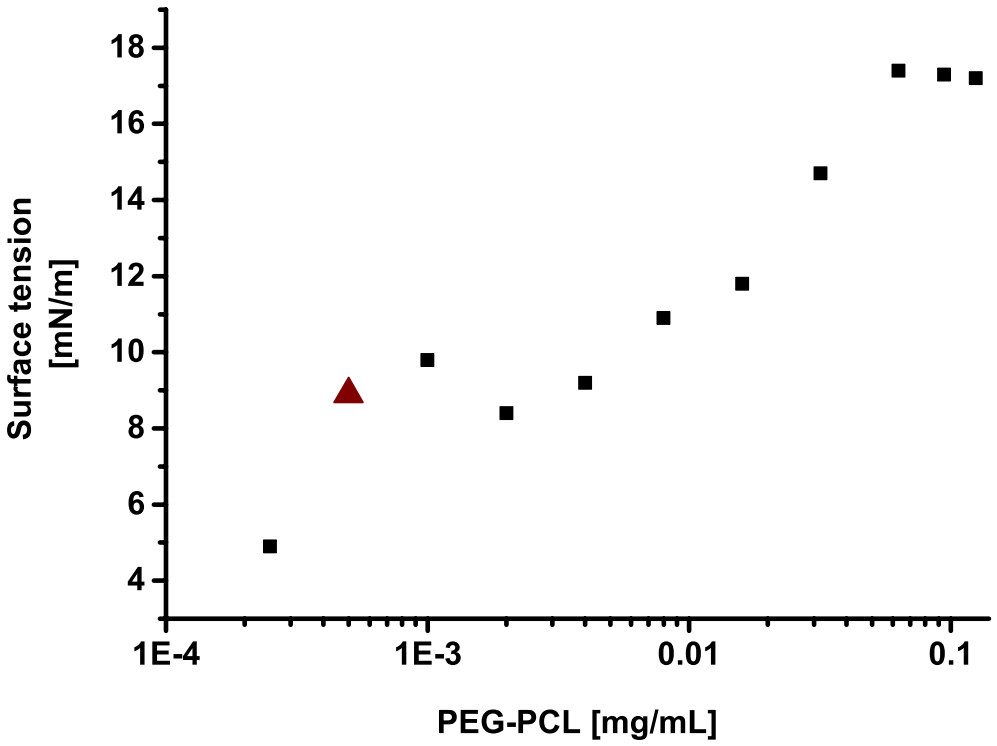

Figure S3 Determination of the critical aggregation concentration (CAC) by surface activity measurments. The CAC is indicated with a red triangle at a PEG-PCL concentration of 0.5 µg/mL (2.8 x 10^{-7} M).

Experimental section.

Measurement of surface activity were performed on a round Teflon trough designed by Fromherz [222]. Measurement was performed at room temperature and 20 mL filling volume compartment was used. The surface pressure was measured by the Wilhelmy method by using plates cut from filter paper (Whatman no. 1). Before each measurement, the trough and the filter paper were cleaned with ethanol and nanopure water. The filter paper was left to equilibrate in water until a constant surface tension was reached. The surface tension, γ_0, of water was set to zero and the surface pressure, π, of the PEG-PCL, which is the difference between the surface tension of pure water, γ_0, and the surface tension of water containing the PEG-PCL, γ, was recorded – i.e. $\pi = \gamma_0 - \gamma$.

Water was stirred with a tiny magnet and small aliquots of the PEG-PCL solution in THF (5 mg/mL) were added. The surface pressure was monitored until the equilibrium was reached. Results are shown of n = 1 experiment.

S4. Filomicelles

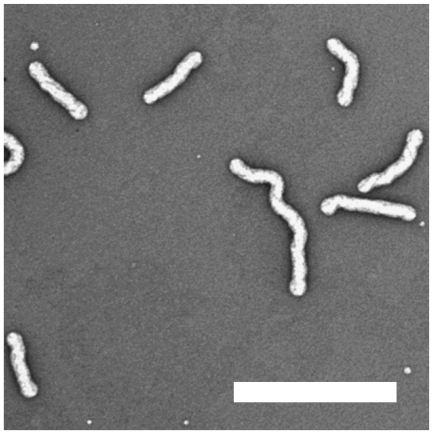

Figure S4 Transmission electron micrograph of PEG-PCL filomicelles after negative staining with uranylacetate. Scale bar: 500 nm.

Experimental section.

PEG-PCL filomicelles were prepared as described previously [179]. In brief, 10 mg of PEG-PCL were dissolved in 1 mL of THF. Then, 10 mL of water were added dropwise under constant stirring at 700 rpm. After 30 min, the suspension was dialyzed (12-14 kDa MWCO) against water for 24 h. Water was exchanged every 8 h to remove traces of THF. NP size and shape was analyzed by transmission electron microscopy (TEM) using a CM-100 (Philips, Eindhoven, Netherlands) operating at 80 kV. Samples were mounted on a 400-mesh carbon copper grid that was pre-exposed to plasma (10 sec) for increased sample binding. Samples were negatively stained unsing a 2% uranylacetate solution (Sigma Aldrich, Buochs, Switzerland) and were dried at room temperature over night.

S5. Lyophilization of Dox-PEG-PCL micelles

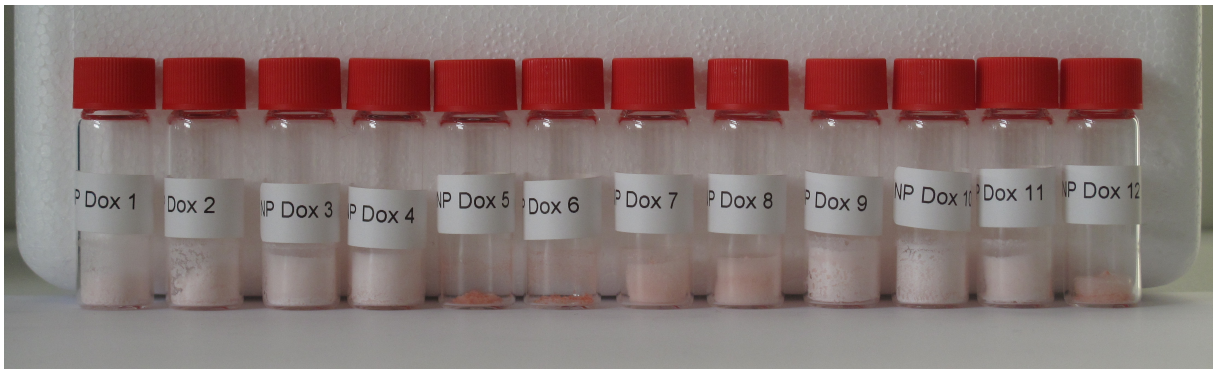

Figure S5 Lyophilizates of Dox-PEG-PCL micelles.

Experimental section and results are summarized in [207].